MEASUREMENT OF DEUTERON TENSOR POLARIZATION IN ELASTIC ELECTRON SCATTERING

Kenneth K. Gustafsson

PP# 00-078

2000

Chapter 1

Introduction

Nuclear physics traces its roots back to the very beginning of the last century. The concept of the nuclear atom was introduced by Rutherford around 1910. The discovery of the neutron by Chadwick in 1932 gave us the concept of two nucleons: the proton (p) and the neutron (n). Yukawa postulated in 1935 that the ("strong") nuclear force interacted via the exchange of π-mesons. The discovery of the π-meson by Powell in 1947 confirmed Yukawa's theoretical model. The hadronic picture of nuclear matter had been born. In this picture baryons (p, n, Λ, Σ, ...) interact via the exchange of mesons (π, ρ, η, ...).

In 1964 Gell-Mann and Zweig introduced the quark model of hadrons. The model depicts hadrons as composite particles consisting of quarks which interact via exchange of gluons. In the quark picture baryons are three-quark composite systems while mesons are quark-antiquark composite systems. The quark model was soon after its introduction confirmed by experiments performed at high en-

ergies.

The hadron (quark) picture is valid in the low (high) energy regime. A central problem in nuclear physics is to explore the transition regime in which the hadronic picture starts failing and the quark degrees of freedom start dominating. Probing few-nucleon systems* with electromagnetic probes, for example scattering electrons from deuterons, provides opportunities to explore this transition regime.

The JLab electron accelerator with its intermediate energy high current continuous wave beam combined with the Hall C high resolution electron spectrometer and a deuteron recoil polarimeter provided experiment E94018 [1, 2] with the opportunity to study the deuteron electromagnetic structure, in particular to measure the tensor polarization observable t_{20}, at higher four momentum transfers than ever before. This dissertation presents results of JLab experiment E94018.

The remainder of this first chapter will present some basic properties of the deuteron, introduce formalism associated with the experiment, give an overview of various theoretical models, and discuss previous measurements of t_{20}.

The experimental setup of the calibration measurement performed at Saturne and in particular the experimental setup of the tensor polarization t_{20} measurement performed at JLab is described in Chapter 2. The data reduction and the data analysis are covered in Chapter 3. The results of the JLab experiment

*The definition of few-nucleon implied here is that the mass number A is less than five ($A < 5$). The bound nuclei in question are: ^{1}H, ^{2}H, ^{3}H, ^{3}He, and ^{4}He.

are presented in Chapter 4 and they are compared to predictions of theoretical models. A summary with concluding remarks together with a brief review of future prospects are also given in Chapter 4. Results of the luminosity scan data analysis are presented in Appendix B.

1.1 Deuteron Properties

The deuteron (a ^{2}H nucleus) consists of a proton and a neutron. It is the lightest of all composite nuclei and has the unique property of having an abnormally low binding energy per nucleon, with no excited bound states. The binding energy E_b of the deuteron is 2.22 MeV, that is 1.11 MeV/nucleon, which is roughly a factor of eight lower than what is typical for stable nuclei (between 7-9 MeV/nucleon [3]).

The parity of the deuteron is positive. The wave function of the deuteron Ψ_D, can be separated into three parts: a proton part, a neutron part, and a component associated with the orbital wave function for the relative motion between the proton and the neutron. The proton and the neutron are an isospin doublet, each with the same intrinsic parity, so the product of their parity is positive. Consequently the orbital wave function component determines the parity of the deuteron.

The angular momentum L determines the parity of the orbital wave function and the positive parity implies even values of L. The total angular mo-

mentum of the deuteron $\vec{J} = \vec{L} + \vec{S}$ is unity*. There are only two ways of combining even values of orbital angular momentum with a total spin of S=0,1 ($\vec{S}_{\rm p} + \vec{S}_{\rm n} = \frac{\vec{1}}{2} + \frac{\vec{1}}{2} = \vec{0}, \vec{1}$) such that the total angular momentum J equals one: (L,S)=(0,1) or (L,S)=(2,1). This means that the deuteron wave function is a quantum mechanical superposition of S- and D-waves and it can be written as:

$$\Psi_{\rm D} \equiv \Psi_{\rm J=1,M} = \frac{1}{\sqrt{4\pi}} \left[\frac{u(r)}{r} + \frac{1}{\sqrt{8}} \frac{w(r)}{r} {\rm S}_{12}(\hat{r}) \right] \chi_{\rm 1,M} \ , \tag{1.1}$$

where $\frac{u(r)}{r}$ and $\frac{w(r)}{r}$ are the radial wave functions, $\chi_{\rm 1,M}$ is the spin component of the wave function, ${\rm S}_{12}(\hat{r})$ is the tensor operator, r is the magnitude of the relative position vector of the nucleons in the deuteron, and $\hat{r} = \frac{\vec{r}}{|\vec{r}|}$. The tensor operator is defined as:

$${\rm S}_{12}(\hat{r}) = 3(\sigma_1 \cdot \hat{r})(\sigma_2 \cdot \hat{r}) - \sigma_1 \cdot \sigma_2, \tag{1.2}$$

where $\sigma_{\rm i}$ are the Pauli spin matrices. The radial wave functions are normalized to unity:

$$\int_0^\infty dr \ [u^2 + w^2] = 1. \tag{1.3}$$

For large $|\vec{r}|$ values the radial wave functions can be written as:

*This can be concluded based on a magnetic moment argument [4].

$$u(r) \to \mathrm{A_s} e^{-\gamma r}, r \to \infty, \tag{1.4}$$

and:

$$w(r) \to \mathrm{A_D} e^{-\gamma r} \left[1 + \frac{3}{\gamma r} + \frac{3}{(\gamma r)^2} \right], r \to \infty, \tag{1.5}$$

where $\gamma = \frac{\sqrt{M_d E_b}}{\hbar}$, and $\mathrm{A_S}$ and $\mathrm{A_D}$ are their asymptotic amplitudes. The asymptotic ratio $\left(\frac{\mathrm{D}}{\mathrm{S}}\right)$ is defined as:

$$\xi \equiv \frac{\mathrm{A_D}}{\mathrm{A_S}} = \lim_{r \to \infty} \frac{w(r)}{u(r)}. \tag{1.6}$$

It is of great interest to know the amount of D-state admixture in the deuteron wave function. This can be quantified by the D-state probability defined as:

$$\mathrm{P_D} = \int_0^\infty dr \; w^2(r). \tag{1.7}$$

Although $\mathrm{P_D}$ is not an observable, typical values inferred from measurements are in the range of 4-7% [3].

Having established some important properties of the deuteron wave function Ψ_D, one can continue by using the wave function in the impulse approximation (IA) to compute various other important quantities. The deuteron magnetic dipole moment can be expressed as:

Mass M_d (MeV) [6]	1875.613 39 ± 0.000 57
Binding energy E_b (MeV) [7]	2.224 573 1 ± 0.000 002 2
Spin/Parity J^π	1^+
Isospin I	0
Magnetic dipole moment μ_d (μ_N) [8]	0.857 406 ± 0.000 001
Electric quadrupole moment Q_d (fm^2) [9]	0.285 90 ± 0.000 30
Root-mean-square radius r_d (fm) [10]	1.962 7 ± 0.003 8
Asymptotic S-wave amplitude (A_S) [17]	0.8846 ± 0.0008
Asymptotic $\left(\frac{D}{S}\right)$-wave ratio ξ [17]	0.0256 ± 0.0004

Table 1.1: Some basic properties of the deuteron ^{2}H.

$$\mu_d^{IA} = \mu_p + \mu_n - \frac{3}{2}\left(\mu_p + \mu_n - \frac{1}{2}\right) P_D, \tag{1.8}$$

where μ_p and μ_n are the dipole moments of the proton and neutron, respectively. The deuteron quadrupole moment is written as:

$$Q_d^{IA} = \frac{1}{\sqrt{50}} \int_0^\infty dr\ r^2 \left[u(r)w(r) - \frac{1}{\sqrt{8}} w^2(r)\right]. \tag{1.9}$$

Finally the expression for the deuteron root-mean-square radius is [5]:

$$r_d^2 = \frac{1}{4} \int_0^\infty dr\ r^2(u^2 + w^2). \tag{1.10}$$

Measured values of all of these quantities are shown in Table 1.1. The above discussion of the static properties of the deuteron will next be followed by a discussion of dynamic properties of the deuteron.

As the deuteron is a spin 1 object its electromagnetic structure can be completely described with three form factors [6]: the charge monopole form factor $G_{\rm C}(Q^2)$, the magnetic dipole form factor $G_{\rm M}(Q^2)$, and the charge quadrupole form factor $G_{\rm Q}(Q^2)$. Here the four momentum transfer squared Q^2 in electron scattering is defined as:

$$Q^2 \equiv -q_\mu^2 = -q^\mu q_\mu = -(\omega^2 - |\vec{q}\,|^2) \simeq 4E_{\rm e}E'_{\rm e}\sin^2\left(\frac{\theta_{\rm e}}{2}\right), \qquad (1.11)$$

where $E_{\rm e}$ is the energy of the incident electron, $E'_{\rm e}$ is the energy of the scattered electron, and $\theta_{\rm e}$ is the scattering angle of the electron. Using the four electromagnetic form factors of the free nucleons: $G_{\rm E}^{\rm p}$, $G_{\rm E}^{\rm n}$, $G_{\rm M}^{\rm p}$, and $G_{\rm M}^{\rm p}$ in the impulse approximation, i.e. assuming that the nuclear current is given by the sum of the free nucleon currents, one can write out expressions for the deuteron electromagnetic form factors. The charge monopole form factor $G_{\rm C}$ can be written as:

$$G_{\rm C} = (G_{\rm E}^{\rm p} + G_{\rm E}^{\rm n}) \int dr(u^2 + w^2)\ {\rm j}_0\left(\frac{qr}{2}\right), \qquad (1.12)$$

where in this expression $\mathrm{q} = |\vec{q}|$ is the magnitude of the three momentum transfer (see Equation 1.11) and $\mathrm{j_n(x)}$ is the $\mathrm{n^{th}}$ order spherical Bessel function. The magnetic dipole form factor $G_{\rm M}$ can be expressed as:

$$G_{\rm M} = 2(G_{\rm M}^{\rm p} + G_{\rm M}^{\rm n}) \int dr \left\{ \left[u^2 - \frac{w^2}{2} \right] {\rm j}_0 \left(\frac{qr}{2} \right) \right\}$$
$$+ \frac{3}{2}(G_{\rm E}^{\rm p} + G_{\rm E}^{\rm n}) \int dr\ w^2 \left[{\rm j}_0 \left(\frac{qr}{2} \right) + {\rm j}_2 \left(\frac{qr}{2} \right) \right], \qquad (1.13)$$

and finally the expression for the charge quadrupole form factor $G_{\rm Q}$ is:

$$G_{\rm Q} = \frac{3}{\eta\sqrt{2}}(G_{\rm E}^{\rm p} + G_{\rm E}^{\rm n}) \int dr\ w \left(u - \frac{w}{\sqrt{8}} \right) {\rm j}_2 \left(\frac{qr}{2} \right). \qquad (1.14)$$

In order to accurately calculate the deuteron electromagnetic form factors one needs to know as well as possible the four free nucleon electromagnetic form factors $G_{\rm E/M}^{\rm N}$. A typical parameterization of the free nucleon form factors is to use the dipole parameterization for the proton electric form factor:

$$G_{\rm E}^{\rm p}(Q^2) = \frac{1}{\left[1 + (\frac{Q}{M_V})^2 \right]^2}\ , \qquad (1.15)$$

where $M_V = 0.84$ GeV [7]. The proton magnetic form factor is then $G_{\rm M}^{\rm p} = \mu_{\rm p} G_{\rm E}^{\rm p}$, and the neutron magnetic form factor is ${\rm G}_{\rm M}^{\rm n} = \mu_{\rm n} {\rm G}_{\rm E}^{\rm p}$. The neutron electric form factor ${\rm G}_{\rm E}^{\rm n}$ is, however, poorly known and consequently increases the uncertainty of the calculated deuteron quantities.

1.2 Experimental Formalism

The differential cross section for elastic scattering of unpolarized electrons by unpolarized deuterons can be written as:

$$\frac{\mathrm{d}\sigma}{\mathrm{d}\Omega} = \left(\frac{\mathrm{d}\sigma}{\mathrm{d}\Omega}\right)_{\mathrm{Mott}} \times \frac{1}{1 + \frac{2E_\mathrm{e}}{M_\mathrm{d}} \sin^2(\frac{\theta_\mathrm{e}}{2})} \times S. \tag{1.16}$$

Here the first term $\left(\frac{\mathrm{d}\sigma}{\mathrm{d}\Omega}\right)_{\mathrm{Mott}}$ stands for the Mott scattering cross section which describes the scattering of a spin $\frac{1}{2}$ (structureless) electron by an infinitely heavy structureless nucleus. The expression for the Mott cross section is:

$$\left(\frac{d\sigma}{d\Omega}\right)_{\mathrm{Mott}} = \frac{\mathrm{Z}^2\alpha^2 \cos^2(\frac{\theta_\mathrm{e}}{2})}{4E_\mathrm{e}^2 \sin^4(\frac{\theta_\mathrm{e}}{2})}, \tag{1.17}$$

where Z is the electric charge of the target nucleus (for deuterium, Z=1), α is the fine structure constant. In Equation 1.16 above M_d stands for the target rest mass (deuteron). The second term in Equation 1.16 takes into account the recoil of the target nucleus. Finally the third term S stands for:

$$S = A(Q^2) + B(Q^2) \tan^2\left(\frac{\theta_\mathrm{e}}{2}\right), \tag{1.18}$$

where $A(Q^2)$ and $B(Q^2)$ are the longitudinal and transverse structure functions of the deuteron, respectively. World data on these two structure functions are shown in Figure 1.1 ($A(Q^2)$) and in Figure 1.2 ($B(Q^2)$). The relation between

the four momentum transfer Q^2 and the kinetic energy $T_{\rm d}$ of the recoil deuteron in elastic e-d scattering is:

$$Q^2 = 2\ M_{\rm d}\ T_{\rm d}. \tag{1.19}$$

The deuteron longitudinal structure function $A(Q^2)$ is dependent on all three deuteron electromagnetic form factors:

$$A(Q^2) = G_{\rm C}^2(Q^2) + \frac{8}{9}\eta^2 G_{\rm Q}^2(Q^2) + \frac{2}{3}\eta G_{\rm M}^2(Q^2), \tag{1.20}$$

where $\eta = \frac{Q^2}{4M_{\rm d}^2}$ is a kinematical factor. The transverse structure function $B(Q^2)$ depends only on $G_{\rm M}(Q^2)$:

$$B(Q^2) = \frac{4}{3}\eta(1+\eta)G_{\rm M}^2(Q^2). \tag{1.21}$$

Because the deuteron is a spin 1 object, an assembly of deuterons can simultaneously be both vector ($t_{1\rm j}$) and tensor polarized ($t_{2\rm j}$). The vector polarization t_{10} can be expressed as:

$$t_{10} = \sqrt{\frac{3}{2}}\left(\frac{\rm N_+ + N_-}{\rm N_+ + N_0 + N_-}\right), \tag{1.22}$$

where $\rm N_\pm$ is the fraction of deuterons in its $|1, \pm 1>$ spin state and $\rm N_0$ is the fraction of deuterons in its $|1, 0>$ spin state. The deuteron tensor moment t_{20} can be expressed in the same intuitive way:

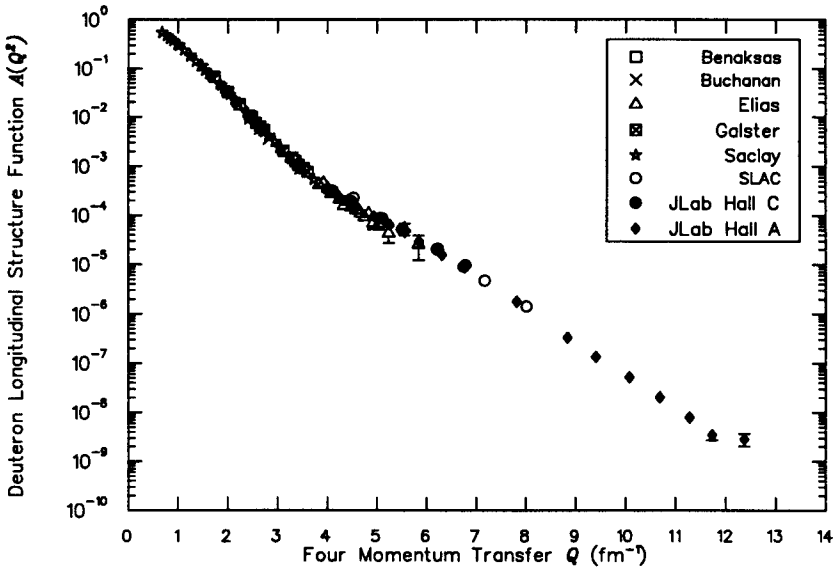

Figure 1.1: The deuteron longitudinal structure function $A(Q^2)$.

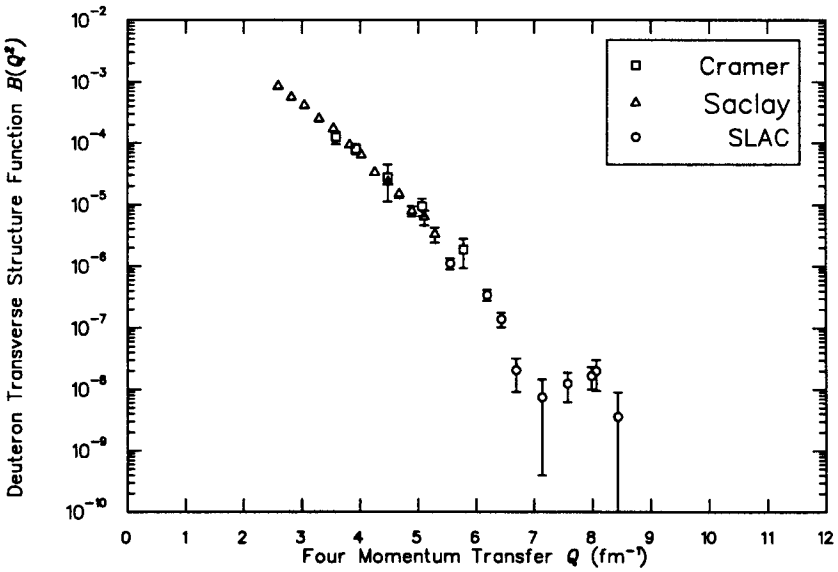

Figure 1.2: The deuteron transverse structure function $B(Q^2)$.

$$t_{20} = \frac{1}{\sqrt{2}} \left(\frac{N_+ + N_- - 2N_0}{N_+ + N_0 + N_-} \right). \tag{1.23}$$

That is, t_{20} is simply a measure of how these three states are populated. It can be shown from Equation 1.23 that the upper and lower boundaries for the t_{20} value are: $t_{20}^{max} = \frac{+1}{\sqrt{2}}$ and $t_{20}^{min} = -\sqrt{2}$.

For elastic e-d scattering the tensor moments t_{ij} can be expressed using the deuteron electromagnetic form factors:

$$t_{20}(G_C, G_Q, G_M, \theta_e) = \frac{-1}{S\sqrt{2}} \left\{ \frac{8}{3}\eta G_C G_Q + \frac{8}{9}\eta^2 G_Q^2 + \frac{1}{3}\eta \left[1 + 2(1+\eta) \tan^2 \left(\frac{\theta_e}{2} \right) \right] G_M^2 \right\}, \tag{1.24}$$

$$t_{21}(G_Q G_M, \theta_e) = \frac{2\eta}{S\sqrt{3}} \left[\eta + \eta^2 \sin^2 \left(\frac{\theta_e}{2} \right) \right]^{\frac{1}{2}} G_M G_Q \sin \left(\frac{\theta_e}{2} \right), \tag{1.25}$$

$$t_{22}(G_M^2) = \frac{-\eta}{2\sqrt{3}S} G_M^2, \tag{1.26}$$

and

$$t_{11}(G_C G_M, G_Q G_M, \theta_e) = \frac{2}{S\sqrt{3}} \sqrt{\eta(1+\eta)} G_M \left(G_C + \frac{1}{3}\eta G_Q \right) \tan \left(\frac{\theta_e}{2} \right). \tag{1.27}$$

The JLab E94018 experiment was a double scattering experiment where the first scattering reaction was the elastic e-d scattering $^2H(\mathrm{e}, \mathrm{e}' \overleftrightarrow{\mathrm{d}})$ process described above. The second scattering was a charge exchange (CE) reaction $^1H(\overleftrightarrow{\mathrm{d}}, \mathrm{pp})\mathrm{n}$ where the recoil deuterons were scattered from a hydrogen target and proton-proton pairs were detected in the final state. The CE reaction is illustrated in Figure 1.3. The CE reaction was studied first theoretically as a potential candidate for an analyzing reaction within an impulse approximation model by Wilkin et al. [8, 9, 10]. Their calculation gave promisingly large analyzing powers and a large cross section for incident deuterons with kinetic energies in the region of interest, up to about 500 MeV. Their prediction was later experimentally confirmed as mentioned in Section 2.2.4.

The cross section $\sigma(\theta, \phi)$ of the CE reaction depends on the incident polarization through:

$$\sigma(\theta, \phi) = \sigma_0(\theta) \left[1 + t_{20} T_{20}(\theta) + 2t_{21} T_{21}(\theta) \cos\phi + 2t_{22} T_{22}(\theta) \cos(2\phi)\right], \tag{1.28}$$

where $\sigma_0(\theta)$ is the cross section for an unpolarized beam, t_{ij} are the tensor polarizations, T_{ij} are the analyzing powers, θ is the polar angle, and ϕ is the angle between the normal of the reaction plane and the spin axis of the incident deuteron (see also Section 3.3.4).

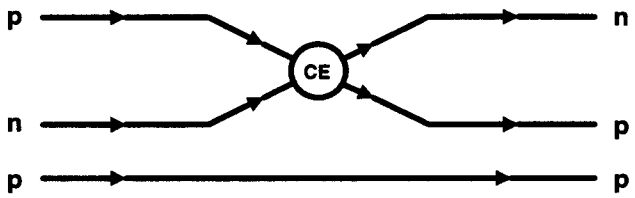

Figure 1.3: A schematic of the charge exchange reaction $^1H(\overleftrightarrow{\mathrm{d}}, \mathrm{pp})\mathrm{n}$.

1.3 Theoretical Overview

The electromagnetic form factors of the deuteron play a very important role in trying to understand the nucleon-nucleon (NN) interaction. As the deuteron observables $A(Q^2)$, $B(Q^2)$, and $t_{20}(Q^2)$ can be expressed by help of the deuteron electromagnetic form factors G_C, G_M, and G_Q these observables, are often calculated by theorists to compare directly with the data. A number of theoretical models exist that make predictions for $A(Q^2)$, $B(Q^2)$, and $t_{20}(Q^2)$. One can cast the various models into five major categories: non-relativistic, relativistic, quark-hadron models, the Skyrme model, and models based on perturbative quantum chromodynamics (pQCD).

It should be noted as a general statement (although not applicable to all models) that the "parameter space" of the theoretical models is quite vast, i.e. a specific model is characterized by, for example, its choice of parameterizations of the free nucleon form factors, its choice of a NN-potential, and its choice of the strengths of certain less-well-known coupling constants required in meson

exchange diagrams when included. This adds to the complexity of comparing differences between models. Moreover, the predictions of the "best" model must, for the same choice of input parameters, reproduce as well as possible the measured data of all three deuteron observables.

Because of the lack of high quality t_{20} data above $Q^2 = 20$ fm^{-2}, consistently good reproduction of all three of $A(Q^2)$, $B(Q^2)$, and t_{20} has remained a challenge. In this Section a brief qualitative description of the various types of models will be given. They are described in slightly more detail in ref. [11] and complete descriptions are found in the references given for each specific type of model. Predictions will not be shown until Chapter 4 where they are compared with the experimental data, and with that from E94018 in particular.

1.3.1 Non-relativistic Models

The non-relativistic impulse approximation (NRIA) is the basis for the traditional models. In the impulse approximation one assumes that the virtual photon emitted by the scattered electron interacts with only one of the nucleons in the deuteron while the other nucleon acts as a passive spectator. This process is illustrated in Figure 1.4. The interaction vertex is a γNN vertex and a proper Feynman graph is shown in Figure 1.5 (a).

The Schrödinger equation is used to produce the deuteron wave function Ψ_D in the non-relativistic approach. In this conventional approach the nuclear force

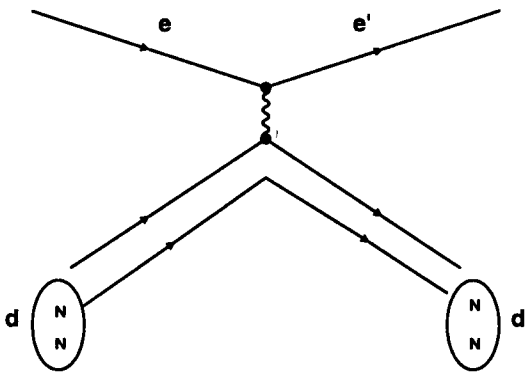

Figure 1.4: Schematic Feynman graph of elastic e-d scattering as envisioned in the one-photon exchange (Born) approximation.

between two nucleons is described by the exchange of mesons. The long-range part of the nuclear force is described by the exchange of a single pion while the medium- and short-range parts are described by two-pion exchange and exchanges of other mesons such as ρ, ω, and σ^*, as illustrated in Figure 1.5 (b) (an example of a specific type of a meson exchange current which is described below). Some of the mesons are charged and as a consequence their motion in the nucleus produces a current. In addition, the exchange of a neutral meson can also produce a current through the recoil of a charged nucleon. In electron-nucleus scattering the virtual photon can couple to either a nucleon or to an exchange meson. The time ordering of the virtual photon-nucleon/meson coupling is of importance as different interaction configurations give rise to different Feynman amplitudes. These meson exchange current (MEC) contributions must be accounted for but in elastic e-d scattering only isoscalar (T=0) MECs can contribute because the

*The σ meson (S=0,T=0) is an artifact used to simulate the effects of two-pion exchange.

deuteron is an isospin zero nucleus (isospin is conserved in strong interactions).

There are two important constraints which must be satisfied by the MEC calculations. Both MEC and relativistic corrections are taken into account through current operators. So, on the one hand, the meson exchange current operator must satisfy the continuity equation with respect to the NN potential used in generating the deuteron wave function Ψ_D. This assures that the nuclear electromagnetic amplitudes are gauge invariant. On the other hand, by modeling the nucleus as a mixture of nucleons and exchange mesons one introduces a non-zero probability for finding mesons inside the nuclei. To account for these exchange mesons the nuclear wave function must therefore be renormalized. In Figure 1.5 (c) a MEC of the recoil type is illustrated and in Figure 1.5 (d) the mesonic MEC type is shown. For a detailed discussions on meson exchange currents the reader is referred to [12].

The radial partial wave functions $u(r)$ and $w(r)$ defined in Section 1.1 above are obtained from the radial Schrödinger equation using a given NN-potential. A number of NN-potentials have been developed during the years. Some of the potentials most commonly found in the literature are the Paris [13], the Nijmegen [14], the Reid [15], and the Argonne v_{18} potentials, which are of configuration space type, and various Bonn potentials [16], which are of momentum space type.

As outlined in ref. [17], the NN-potentials are traditionally constructed by fitting np-scattering data for T=0 states and either np- or pp-scattering data

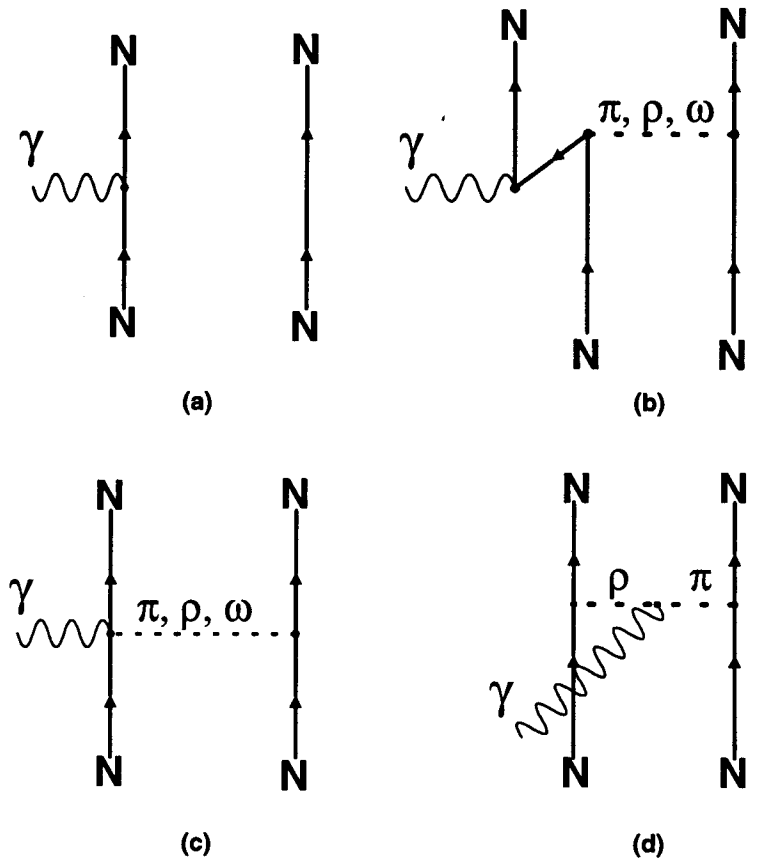

Figure 1.5: (a) A Feynman graph of elastic e-d scattering in the Born approximation. The nucleon on the left interacts at the γNN vertex while the nucleon on the right is only a spectator. (b) A meson exchange current of the pair type. The exchanged meson can be a π, ρ, or an ω meson. (c) A meson exchange current of the recoil type. (d) A meson exchange current of the mesonic type. The exchanged ρ-meson is transformed into a π-meson after absorption of the virtual photon at the $\rho\pi\gamma$ interaction vertex.

for T=1 states. Most Bonn potentials use np-data for the T=1 channel while the Reid, the Nijmegen, and the Paris potentials use the pp-scattering data for the T=1 channel. The advantage of the Argonne v_{18} NN-potential is that it is constructed using both np-scattering data ($T = 0$ and $T = 1$ channels) and pp-scattering data ($T = 1$ channel) as well as low-energy nn-scattering parameters and deuteron properties [17].

1.3.2 Relativistic Models

The need for relativistic models has grown as modern nuclear physics measurements are being carried out at increasingly larger four momentum transfers and increasing energy transfers. For the experiments carried out at JLab, typical four momentum transfers are of the same order as the mass of the nucleon (≈ 1 GeV).

There are two main categories of relativistic models: explicitly covariant quantum field models (QFM) and relativistic Hamiltonian dynamics (RHD) models. There are two main subcategories in the QFM approach: one which is based on the Bethe-Salpeter equation (BSE) [18] or its three dimensional (3D) reduction and another which is based on Light Front Dynamics (LFD). In the BSE formalism the electromagnetic amplitudes are evaluated based on Feynman diagrams and their associated rules. The 3D reduction approach of the BSE formalism results in equations of the "quasi-potential" type [19].

Quantum Field Models

- **Bethe-Salpeter formalism**

  Salpeter and Bethe applied the relativistic S-matrix formalism of Feynman to a bound-state problem of two interacting fermions and hence derived what became to be known as the Bethe-Salpeter equation [18]. The BSE can be written in a very general form as [20]:

$$M = V + \int V\ G\ M, \tag{1.29}$$

  where M is the scattering amplitude, V is the relativistic kernel, and G is the free two-nucleon propagator. The usual characteristic of all quasipotential equations is the replacement of the free two-nucleon propagator by a new propagator that includes a delta-function constraining the relative energy of the intermediate states and thereby reducing the four-dimensional equation to three dimensions [21].

  Gross, Van Orden and collaborators have performed calculations within the quasipotential equation framework [22]. They used a one-boson-exchange (OBE) model using the Gross (spectator) equation. In their calculation the spectator nucleon is restricted to its positive mass shell [20]. This approach can be viewed as a covariant manifestation of the non-relativistic potential models based on the physics of meson exchange.

Hummel and Tjon used also a quasipotential OBE model in their calculations but both nucleons were treated in a symmetrical way, i.e. both nucleons were equally off the mass shell ("equally off-shell formalism") [23, 24]. They studied relativistic two-loop contributions from both the $\rho\pi\gamma$ and the $\omega\epsilon\gamma$ meson exchange currents.

Phillips, Wallace and Devine have done calculations within the framework of an instant quasipotential formalism. The reduction to three-dimensions is done by performing integrations over the 0^{th} component of the relative momentum of the nucleon-nucleon system, i.e. they did not use δ-functions in their reduction scheme. Their approach leads to the construction of "Equal-Time" (ET) Green's functions [25, 26, 27, 28]. They used a OBE model for the NN-interaction and included the following six mesons (masses in MeV in parenthesis): $\pi(138)$, $\eta(549)$, $\sigma(550)$, $\rho(769)$, $\omega(782)$, and $\delta(983)$. They also considered the contribution from the $\rho\pi\gamma$ MEC [29] and observed an improvement in the agreement with particularly the data of the deuteron observable $A(Q^2)$. In their calculations they have been able to include the following effects of relativity: negative-energy states, relativistic kinematics, the effect of boosting the two-body system from one Lorentz frame to another, and including relativistic pieces of the electromagnetic current. As they have pointed out, it is of importance to retain the gauge invariance of electromagnetism [29], i.e. the constructed deuteron electromagnetic cur-

rent must be conserved.

- **Light Front Dynamics**

  In the LFD approach the state vector describing the system is expanded in Fock components with increasing numbers of particles. The state vector is defined in a four dimensional spacetime. The Fock components, the relativistic wave functions in the LFD formalism, are direct generalizations of the non-relativistic wave functions. Carbonell and Karmanov have performed calculations using the LFD formalism [30, 31, 32] and they made predictions for the deuteron observables. They used a relativistic deuteron wave function with a Bonn OBE kernel. It should be noted that relativistic dynamics and MECs are naturally included in the LFD formalism except for the $\rho\pi\gamma$ MEC.

Relativistic Hamiltonian Dynamics

Both Coester [33, 34] and Frankfurt [35] have performed calculations based on a Hamiltonian light-front dynamics formalism, also called Light Cone Quantum Mechanics. This formalism depicts the quantum mechanics of particles in contrast to the quantum mechanics of fields that was described in the paragraphs above. This approach allows the construction of internally consistent Poincaré invariant models of elastic e-d scattering that use conventional deuteron wave functions and empirical nucleon form factors. These models are mathematically consistent for

arbitrarily high momentum transfers. The relativistic covariance in these models is achieved by boosting the amplitudes calculated in one special Lorentz frame to any arbitrary Lorentz frame [20].

1.3.3 Quark-Hadron Models

The general goal of quark-hadron models is to bridge the gap between the domain of nucleon degrees of freedom and the domain of quark degrees of freedom by combining ingredients of both types of models within one single model. This has been done within the framework of the quark cluster model (QCM) which is a natural extension of the non-relativistic constituent quark model for one baryon to two or more interacting baryons.

One expects the quark degrees of freedom to dominate the short-range region (corresponding to $r < 0.8 - 1.0$ fm in coordinate space) while the medium-range and the long-range regions are described by meson exchange between the nucleons. From a theoretical point of view, the meson exchange currents are necessary if the total electromagnetic current of the nucleus is to fulfill the continuity equation [36]. Doubts about the validity of conventional MEC calculations at high Q^2 have been raised. It has been argued that a simultaneous creation of three $q\bar{q}$ pairs accompanied by the exchange of two gluons is required by the traditional picture of the $\pi N\bar{N}$ pair current but that at high momentum transfers a single $q\bar{q}$ creation, i.e. a microscopic $\pi q\bar{q}$ pair current, is likelier [36].

The transition between the inner and outer regions can be handled by either abruptly separating the two regions at a characteristic transition radius or by allowing a gradual merging of two three-quark baryon clusters into six-quark clusters. The former approach is used in hybrid quark hadron models (HQHM) while the latter alternative has been used in the resonating group model (RGM).

In the HQHM approach the deuteron wave function is calculated from a six-quark Hamiltonian in which quarks interact via one-gluon exchange but also one-pion-exchange (note: on the quark level!) and a phenomenological σ-exchange. Buchmann and collaborators were able to conclude that for their calculated tensor polarization t_{20} the quark exchange currents were as important as conventional MECs at high Q^2 [36].

In the RGM approach the short-range repulsive NN force has been explained as a consequence of the gluon exchange interaction and the antisymmetrization of six-quark wave functions. A mid-range potential, a σ-exchange interaction, was introduced to merge gradually the short- and long-range regions [37, 38]. The long-range region was governed by one-pion-exchange (OPE) between baryons.

The predictions of a particular hybrid quark hadron model, labeled the R-matrix boundary condition model [39, 40, 41, 42, 43], by Lomon et al. are shown together with experimental data in Chapter 4.

1.3.4 The Skyrme Model

The Skyrme model is an effective field theory which describes the self-interaction of mesons. The model is constructed on an SU(2) field. Stable soliton solutions can be constructed by expressing the Lagrangian as derivatives of the field. A conserved quantum number of the model (an integer-value topological charge) is identified as the baryon number, i.e. the topological solutions of the self-interacting meson fields are baryons. The soliton solution with B=0 are associated with the pion, while the B=1 solution represents the nucleon. The properties of the soliton solutions with baryon numbers of up to 6 have been studied [44]. The interesting connection between the Skyrme model and QCD is that in the limit of an infinite number of QCD colors, an effective Lagrangian of the Skyrme type emerges for QCD [45]. Nyman and Riska have calculated the deuteron electromagnetic form factors within the Skyrme formalism using the Paris NN-potential. Their predictions agreed well with previous data [46].

1.3.5 Models based on Perturbative QCD

With the exception of the quark hadron models, those models described above belong to what has been labeled "classical nuclear physics", i.e. phenomenological theory written in terms of nucleons bound together by a finite number of different types of mesons [47].

As mentioned above one important objective of medium energy nuclear physics

is to find the transition regime in which models based on nucleon degrees of freedom (the nucleon-meson picture) do not sufficiently well predict the measured quantities any longer but where models based on quark degrees of freedom (the quark-gluon picture) start succeeding. QCD emerged in the 1960s and was called for by data from deep inelastic lepton-hadron scattering experiments. The strong coupling constant α_s is sufficiently small at high energies that QCD calculations can be carried out using perturbation theory techniques carried over from quantum electrodynamics (QED). This approach is labeled perturbative QCD (pQCD). What is of interest is to see whether pQCD model predictions describe observables measured at four momentum transfers obtainable at JLab, typically corresponding to length scales (~ 0.1 fm) much smaller than the size of a nucleon.

The so called dimensional counting rules of pQCD predict that for a general reaction, $\mathrm{A} + \mathrm{B} \rightarrow \mathrm{C} + \mathrm{D}$, one gets:

$$\left(\frac{\mathrm{d}\sigma}{\mathrm{d}\Omega}\right)_{\mathrm{A+B\rightarrow C+D}} \sim s^{2-\mathrm{n}} \ \mathrm{f}\left(\frac{t}{s}\right), \tag{1.30}$$

where s is the Mandelstam variable $s = (p_\mathrm{A} + p_\mathrm{B})^2$, t is the Mandelstam variable $t = (p_\mathrm{A} - p_\mathrm{C})^2$, p_i is the four momentum of the i^{th} particle, and n is the combined number of elementary fields (quarks, leptons, and photons) in both the initial state and the final state, i.e. $\mathrm{n} = \mathrm{n_A} + \mathrm{n_B} + \mathrm{n_C} + \mathrm{n_D}$.

For elastic e-d scattering one has:

$$\left(\frac{d\sigma}{d\Omega}\right)_{ed\to ed} \sim (Q^2)^{-10}. \tag{1.31}$$

The present data of the dominant structure function $A(Q^2)$ of the deuteron appear to be consistent with pQCD dimensional counting rules above $Q^2 \geq 100\ \mathrm{fm}^{-2}$ [48].

The electromagnetic current matrix elements, i.e. the helicity transition amplitudes, for elastic e-d scattering at high Q^2 can in pQCD be written as:

$$G^{I}_{hh'}(Q^2) \equiv < p'h'|\epsilon_I \cdot J|ph >, \tag{1.32}$$

where $|p, h >$ is the state vector of a deuteron with momentum p and helicity h, I denotes the helicity of the quark, and J is the electromagnetic current of the deuteron, ϵ_I is the polarization vector of the photon. If the momentum of the virtual photon is shared equally among the constituents (six quarks) of the deuteron, i.e. the assumption of the democratic chain (cascade) model, there will be three rules which govern the Q^2 and spin dependence of the helicity transition amplitudes [47]. The process is illustrated in Figure 1.6 and the rules are:

- the one-gluon rule: The contribution to the amplitude is such that it is either proportional to Q and conserves quark helicity or is proportional to m (a mass scale) and flips quark helicity according to whether the absorbed

gluon is transverse (T) or longitudinal (L), respectively. This part of the process is illustrated in Figure 1.7.

- the two-gluon rule (or gluon-photon rule): If one gluon is absorbed and one emitted as illustrated in Figure 1.8, the largest amplitude is constant in Q^2 and the quark helicity is conserved. In this case, one gluon is transverse and the other longitudinal. If both gluons are longitudinal then the amplitude is of the order $O(\frac{m}{Q})$ with quark helicity flipped, and if both gluons are transverse the amplitude is zero.

- the transverse gluon rule: Two quark lines connected by a transverse gluon have opposite helicity. This follows because the helicity direction of an absorbed transverse gluon is the same as the helicity direction of the quark that absorbs it; for an emitted transverse gluon the directions are opposite. There is no helicity correlation for quark lines connected by a longitudinal gluon.

There are three independent $G^{\mathrm{I}}_{\mathrm{hh'}}$ matrix elements: G^L_{00}, G^L_{+-}, and G^T_{+0}. The deuteron electromagnetic form factors can be expressed in terms of the helicity transition amplitudes in the light cone formalism as:

$$G_{\mathrm{C}}(Q^2) = \frac{1}{2p^+(2\eta+1)}\left[\frac{(3-2\eta)}{3}\,G^+_{00} + \frac{8}{3}\sqrt{2\eta}\,G^+_{+0} + \frac{2}{3}(2\eta-1)\,G^+_{+-}\right], \tag{1.33}$$

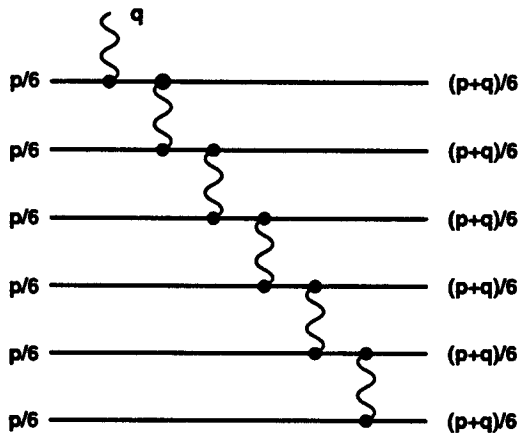

Figure 1.6: Elastic e-d scattering at high Q^2 with the momentum of the virtual photon shared equally among the constituents of the deuteron.

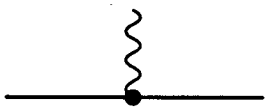

Figure 1.7: A subgraph of Figure 1.6 that is an illustration for the "one-gluon rule", i.e. for the absorption process of one gluon by a single quark.

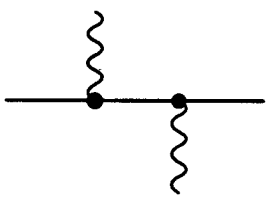

Figure 1.8: A subgraph of Figure 1.6 that is an illustration for the "two-gluon rule", i.e. for the absorption and subsequent emission process of a gluon by a single quark.

$$G_{\rm M}(Q^2) = \frac{1}{2p^+(2\eta+1)}\left[2\,{\rm G}^+_{00} + \frac{2(2\eta-1)}{\sqrt{2\eta}}\,{\rm G}^+_{+0} - 2\,{\rm G}^+_{+-}\right], \tag{1.34}$$

$$G_{\rm Q}(Q^2) = \frac{1}{2p^+(2\eta+1)}\left[-{\rm G}^+_{00} + \sqrt{\frac{2}{\eta}}\,{\rm G}^+_{+0} - \frac{\eta+1}{\eta}\,{\rm G}^+_{+-}\right], \tag{1.35}$$

with

$$\mathrm{G}^+_{hh'} \equiv < p'h'|J^+|ph >, \tag{1.36}$$

where $J^+ \equiv J^0 + J^3$.

The leading helicity amplitude for e-d scattering as $Q^2 \to \infty$ is the G^L_{00} amplitude. By neglecting the other helicity amplitudes one gets

$$\frac{G_{\rm C}}{G_{\rm Q}} = \frac{2}{3}\eta, \tag{1.37}$$

and

$$t_{20} = -\sqrt{2}\left[\frac{1+\tan^2\left(\frac{\theta}{2}\right)}{1+4\tan^2\left(\frac{\theta}{2}\right)}\right], \tag{1.38}$$

as has been shown by Carlson [49]. However, Kobushkin and Syamtomov have pointed out that the helicity-one-flip matrix element G^L_{+-} cannot be neglected [50, 51]. Including the G^L_{+-} element decreases the t_{20} value.

1.4 Previous Measurements

Because measuring either the tensor moment t_{20} or the analyzing power T_{20} of the deuteron gives us important knowledge about the NN interaction, these polarization observables have been measured many times in the past for lower four momentum transfers. There are two main types of experiments which have been carried out. In the first type unpolarized electrons are scattered from an unpolarized deuterium target producing recoil deuterons that are tensor polarized. A polarimeter is used for measuring the tensor moment t_{20} of the recoil deuterons. In the second type an internal polarized deuterium gas target is utilized together with unpolarized electrons of a storage ring. The deuterium atoms of the target are kept tensor polarized with a magnetic holding field and the analyzing power T_{20} is measured. The analyzing power T_{20} contains the same information on the deuteron form factors as the tensor moment t_{20}. That is, $T_{20} = T_{20}(G_C G_Q, G_Q^2, G_M^2)$ and thus measuring T_{20} can be used in the same manner as measuring t_{20} is used in the polarimeter type experiments.

MIT-Bates 1984 & 1990

The t_{20} experiments carried out at the MIT-Bates Linear Accelerator Center in 1984 and 1990 were both of the recoil deuteron polarimeter type. In 1984 t_{20} was measured for two Q points: 1.7 fm^{-1} and 2.0 fm^{-1} [52, 53]. A windowless D_2O waterfall target was used as primary target and it provided 0.38 mm and 0.64 mm thick laminar flows of heavy water. The analyzer used in the polarimeter

was based on the $^3\mathrm{He}(\overleftrightarrow{\mathrm{d}},\mathrm{p})^4\mathrm{He}$ reaction.

In the 1990 t_{20} measurement three Q points were covered, 3.6 fm^{-1}, 4.2 fm^{-1}, and 4.6 fm^{-1} [54, 55, 56, 12]. The primary target used in this second experiment was a 7 cm long liquid deuterium target and the secondary target in the AHEAD polarimeter was a liquid hydrogen target that was 27 cm long and had a 10 cm diameter. The polarimeter was part of the deuteron arm which was located at a fixed angle of 41° throughout the measurement. Elastic deuteron proton scattering $^1\mathrm{H}(\overleftrightarrow{\mathrm{d}},\mathrm{pd})$ was used as the analyzer for the tensor polarized recoil deuterons which had kinetic energies in the 60 MeV to 170 MeV range. The JLab t_{20} measurement is most similar to the MIT-Bates 1990 experiment.

Novosibirsk 1985 & 1990

The two T_{20} measurements carried out in Novosibirsk in 1985 and 1990 were both of the internal gas target type. In 1985 the experiment was carried out at the VEPP-2 electron storage ring. A jet of polarized deuterium atoms was employed as an internal target and a target thickness of $\sim 10^{11}$ $\frac{\mathrm{atoms}}{\mathrm{cm}^2}$ was achieved. The analyzing power T_{20} was measured at two four momentum transfers Q: 0.988 fm^{-1} and 1.34 fm^{-1} [57, 58, 59].

In 1990 a new T_{20} measurement was carried out at the VEPP-3 electron storage ring. A 94 cm long open-ended tube with an elliptical cross section (24×46 mm^2) was used as a dwell target cell (located inside the VEPP-3 ring). The much improved target thickness was 3×10^{12} $\frac{\mathrm{atoms}}{\mathrm{cm}^2}$, that is a gain by a factor

of 15 was achieved. The average polarization of the target nuclei in the dwell cell is reduced due to for example collisions with the target cell walls. Neither an *in situ* polarization measurement nor an exact calculation of the depolarizing effects existed, which led the experimenters to normalize the datum at the lowest Q value (1.97 fm^{-1}) to a theoretical value of T_{20} given by the Paris potential [60]. Having determined the degree of polarization in the target cell in this indirect way the resulting polarization value was then used for the two higher, 2.49 fm^{-1} and 2.93 fm^{-1}, four momentum transfer data points [60].

NIKHEF 1996 & 1997

At the AmPS electron storage ring at NIKHEF in Amsterdam, two T_{20} measurements were carried out in 1996 and 1999. The internal gas target used was a open-ended T-shaped dwell cell 40 cm long with a diameter of 1.5 cm. The target cell was cooled down to 100 K (150 K) in the 1996 (1999) measurement. The obtained target thickness was 2×10^{13} $\frac{\text{atoms}}{\text{cm}^2}$, an order of magnitude higher than previously obtained. The electron beam current achieved in the AmPS storage ring was 120 mA (150 mA) with a lifetime of 15 min (33 min) in 1996 (1999). As mentioned above, the target nuclei in the dwell cell are depolarized in a number of ways, hence it is of great importance to measure the polarization of the target nuclei *in situ*. This was successfully done for the very first time at NIKHEF [61]. The asymmetry measured was

$$A_{\rm d}^{\rm T} = \frac{{\rm N}^+ - {\rm N}^-}{t_{20}^+ {\rm N}^- - t_{20}^- {\rm N}^+}, \tag{1.39}$$

where t_{20}^+ (t_{20}^-) is the tensor polarization of ideally $\frac{+1}{\sqrt{2}}$ ($-\sqrt{2}$), and $\rm N^+$ ($\rm N^-$) is the number of events with the target polarization positive (negative). A measurement at Q=1.6 fm^{-1} [62, 63] was carried out in 1996 and additional measurements at Q: 2.03 fm^{-1}, 2.35 fm^{-1}, and 2.79 fm^{-1}, were carried out in 1999 [61, 64, 65]. Chapter 4 will contain a comparison not only to theoretical calculations but also to the previously measured data summarized here.

Chapter 2

Experimental Setup and Procedure

In order to measure t_{20} two separate experiments were performed. The reason can be seen from the expression for the efficiency:

$$\epsilon(\theta,\phi) = \epsilon_0(\theta)\left[1 + t_{20}T_{20}(\theta) + 2t_{21}T_{21}(\theta)\cos\phi + 2t_{22}T_{22}(\theta)\cos(2\phi)\right]. \tag{2.1}$$

In the first experiment the polarimeter POLDER was calibrated, that is, the unpolarized efficiency $\epsilon_0(\theta)$ and the analyzing powers $T_{ij}(\theta)$ were measured using a beam of deuterons with known tensor polarization, which translates into known tensor moments $t_{ij}(\theta)$. In the second experiment one was able to measure the unknown tensor moments t_{ij} by help of the now known analyzing powers T_{ij}. In this chapter the calibration experiment will first be presented and the rest of the chapter is dedicated to presenting the main focus of this work that is the JLab t_{20} experiment.

2.1 The Calibration Experiment at Saturne

The t_{20} POLDER calibration experiment was carried out at the Laboratoire National Saturne (LNS), Saclay, France, in the summer of 1996. The tensor polarized deuteron beam of the Saturne 2 [66] synchrotron was used for the polarimeter calibration.

The polarized source HYPERION* was of an atomic beam type that could deliver 386 keV deuterons. The source is depicted in Figure 2.1. It consists of a dissociator which dissociates gas molecules into atoms. The nozzle of the dissociator is cooled to 70 K in order to reduce the velocity of the atomic beam before it goes through a focusing sextupole magnet into the radiofrequency transitions part. The following sets of transitions are used: 10.5 MHz (labeled small), 343 MHz (medium), and 415 MHz (large). The atoms continue from this stage to the ionizer and go via electrostatic lenses and an electrostatic mirror to a spin rotating solenoid. Finally the ions go through an acceleration tube. HYPERION could produce deuterons in eight different states (labeled 1 through 8) but only four states (states 5 through 8) were used in the calibration, the properties of which are shown in Table 2.1. The vector and tensor polarization can in an irreducible tensor representation be expressed as:

$$\rho_{10} = \sqrt{\frac{3}{2}}(\mathrm{f}_+ - \mathrm{f}_-), \tag{2.2}$$

*The source was named after one of the moons of the planet Saturne.

$$\rho_{20} = \sqrt{\frac{1}{2}}(f_+ + f_- - 2f_0), \tag{2.3}$$

where (f_i, i="+","0","-",) represents the fractional number of deuterons in the corresponding spin state. The polarization of the deuterons was measured with a low energy polarimeter based on the $^2H(\overleftrightarrow{d}, p)^3H$ reaction. The energy of the protons produced in this reaction were approximately 3-4 MeV. Details of the low energy polarimeter can be found in references [67, 68].

From HYPERION, the deuterons were injected into the MIMAS synchrotron which boosted their energy to 45 MeV before they were sent to the Saturne 2 synchrotron. After reaching the desired energy the deuterons were extracted into the beamline leading up to the SPES1 spectrometer as illustrated in Figure 2.2. The SPES1 spectrometer had a quadrupole-sextupole-dipole (QSD) magnetic channel and a total bend of 97°. In order to precess the vertical spin polarization a solenoid magnet, OPTIMIST, was installed in front of the SPES1 spectrometer as shown in Figure 2.3. Further precession of the deuteron spin took place inside the SPES1 spectrometer and this was taken into account in the analysis [69]. The deuteron kinetic energies covered in the calibration experiment are shown in Table 2.2. The cross sectional area of the incident beam of deuterons on POLDER was [6 (vertical) $\times$ 4 (horizontal)] cm^2.

It should be noted that the analysis of the JLab t_{20} Saturne calibration data was similar to the analysis of the JLab t_{20} data. The data analysis itself will be

discussed later in Chapter 3.

2.1.1 Saturne deuteron beam depolarization

A problem with the polarization of the deuteron beam at Saturne was observed during the calibration experiment in 1996. This was observed for calibration runs with energies between 240 MeV and 520 MeV, and out of the 13 different calibration energies in this energy range six were affected, these are indicated by a * in Table 2.2. It turned out that a quadrupole magnet which was used to change the vertical tune during acceleration malfunctioned [70]. The source of the problem was that the power supply of the quadrupole was at a constant current setting whereas the current needed to be ramped up with increasing energy of the deuteron beam. Depolarization arises in periodic machines as conditions for certain resonances are fulfilled. The resonance associated with the calibration experiment depolarization problem was particularly strong. Moreover, the strength of the resonance depended on the deuteron beam emittance so that the depolarization varied with the beam settings.

As a result, the degree of depolarization changed from one run to another even for a single given calibration energy. This problem was corrected for using the assumption that the analyzing powers of the calibration run of 1996 were proportional the analyzing powers of the calibration run of 1993, i.e. $T_{2j}(1996) \propto T_{2j}(1993)$. The details of the correction procedure are described in ref. [70]. Be-

Polarization State	Transitions			P_z	P_{zz}	Vector Polarization ρ_{10}	Tensor Polarization ρ_{20}
	ST	MT	LT				
5	-	-	+	$+\frac{1}{3}$	+1	$+\frac{1}{\sqrt{6}}$	$+\frac{1}{\sqrt{2}}$
6	+	-	+	$-\frac{1}{3}$	+1	$-\frac{1}{\sqrt{6}}$	$+\frac{1}{\sqrt{2}}$
7	-	+	+	$+\frac{1}{3}$	-1	$+\frac{1}{\sqrt{6}}$	$-\frac{1}{\sqrt{2}}$
8	+	+	+	$-\frac{1}{3}$	-1	$-\frac{1}{\sqrt{6}}$	$-\frac{1}{\sqrt{2}}$

Table 2.1: Different polarization states of the deuteron beam at Saturne. ST=small transition, MT=medium transition, and LT=large transition.

Hodoscope Position	Z_{H1} (cm)	Z_{H2} (cm)	Settings of the Kinetic Energy of the Deuteron Beam T_d (MeV)
1	+32	+110	160, 170, 180, 200, 210, 220
2	+40	+135	240*, 250, 260, 280, 300*, 340*
3	+47	+165	360*, 375, 390, 420*, 450, 485, 520*

Table 2.2: A table of the kinematical settings of the calibration experiment at Saturne. Z_{H1} and Z_{H2} denotes the distances from the center of the target to the two hodoscopes H1 and H2, respectively. The calibration energies affected by the deuteron beam depolarization problem of Saturne are marked with a *.

cause of the corrections required due to the depolarization problem, a systematic error was added to the calibration data as shown in Tables 3.7, 3.8, and 3.9. Documentation on the data acquisition of the calibration experiment can be found in references [71, 11].

2.2 The t_{20} Experiment at Jefferson Lab

The main focus of this work is the E94018 experiment carried out at the Thomas Jefferson National Accelerator Facility [72] (JLab), in Newport News, Virginia.

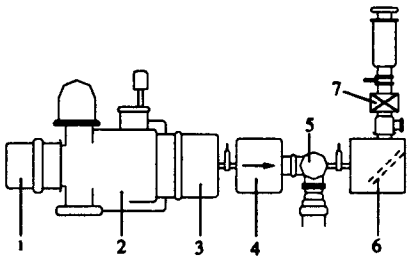

Figure 2.1: Plan view of the polarized deuteron beam source HYPERION. (1) Dissociator, (2) sextupole magnet, (3) radiofrequency transitions, (4) ionizer, (5) electrostatic lens, (6) electrostatic mirror, (7) spin rotating solenoid SOLSPIN.

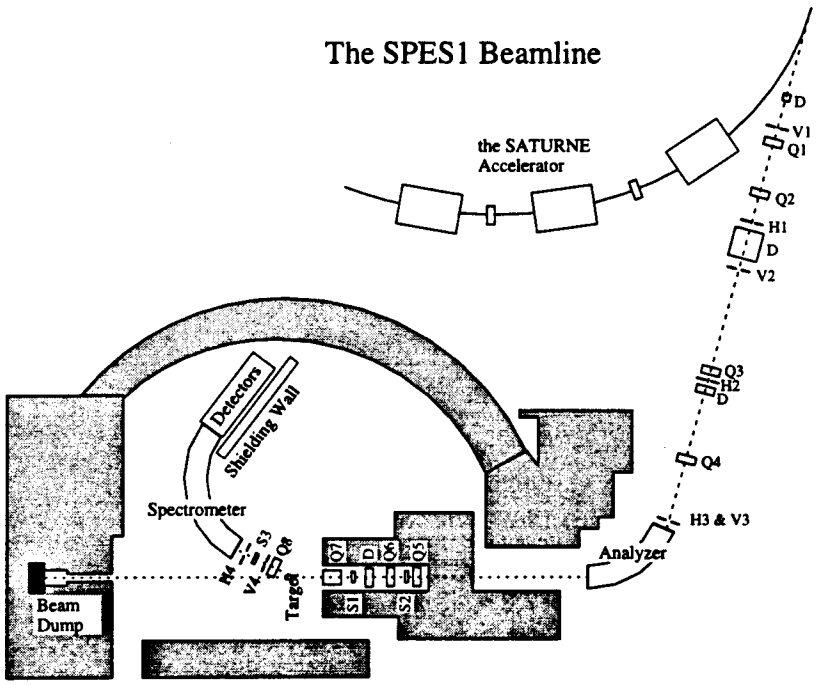

Figure 2.2: An overview of the experimental setup during the calibration experiment at Saturne. The Saturne accelerator can partially be seen at the upper part of the figure. The SPES1 spectrometer and the detector package are shown inside the experimental hall itself in the lower part of the figure.

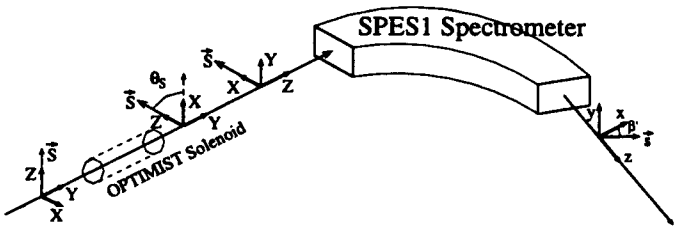

Figure 2.3: The magnets of the calibration experiment. To the left is the OPTIMIST solenoid that rotates the deuteron spin from being vertically polarized to being horizontally polarized. The SPES1 spectrometer bends the incident deuteron beam by 97° degrees. The direction of the deuteron spin is precessed in SPES1 by 16°.

E94018 was run in the summer of 1997. The main components of the experimental setup will be described in detail in the next few sections.

2.2.1 Accelerator and Electron Beam

The electron accelerator CEBA (Continuous Electron Beam Accelerator) at JLab has five main components: the injector, two linear accelerators (LINACs), and two semicircular arcs. The layout of the two LINACs and the two arcs are in the form of a racetrack with a circumference of about 1400 m as illustrated in Figure 2.4, and the accelerator is located 5 m underground. The beam switchyard and three experimental halls are shown in Figure 2.5. The injector consists of a thermionic electron gun and 18 superconducting radio frequency (RF) resonant cavities, it is capable of producing three interleaved beams. The electrons are accelerated to 45 MeV during the injector stage. Each LINAC consists of 160 niobium superconducting 5-cell RF cavities, depicted in Figure 2.6. The cavities

are grouped in pairs and in each thermally insulated cryomodule there are four of these cavity pairs, hence 20 cryomodules per LINAC. Each RF cavity is powered by a 5 kW klystron driven at a frequency of 1497 MHz. The superconducting cavities are operated at 2 K with cooling provided by a 4.8 kW superfluid helium refrigeration plant. The advantage of having superconducting cavities is that there is little heating of the cavities due to power deposition by the RF fields. The duty factor of CEBA is 100%, i.e. it produces a "continuous wave" (CW) electron beam*. At the time of E94018, the maximum energy of the electron beam in each LINAC was 400 MeV. The recirculating arcs, labeled "West" and "East", consist of four and five layers, respectively, of bending magnets vertically stacked on top of each other, allowing the electron beam to be recirculated at most four times. At the end of the South LINAC and before the West arc the electron beam is extracted, resulting in beam energies between 0.8-4.0 GeV†. CEBA can provide both unpolarized and polarized electron beams, although for E94018 only unpolarized beam was used. The beam current was typically 100-110 μA.

The properties of the electron beam produced by CEBA are as follows: the beam spot size is typically (FWHM) 100 μm (horizontal) $\times$ 200 μm (vertical). The fractional energy spread ($\frac{\sigma_E}{E}$) is $\sim 2.5 \times 10^{-4}$ and the angular emittance is 2×10^{-9} mrad at 1 GeV (ϵ_{RMS}-value) and somewhat lower at higher energies

*What really determines whether a particle beam is considered "continuous" or not is the rate at which the data acquisition system can operate [73].

†The long term plan of JLab calls for a beam energy upgrade to 12 GeV by year 2005 and to 24 GeV after year 2010 [74].

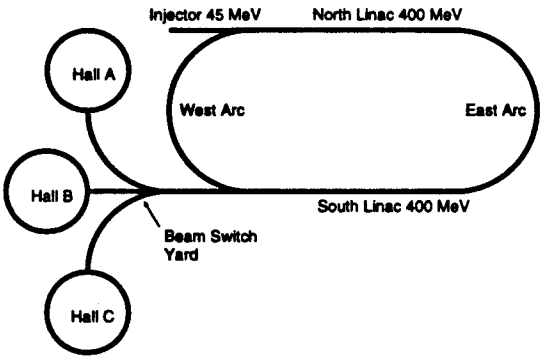

Figure 2.4: The Continuous Electron Beam Accelerator (CEBA), the beam switchyard, and the experimental halls.

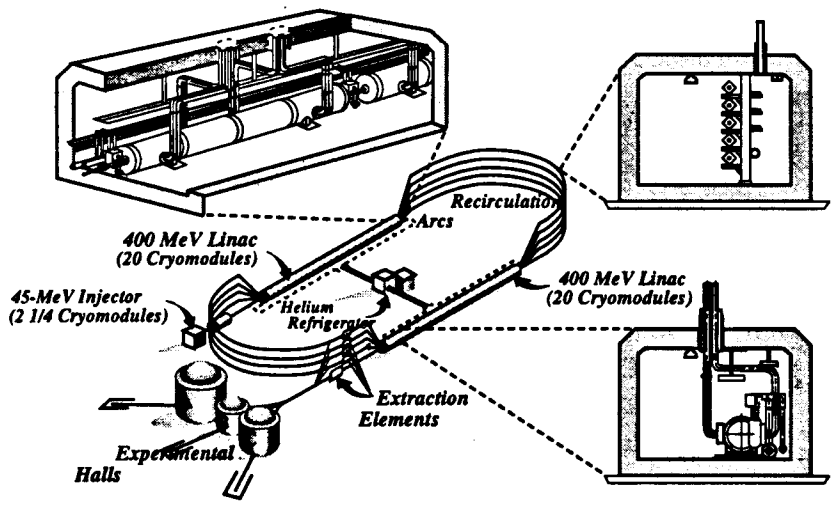

Figure 2.5: The Continuous Electron Beam Accelerator (CEBA). Cryogenic modules can be seen top left. The design of the arcs, with the bending magnets vertically stacked on top of each other, can be seen top right and the helium coolant system is shown bottom right. The racetrack shaped accelerator and the three experimental halls are shown in the middle of the picture.

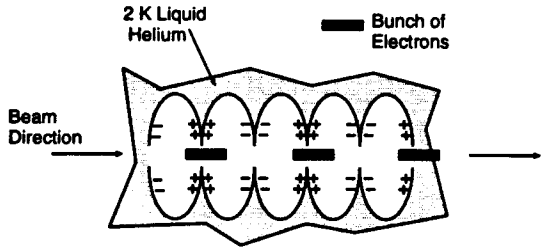

Figure 2.6: A schematic of a 5-cell superconducting radio frequency (RF) resonant cavity. Figure courtesy of D. van Westrum.

[75, 76]. Operating experience of CEBA is documented in [77, 78]. Between the accelerator and the experimental Hall C there are two major beam line components: the Beam Switch Yard (BSY) and the arc of Hall C. In the BSY, the beam is extracted into each of the experimental halls (or to a special beam dump line). This is done in such a way that 1/3 of the bunches of electrons goes to each experimental hall. Therefore the frequency of the beam microstructure in each hall is 499 MHz, one third of the frequency of the accelerator, resulting in $\sim$ 2 ns between beam bunches, each of which is on the order of $\sim$ 1 ps long. Beams of independent currents, and different but correlated energy can simultaneously be delivered to the three experimental halls. The Hall C arc is a 41.6 m long beamline segment containing 8 dipoles, 12 quadrupoles, 8 sextupoles, and 8 pairs of beam correctors [79], shown schematically in Figure 2.7. The deflection angle of the arc is 34.3°. The Hall C arc and the part of the beam line which resides inside the experimental hall itself contains a number of beam diagnostic instruments: beam current monitors (BCM), beam positions monitors (BPM), beam

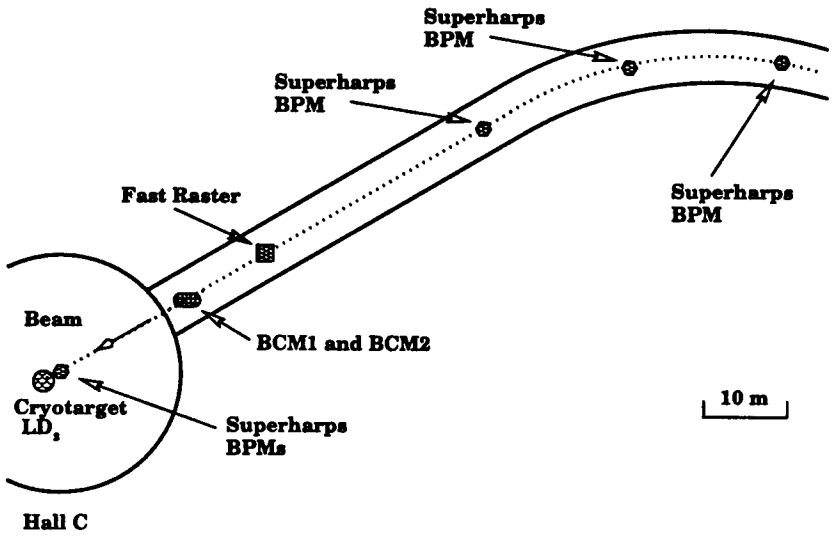

Figure 2.7: A schematic of the Hall C beam line and some key elements of its associated hardware.

profile monitors (harps/superharps) which are shown in the detailed schematic of the beamline in Figure 2.8. A small overview of these will next be given.

Beam Current Monitors

Three types of beam current monitors are utilized at JLab: a Faraday cup type for the injector, monitors of the resonant cavity type, and a parametric current transformer used to calibrate the resonant cavities. Integrated charge measurements are an integral part of the luminosity analysis which is described in detail in Appendix B. The parametric DC current transformer monitor (a.k.a. an Unser monitor) consists of a toroidal sensor which fits over the beam pipe. The average signal level of the Unser is highly susceptible to stray RF fields, magnetic fields, temperature changes, and even mechanical vibrations. Therefore the monitor

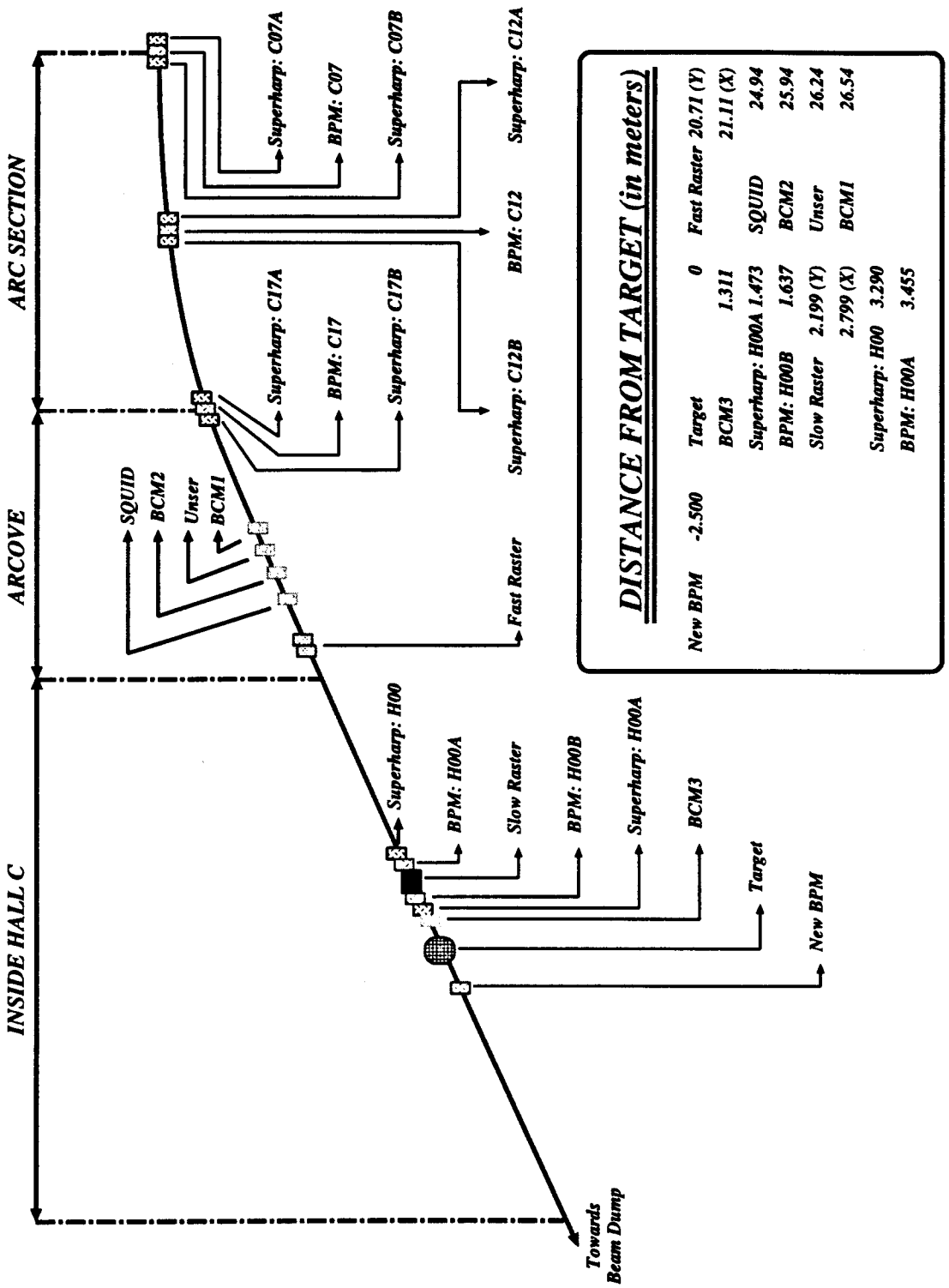

Figure 2.8: A more detailed schematic of the Hall C beam line. Figure courtesy of P. Guèye.

is shielded with a copper RF shield and a mu-metal magnetic shield and it is kept thermally insulated at an elevated temperature (110°F). The monitor has excellent linearity and a very well known (1 part in 10^3) and stable gain. But it has a very poor signal-to-noise ratio plus substantial offset drifts, typically on the order of $\sim$ 1 μA/24 hours. It is possible to check the gain with a precision DC voltage source in combination with precision resistors, allowing it to be used as an absolute current standard for the cavity monitors.

The resonant cavity monitor is a cylindrical wave guide through which the electron beam travels unimpeded. The three cavities used for Hall C (labeled BCM1, BCM2, and BCM3) are made of stainless steel (Type 304). As the 499 MHz beam passes through it excites the 1497 MHz TM_{010} resonant mode of the cavity. This mode is insensitive to the beam position. The strength of the excitations are measured with wire loop pickup antennas, and the measured signals are proportional to the beam current. These monitors have a good signal-to-noise ratio, and because their temperature is controlled to 0.3° F they have both reasonable gain and offset stabilities.

The cavity monitors are not linear over the whole range of currents needed to be measured and, in addition, they cannot measure currents absolutely so they must periodically be re-calibrated utilizing the Unser monitor mentioned above. A schematic of the setup of the beam current monitors is shown in Figure 2.9. Documentation on the BCMs can be found in references [80, 81, 82, 83, 84, 85, 73].

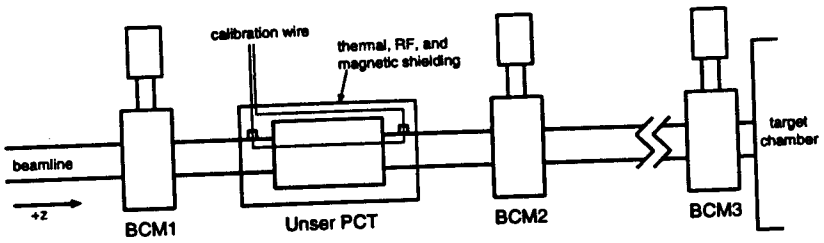

Figure 2.9: The beam current monitor setup showing the cavity monitors BCM1, BCM2, and BCM3 together with the Unser monitor. Figure courtesy of C. Bochna.

Beam Position Monitors and Harps

The position of the electron beam at various locations is measured with two different kinds of monitors: cavity based Beam Position Monitors (BPMs) and (super)harps (a.k.a. beam wire scanners). The BPMs are cylindrical resonant cavities mounted in the beam line, with two pairs of antennas in each cavity. The antennas are located at $\pm 45°$ and $\pm 135°$ with respect to vertical axis. The difference over the sum of the paired signals is converted into a beam position independent of current. This approach is non-disruptive and the beam position can continuously be monitored with the BPMs. The BPMs are calibrated with the help of the superharps. Documentation on the BPMs and the (super)harps can be found in references [86, 87, 88, 89, 90] Normally, the beam position is measured in two locations, allowing determination of both the position and angle of the beam when it hits the target. However, during E94018 only one of the monitors was properly recorded so the incident angle was not determined on an event by event basis. A (super)harp consists of a frame with three 22 μm diameter

tungsten wires, two vertical wires and one horizontal wire. The vertical and horizontal wires give horizontal and vertical position information, respectively. The frame with the wires is moved in and out of the electron beam with the help of a DC stepper motor. The measurement is intrusive, so data cannot be taken at the same time a measurement is carried out. An uncertainty of ± 10 μm in an absolute beam position measurement can be achieved with the superharps. The electron beam energy is determined based on the superharp information in the Hall C arc area (see the second paragraph below). They are also used to measure the beam profile, and the emittance and dispersion of the electron beam.

Beam Raster

The 100% duty factor high current ($\sim$ 120 μA in hall C) 4 GeV electron beam with a small beam spot size gives rise to a very high continuous power intensity in excess of 3 $\frac{\text{mA}}{\text{mm}^2}$. In order to protect the primary target and also the beam dump one needs to dilute the power intensity. This is done by sweeping the electron beam rapidly in a periodic fashion both horizontally and vertically with the help of two air core dipole magnets located about 21 m upstream of the target, as shown in Figure 2.10. The magnets were driven by sinusoidal signals with two different frequencies ($f_{\text{x}}^{\text{FR}} = 16.78$ kHz (horizontal), $f_{\text{y}}^{\text{FR}} = 22.9$ kHz (vertical)), chosen such that unstable Lissajous patterns are formed on the target cell. In this way the beam spot is effectively spread out over an entire square

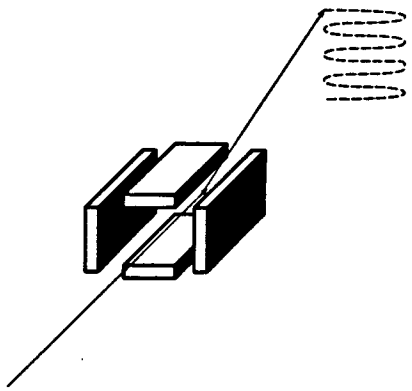

Figure 2.10: A schematic of the beam raster that shows the two magnet pairs. One pair deflects the electron beam horizontally and the other pair deflects the electron beam vertically.

with sides of twice the FR amplitude (typical amplitude of 0.5-2 mm). However, because of the sinusoidal driving signals the beam will spend more time at the edges of the square and the power intensity is at a maximum in these locations as shown in Figure 2.11. A slow raster (SR), located 2.5 m upstream of the target, protects the beam dump. It is needed only for beam currents exceeding 80 μA at 4 GeV, and was thus only used at the highest Q^2 t_{20} data point. The sweeping frequencies of the slow raster are $f_x^{SR} = 62.0$ Hz (horizontal) and $f_y^{SR} = 91.0$ Hz (vertical). Documentation on the beam rasters and also on their implementation in the analysis code can be found in references [91, 86, 92, 93].

Beam Energy Measurement

The energy of the electron beam can be measured at three different locations: in the East bending arc of the accelerator, in the Hall C arc, and finally inside Hall

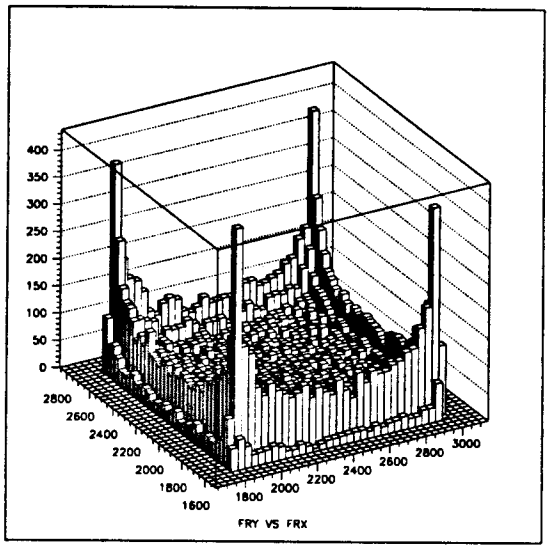

Figure 2.11: A two dimensional histogram showing the vertical faster raster signal (f_y^{FR} = 22.9 kHz) vs. the horizontal faster raster signal (f_x^{FR} = 16.78 kHz). Because sinusoidal signals are used the electron beam will spend more time at the edges and particularly at the corners of the covered area as can be seen in this figure.

C.

The relative uncertainty ($\frac{\sigma_{E_e}}{E_e}$) achieved in the beam energy measurement in the East arc is at least a few times 10^{-3}. The uncertainty stems from variations in the path lengths of the electrons in the bending arc, uncertainty in the fields integral $\oint B \cdot dl$, and the large momentum acceptance of the arc.

The beam energy measurement using the Hall C arc is in principle more precise. The beam position is measured with superharps at three locations in the arc: in the beginning, in the middle, and at the end. Some of the bending magnets are field mapped so by knowing the currents in the magnets one knows the bending fields through the relation B = B(power supply current), too. The

Data Point	E^{nominal} (GeV)	E^{used} (GeV)	$\theta^{\text{nominal}}_{\text{HMS}}$ (°)	$\theta^{\text{used}}_{\text{HMS}}$ (°)
1	1.411	1.412	35.81	35.71
2a	1.645	**1.645**	33.57	33.39
2b	1.645	**1.649**	33.57	33.39
3	2.096	2.098	29.93	29.72
4a	2.445	**2.447**	27.62	27.6
4b	2.445	**2.446**	27.62	27.6
5a	3.245	3.251	23.43	**23.36**
5b	3.245	3.251	23.43	**23.43**
6	4.045	4.048	20.33	20.33

Table 2.3: Table of the nominal and the used values of the electron beam energies and HMS spectrometer angles.

relative uncertainty achieved for the energy measurement is of the order of 1×10^{-3}.

The beam energies used for the six kinematical points are tabulated in Table 2.3. Documentation on beam energy measurements and corrections to the measurements can be found in references [94, 75, 95, 96, 97].

2.2.2 Scattering Chamber and Primary Target

A plan view of endstation C is shown in Figure 2.12. The main components of Hall C are the primary targets, the electron arm (the High Momentum Spectrometer), and the deuteron arm. The primary targets of Hall C are located inside a vacuum vessel called the scattering chamber. The scattering chamber is a large vertically standing cylindrical tank made of a single forged ring of 6061-T6 aluminum, depicted in Figure 2.13. The dimensions of the scattering chamber are shown in Table 2.4.

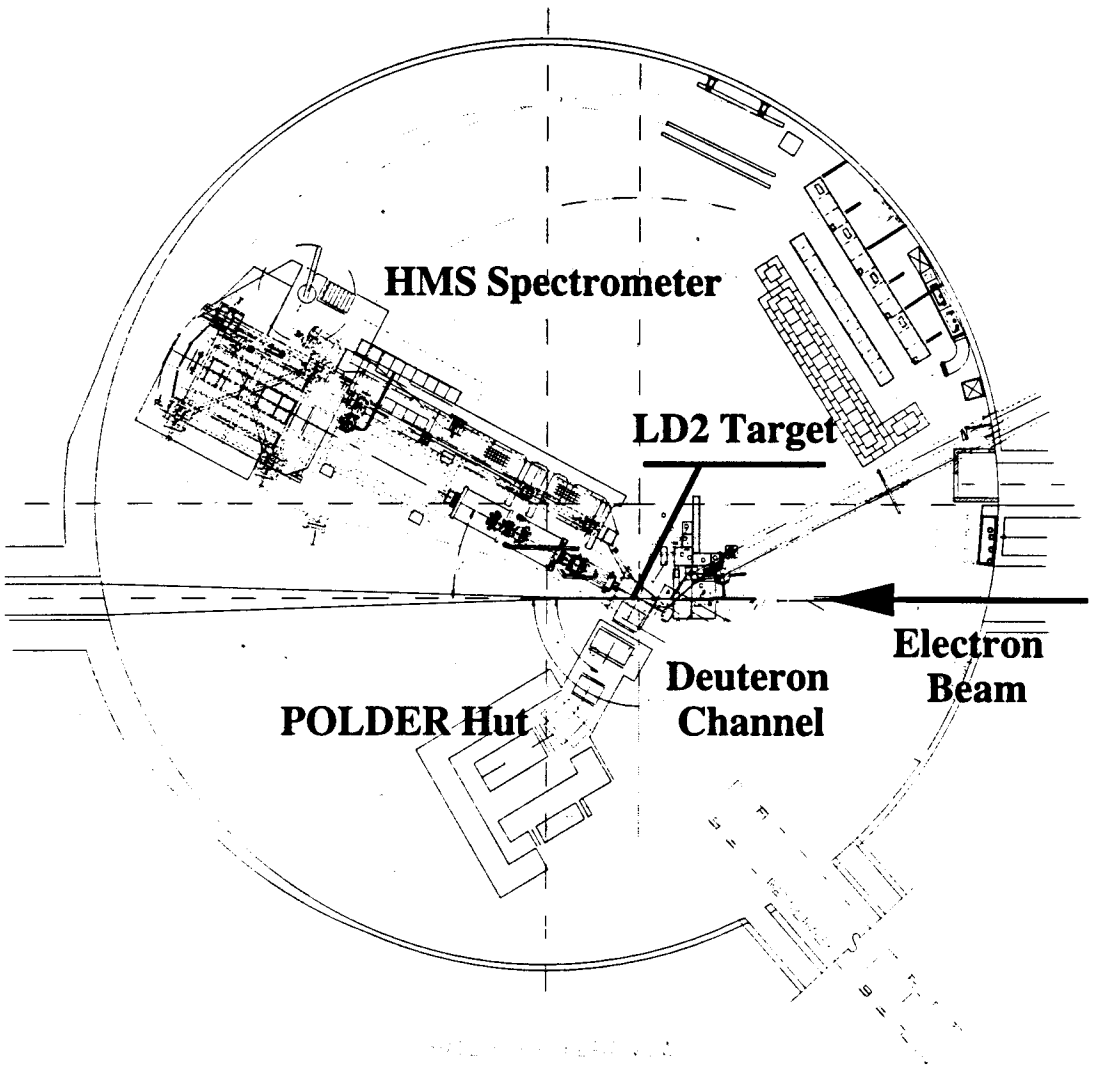

Figure 2.12: Plan view of Hall C during the t_{20} experiment

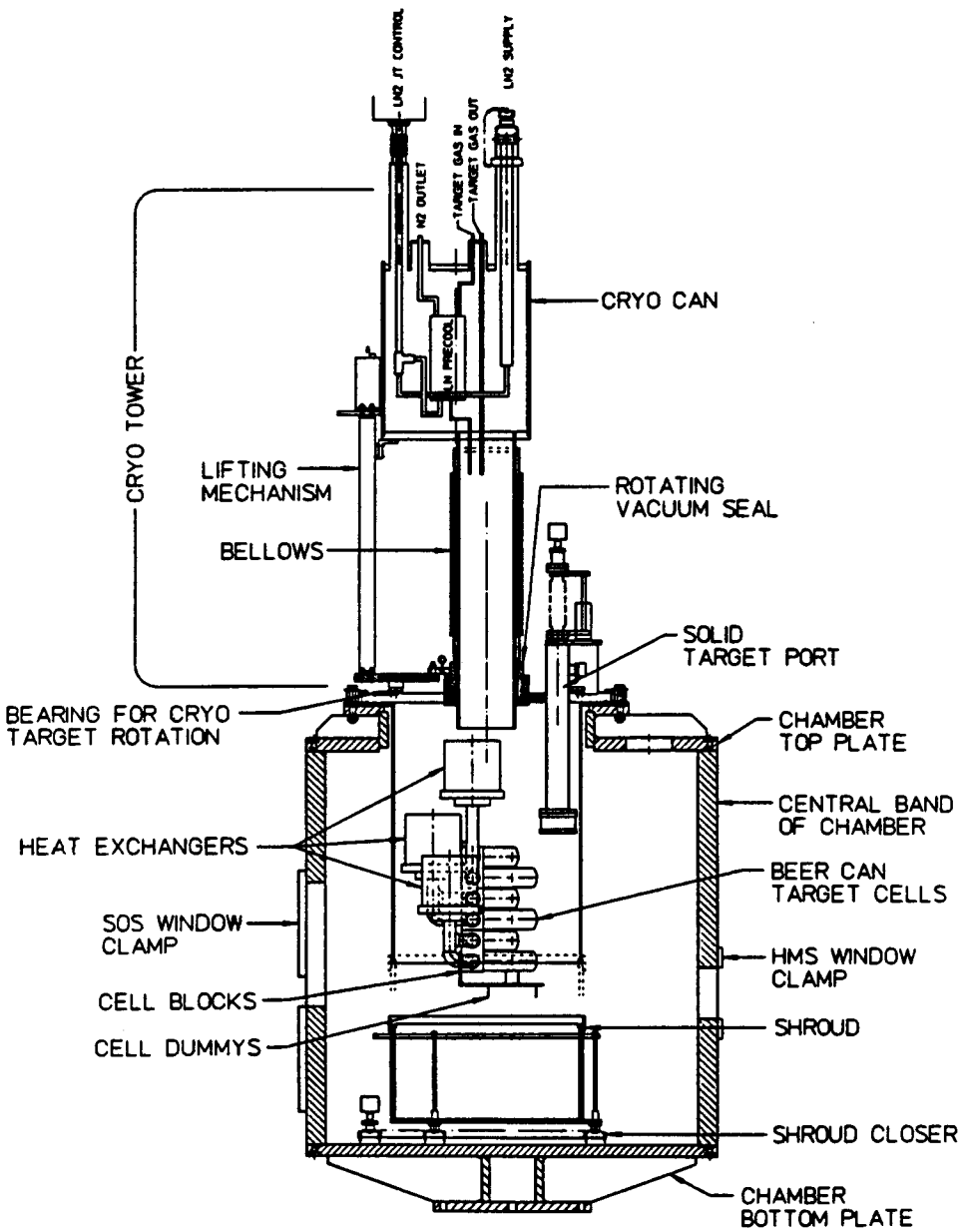

Figure 2.13: A side view of the scattering chamber of Hall C. The three target loops and their associated heat exchangers are shown. Figure courtesy of B. Terburg.

Height (cm)	136.5
Diameter outer (cm)	135.9
Wall thickness (cm)	6.35
Typical vacuum (torr)	10^{-6}

Table 2.4: Table of the properties of the Hall C scattering chamber.

The purpose of the scattering chamber is to thermally insulate the cryotargets (typical temperature around 20 K) from the ambient room temperature air (around 290 K) in the experimental hall. The high vacuum ($\sim 10^{-6}$ torr) minimizes the conductive heat load on the cryotargets. In addition, the vacuum minimizes multiple scattering of the incident and exiting electron beam and of the scattered particles before they exit the scattering chamber and enter the spectrometers. The vacuum is maintained by continuously pumping on the scattering chamber with a Leybold Turbovac 1000 turbomolecular pump (TMP) backed by a Leybold Trivac D65B 53 cfm mechanical pump.

There are two exit windows towards the two spectrometers. On the HMS side was an aluminum window with a height of 20.32 cm and a thickness of 0.20 mm. The deuteron channel (DC) side had a window made of a 0.152 mm Kevlar layer combined with a 0.038 mm Mylar layer. These polymer windows were damaged quickly in the high radiation environment and had to be replaced twice due to leakage. But, particularly at the lowest kinematic points it was desirable to keep the window on the DC side as thin as possible in order to minimize absorption and scattering of the recoil particles. However, after two failures, the polymer window was replaced with aluminum window about half way through the experiment.

Primary Target

The primary target system of Hall C consists of two main subsystems: the solid targets and the cryotargets. During E94018, the solid target ladder held a BeO screen for viewing the beam, two ^{12}C targets and a slanted ^{12}C foil. The ^{12}C targets, were used for optics studies of the HMS spectrometer.

The cryotarget is a multiloop setup consisting of three self contained target loops. The stack with these loops is suspended from the cryotower which rests on the top plate of the scattering chamber. For E94018, the LD2 target was the main target for the experiment. In addition, a redundant liquid LH2 target was used for calibration purposes (for the $A(Q^2)$ measurement). The middle loop was left empty and reserved as a spare.

The main components of each loop are a heat exchanger, a target cell block, two target cells, a circulation fan, two heaters, and a number of sensors [98, 99, 89]. A schematic view is shown in Figure 2.14. The heat exchanger is a stainless steel cylinder surrounding 6.35 mm diameter copper fin tubing with 11 fins per 2 cm. The 15 K gaseous helium coolant from the End Station Refrigerator (ESR) is carried inside the fin tubing and the target fluid is forced to flow past these cooling elements. A 3-phase AC axial circulation fan with screw-like aluminum blades (outer diameter 7.15 cm) is located at the center of the heat exchanger and pumps the cyrogen through two target cells and back to the heat exchanger. The target cells are connected to the heat exchanger with a cell block machined

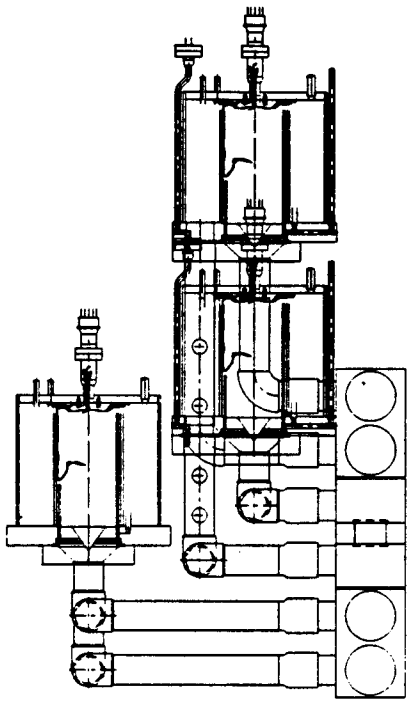

Figure 2.14: The heat exchangers of the three target loops. An endview of the target cells themselves can be seen on the lower right hand side of the figure.

from a solid block of 6061-T6 aluminum. A schematic of the cell block is shown in Figure 2.15.

The target cells are made out of 3004 aluminum cans (beer can blanks manufactured by Coors Brewing Company^{TM}) with 0.0127 cm side walls. The bottom of the original aluminum can was punched out into the shape of a dome as shown in Figure 2.16 and the thickness of the dome is reduced by chemical etching*. The convex shaped upstream window is made of 0.071 mm 5052-OMF aluminum foil. Because of the curvature of the two target cell windows the effective target

*About 0.21 mm of aluminum was etched off in 20 minutes in a 25% NaOH solution at +50°C [100].

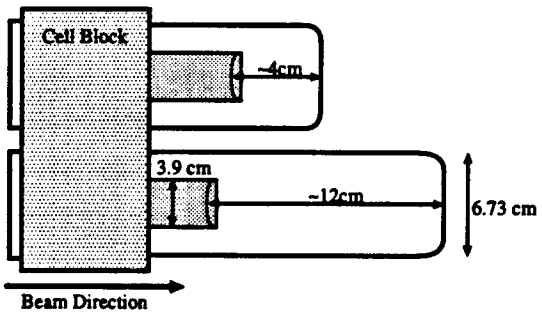

Figure 2.15: A close-up view of a target cell block with its associated short and long target cells.

Target Loop	Cryogen	Short target cell (cm)	Long target cell (cm)
1	LH2	4.53 ± 0.01	12.48 ± 0.04
2	empty	4.08 ± 0.01	12.46 ± 0.04
3	LD2	4.45 ± 0.01	12.46 ± 0.04
dummy	N/A	4.03 ± 0.02	N/A

Table 2.5: Table of the lengths of the various target cells used during E94018 [?].

length varied with the horizontal/vertical position of the electron beam. In order to solder the target cells to the target block it was necessary to copper plate the areas of the solder joints. The thickness of the copper plating was 0.102-0.127 mm. The copper plating (in addition, to the chemical etching mentioned above) was performed at the University of Maryland Machine Shop. The two target cells had nominal lengths of 4 cm and 12 cm; the lengths of the different target cells used during E94018 are shown in Table 2.5. The 12 cm target cell of the liquid deuterium (bottom) loop was used as the main target during E94018.

There are two heaters for each target loop: a low power (LP) heater and a high power (HP) heater. The LP heater (24 Ω resistance) has a maximum power

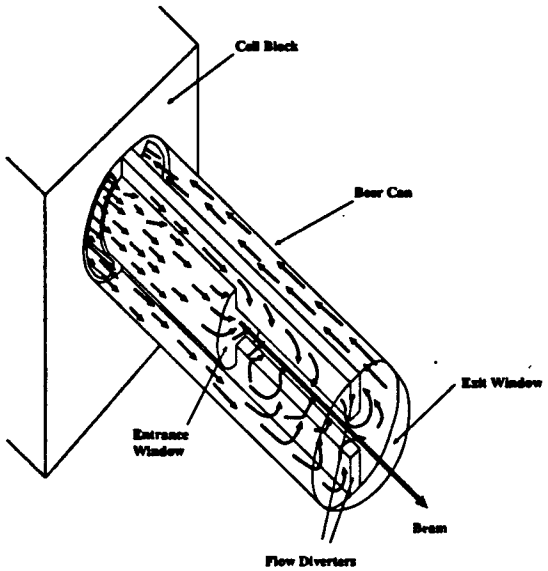

Figure 2.16: A schematic of a target cell which also shows the flow pattern of the cryogen.

output of $\sim$ 80 W and the HP heater (2 Ω resistance) has a maximum power output of $\sim$ 800 W.

The target temperature was monitored with Lakeshore Cernox semiconductor resistors. These sensors had an uncertainty of 100 mK for absolute temperature measurements and a 50 mK uncertainty for measuring temperature changes.

The operating temperature and pressure of the LD2 loop were (T,P)=(22 K,1.2 atm) and for the LH2 loop they were (T,P)=(19 K,1.2 atm). For both loops this corresponds to a 2 K subcooled state. The advantage of operating the cryotargets in a subcooled state is that the loops are less sensitive to small sudden changes in the heat load/coolant power. The target loops are run in a constant heat load mode. The electron beam deposits energy in the cryogen in

the target cell as it goes through according to the expression:

$$P_{\text{beam}} = I_{\text{beam}} \times \frac{\mathrm{d}E}{\mathrm{d}x} \times \rho \times t, \tag{2.4}$$

where P_{beam} is the power deposited, I_{beam} is the current of the electron beam, $\frac{dE}{dx}$ is the stopping power, ρ is the density of the cryogen, and t is the target length. In the constant heat load mode the heat load, i.e. $P_{\text{beam}} + P_{\text{heater}}$, is kept constant. The low and high power heaters are adjusted for decreases/increases in the electron beam current. This ensures a stable temperature in the target and hence a constant target density. The cold parts of the target loops are wrapped in super-insulation (aluminized Mylar) in order to reduce radiative heat transfer. Although knowledge of the absolute target density was not critical for the t_{20} measurements, it was important for the corresponding measurements of $A(Q^2)$ and was therefore systematically studied during the experiment. These studies are discussed in detail in Appendix B.

On the bottom of the stack of cryotargets was a dummy target simulating the endcaps of the 4 cm target cell. The dummy target was made of two flat aluminum strips set apart 4 cm with a total thickness of ten times the cell windows in order to simulate the radiation losses in the target fluid.

In addition to the above hardware, the primary target had a gas handling system and a complex target control system. The gas handling system is described in ref. [90]. The target control system is used to monitor and regulate the entire

Compound	Detection limit	D_2 Sample-1	D_2 Sample-2	H_2 Sample
H_2	0.001 (%)	1.24	1.28	99.9+
HD	0.001 (%)	0.77	0.78	nd
D_2	0.001 (%)	97.9+	97.9+	nd
N_2	4 (ppm)	nd	nd	10
O_2	4 (ppm)	nd	nd	nd
Ar	4 (ppm)	nd	nd	nd
CO	4 (ppm)	nd	nd	nd

Table 2.6: The results on the target gas purity of the two D_2 samples and the single H_2 sample. nd = less than detection limit.

cryotarget system. The nerve center of the target control system is the Input-Output-Controller (IOC), a single board VME computer (Motorola MVME-162-12). The software part of the target control is EPICS running on VxWorks on the IOC. The IOC was connected via the Hall C ethernet to a HP9000 workstation and to a PC. The target Graphical User Interface (GUI) which is an EPICS client, was a Tcl/Tk script running under X Windows. Documentation on the target control system can be found in references [101, 102, 103, 104].

In order to determine the purity of the target gases two samples of the deuterium target gas and one sample of the hydrogen target gas were taken at the end of the E94018 run. The target gas samples were analyzed at Atlantic Analytical Laboratory using gas chromatography and the results are shown in Table 2.6.

An excellent review on the primary target can be found in ref. [90].

Beam Dump

As the electron beam exits the scattering chamber it enters the 25 m long beam dump pipe which reaches up to the beam dump tunnel at the end of the experimental hall. To keep the radiation background in the experimental hall low the pipe was filled with helium. The beam dump tunnel extends 33 m and is heavily radiation shielded. The dump consists of a heat exchanger inside a pressure vessel both of which are made of aluminum 6061. The heat exchanger is cooled by a closed loop deionized water circuit. The power deposited by a 200 μA 4 GeV beam is $\sim$ 0.5 MW. Two thirds of the power is deposited in the aluminum elements of the heat exchanger while the rest is deposited in the deionized water. The peak temperature in the aluminum plates is $\sim$ +190°C [105].

2.2.3 Electron Arm

The scattered electrons were detected in the High Momentum Spectrometer (HMS). This spectrometer is one of two standard spectrometers of Hall C (the other one being the Short Orbit Spectrometer (SOS) [106] which was not used in the t_{20} experiment). The HMS is a medium resolution, large acceptance magnetic spectrometer with a 25° vertical bend for its central ray. Its magnetic channel depicted in Figure 2.17 consists of three consecutive focusing quadrupoles (Q1, Q2, and Q3) followed by a dispersive element, the dipole (D), which determines the central momentum. All four magnets are superconducting: they are precooled

with liquid nitrogen and their main coolant is liquid helium (2 K) delivered by the ESR. The quadrupoles are cold iron magnets with soft iron wrapped around the coils to enhance the field at the center while at the same time reducing magnetic stray fields. (The quadrupoles have additional windings for multipole corrections but these have never been used.) Q1 and Q3 focus in the dispersive direction while Q2 focuses in the transverse direction. The quadrupoles are powered by Danfysik System 8000 power supplies (I_{max} = 1250 A, U_{max} = 5 V). The power supply of the dipole is also a Danfysik 8000 series type but with a higher rating (I_{max} = 3000 A, U_{max} = 5 V). These power supplies are water cooled with the low conductivity water (LCW) system of Hall C. The quadrupoles are field mapped and hence the magnetic fields are set by current. There is a nuclear magnetic resonance (NMR) probe inside the dipole with which one sets and regulates its magnetic field. The central field excitation of the dipole for a 4 GeV momentum setting is $\sim$ 1.1 T. The bend radius of the dipole is $\sim$ 12 m and it has a straight pole face and a gap width of 42 cm. The physical dimensions of the dipole are 6 m (length) $\times$ 4.5 m (height) $\times$ 2.8 m (width). The entire magnetic channel of the spectrometer is held at a vacuum of 10^{-4} PSIA. The four magnets and the HMS detector stack are all supported by a single carriage which rotates on rails around the pivot of Hall C (the HMS is limited to a 12.5° – 90° scattering angle rotation). The lead-lined concrete shield house of the detector package is supported on a separate carriage in order to distribute the weight of the entire

spectrometer. The entrance and exit windows of the magnetic channel of HMS were made of layers of 0.0381 cm Kevlar and 0.0127 cm Mylar. A slit system consisting of three collimators made of 6.35 cm thick Heavymet (a machinable tungsten alloy, 90% W, 10 % NiCu, density $\rho = 17\ \frac{g}{cm^3}$) was located in front of Q1. In the normal HMS setup there are small and large octagonal shaped collimators and, in addition, a sieve slit collimator (a collimator with an array of small holes) used for optics studies. The apertures of the collimators are flared shaped in order to match the geometrical acceptance of the spectrometer. During data taking of the t_{20} experiment none of these collimators was used. For the absolute cross section measurements in E94018, the small collimator was replaced with a specially designed collimator that ensured 100% overlap of the HMS and DC solid angles for elastic e-d scattering [107]. The HMS was run in a point-to-point tune both in the dispersive and non-dispersive direction. This tune provides an optimal vertex reconstruction at the target which is suitable for usage with an extended target. The specifications on the HMS performance are shown in Table 2.7. The HMS was set at angles between 20° and 36° and its central momentum was set at values between 0.8 GeV and 3.2 GeV during E94018. The kinematic settings used during the experiment are shown in Table 2.8.

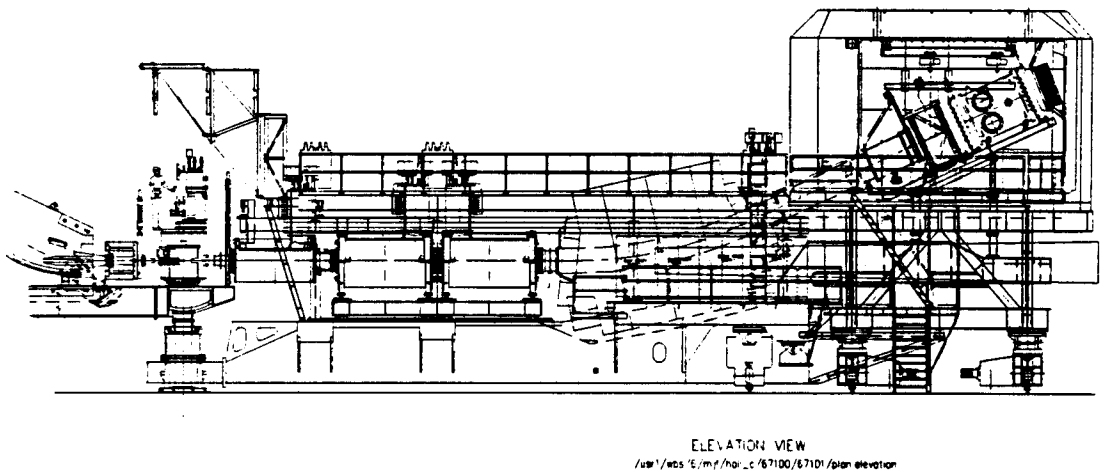

Figure 2.17: The High Momentum Spectrometer (HMS) of Hall C. This blueprint drawing shows the carriage and the three quadrupole magnets and the dipole magnet. The shielding hut is on the top of the carriage to the right and the HMS detector package is shown inside the hut. The pivot on which the scattering chamber is located is to the left. To the far left parts of the second standard Hall C spectrometer, the Short Orbit Spectrometer (SOS) can be seen.

Quantity	Specification
P_{max} (GeV)	7.4
Momentum bite $(p_{max} - p_{min})/p_0$	± 10%
Momentum resolution $(\frac{\delta p}{p})$	< 0.1%
Solid angle (dΩ)	8.1 msr
Scattering angle bite	± 32 mr
Scattering angle precision	± 0.8 mr
Out of plane angle	± 85 mr
Out of plane angle precision	± 1.0 mr
Extended target acceptance	∼ ± 10 cm
Vertex reconstruction accuracy (beam direction)	2-3 mm
Scattering angle limit	12.5° – 90°

Table 2.7: Performance characteristics of the High Momentum Spectrometer (HMS).

Data Point	Q (fm^{-1})	E_{beam} (GeV)	E'_e (GeV)	θ_{HMS} (°)	T_d (MeV)	β_d	β_p	σ(ed→ed) (nb/sr)
1	4.1	1.411	1.233	35.82	170	0.405	0.67	689
2	4.5	1.645	1.433	33.57	205	0.437	0.69	357
3	5.1	2.096	1.823	29.93	268	0.487	0.74	144
4	5.5	2.445	2.127	27.62	312	0.518	0.77	88
5	6.2	3.245	2.838	23.43	402	0.569	0.81	40
6	6.8	4.045	3.563	20.33	476	0.605	0.83	23

Table 2.8: A table of the kinematical settings of the t_{20} experiment.

The Detector Package of HMS

The detector package of the HMS is located inside thick lead-lined concrete walls which protects the instruments from background radiation in the experimental hall and thus reduces the background noise in and aging of the detector elements. The HMS detector package consists of four major components: drift chambers, a hodoscope, a Cherenkov counter, and a calorimeter. Only the first two were used in the data analysis of E94018, where the drift chambers provided tracking information while the hodoscope provided timing information. There are two planar multiwire drift chambers as shown in the schematic of the HMS package in Figure 2.18. Each drift chamber has six planes of sense wires with an interplanar spacing of 1.8 cm. Two of these planes (labeled x and x′) are oriented in the horizontal direction while two of the other planes (labeled y and y′) are orthogonal to the horizontal planes*. The final two planes constitute the stereoplanes (labeled u and v) which are inclined $+15°$ and $-15°$ with respect to the x and x′ planes, respectively. For particles traversing the drift chambers the sequence of these planes are x, y, u, v, x′, and y′. The sense wires (the anodes) are grounded and they are surrounded by field (guard) wires (the cathodes) kept at a negative potential (typically -1800 V to -2500 V depending on the location of the field wire in the drift chamber). The sense wires are made of 25 μm diameter gold-plated tungsten wires while the field wires are made of 150 μm diameter gold-plated

*The JLab Hall C coordinate system is documented in ref. [106].

beryllium wires. The sense wire spacing is 1 cm and there are 113 x/x′ wires, 52 y/y′ wires, and 107 u/v sense wires. The active area of the drift chambers are 52 cm (horizontal) × 113 cm (vertical). The wires are mounted in an aluminum frame with thin entrance and exit windows made of Mylar. The gas mixture used in the drift chambers is of an argon-ethane (50/50 by weight) composition with some ($\sim$ 1%) isopropyl achohol mixed in it. The distance between the first (DC1) and the second drift chamber (DC2) was 81.2 cm. The signals from the sense wires go first to pre-amplifier and discriminator cards (either a LeCroy 2735DC or a Nanometric N-277-L). From there the signals go to a multihit TDC (Fastbus LeCroy 1877). Further details on the drift chambers and their performance can be found in ref. [108].

The hodoscope of the HMS consists of two crossed pairs of scintillator paddles. The first pair (labeled S1) is located after the second drift chamber (DC2) but before the gas Cherenkov detector while the second pair (labeled S2) is located after the Cherenkov detector. S1 and S2 are separated by $\sim$ 2.2 m. Each pair consists of an x-layer (S1X/S2X) and a y-layer (S1Y/S2Y). There are 16 scintillator paddles in each x-layer and 10 scintillator paddles in each y-layer. The paddles are made of Bicron BC404 plastic scintillator material and are 1 cm thick, 8 cm wide and the x-paddles (y-paddles) are 75.5 cm (120.5 cm) long. Each layer of paddles is stacked in such a way that there is a 0.5 cm overlap at each interface between two adjacent paddles in order to avoid zones with ineffi-

cient detection (in the case of only a small overlap) and dead zones (in the case of no overlap whatsoever). The effective detection area is a rectangle of 120.5 cm (vertical) × 75.5 cm (horizontal). The paddles are wrapped in a layer of aluminized Mylar and two layers of Tedlar PVF film (i.e., a black plastic film) to make the system light tight. UVT lucite light guides are glued to both ends of the scintillator paddles and Philips XP2282B photomultiplier tubes (PMTs) are glued to the light guides. The signals from the PMTs go to both ADCs (Fastbus LeCroy LRS 1881M) and high resolution TDCs (Fastbus LeCroy 1872A). The per plane timing resolution of the hodoscope comes out to be $\sim$ 0.1 ns.

The gas Cherenkov detector consists of a cylindrical aluminum tank 160 cm long with a diameter of $\sim$ 150 cm. It is located between S1 and S2. The lead glass shower calorimeter is located after S2 and consists of four layers of 13 vertically stacked $(10 \times 10 \times 70)$ cm^3 TFI lead glass blocks. Both of these detectors can be used for improved particle identity (PID) determination (on-line in the trigger, off-line in the analysis code) and were used during E94018 for loose rejection in the electronics on-line. They were not required in the off-line analysis of the t_{20} data. All the detectors of HMS were powered by CAEN high voltage power supplies. The HMS detector stack has been well documented in ref. [94].

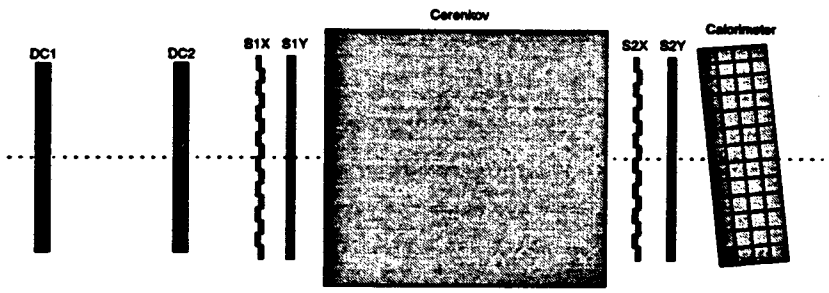

Figure 2.18: The HMS detector package. From left to right: the two drift chambers; the x- and y-planes of the front part, S1, of the hodoscope; the gas Cherenkov detector; the x- and y-planes of the back part, S2, of the hodoscope; and finally the lead glass shower detector.

2.2.4 Deuteron Arm

The recoil deuterons from the elastic electron deuteron scattering reaction $^2H(e, e' \overleftrightarrow{d})$ were transported through the deuteron channel (DC) to the polarimeter POLDER. The deuteron channel was a specially designed magnetic channel consisting of three quadrupoles (labeled Q_1, Q_{2S}, and Q_3) and a dipole (labeled D), i.e. it was of a $Q_1Q_{2S}Q_3D$ design as shown Figure 2.19. All four elements were warm magnets (in contrast to the superconducting ones of the HMS mentioned above). The effective lengths and the field strengths of the magnets are shown in Table 2.9. The quadrupoles Q_1 and Q_3 focused in the vertical direction while Q_{2S} focused in the horizontal direction. The quadrupole Q_{2S} had a large asymmetric aperture and was equipped with correction coils which formed a sextupolar field for second order optics corrections. Incident deuterons were bent horizontally by a dipole through an angle of 25°. The deuteron channel also protected the polarimeter

Magnet	Effective length (cm)	Field strength ($\frac{T}{m}$)
Q_1	96.5	8.22
Q_{2S}	100.6	3.89
Q_3	96.5	3.47
D	126	2.3

Table 2.9: Properties of the magnets of the deuteron channel.

from direct view of the primary target, thus decreasing the background. In addition, the polarimeter was located inside a radiation shield consisting of thick blocks of concrete mixed with iron. A helium bag was used along the deuteron flight path in the DC in order to minimize multiple scattering. The bag had both an entrance and an exit window made of Mylar (thickness: 0.15 mm/window). The deuteron arm could not be rotated but was located at the same fixed angle, 60.5°, throughout the experiment. The fields of the magnets were tuned separately for each of the six kinematical settings of E94018 in order to optimize the focus of the incident deuterons on POLDER.

Polarimeter POLDER (POLarimètre à DEuton de Recul)

The polarimeter was the key instrument of the t_{20} experiment. It is the product of a long-term research effort. The feasibility study of the charge exchange reaction $^1H(\overleftrightarrow{d}, pp)n$ which POLDER is based on started with the EMRIC detector in 1989 [109], in which the analyzing powers and the cross section for both 200 MeV and 350 MeV incident deuterons were studied [110, 111]. The promising results

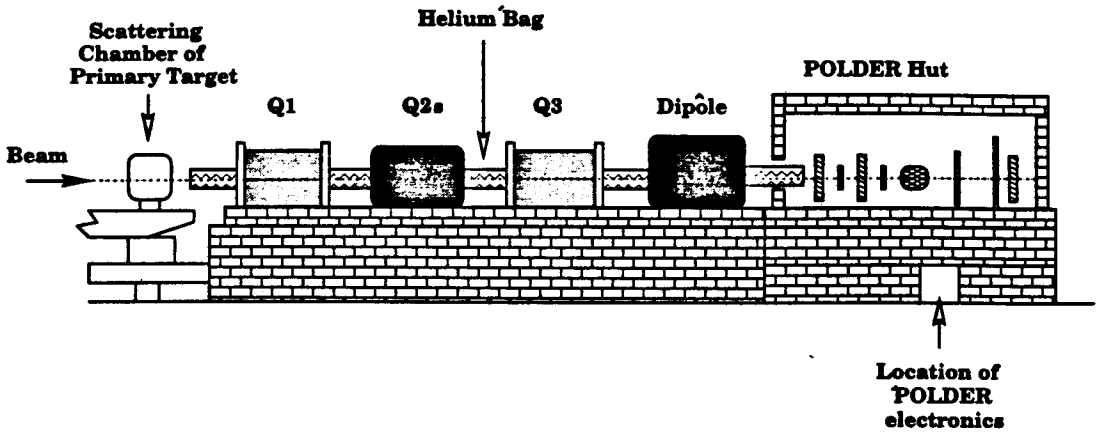

Figure 2.19: A schematic of the deuteron channel. The incident electron beam is depicted as arriving from the left. The primary deuterium target is located inside the scattering chamber. The deuteron channel consists of three quadrupole magnets which are labeled Q_1, Q_{2S}, and Q_3. These quadrupoles are followed by a dipole magnet and the POLDER shielding hut. Figure courtesy of K. Hafidi.

motivated the construction of POLDER in 1991. The analyzing powers and the cross sections for 200 MeV and 350 MeV incident deuterons were for the first time measured with POLDER in 1992 [112]. The polarimeter was calibrated for 175-500 MeV incident deuterons in 1993 [113, 114, 115] and in 1995 used in a $^1\mathrm{H}(\vec{\mathrm{p}}, \overleftrightarrow{\mathrm{d}})\pi^+$ experiment at Saturne [116]. Finally POLDER was calibrated with 140-520 MeV deuterons in the summer of 1996 and hence prepared for the JLab t_{20} experiment as mentioned in the beginning of this chapter.

POLDER consists of three major components: the incident deuteron detectors, the secondary target, and finally the proton pair detectors. These components will be described in the next few paragraphs and some of their geometrical characteristics are shown in Table 2.10. A schematic of POLDER is shown in

Figure 2.20.

Incident Deuteron Detectors

In order to precisely measure the $^1H(\overleftrightarrow{d}, 2p)n$ scattering rate one needs to know a number of properties of the incident recoil deuterons: the direction of their trajectory, their impact points on the secondary target, and timing information in order to identify them as deuterons. This was achieved in POLDER by the use of a pair of multiwire proportional chambers (MWPC1 and MWPC2) and a pair of plastic scintillator detectors (Start1 and Start2).

Each multiwire proportional chamber had 3 wire planes (anode planes) and 4 cathode planes. A wire plane consisted of 158 15 μm diameter tungsten wires (the tungsten being doped with rhenium and gold). The spacing of the wires was 1.27 mm. The anode plane-cathode plane spacing was 4 mm. The core of the cathode plane was made of fiber glass (G10). This plane was covered on both sides by a layer of aluminized Mylar (23 μm Mylar and 0.03-0.05 μm aluminum) which formed the conducting layer. The wire planes were grounded while the cathode planes were kept at -3150 V. The three wire planes were oriented such that they were rotated 60° with respect to each other (i.e. the 1st plane at 0°, 2nd at 60°, 3rd at 120°). This ensured an optimal collection of coordinate information in both the x- and the y-direction. The detection area of a wire plane was $\sim 20 \times 20$ cm^2. The wire and cathode planes were mounted on an aluminum frame (hexagonal

shaped because of the 60° rotations of the wire planes) with aluminized Mylar (50 μm Mylar and 12 μm aluminum) entrance and exit windows. The MWPCs were filled with a gas mixture of 70% argon, 29.5% ethane, and 0.5% freon. MWPC1 (MWPC2) was located 92.7 cm (44.3 cm) upstream from the secondary target. The signals from the anodes went to a pre-amplifier and discriminator (ASIC* chip with a preamp and a discriminator) and from there to a multihit TDC (Fastbus LeCroy 1877). The MWPC of POLDER are well documented in ref. [71].

The Start1 detector was 15 cm (height) × 20 cm (width), made of 1 mm thick Bicron BC412 plastic scintillator material. The Start2 detector was a 12 cm diameter disk made of 2 mm thick BC412 scintillator material. Both Start detectors were optically coupled to two 51 mm diameter Philips XP2020 photomultiplier tubes each. The signals from the two PMTs of each Start detector were combined and the two resulting signals, one from Start1 and the second one from Start2, were used for triggering purposes. The raw signals from the PMTs were also fed into four ADCs and hence pulse height information was acquired. This pulse height information was used together with time of flight from the primary target to discriminate between recoil deuterons and background protons. Start1 (Start2) was located 92.7 cm (44.3 cm) upstream from the secondary target. MWPC1/2 was positioned in front of Start1/Start2 in order to minimize

*ASIC = Application Specific Integrated Circuit.

Detector Element	Geometrical Shape	Dimension (cm)	Thickness	z-position (cm)
MWPC1	hexagonal	29	3 planes	-92.75
Start1	rectangular	W 20 × H 15	2 mm	-78.8
MWPC2	hexagonal	29	3 planes	-44.35
Start2	circular	6 (diameter)	2 mm	-32.2
LH2 target	cylindrical	12 (diameter)	20 cm	0
H1 hodoscope	square	38	2 mm	+32 /+40 /+47
H2 hodoscope	square	85	10 mm	+110 /+135 /+165
MWPC3	hexagonal	29	3 planes	+191.8

Table 2.10: A table of the geometrical characteristics of the detector elements of POLDER.

the effect (multiple scattering, absorption, ...) of the scintillator material seen by the incident deuterons. The signals from the PMTs of both Start detectors went first through an amplifier and to ADCs (Fastbus) and also to constant fraction discriminators as shown Figure 2.24.

Test Detectors

A set of test detectors were used for tuning the deuteron channel. The test detectors consisted of a pair of scintillators and a pair of straw chambers. The scintillators T1 and T2 were similar to Start1 and Start2 but were of larger dimensions [117, 107]. The straw chambers consisted of a set of cylindrical tubes, or straws, with a thin wire running along the central axis of each tube. The straws had an inner diameter of 0.522 cm and were made of one layer of 10 μm thick aluminum foil and two layers of 50.8 μm thick Mylar. The wire was made of 25.4 μm diameter LUMA wire (gold plated tungsten with a few percent of rhenium

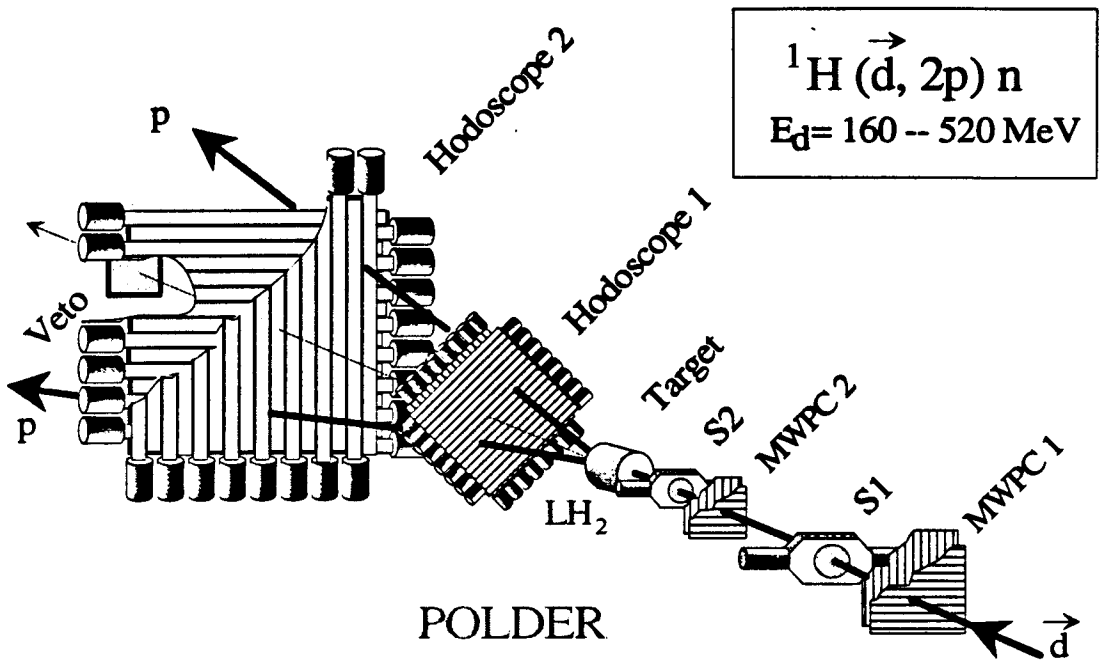

Figure 2.20: A schematic of the detector package of POLDER. From lower right to upper left: the two wire chambers, MWPC1 and MWPC2, and the two scintillator detectors, S1 and S2. The liquid hydrogen target and the two hodoscopes, H1 and H2. Finally the third wire chamber, MWPC3 (not shown), and the veto detector.

added) and it was held at high positive voltage while the straw was grounded. The gas used in the straw chambers was a 50/50 mixture of Argon and ethane. Documentation on the straw chambers can be found in ref [118].

Secondary Target

The secondary target was a liquid hydrogen (LH2) target and provided the basis for the analyzing reaction $^1H(\overleftrightarrow{d}, pp)n$. The 14 cm diameter and 20.3 cm long* cylindrical target cell shown in Figure 2.21 was made of 290 μm thick Mylar. The cell was mounted on a stainless steel flange which also held the 50 μm titanium entrance window of the cell. The cell was wrapped in ten layers of 6 μm thick aluminized (250 Å thick aluminum layer) Mylar in order to thermally insulate it. The target cell contained 3.08 L of LH2 at a temperature of 20 K and a pressure of 1100 mb, i.e. on the vapor pressure curve of LH2. The target was located inside a small vacuum chamber (shown in Figure 2.22) which had a volume of $\sim$ 100 L and was maintained at a typical pressure of $\sim 7 \times 10^{-7}$ mbar. The entrance (exit) window of the vacuum chamber was made of 50 μm (100 μm) thick Kevlar doped with titanium. The cooling of the target was provided by a two-stage 10 W cryostat. There were 4 temperature, 5 pressure, and 2 liquid level sensors associated with the secondary target and the target control system (AUTOMATON) was run on a PC. Further documentation can

*The target cell is actually 20.6 cm long at room temperature. Due to thermal contraction it is approximately 20.3 cm long at a temperature of 20 K [119].

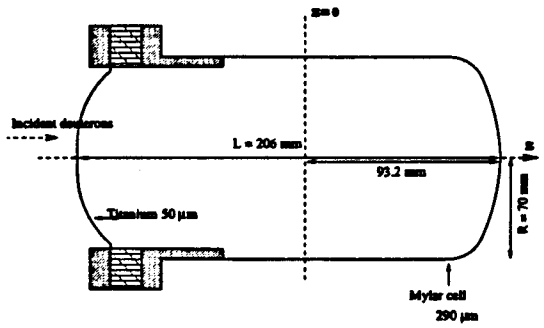

Figure 2.21: The target cell in POLDER.

be found in references [71, 119].

Proton Pair Detectors

The purpose of the hodoscopes of the polarimeter was to identify the proton-proton pairs (pp-pairs) of the final state of the charge exchange reaction and to measure their angular distribution. The smaller hodoscope (labeled H1) consisted of two orthogonal planes of plastic scintillator bars. There were 30 bars per plane. Each bar in H1 measured $(37.5 \times 1.12 \times 0.2)$ cm^3. The bars were made of Bicron BC412 plastic scintillator material. The space between the centers of the bars was 1.15 cm, i.e. there were small dead zones between adjacent bars. The bars are individually wrapped in aluminized Mylar. Each bar is optically coupled to a 13.5 mm diameter Hamamatsu R960 photomultiplier tube at one of its ends. The thickness of the H1 bars was kept small (2 mm) in order to avoid detection of neutral particles, and to reduce both energy loss and multiple scattering experienced by the protons while traversing the bars. The larger hodoscope (labeled

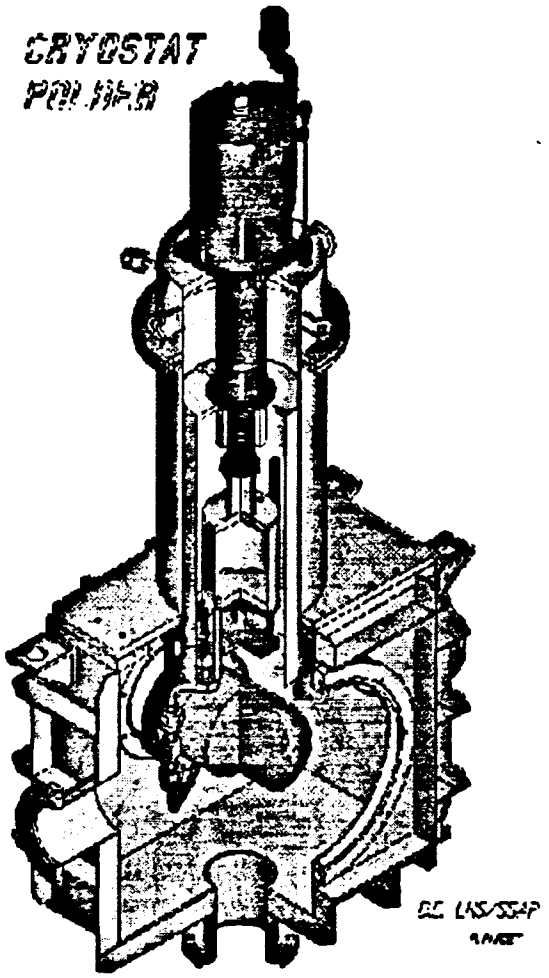

Figure 2.22: The cryostat of POLDER. The upper part contains the compressor and the lower part functions as the scattering chamber. The target cell itself can be seen inside the scattering chamber.

H2) was simply a scaled up version of H1. However, the bars of H2 were made of NE100 scintillator material and they measured ($84.5 \times 3.38 \times 1$) cm^3. The space between the centers of the bars in H2 was 3.4 cm and so there were also small dead zones in H2. The bars of H2 were also thicker (1 cm) than the bars of H1. This caused a minor problem for kinematical point 1, for which a fraction of the charge exchange protons were absorbed in the first plane of H2 and consequently never made it to the second plane [120, 11]. The PMTs of H2 were 51 mm diameter Philips XP2262B. The two planes of H2 constituted an x- and y-plane while H1 was rotated 45° with respect to H2 and had an u- and v-plane. The distances from the secondary target to H1 and H2 varied with incident deuteron energy. Three sets of positions were used during the calibration and the t_{20} experiment and characteristics of these are shown in Table 2.2. The chosen distances of the hodoscopes represent a compromise of maximizing simultaneously both the solid angle and the angular resolution of the hodoscopes. The angular resolution varies between 1.4° and 2° depending on the hodoscope position. Approximately 90% of the charge exchange cross section falls within an opening angle of 20° (with respect to the incident deuteron beam) for 200 MeV incident deuterons while the corresponding opening angle is 15° for 400 MeV incident deuterons. At the energies used in t_{20}, the characteristics and kinematics of the ^{1}H($\overleftrightarrow{\text{d}}$, pp)n reaction were such that CE events could be discriminated from parasitic reactions by requiring that two charged particles were detected with velocities close to those of

the incident deuterons. This was done by measuring flight time (TOF) between hits in the Start2 detector and hits in H1 and H2. Also the thicknesses of the hodoscope bars were kept at a minimum in order to avoid detection of neutral particles and to reduce the reaction rate in the detectors. These thin plastic scintillators were mostly sensitive to charged particles. Therefore the coincidence signals in several bars of the hodoscope was a reliable signature of the detection of a charged particle. The signals from the PMTs of H1 were first sent to a fast amplifier and next to a discriminator. Finally they were sent to multihit TDCs (Fastbus LeCroy 1877). The signals from the PMTs of H2 were sent directly to a discriminator without amplification and then to a multihit TDCs (also Fastbus LeCroy 1877). Further documentation can be found in references [11, 71].

MWPC3 and the Veto detector

Downstream from H2 there was an additional multiwire proportional chamber (labeled MWPC3), used only for aligning the detector elements of POLDER on the software level in the data analysis code. The signals from the anodes of MWPC3 were first sent through a delay line before being amplified, discriminated, and then sent to a multihit TDC (Fastbus Lecroy 1877).

Finally, downstream of MWPC3 there was a veto detector consisting of a lead absorber and a ($15 \times 15 \times 1.1$) cm^3 slab of NE100 plastic scintillator with a Philips XP2020 PMT. The veto detector was only used during the calibration

experiment. The high current deuteron beam of Saturne gave rise to background which mimicked pp-pairs due to multiple incident deuterons hitting H1 and H2. By utilizing the veto detector one could discriminate against these spurious signals. The signal from the PMT was sent to an amplifier and then to a constant fraction discriminator and an ADC (Fastbus).

2.2.5 Trigger

There were three important types of trigger for E94018. The HMS trigger was defined as simultaneous (coincidence) hits in three-out-of-four (3/4) scintillator planes of the HMS hodoscopes (the planes being any combination of detectors in three out of four of the S1X, S2X, S2X, and S2Y planes). This trigger indicated that a scattered negative particle was detected in the HMS. The second trigger type defined coincidence hits in the POLDER Start1 and Start2 detectors, indicating that a recoil deuteron entered the polarimeter. Finally a charge exchange trigger in POLDER was defined as at least three hits in each of the hodoscopes H1 and H2. With these three triggers the following event types were defined:

- e^--event (HMS trigger)
- d-event (POLDER trigger)
- ed-event (HMS trigger $\cap$ POLDER trigger)
- e-CE-event (HMS trigger $\cap$ POLDER trigger $\cap$ CE-trigger)

2.2.6 Data Acquisition

The data acquisition (DAQ) system in Hall C is based on CODA (CEBAF Online Data Acquisition, version 1.4) [121]. CODA is a set of routines which are run on both the main DAQ computer (one of the two available HP9000/735 workstations*) and on several single board computers (Read-Out Controllers, ROCs). The ROCs function as interfaces between the HP9000/735 and the front-end digitizing electronics. Both Fastbus and VME crates were used and a diagram of the DAQ is shown in Figure 2.23. The Fastbus/VME crates house the ADCs, TDCs, and scalars modules that contain event information. The IOCs run a Unix like operating system called VxWorks. The TS (trigger supervisor) generates triggers that cause the ROCs to be read out. The read-out is done in a sparsified mode (aka. "zero-suppression"), i.e. only "non-zero"† channels are read out in order to minimize the amount of data recorded. A CODA Event Builder (EB) process running on the HP builds an event out of data fragments read from the ROCs. The events were then written to local 9 GB hard disks in CODA format. A CODA graphical user interface (GUI) called RunControl runs on the HP, too. This interface to the DAQ system is the one mainly used by the experimentalist running her/his experiment from Hall C counting house. In addition to information being recorded for each event (mainly detector signals), the scalar values are recorded

*The computer live time was approximately 97-99% for kinematical points 4, 5, and 6.

†The concept of a "non-zero" channel is different for an ADC and a TDC. Please, see ref. [75].

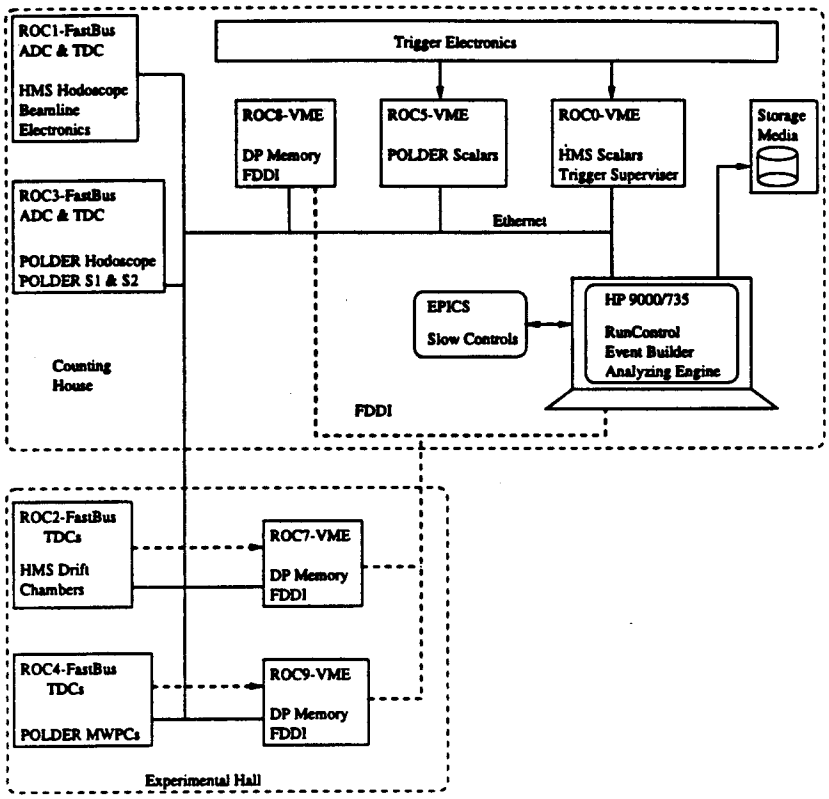

Figure 2.23: The data acquisition system (DAQ) of Hall C during E94018. Figure courtesy of W. Zhao.

every 2 seconds, and the slow control information (cryotarget temperature and pressure, detector high voltages, magnet power supply settings) is being recorded every 30 seconds. The slow control is handled by the Experimental Physics and Industrial Control System (EPICS) [122]. All data log files associated with an experiment are moved from the hard disks of the Hall C to permanent storage on the JLab "Silo" (a StorageTek robotic tape library). The DAQ system is well documented in references [75, 89]. General overviews on DAQ systems are hard to come by but ref. [123] is worth mentioning.

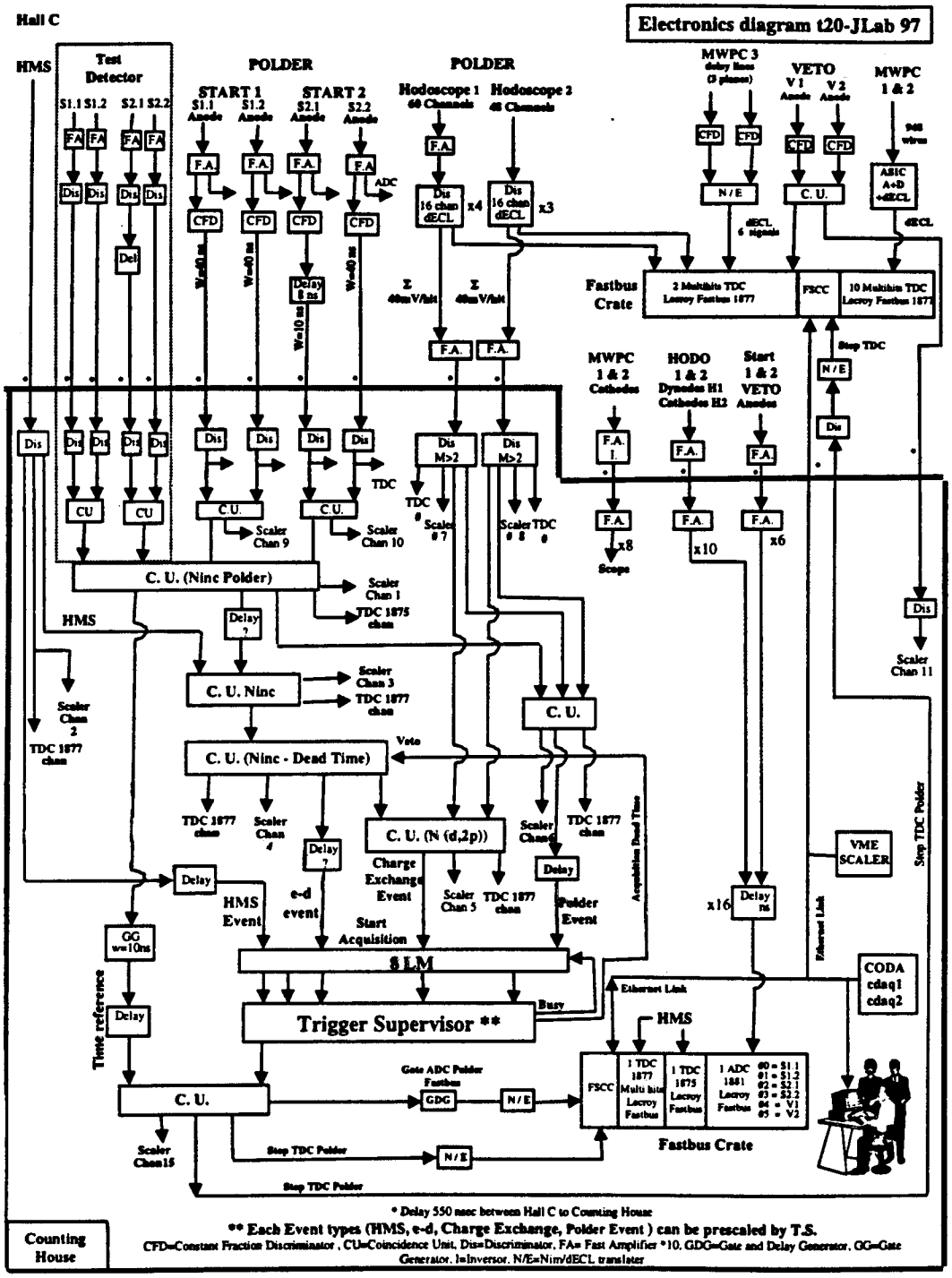

Figure 2.24: An electronics diagram of the t_{20} data acquisition system. Figure courtesy of L. Eyraud.

Chapter 3

Data Reduction and Analysis

E94018 ran continuously for four and a half months in 1997 from April through mid September apart for a break during the month of July. During this time period data were acquired at six different kinematical settings. As the cross section for elastic electron deuteron scattering decreases rapidly with increasing Q^2, considerably more time was spent collecting data at the higher Q^2 data points. As can be seen in the fifth column of Table 3.1 the data analysis task was split between four institutions* and the task force consisted mainly of four thesis students plus one postdoc. In this way the results from the independent analyses could be cross-checked. The analysis results of ISN, MIT, and CEA/Saclay have been reported in references [124, 120, 11], respectively. In addition to the measurement of t_{20} a measurement of the deuteron structure function $A(Q^2)$ was performed during E94018. That particular part of the data was analyzed separately and the

*Massachusetts Institute of Technology (MIT), Commisariat a l'Energie Atomique/Saclay (CEA), Institut des Sciences Nucléaires de Grenoble (ISN), University of Maryland, College Park (UMCP).

Data Point	Q (fm^{-1})	$\frac{d\sigma}{d\Omega}$ (ed→ed) (nb/sr)	Data Acquisition Time ("real" days) [71]	Institutions responsible for data analysis
1	4.1	689	6	MIT & CEA & ISN
2	4.5	357	17	MIT & CEA & ISN
3	5.1	144	13	MIT & CEA
4	5.5	88	27	MIT & CEA & UMCP
5	6.2	40	26	CEA & UMCP
6	6.8	23	31	CEA & UMCP

Table 3.1: A table showing the six kinematical points of the JLab E94018 experiment and some characteristics of these data points. The number of days spent on collecting data for each kinematical point is shown in column four. The division of the data analysis task is shown in the fifth column and the abbreviations used are described in the text.

analyses are described in references [117, 107] and the results were reported in ref. [125]. The data analysis presented in this chapter was carried out between October 1997 and September 1999. The results of the data analysis are presented in Chapter 4. The data sets used at MIT, Saclay and UMCP were predominantly the same but they were not, however, identical.

3.1 Computational Aspects

The computing associated with the data analysis presented here was carried out using IBM RS6000 (7030/3AT) workstations running Unix AIX 4.1. The raw data had been written to 8mm Exabyte tapes (5 GB/tape) and the total amount of raw data (Saturne calibration data and JLab t_{20} data) amounted to almost 400 GB. The analysis code is a hybrid of mainly Fortran 77 and to a lesser extent

C. The analysis code originated on a HP-UX platform but has been ported to a large number of mainly Unix platforms. The analysis code, labeled **ENGINE**, is documented in ref. [75]. The standard Hall C **ENGINE** consists of two main parts of source code: an active part (below the treplay/ directory) and a large library part (below the Csoft/ directory). Source code the user needs to modify for his particular analysis is copied from the Csoft/ directory to the treplay/ directory as source code fragments existing in the treplay/ supersedes source code in Csoft/. In the E94018 analysis code there was an additional third part, a smaller library part containing source code relevant to the analysis of the POLDER quantities (below the Psoft/ directory). The output of ENGINE is normally scalar text files, HBOOK histogram files, and PAW Ntuple files. The output necessary for the t_{20} (POLDER) analysis was compactly written into binary files. For the analysis of the Saturne calibration experiment a separate analysis code, labeled **ligne**, was used. However, it also used the same Psoft/ source code routines. A flow chart of the POLDER event reconstruction is shown in Figure 3.1 and Figure 3.2. Moreover, several different software tools were used in various stages of the analysis process. These include Physica [126], PAW++ [127], Perl [128], and MINUIT [129].

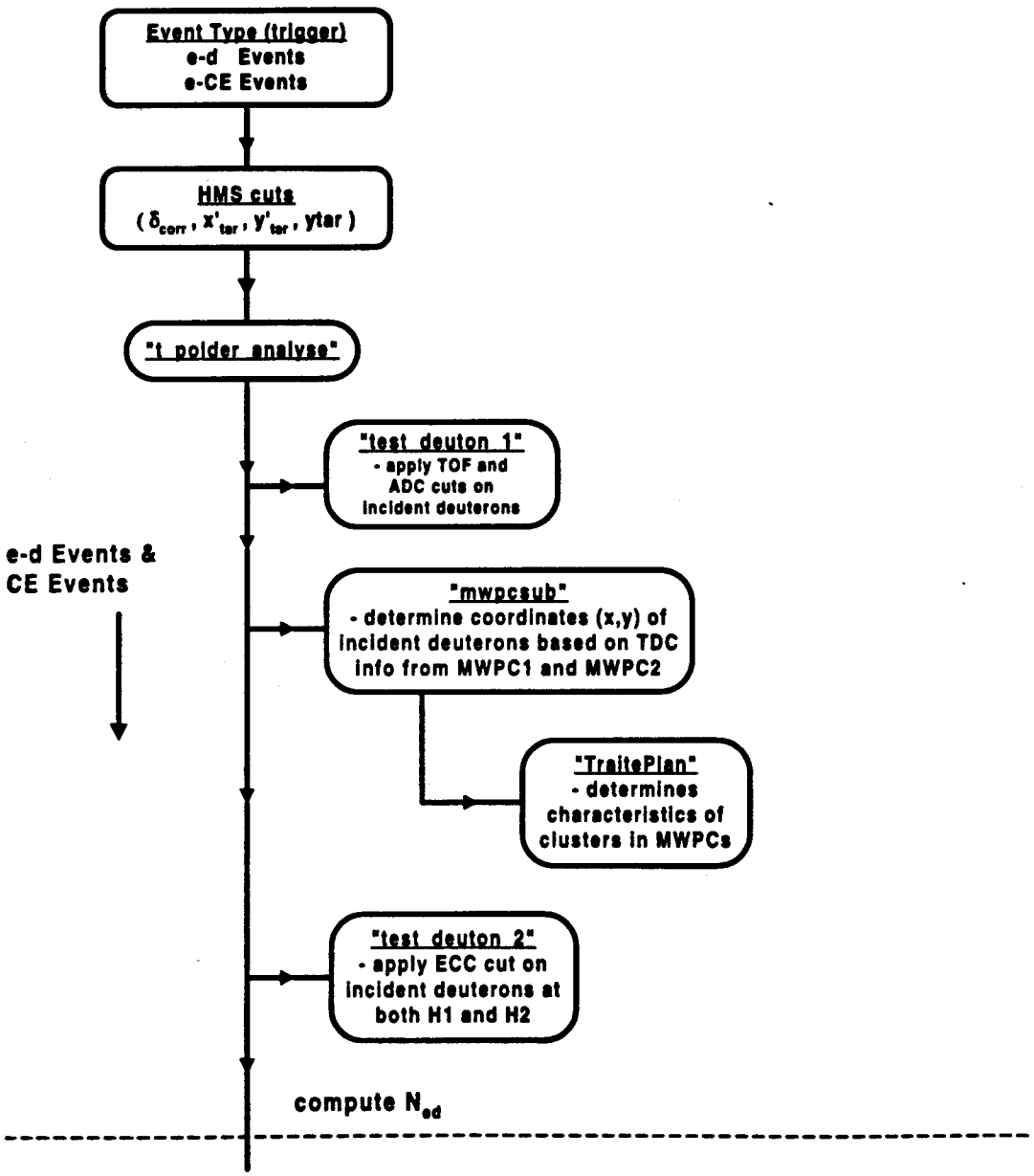

Figure 3.1: A flow chart with brief explanations of the POLDER event reconstruction. The names of software routines are within quotation marks. Both the ed and CE events are processed thorugh the shown stages. This flow chart continues in Figure 3.2.

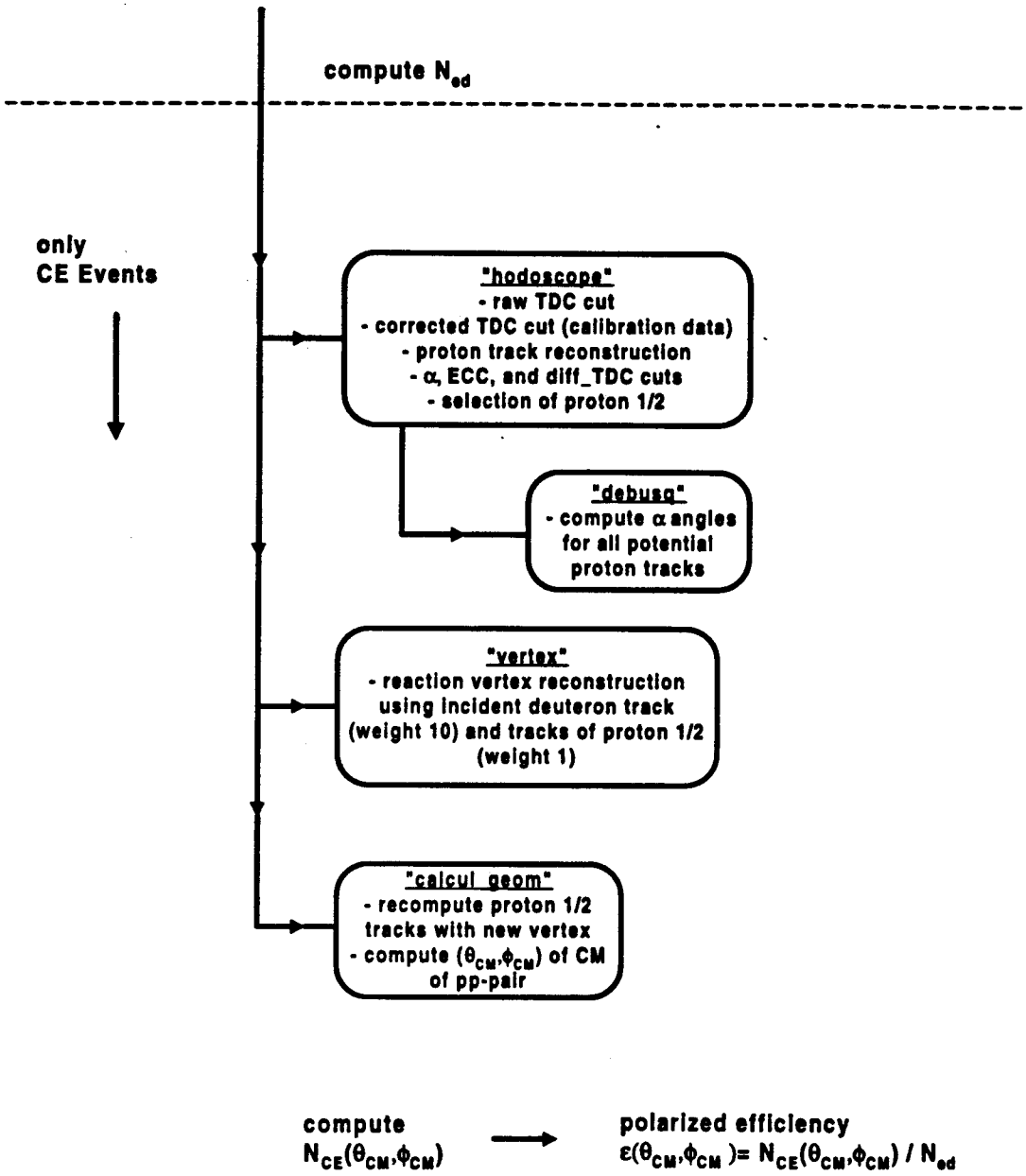

Figure 3.2: A continuation of the flow chart shown in Figure 3.1. This part of the flow chart shows stages through which only CE events go. The names of software routines are within quotation marks.

3.2 Alignment of the Detector Elements of POLDER

It is vital to know the positions of the detector elements of POLDER with respect to themselves because the angular distributions of the Saturne calibration data and the JLab t_{20} data are compared in the analysis. Therefore the alignment of the detector elements is important and it was done on the software level in the analysis. Because one needs to simultaneously move hodoscopes H1 and H2 in between different kinematical settings it becomes necessary to realign the detector elements after each change. During E94018 data for the six kinematical settings were collected in the following sequence (data point number): $2 \rightarrow 4 \rightarrow 1 \rightarrow 3 \rightarrow 4 \rightarrow 5 \rightarrow 6 \rightarrow 2 \rightarrow 6$. This sequence translates into the following sequence of hodoscope positions: $\mathrm{I} \rightarrow \mathrm{II} \rightarrow \mathrm{I} \rightarrow \mathrm{II} \rightarrow \mathrm{III} \rightarrow \mathrm{I} \rightarrow \mathrm{III}$. One needs a set of alignment parameters for each change of hodoscope positions.

The method for determining the alignment parameters is based on a procedure where a detector element is aligned with the help of two other detector elements. This procedure is repeated three times in the following order: first MWPC3 is aligned using MWPC2 and H2. Next MWPC1 is aligned using MWPC2 and MWPC3, and finally H1 is aligned using MWPC1 and MWPC2. For the JLab t_{20} data, recoil deuterons from e-d coincidence events were used for this procedure. The alignment parameters are determined in the first step in the following

Data Point	MWPC1		H1	
	Δ_x (mm)	Δ_y (mm)	Δ_x (mm)	Δ_y(mm)
4	1.39	0.96	0.76	1.10
5	1.28	1.23	0.97	0.68
6	1.30	1.35	0.90	0.66

Table 3.2: The alignment parameters used for kinematical points 4, 5, and 6. The uncertainty in these offset parameters are of the order of a few hundredths of a millimeter [116].

way: the axis of reference is chosen along the centers of wire chamber MWPC2 and of hodoscope H2. Then the coordinate information of a deuteron hit in MWPC2 and H2 is used to reconstruct a track, which is then projected onto MWPC3 in order to give the computed location of the hit. At the same time one has coordinate information of where that deuteron hit MWPC3. The difference between these two pieces of coordinate information corresponds to the magnitude of the offset of MWPC3 with respect to the chosen axis of reference MWPC2-H2. Using a large number of deuteron events the computed differences will create a Gaussian distribution whose centroid has the value of the offset parameter needed to properly align the detector element in question. These Gaussian distributions for MWPC3, MWPC1, and H1 for a calibration run are shown in Figure 3.3. The detector elements can be aligned to a precision much better than a millimeter [116] using this method and the high statistics of incident deuterons. The alignment parameters used for kinematical points 4, 5, and 6 are shown in Table 3.2.

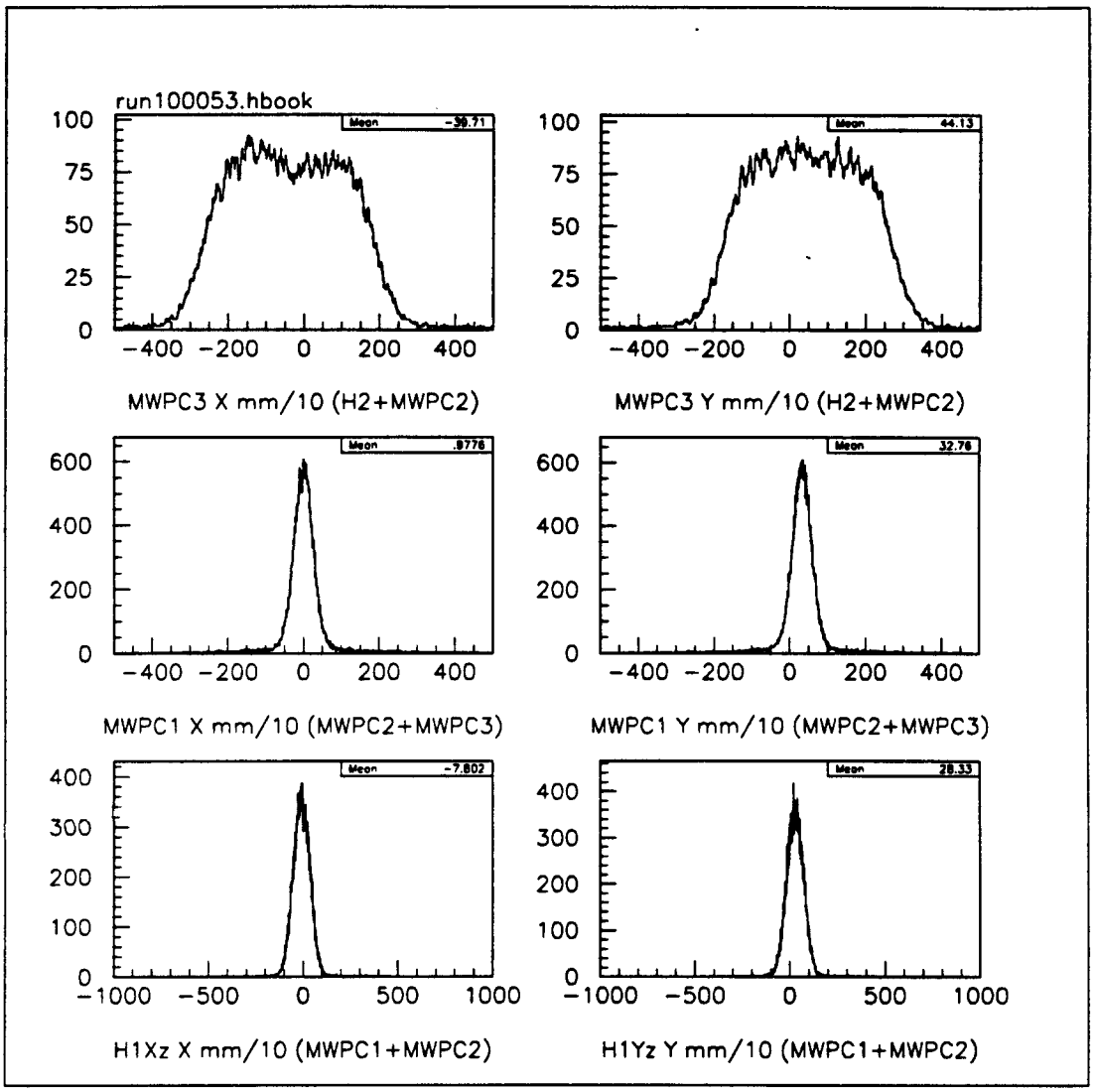

Figure 3.3: Histograms from the alignment procedure. The top two histograms show the differences (x and y) between the measured hit positions and the corresponding computed (using MWPC2 & H2) hit positions of incident deuterons in MWPC3. The histograms in the middle and on the bottom are the corresponding ones for MWPC1 and H1. The units on the horizontal axis are in tenths of millimeters.

3.3 Event Selection

The analysis of the JLab t_{20} data is next described. In the analysis the e-d- and e-CE-event types which were described in Section 2.2.5 get processed. In other words, the first criterion is appropriate triggers in both spectrometer arms within the coincidence timing window. In the analysis it is assured that one is detecting an elastically scattered electron in the HMS. Next one assures that the trigger in the deuteron detectors corresponds to a recoil deuteron. In the case of a e-CE-event the final step is to make sure that the trigger from the POLDER hodoscopes H1 and H2 corresponds to a proton-proton pair in the final state of a charge exchange reaction induced by the incident recoil deuteron. The details of this multiple step filtration process is next described.

3.3.1 HMS cuts

The main difference in the data analyses of the Saturne calibration data and the JLab t_{20} data is the HMS component. At Saturne, a pure deuteron beam was utilized, while a secondary beam of deuterons produced in elastic e-d scattering was used at JLab. Hence steps had to be taken to keep this secondary beam as clean, i.e. purely consisting of recoil deuterons from elastic e-d scattering, as possible. The background consists mainly of random coincidences between electrons and protons. These protons stem from parasitic deuteron breakup ^{2}H(e, e'p)n reactions. In the Saturne calibration experiment, emphasis was put on limiting

the background due to multiple simultaneous incident deuterons from the high incident deuteron flux of 10^5 deuterons/s.

The HMS cuts were:

- one and only one track at the focal plane of the HMS. The tracking routine tries to reconstruct one or more tracks for each HMS trigger. By constraining the number of tracks to equal one, one avoids both bad events for which the software was unable to reconstruct a track (=zero tracks) and ambiguous events with multiple tracks at the focal plane.

- x'_{tar} (y'_{tar}) cut, i.e. a cut on x'_{tar} (y'_{tar}) which corresponds to a cut on the angle at the primary target between the horizontal (vertical) plane and the direction of the scattered electron. Representative distributions of x'_{tar} and y'_{tar} for kinematical points 4, 5, and 6 are shown in Figures 3.4 and 3.5.

- ytar-cut, i.e. a cut on the reconstructed z-location of the ^{2}H(e, e'd) reaction vertex. The quantity 'ytar' is simply a projection of the z-axis perpendicular to the direction of the spectrometer, i.e. ytar = z $\sin(\theta_{HMS})$, as illustrated in Figure 3.6. Representative distributions of ytar for the kinematical points 4, 5, and 6 are shown in Figure 3.7. The events in the histograms of Figure 3.7 are e-d events constrained to having at least one reconstructed electron track at the focal plane of the HMS. For each run there were 50,000 events replayed so the number of entries of the histograms shows to what degree

one finds at least one track at the HMS focal plane for the three different kinematical settings.

- δ_{corr} cut, i.e., a cut on the momentum of the scattered electron, with a correction applied due to the recoiling deuteron: the main purpose of this cut is to distinguish the elastically scattered electrons from lower energy electrons which stem from, for example, deuteron breakup reactions. The δ_{corr} quantity is computed as:

$$\delta_{\text{corr}} = \frac{\left[\frac{1+\frac{2E}{M_d}\sin^2(\frac{\theta}{2})}{1+\frac{2E}{M_d}\sin^2(\frac{\theta_0}{2})}\right] p - p_0}{p_0}, \tag{3.1}$$

where p_0 is the central momentum setting of the HMS spectrometer, p is the measured momentum of the scattered electron, θ_0 is the central angle setting of the HMS, and θ is the measured scattering angle of the electron. This is a modified expression of the normally used and simpler quantity δ:

$$\delta = \frac{p - p_0}{p_0}. \tag{3.2}$$

The advantage of making a cut on the δ_{corr} quantity over making a cut on the δ quantity can be seen if one compares the distributions of these two quantities, shown in Figure 3.8. The kinematic broadening is removed in the δ_{corr} quantity and the width of the elastic scattering peak is only due to the resolution of the HMS spectrometer. Representative distributions of δ_{corr} for kinematical points 4, 5, and 6 are shown in Figure 3.9.

The Cherenkov counter and the lead glass calorimeter of the HMS detector package were not used in the off-line data analysis. Making a cut on the corrected momentum quantity δ_{corr} together with a cut on the coincidence time (see below) was clearly sufficient for identifying the elastically scattered electrons. Hence it was deemed unnecessary to include the Cherenkov counter and the lead glass calorimeter in the analysis.

3.3.2 Deuteron Cuts

There are four types of deuteron cuts: time-of-flight (TOF), cut on pulse height spectra (ADC), cuts on multiwire proportional chamber (MWPC) quantities, and geometrical constraints on the deuteron tracks at the POLDER hodoscopes. A description of these follows:

- TOF-cut: this cut is effectively a coincidence timing cut. The triggers used are the HMS trigger and the POLDER trigger. Three different TOFs are used and their characteristics are shown in Table 3.3. These three redundant cuts help distinguish between recoil deuterons and background protons. Representative distributions are shown in Figure 3.10. The effectiveness of the HMS δ_{corr} cut is illustrated in Figure 3.11.

- ADC-cut: for each Start detector the signals from its two PMTs are added and pulse height analyzed by an ADC (as mentioned in the previous chapter). The incident recoil deuterons deposit more energy in the Start detec-

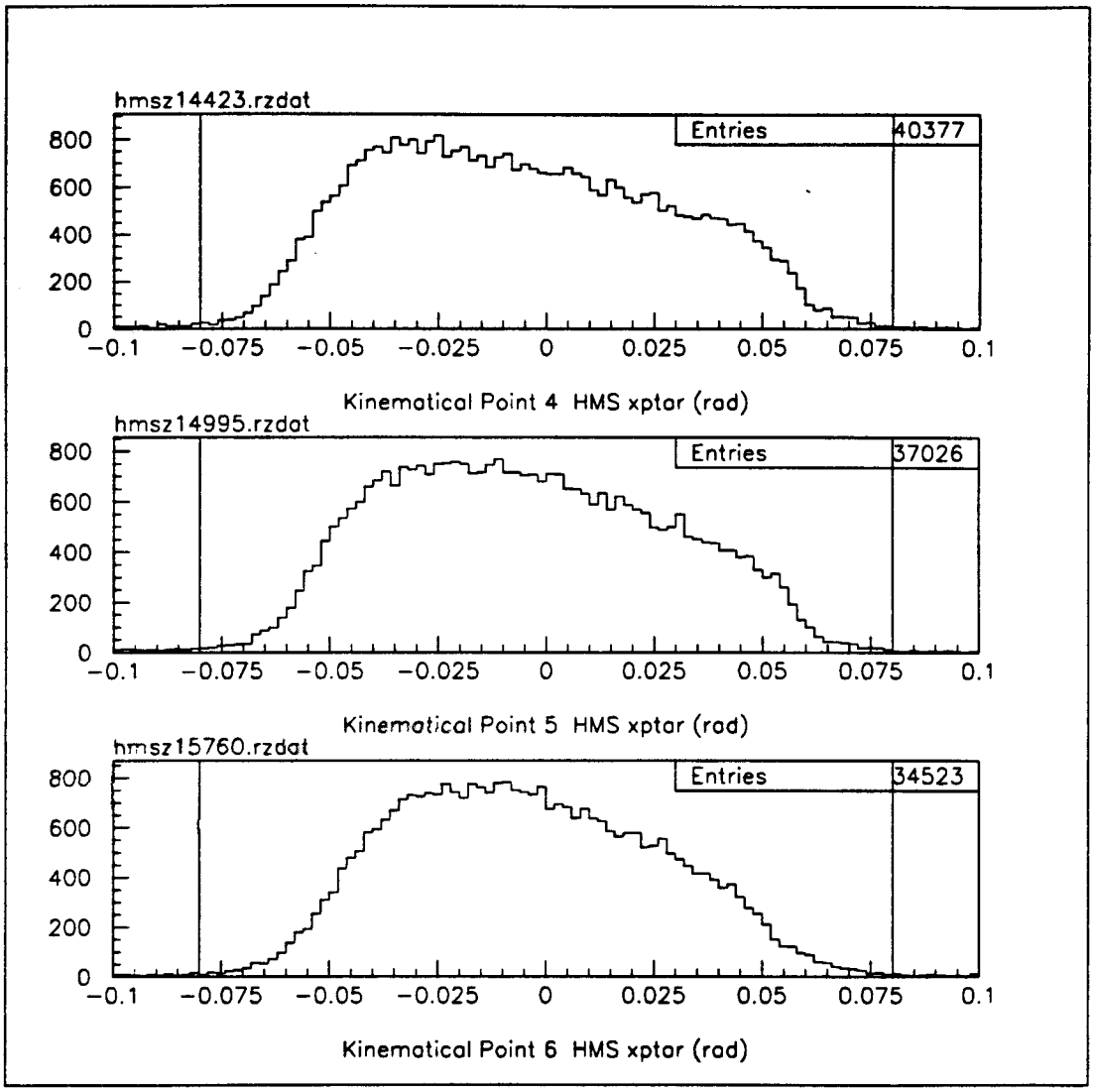

Figure 3.4: Distributions of the HMS x'_{tar} quantity for kinematical points 4, 5, and 6. The x'_{tar} cut applied to *all* three data points was [-80,+80] (mrad). The locations of these cuts are illustrated with vertical lines in the histograms.

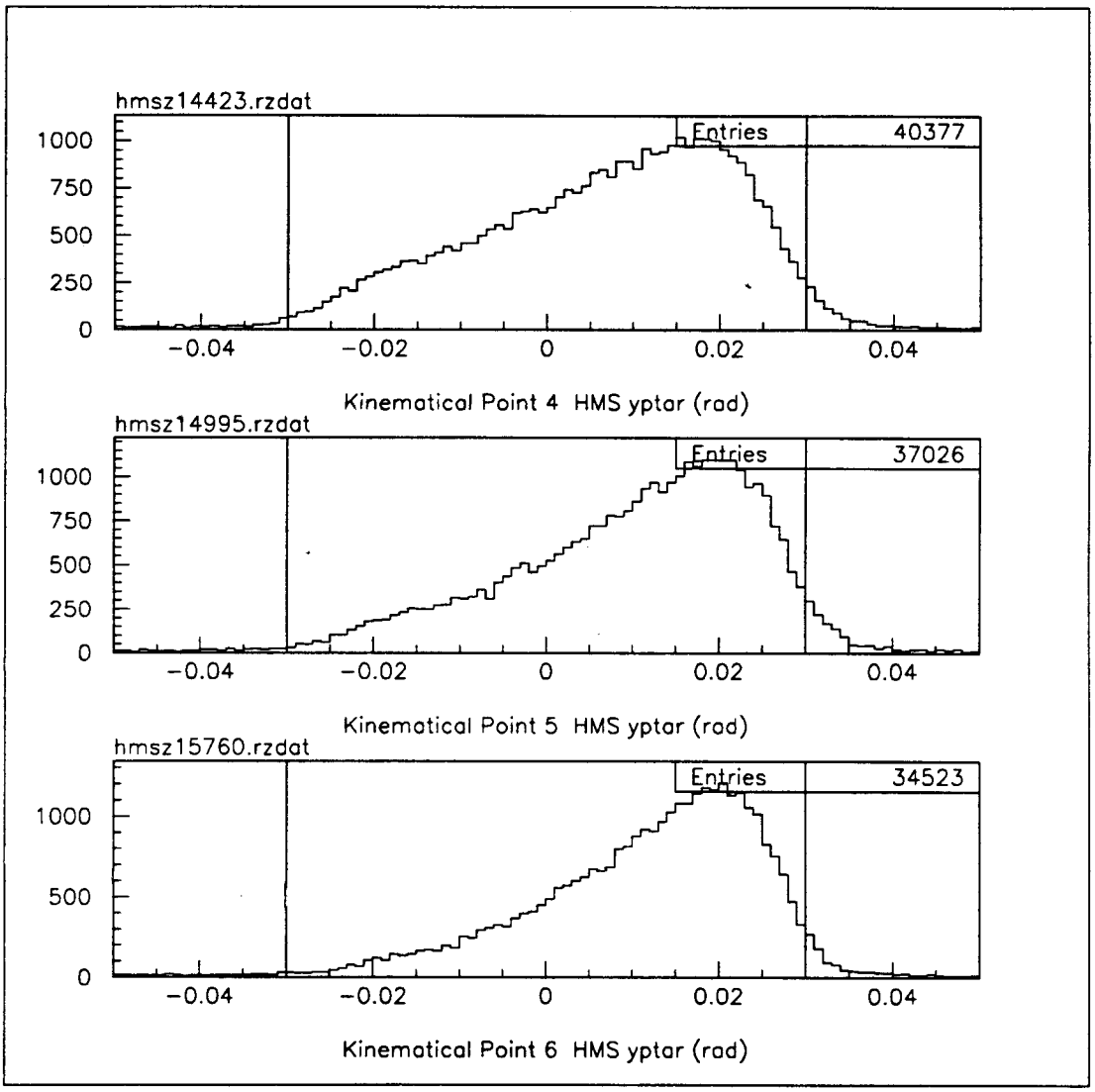

Figure 3.5: Distributions of the HMS y'_{tar} quantity for kinematical points 4, 5, and 6. The y'_{tar} cut applied to all three data points was [-30,+30] (mrad). The locations of these cuts are illustrated with vertical lines in the histograms.

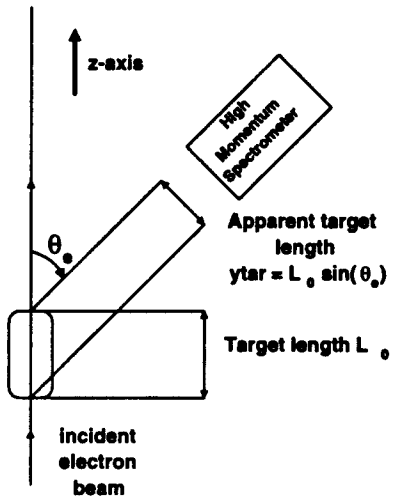

Figure 3.6: An illustration showing how the quantity ytar is defined. Ytar is effectively a projection of the target length perpendicular to the direction of the electron spectrometer HMS.

	Start trigger	Stop trigger	TDC type	Resolution of TDC (ns)
tof1	HMS	POLDER	multihit	0.5
tof2	POLDER	HMS	HR	0.1
tof3	HMS	POLDER	HR	0.1

Table 3.3: A table showing the characteristics of the three different time-of-flight (TOF) quantities which were used in the analysis. Here HR stands for High Resolution.

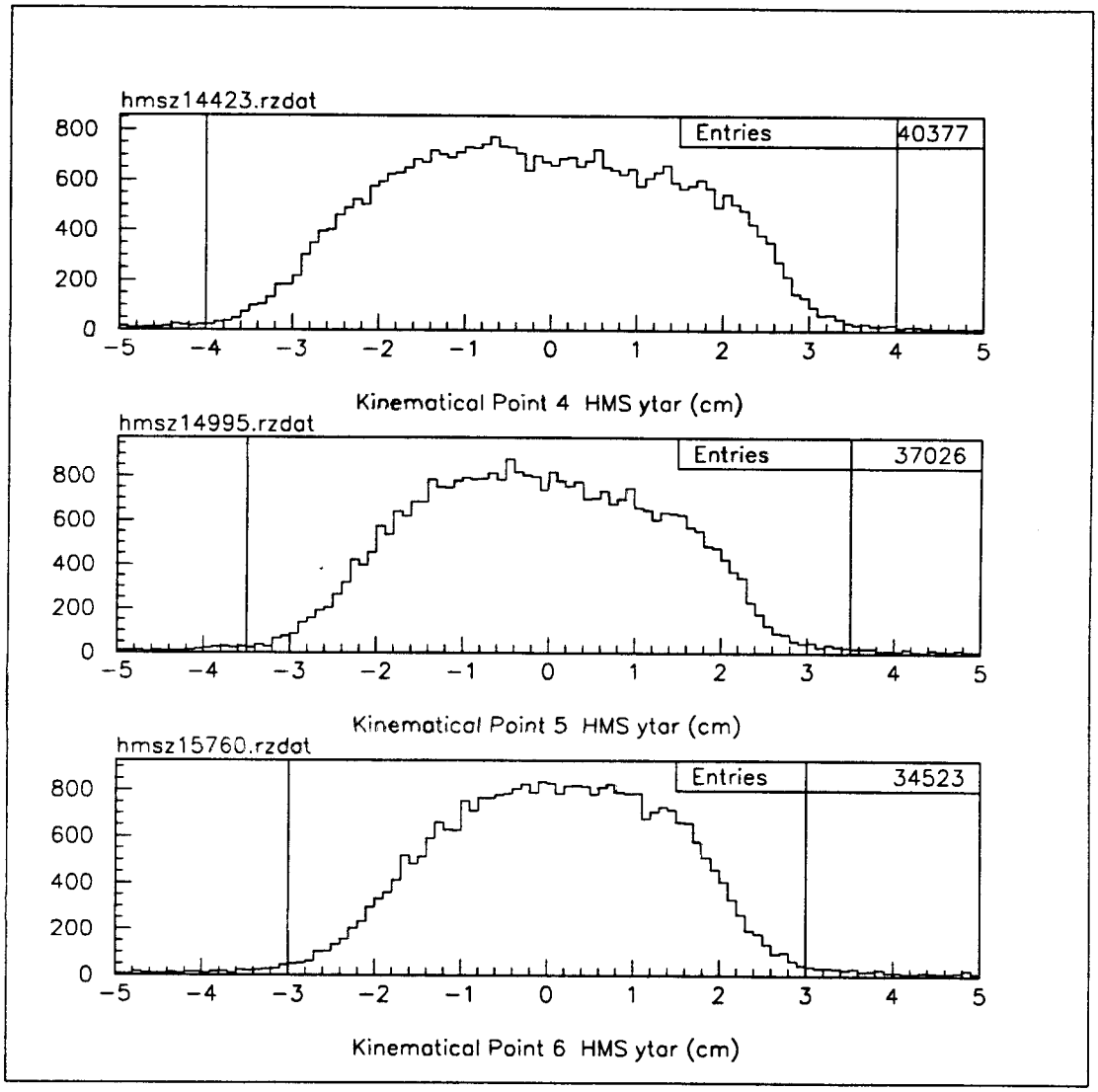

Figure 3.7: Distributions of the HMS ytar quantity for the three kinematical points. The ytar cuts applied were [-4,4], [-3.5,3.5], and [-3,3] (cm) for kinematical points 4, 5, and 6, respectively. The locations of these cuts are illustrated with vertical lines in the histograms.

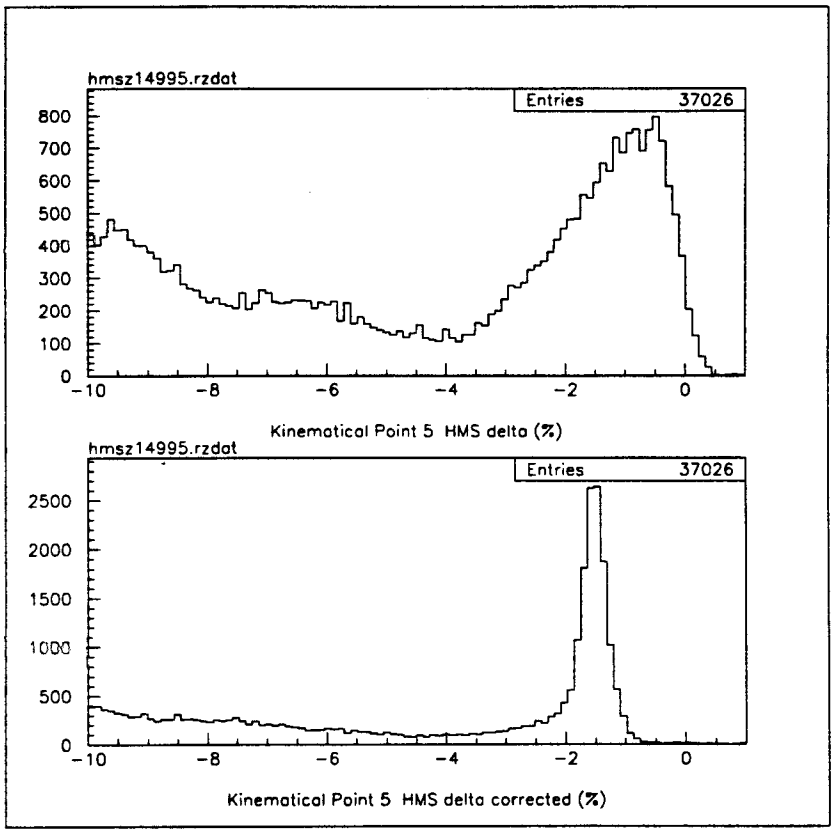

Figure 3.8: Distributions of the δ (top) and δ_{corr} (bottom) quantities for kinematical point 5. The elastic peak of e-d scattering is much more clearly distinguishable in the δ_{corr} distribution and hence it is easier to determine a suitable cut for this quantity.

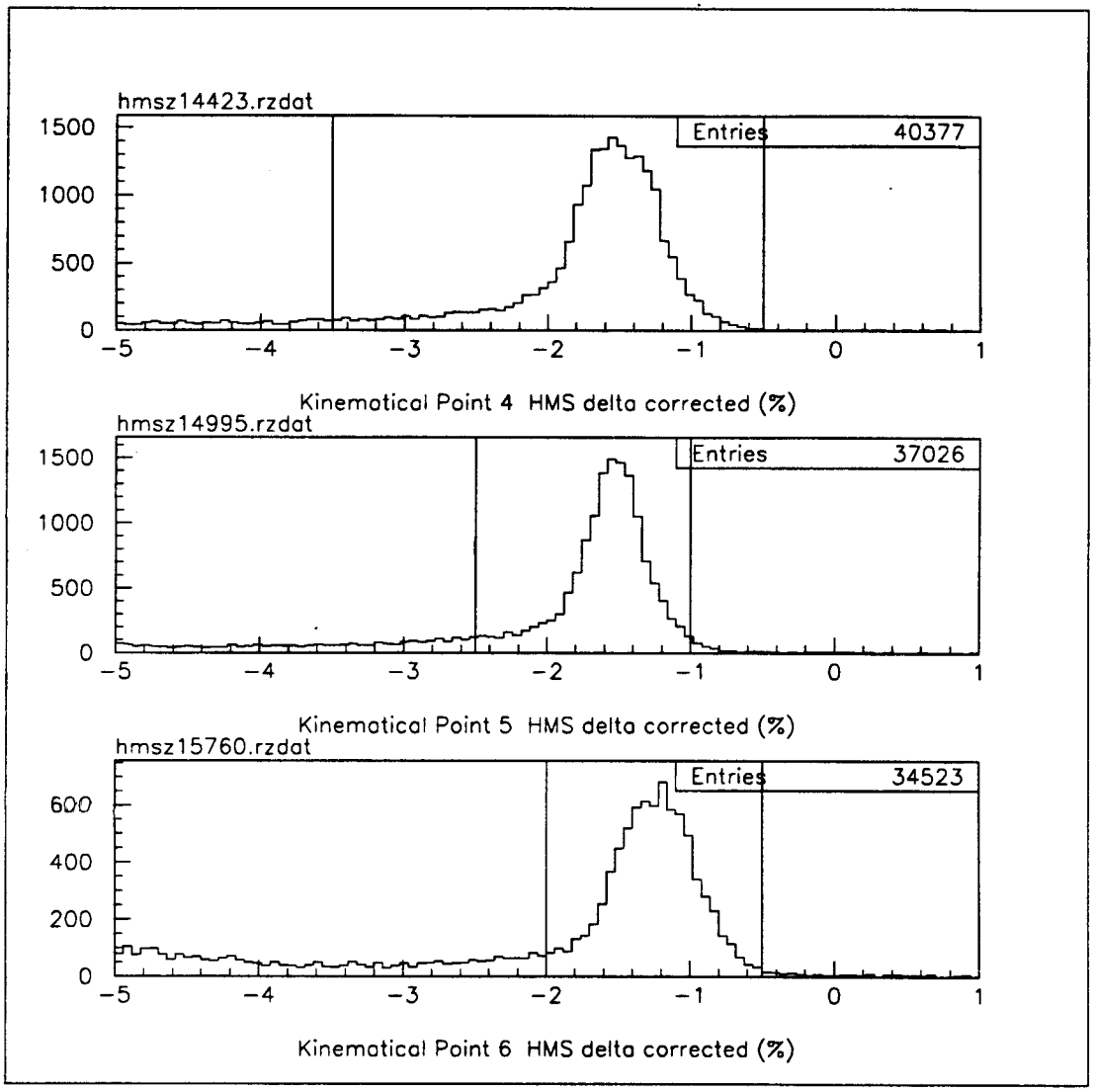

Figure 3.9: Distributions of the δ_{corr} quantity for kinematical points 4, 5, and 6. The δ_{corr} cuts applied were [-3.5,-0.5], [-2.5,-1.0], and [-2.0,-0.5] (%) for points 4, 5, and 6, respectively. The locations of these cuts are illustrated with vertical lines in the histograms.

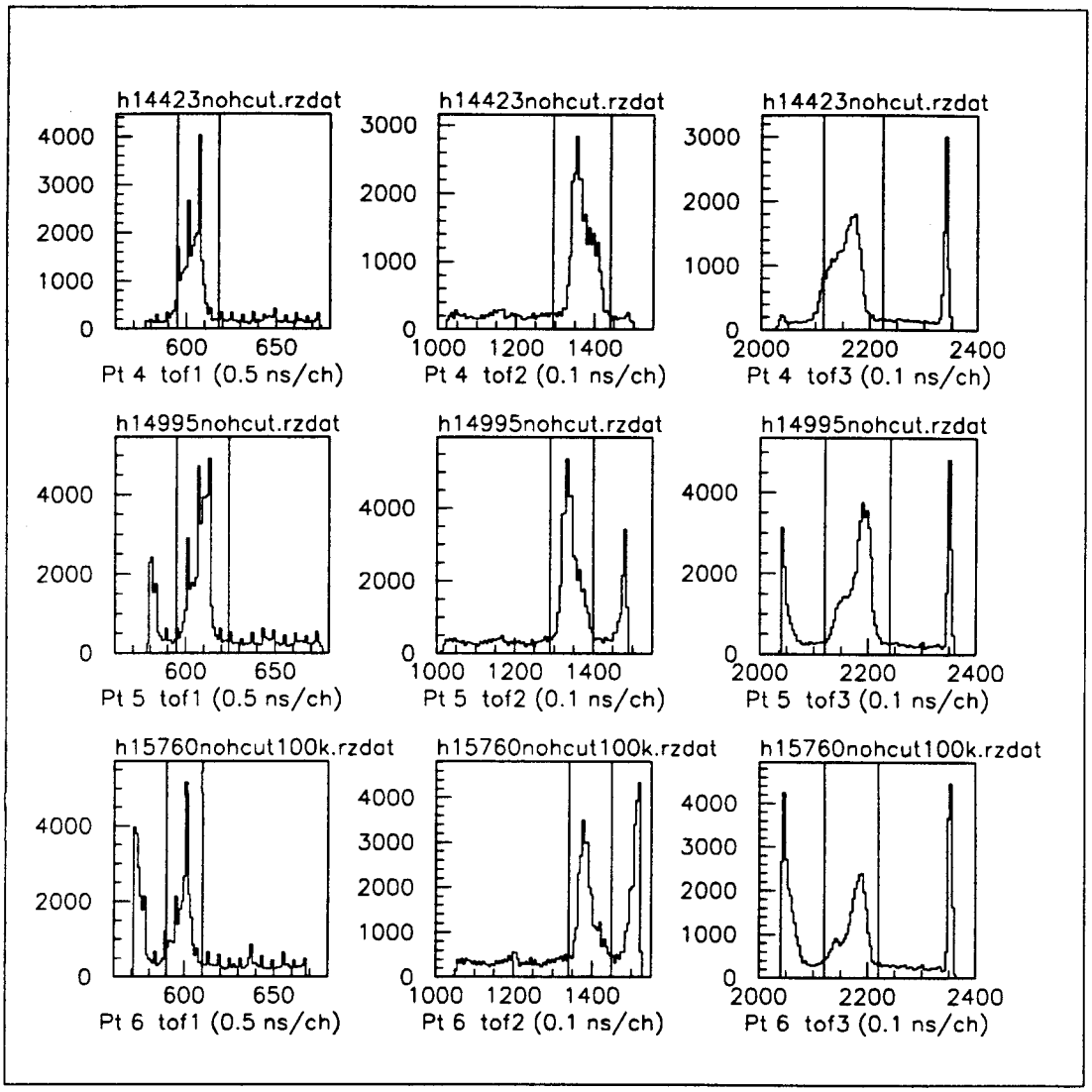

Figure 3.10: Distributions of the three different TOFs (tof1, tof2, and tof3) for the three kinematical points 4, 5, and 6. The vertical lines indicate the locations of the applied cuts. No HMS cuts except "one track at the focal plane" have been applied for these raw TOF distributions.

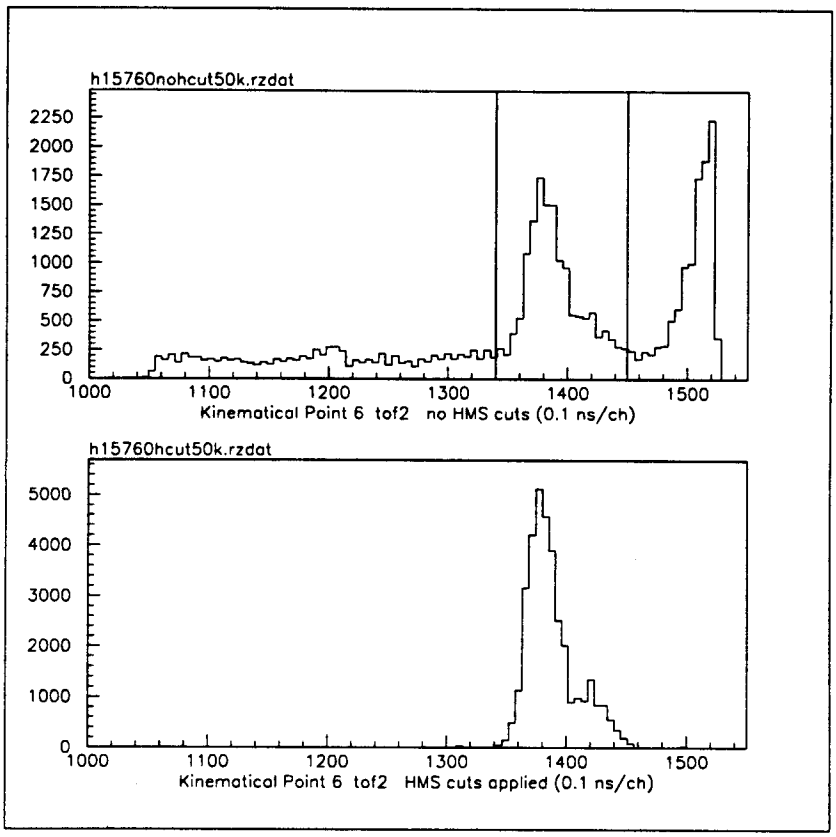

Figure 3.11: An illustration of the effectiveness of the HMS cuts, in particular the momentum cut δ_{corr}. The top histogram shows a raw tof2 distribution for kinematical point 6. The vertical lines indicate the locations of the tof2-cuts. The bottom histogram shows the tof2 but now with the HMS cuts applied. As can be seen, the entire proton peak has disappeared, and so has almost all of the rest of the background. Note: the total number of counts in both histograms are identical, that is in order to avoid confusion the reader should ignore the scale on the vertical axis.

tors than the background protons do. Hence one can, by applying a cut at the lower edge of the ADC spectrum, discriminate against background protons. The energy deposited in the Start detectors will be higher if an event has multiple incident particles (deuterons, protons). One can discriminate against these types of events by applying a cut at the upper edge of the ADC spectrum. Multiple incident deuterons events were always negligible in the JLab data, but occurred in the calibration experiment. Representative ADC histograms are shown in Figure 3.12.

- MWPC cut: the condition is that at least two-out-of-three wire planes of both MWPCs give a signal.

- exterior cone cut (ECC): the reconstructed tracks of the incident recoil deuterons are projected onto the POLDER hodoscopes H1 and H2. A simple geometrical cut is applied at both H1 and H2. The tracks of the deuterons are required to fall within a circle with a radius of 7 cm centered at the middle [(x,y)=(0,0)] of the hodoscopes as illustrated in Figure 3.13.

The effect of the various deuteron cuts on e-d events for kinematical points 4, 5, and 6 are illustrated in Figures 3.14, 3.15, and 3.16. The pulse height spectra cuts of the Start detectors have only a small impact as they follow the HMS and TOF cuts which were already applied. The MPWC cuts reduces the number of multiple incident particles and the external cone cuts do the rest of the job. The

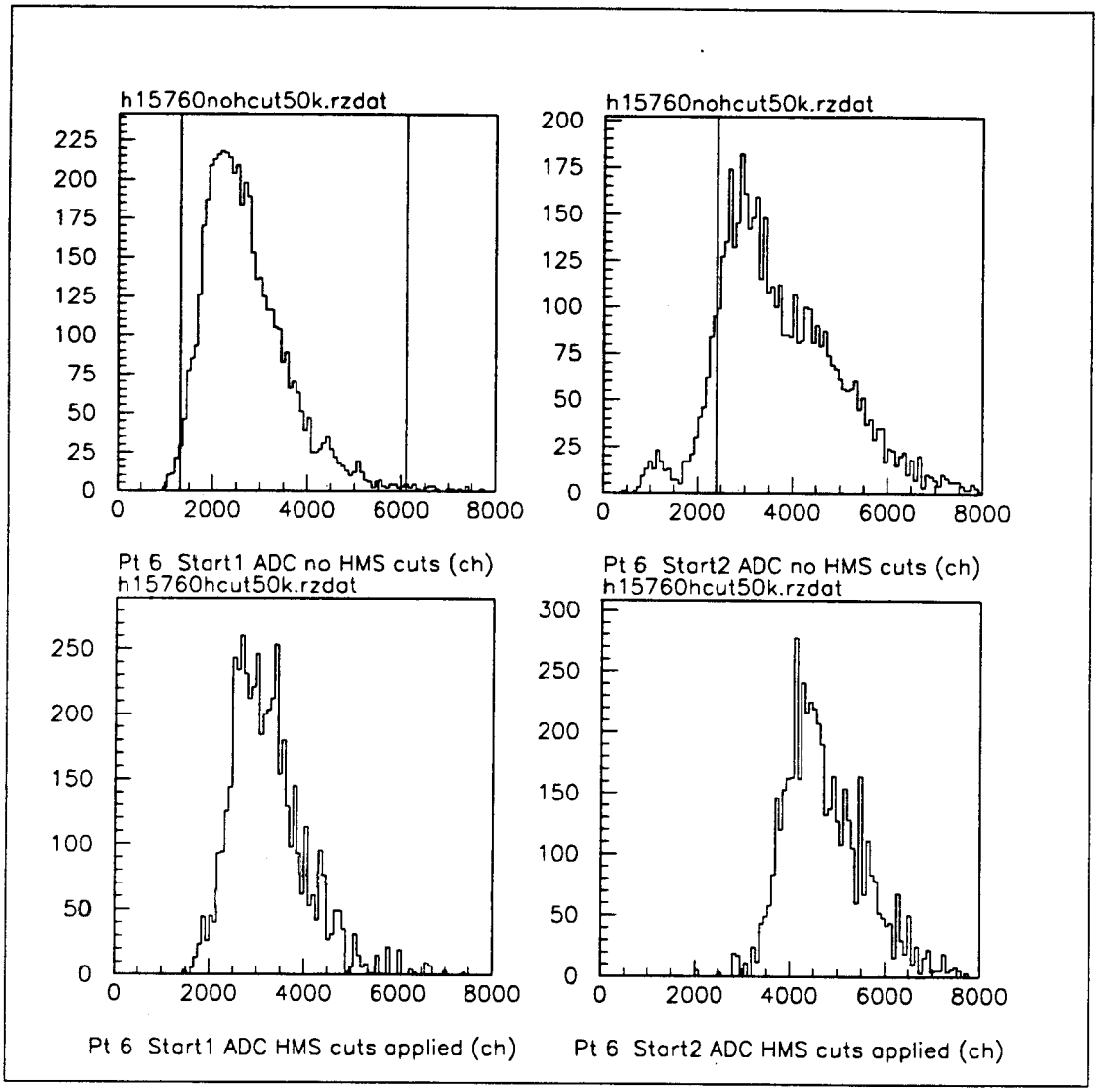

Figure 3.12: The top two histograms show the raw ADC pulse height spectra of the Start1 and Start2 detectors. The vertical lines indicate the locations of the ADC cuts. The bottom histograms show the effect of applying the HMS cuts to these ADC pulse height spectra. The HMS cuts remove background protons from the lower edge of the spectra as can be clearly seen. Note: the total number of counts in the top/bottom histograms are identical, that is in order to avoid confusion the reader should ignore the scale on the vertical axis.

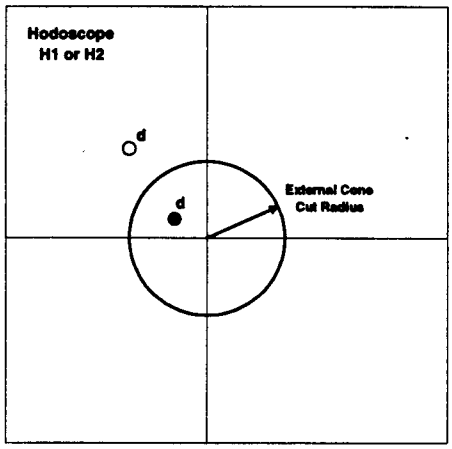

Figure 3.13: An illustration of the external cone cut (ECC) which is applied to the projected tracks of the incident deuterons at H1 and H2. The large square in the figure represents the hodoscope (either H1 or H2). The small filled circle within the deuteron ECC-circle represents the projected track of an accepted incident deuteron event. The small empty circle outside the deuteron ECC-circle represents the projected track of a rejected incident deuteron event.

ECC radius is the same at both H1 and H2 and consequently the more limiting solid angle at H2 has a larger impact.

3.3.3 Charge Exchange Cuts

The HMS and deuteron cuts are applied to the e-CE-events, too. In addition, in order to identify the pp-pairs of the CE reactions one looks for two charged particles at forward angles with velocities close to those of the incident deuterons. This is done by applying the following CE cuts:

- raw TDC cut: an "internal" POLDER time-of-flight (TOF) cut was used. The TOF is measured between the Start2 detector and the hits in H1 and

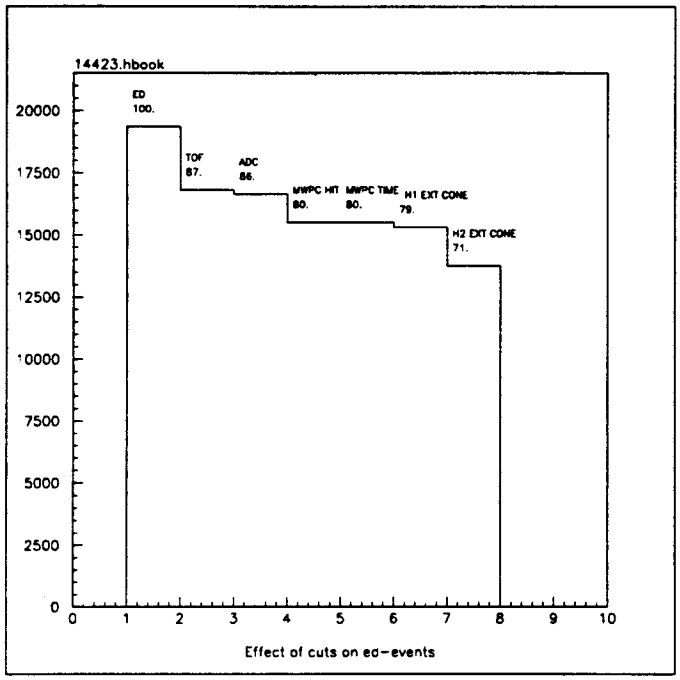

Figure 3.14: The effect of the various deuteron cuts for kinematical point 4. The first bin with "100% ED" events corresponds to events which have passed the HMS cuts.

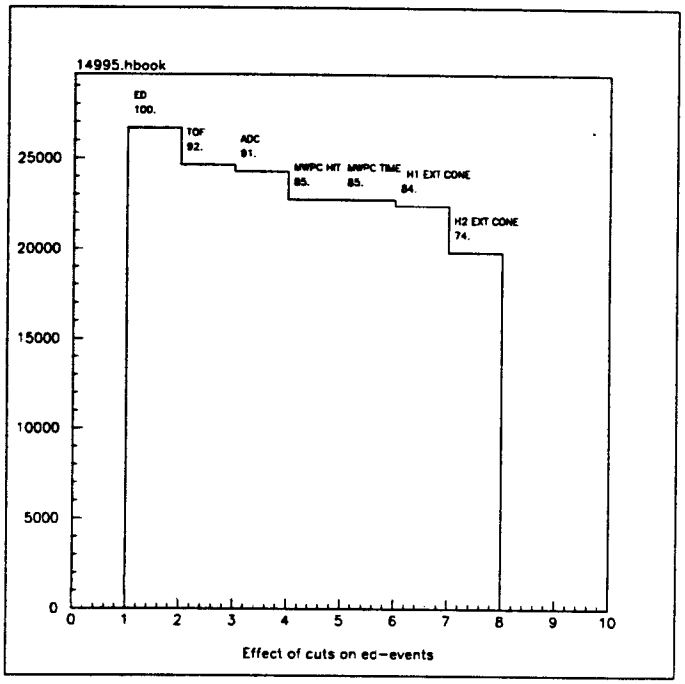

Figure 3.15: The effect of the various deuteron cuts for kinematical point 5.

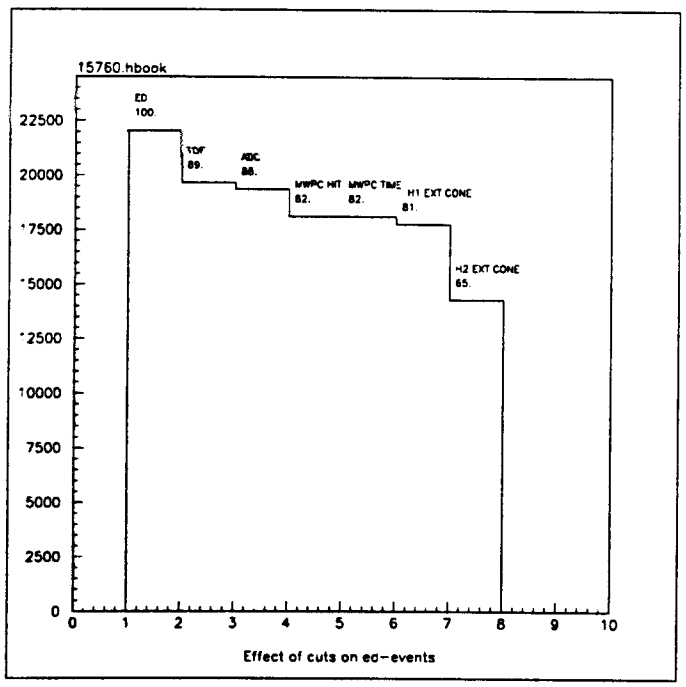

Figure 3.16: The effect of the various deuteron cuts for kinematical point 6.

H2. By requiring the final states protons of the CE reaction to hit the hodoscope bars within a set time interval after detecting an incident deuteron it is assured that the protons stem from the detected incident deuteron. The acceptable time interval was restricted to select the protons that travel at velocities close to those of the incident deuterons. Each hodoscope bar (total of 108 bars in H1 and H2) is assigned its own characteristic raw TDC cut interval. The flight path distances are, of course, different to H1 and to H2 but they also differ slightly to the individual bars within the same hodoscope plane. Moreover, these individual cuts of each bar also account for variations in timing due to the electronics, such as different cable lengths to the PMTs of the individual hodoscope bars.

- incoherent trajectories cut: each selected proton has a hit coordinate, i.e. (x,y)-values, at both H1 and H2. It is possible to construct two tracks, each track going from the reaction vertex* to the location of the hit at the hodoscope in question. The opening angle between these two tracks is labeled α and an illustration of the definition of this angle is shown in Figure 3.17. An upper limit, α_{max}, is set on this angle and the limit is adjusted for the different hodoscope positions as shown in Table 3.4. In Figure 3.18 distributions of the α angles of all potential proton tracks from two calibration runs are shown. Representative distributions of the α-angle of the

*The vertex is assumed at this point in the analysis to be $(x,y,z)=(x_d,y_d,0)$ where (x_d,y_d) are the coordinates of the incident deuterons.

Hodoscope Position	Angle α_{max} (°)
2	3.5
3	3.0

Table 3.4: A table showing the α_{max} cut values for hodoscope positions 2 and 3.

selected "proton 1" and "proton 2" are shown in Figure 3.19. (The meaning of "proton 1/2" is described below in Section 3.3.4.) The top histograms in Figure 3.19 show these distributions for calibration run # 100069, which used hodoscope position 2. The bottom histograms show these distributions for calibration run # 100098 which used hodoscope position 3. The arrows indicate the locations of the α-cuts: 3.5° for hodoscope position 2 and 3.0° for hodoscope position 3. Hits in the scintillator bars are considered more important than the value of the α-angle itself. That is, in choosing between selecting a potential "proton 2" with an α-angle less than the cut value but with a hit in an identical scintillator bar as the already selected "proton 1" vs. choosing a "proton 2" with an α-angle larger than the cut value but with hits in different bars than the already selected "proton 1", the latter alternative is favored. This leads to a "proton 2" α-angle distribution which extends beyond the cut value as can be seen in Figure 3.19.

- corrected TDC cut: the time it takes the scintillation light to reach the PMT depends on how close to the end of the bar the proton hits the bar. For the Saturne calibration data the raw TDC cuts are slightly modified

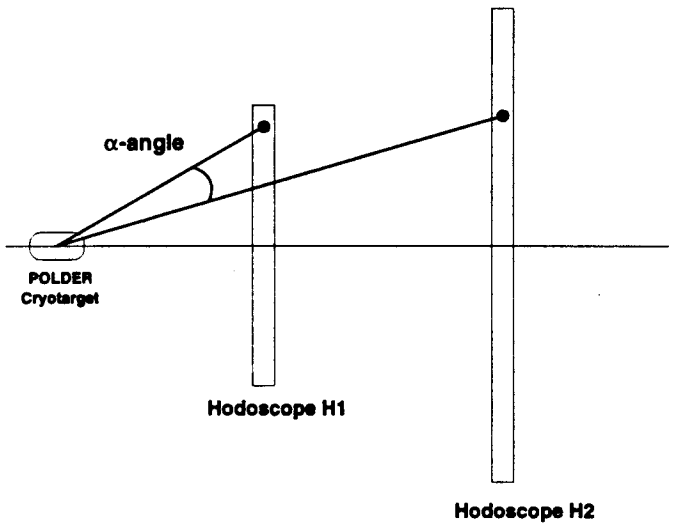

Figure 3.17: An illustration of the definition of the α-angle. The α-angle is the angle between the track segments vertex $\rightarrow$H1 and the track segment vertex $\rightarrow$ H2, where vertex $\rightarrow$ H1 (or H2) stands for the track between the center of the cryotarget of POLDER and the proton hit in H1 (or H2). The more collinear these two track segments are the smaller the α-angle and the likelier it is that they belong to the same emerging proton of a CE-event.

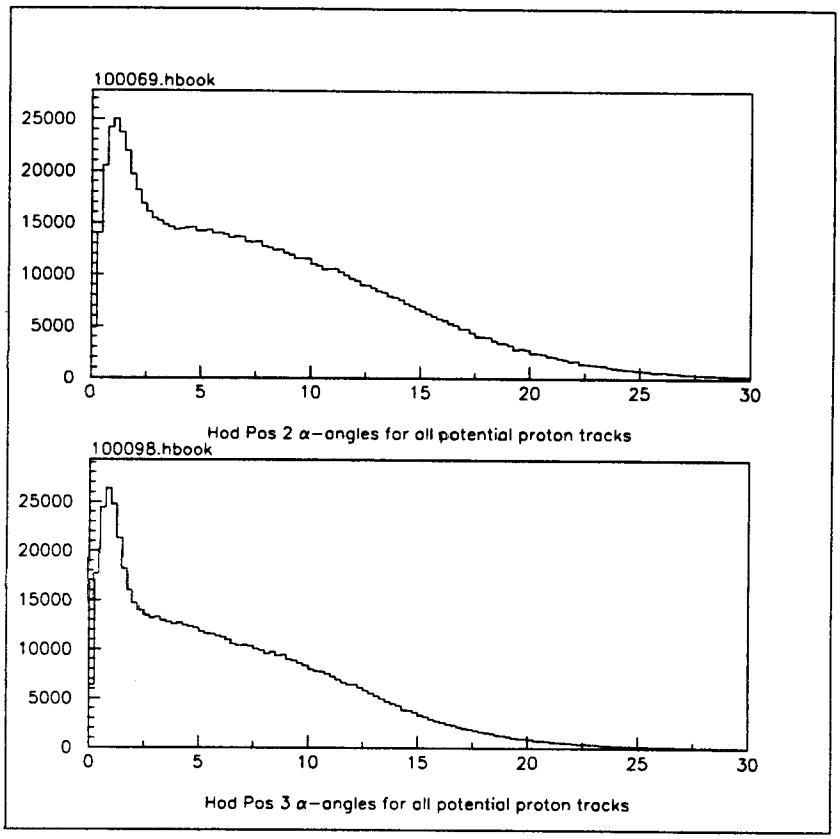

Figure 3.18: A figure showing two histograms of the α-angle of all the potential proton tracks found by the POLDER tracking algorithm. The top histogram is from a calibration run with the hodoscopes in position 2 while the bottom histogram is from a calibration run with the hodoscopes in position 3.

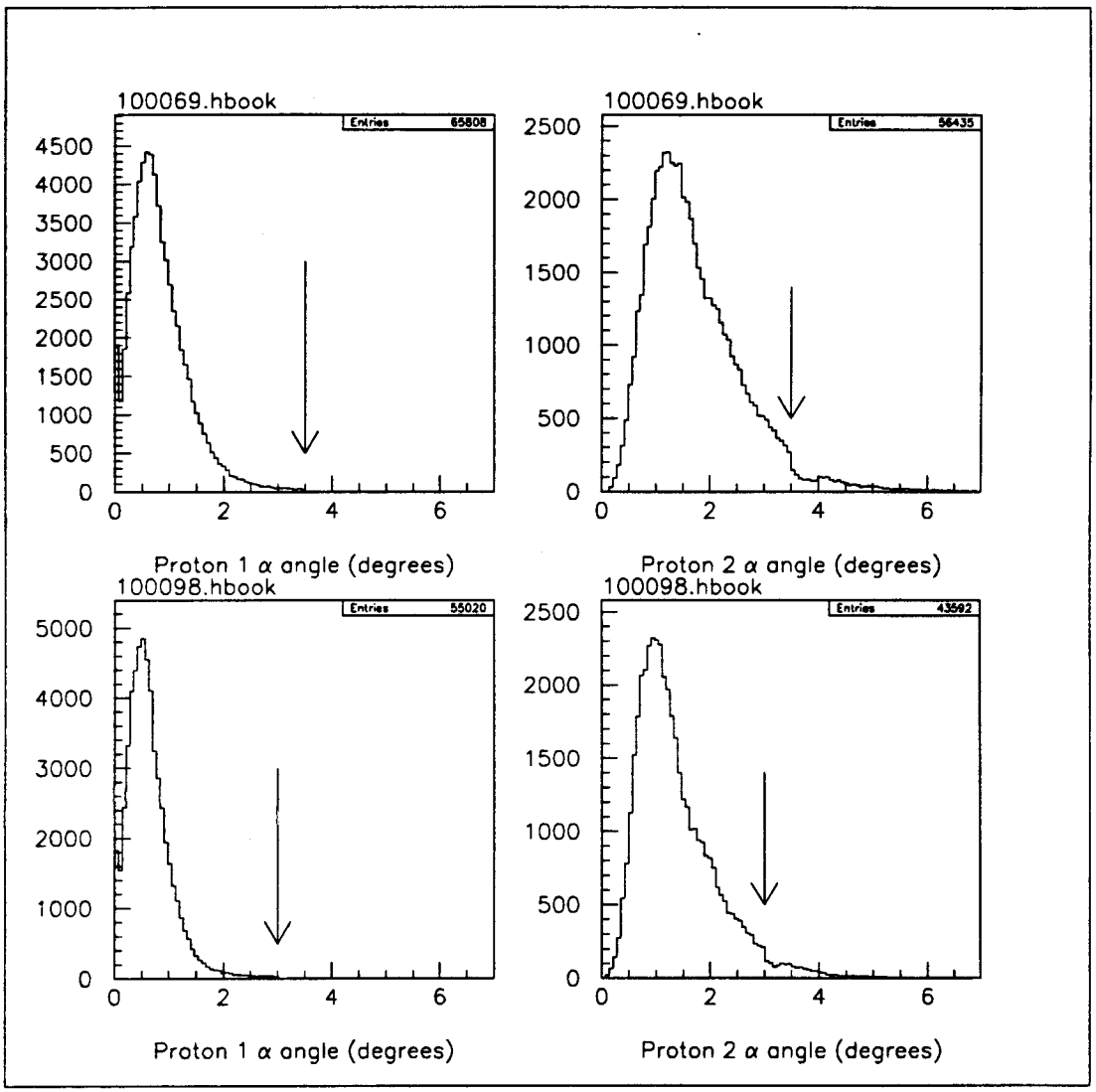

Figure 3.19: α-angle distributions for the selected "proton 1" and "proton 2". The top histograms show these distributions for calibration run # 100069 which used hodoscope position 2. The bottom histograms show these distributions for calibration run # 100098 which used hodoscope position 3. The arrows indicate the locations of the α-cuts: 3.5° for hodoscope position 2 and 3.0° for hodoscope position 3.

to correct for these light propagation times in the scintillators bars [114]. This correction was deemed unnecessary for the JLab t_{20} data [130].

- additional MWPC cut: a condition of two or fewer hits in the same wire plane. This is required for all six wire planes of the two MWPCs.

- difference in TDC values: one requires that the TDC signals of the two protons of the selected pp-pairs do not differ too much from one another. This requirement is implemented at all four hodoscope planes (H1U, H1V, H2X, and H2Y). Due to this condition the magnitude of the momenta of the individual protons of any selected proton-proton pair will be of the same order, i.e. $|\vec{P}_{\text{proton1}}| \approx |\vec{P}_{\text{proton2}}|$.

- internal cone cut (ICC): one only accepts CE protons which are not too close to the track of the incident deuterons. Both at H1 and H2 one computes the distances between the incident deuteron and the locations of the hits of the two CE protons. At H1 a minimum separation of 1.6 cm is required while at H2 the corresponding limit is 4 cm. This cut, the CE ICC, is illustrated in Figure 3.20.

- exterior cone cut (ECC) for CE events: ϕ-symmetry in the acceptance of pp-pairs is enforced by demanding that both protons of a CE pp-pair are detected within a circle centered around the hits of the incident deuteron at H1 and H2 of that particular event. The radii of these circles are computed

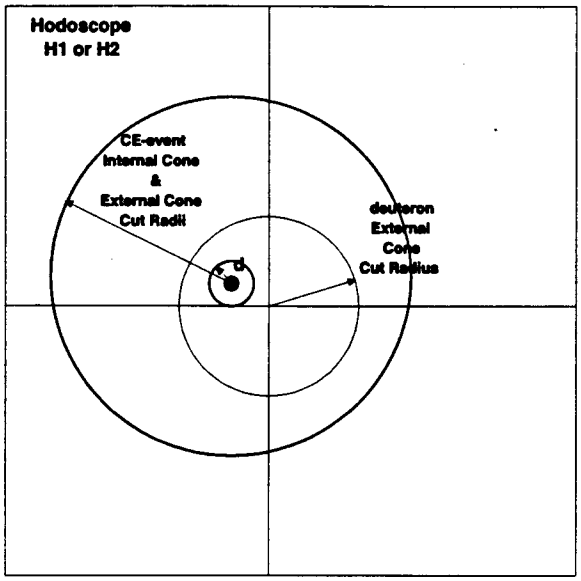

Figure 3.20: An illustration of the internal cone cut (ICC) and external cone cut (ECC) that are applied to the pp-pairs of the CE-events. The large square in the figure represents the hodoscope (either H1 or H2). The deuteron ECC-circle is shown in the same fashion as in Figure 3.13. The small filled circle within the deuteron ECC-circle represents the projected track of an accepted incident deuteron event. The CE ICC-circle (small radius) and the CE ECC-circle (large radius) of the CE-event associated with this particular incident deuteron event are concentric around the position of the incident deuteron.

as: (hodoscope width/2)- radius used for the exterior cone cut (7 cm). This cut, the CE ECC, is also illustrated in Figure 3.20. The emerging CE-event protons must fall within the two CE ICC and ECC circles shown in Figure 3.20 in order to be accepted. The ICC assures that the pp-pair is not too close to the incident deuteron while the CE ECC assures a symmetric ϕ-acceptance and hence avoids false ϕ-asymmetries. The reader is reminded that the ϕ-asymmetries are associated with the t_{21} and t_{22} components of the cross section.

The cone cut radii were chosen such that one minimized the error on the tensor moment t_{20} itself [131]. The figure of merit for a polarimeter can be expressed as:

$$F_{ij}^2 = \int \epsilon(\theta,\phi) T_{ij}^2(\theta) d\Omega = \int \left(\frac{N_{CE}(\theta,\phi)}{N_d} \right) T_{ij}^2(\theta) d\Omega. \tag{3.3}$$

The error on t_{20} can be expressed as [54, 132]:

$$\Delta t_{20}^2 = \frac{1}{F_{20}^2 N_d}. \tag{3.4}$$

Combining these two expressions one gets:

$$\Delta t_{20}^2 \propto \frac{1}{N_{CE}(\theta,\phi)\ T_{20}^2(\theta)}\ , \tag{3.5}$$

which is the quantity one wants to minimize and hence the expression in the denominator is maximized. This denominator was evaluated for various cone cut radii. Keeping the ECC radii at H1 and H2 identical ("symmetric") does not absolutely maximize the $N_{CE}(\theta,\phi)\ T_{20}^2(\theta)$ quantity. To keep the solid angle the same at H1 and H2 one obviously needs to use a larger radius at H2 than at H1. The possibility of using an asymmetric ECC cut in particular for kinematical point 6 which has the lowest statistics was investigated at Maryland. The results of this investigation are illustrated in Figure 3.21. The optimum cut turned out

θ_{CM}-bin	$(r_{H1}, r_{H2}) = (7\text{ cm}, 7\text{ cm})$ Counts	T_{20}	$(r_{H1}, r_{H2}) = (8\text{ cm}, 12\text{ cm})$ Counts	T_{20}
1	0	-.0678	0	-.0492
2	79	-.0906	108	-.0944
3	120	-.1179	142	-.1329
4	151	-.1489	150	-.1694
5	93	-.1303	87	-.1508
6	64	**-.0671**	58	**-.0721**
7	32	**+.0653**	19	**+.0869**
8	11	+.1490	1	+.2516
9	4	0.0	0	0.0
10	0	0.0	0	0.0
11	0	0.0	0	0.0
12	0	0.0	0	0.0
13	0	0.0	0	0.0
Total (counts)	**554**		**565**	

Table 3.5: A table showing the number of counts and the T_{20} analyzing power values in the different θ_{CM}-bins for two different choices of ECC radii. These values are for the T_d=460 MeV calibration energy.

to be $(r_{H1}, r_{H2}) = (8\text{ cm}, 12\text{ cm})$. However, this cut limits the accessible θ_{CM} range and these optimum values of the ECC radii do not consequently give sufficient counts in the higher θ_{CM} bins and hence de-emphasizes the zero crossing of the tensor analyzing power T_{20} in the χ^2 fit. The number of counts per θ_{CM}-bin and the associated values of the analyzing power T_{20} for two possible choices of ECC radii are shown in Table 3.5. The symmetric 7 cm radius ECC was in the end selected over the asymmetric $(r_{H1}, r_{H2}) = (8\text{ cm}, 12\text{ cm})$ ECC cut for kinematical point 6. In fact, the 7 cm symmetric cut was used for all six kinematical points.

The effect of the various deuteron and CE cuts on CE events for kinematical points 4, 5, and 6 are illustrated in Figures 3.22, 3.23, and 3.24.

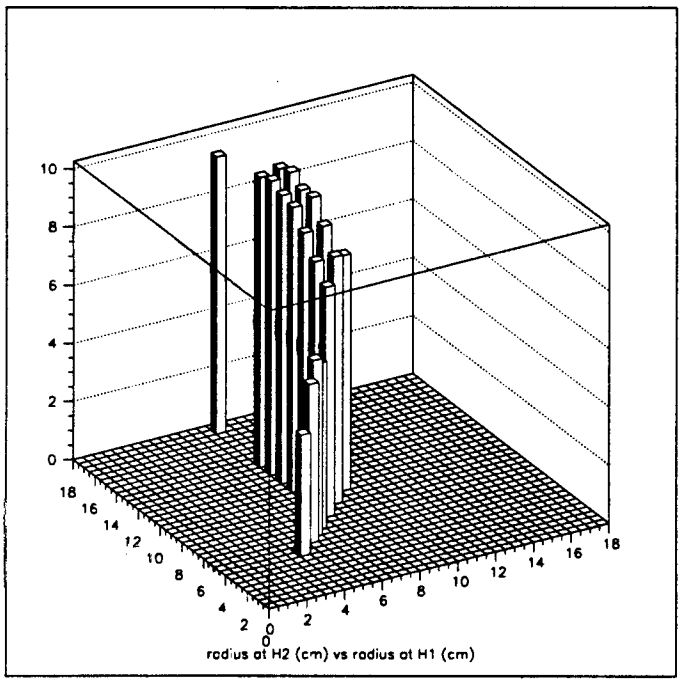

Figure 3.21: The $N_{CE}(\theta, \phi)\ T_{20}^2(\theta)$ quantity for different values of r_{H1} and r_{H2}. Based on these values one can conclude that $(r_{H1}, r_{H2}) = (8\text{ cm}, 12\text{ cm})$ gives an optimum value.

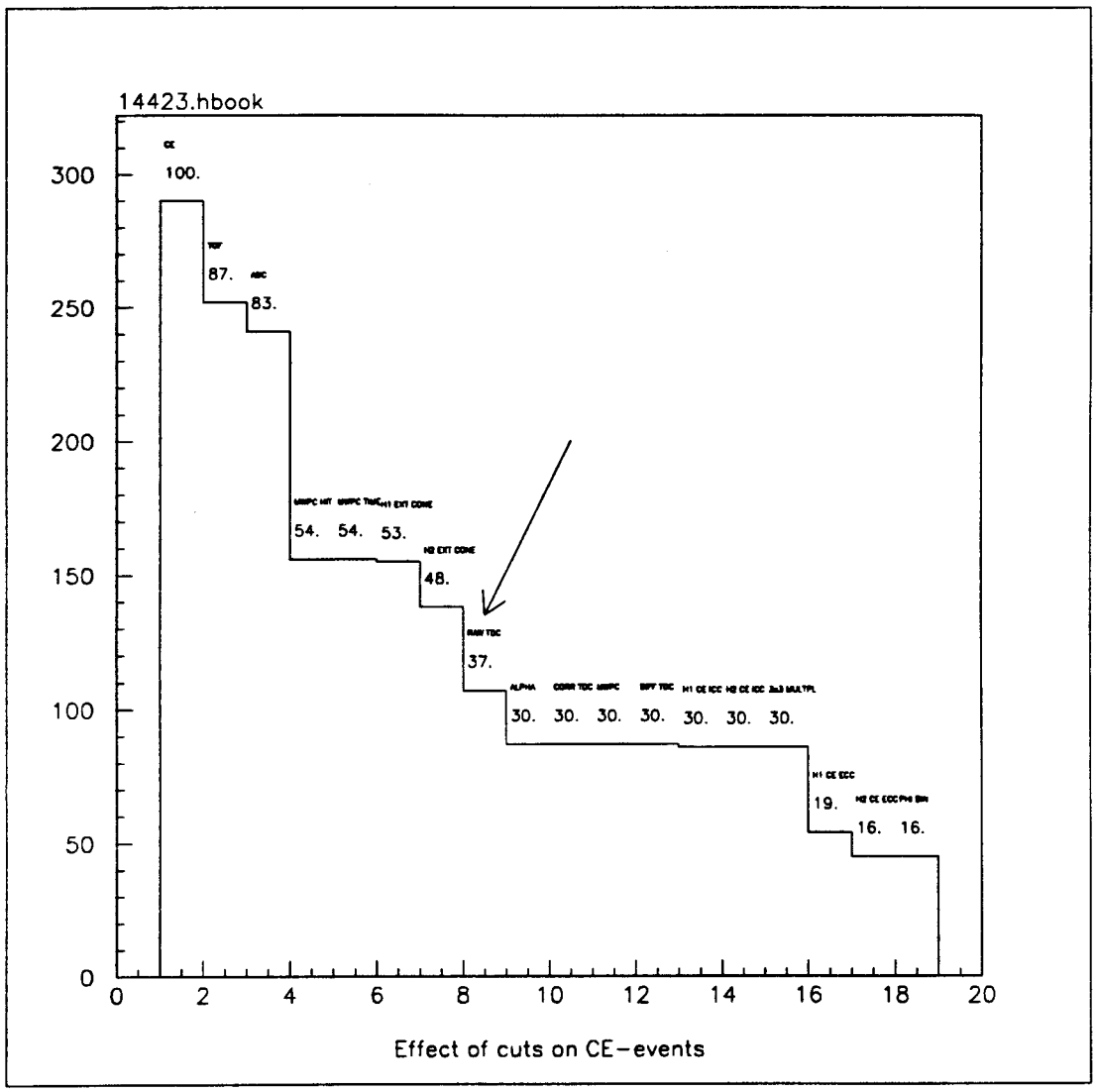

Figure 3.22: A histogram showing the effect of the various deuteron and CE cuts on CE events for kinematical point 4. The arrow indicates the bin where the very first CE cut (the raw TDC cut) is applied.

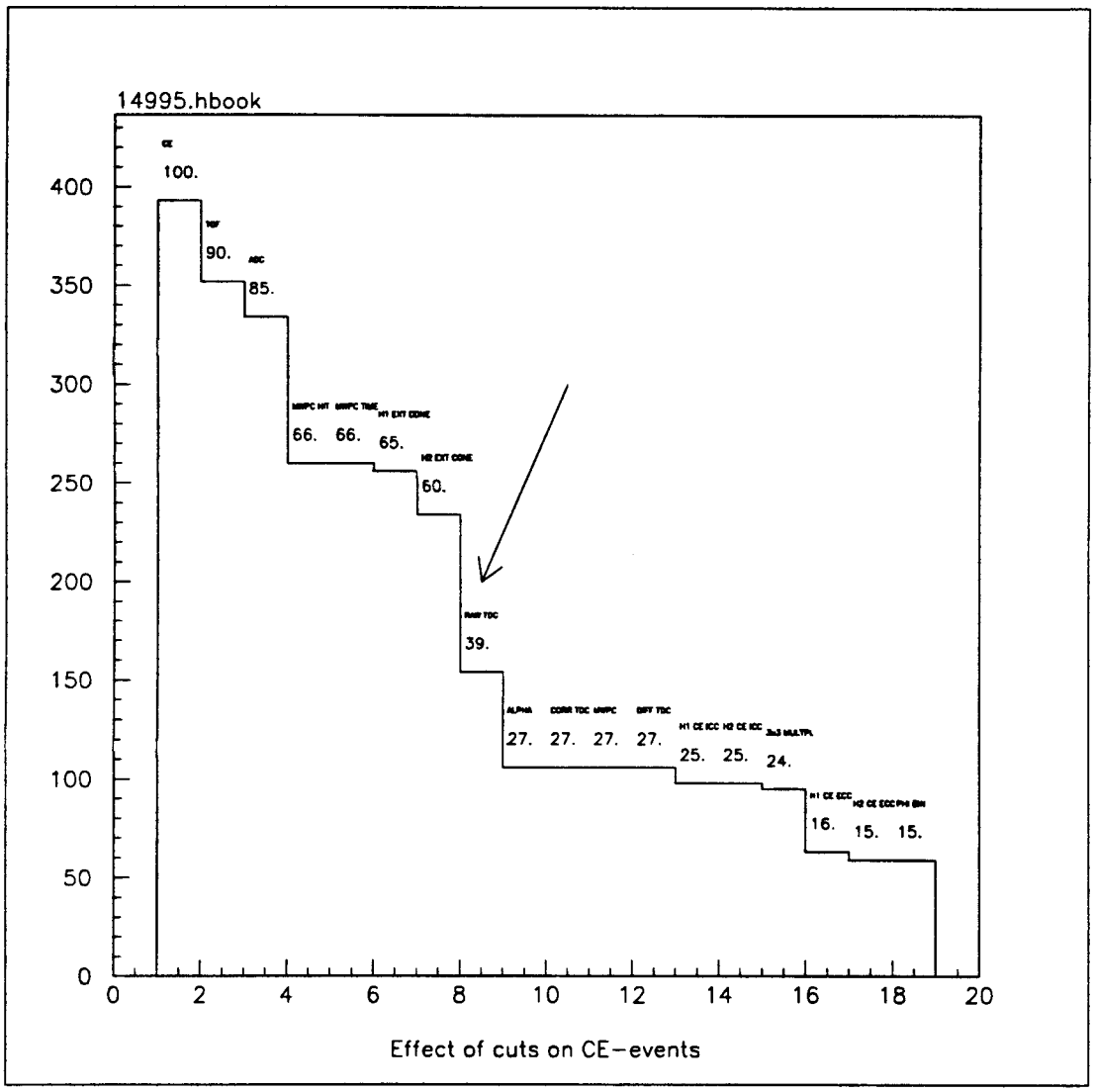

Figure 3.23: A histogram showing the effect of the various deuteron and CE cuts on CE events for kinematical point 5. The arrow indicates the bin where the very first CE cut (the raw TDC cut) is applied.

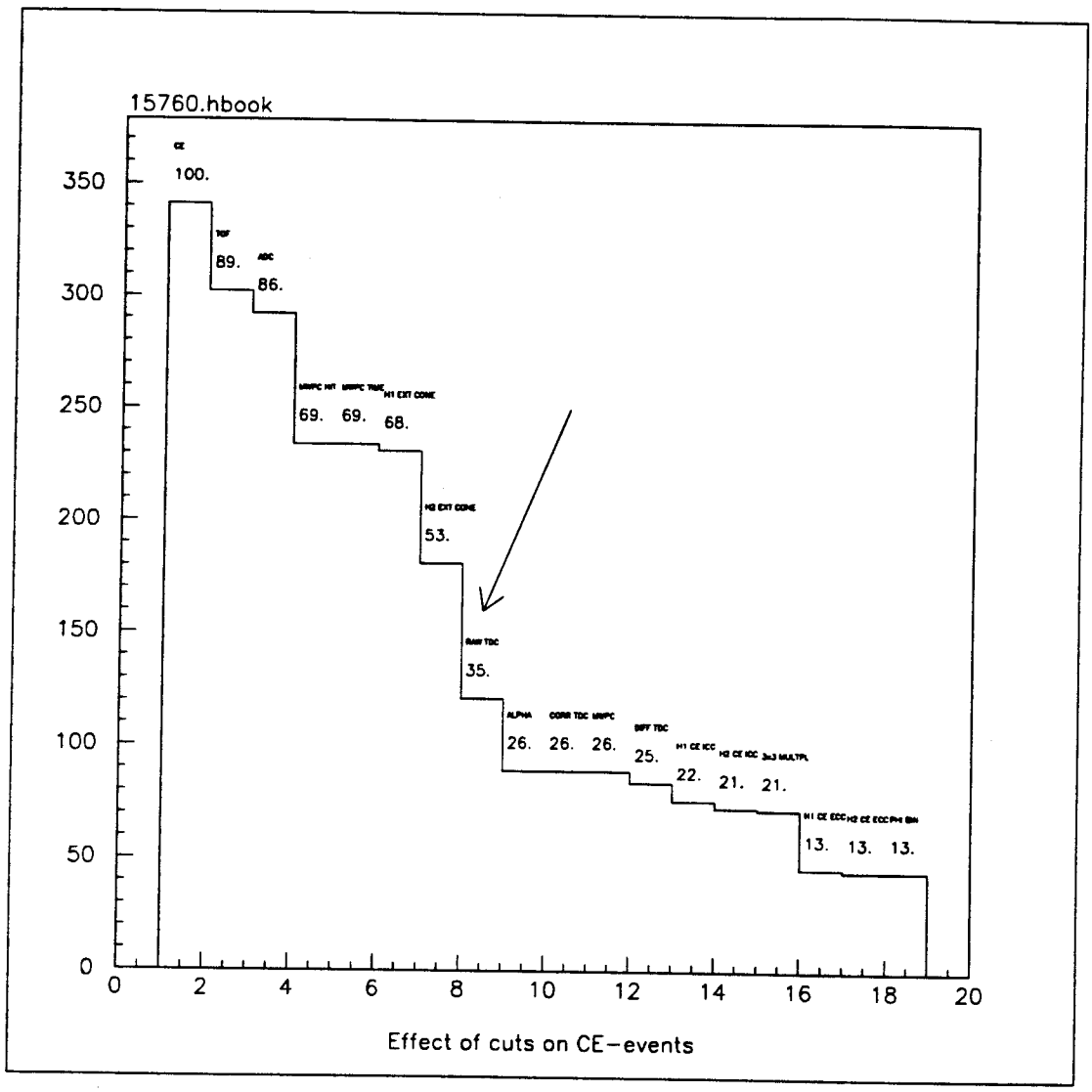

Figure 3.24: A histogram showing the effect of the various deuteron and CE cuts on CE events for kinematical point 6. The arrow indicates the bin where the very first CE cut (the raw TDC cut) is applied.

3.3.4 Event Reconstruction & Tracking

Track Reconstruction in the HMS

The tracking in the HMS uses information from its two drift chambers and timing information from its hodoscopes. Before track reconstruction for the event under study is attempted there must be at least a single wire hit in each sense wire plane in five out of the six sense wire planes of both drift chambers. The location of a hit in a drift chamber is determined by the location of the hit wire plus a drift distance. The drift distance is computed as the drift velocity multiplied by the time difference between the signal in the wire and the hit in the hodoscope scintillator. As mentioned in Chapter 3 the spacing between the sense wire planes is 1.8 cm while the sense wires in each plane are set 1 cm apart. The algorithm starts with pairing together hit sense wires that are sufficiently perpendicular, that is wires from the x (or x′) plane and y (or y′) plane or the u (or v) plane and y (or y′) plane. These pairs are grouped into "combos", and combos which are sufficiently close are grouped into space points [94]. Short miniature tracks, labeled stubs, are fitted through each space point for each of the two drift chambers separately. Next, sufficiently collinear stubs from the two drift chambers are linked into complete particle tracks. A χ^2 is computed for each track and its value reflects the collinearity of the two stubs it linked together. If multiple tracks are detected the track with the smallest χ^2 is selected. The final track is projected to a detector plane located halfway between the two drift chambers

(which are 81.2 cm apart). Typical position resolutions achieved with the two drift chambers were 140 μm (200 μm) in the dispersive (non-dispersive) direction [75]. The better resolution in the dispersive direction is due to the u and v stereoplanes which are only at $\pm 15°$ angles with respect to the x and x′ wire planes. This location is the intersection of the focal plane and the central ray of the spectrometer*. The computed position coordinates of the track at the detector plane are labeled x_{fp} and y_{fp}, while the direction of the track is defined by its slopes, with respect to z, labeled x'_{fp} and y'_{fp}. The reconstructed target quantities δ, x'_{tar}, y'_{tar}, and ytar are then computed based on these focal plane quantities. The transformation from the focal plane quantities to the reconstructed target quantities is done using a transport matrix which models the magnetic channel of the HMS. The transformation and the principle for determining the transport matrix are described in ref. [106]. The efficiency of the HMS tracking is not important for the t_{20} measurement as the determination of the tensor polarization of the recoil deuterons is based on a relative measurement (# of CE events / # of e-d events) and not on an absolute measurement of the incident deuteron flux. More detailed documentation on the HMS tracking is found in references [75, 94, 106].

*The focal plane is a surface along which, in the dispersive direction, the position of a particle depends (to first order) only on its momentum.

Event Reconstruction

The e-d and CE-events are reconstructed in the following sequence. The HMS cuts (which were described above) are first applied to the event, followed by the deuteron TOF and ADC cuts. Next, the MWPC information is processed, giving the x- and y-coordinates of the incident deuterons, and the external cone cut is then applied to the reconstructed tracks of the incident deuterons. The quantity "multiplicity" is defined as the number of hit scintillator bars per hodoscope. The CE-event trigger condition required a multiplicity of three simultaneously for both hodoscope H1 and hodoscope H2. However, the trigger was set up in such a way that each scintillator plane (be it H1U, H1V, H2X, or H2Y) had at least one hit in order to give a pair of orthogonal coordinates [(u,v) or (x,y)]. After the hodoscope hits are identified, reconstruction of all possible proton tracks is performed by using the information of all hits in the scintillator bars. There exists an ambiguity in the proton track reconstruction that is illustrated in Figure 3.25. In an event where two bars fire in the x-plane and two bars fire in the y-plane there are two solutions to where exactly the bars were hit. In order to avoid this sort of an ambiguity the first hodoscope (H1) was rotated 45° with respect to the second hodoscope (H2).

The limitation on how well the coordinates of the CE reaction protons are known is set by the physical widths of the scintillator bars of the two hodoscopes. The widths of the scintillator bars are 1.12 cm and 3.38 cm for H1 and H2, re-

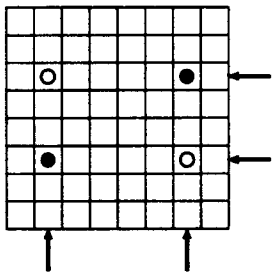

Figure 3.25: An illustration of the ambiguity arising in reconstructing tracks of CE protons. The filled circles represent real hits while the empty circles represent hits which would give rise to identical signals in the scintillator bars.

spectively. The absolute location of a hit in a scintillator bar is thus not known to a precision better than that given by these widths. In the data analysis a randomization procedure was implemented in the determination of the coordinates of the proton hits. If, for example, a scintillator bar in the H2X layer was hit, then the x-coordinate for this hit consisted of the x-coordinate of the hit bar plus a fraction of the width of the scintillator bar itself. The fraction was determined by sampling from a uniform random number distribution with values between zero and one. This randomization process made the distributions of x- and y-coordinates of the protons smooth.

Hits from H1 and H2 were next paired together in the event reconstruction. As mentioned above there is an opening angle between the track segment "vertex-to-H1" and the track segment "vertex-to-H2"*. This opening angle is labeled α and its definition was already illustrated in Figure 3.17. A constraint on this opening

*At this stage in the analysis the reaction vertex is taken to be at the center of the target (z=0) and its (x,y)-coordinates are those of the incident deuteron.

angle is made and the threshold values for two of the hodoscope positions were shown in Table 3.4. To find the protons of the CE-event under scrutiny, two proton tracks need to be selected out of all potential candidate tracks. The first proton, labeled "proton 1", is taken to be the reconstructed proton track with the very smallest α-angle of all available potential tracks. The second proton of the pp-pair, labeled "proton 2", is taken to be the one with the second smallest α-angle.

The z-coordinate of the reaction vertex was set to z=0. This decision was based upon the fact that the z-resolution of the proton track reconstruction was poor (standard deviation of ± 7 cm compared with an overall target length of 20 cm) and thus the above assumption was deemed precise enough*. The (x,y)-coordinates of the reaction vertex were determined by using the coordinates of the incident deuterons and the coordinates of the CE reaction protons.

The precision of the incident deuteron track reconstruction was much better than for the CE event proton track reconstruction. The MWPCs give a precision of the deuteron tracks of the order of a millimeter while the angular resolution of the hodoscopes limits the precision of the proton tracks to the order of a cm. Therefore a weighting factor of 10 was given to the incident deuteron (x,y)-coordinates while the coordinates of the protons at z=0 were weighted by unity†.

*In the Saclay analysis, this assumption was not made [11], but the results from both approaches agree well.

†The Saclay analysis team opted to use a weighting factor of 100 for the incident deuterons.

As each selected proton has a hit in both H1 and H2 there existed a choice: to utilize the hit at H1 (x_{H1},y_{H1}) or to utilize the hit at H2 (x_{H2},y_{H2}). In the analysis the hit at H2 was used for several reasons. For example, there are small gaps between the scintillator bars in the two hodoscopes. These gaps give rise to dead zones, and, relatively speaking, the dead zone is smaller for H2. In addition, the efficiency of H2 is also higher because it has thicker scintillator bars than H1. Finally H2 is further away from the POLDER target and hence the resolution of its TDC spectra is better, i.e. one can more efficiently discriminate against background particles which hit the scintillator bars either slightly earlier or later than the CE protons which one is looking for. Knowing the tracks of the proton-proton pair of the CE event and the reaction vertex one proceeds to calculate the center-of-mass quantities of the pp-pairs. These quantities are the polar angle θ_{CM} and the azimuthal angle ϕ_{CM} whose definitions are shown in Figure 3.26.

3.3.5 Background

In addition to the reaction channel of interest, that is elastic e-d scattering ^{2}H(e, e' $\overleftrightarrow{\text{d}}$), the inelastic scattering (electrodisintegration) channel ^{2}H(e, e'p)n and the photodisintegration channel ^{2}H(γ, pn)e' contribute to the final state and hence give rise to background particles (protons) in POLDER. As described above, the elastic scattering events are selected by setting cuts on the primary vertex position and on δ_{corr} as determined by the HMS. Moreover, there are the ADC

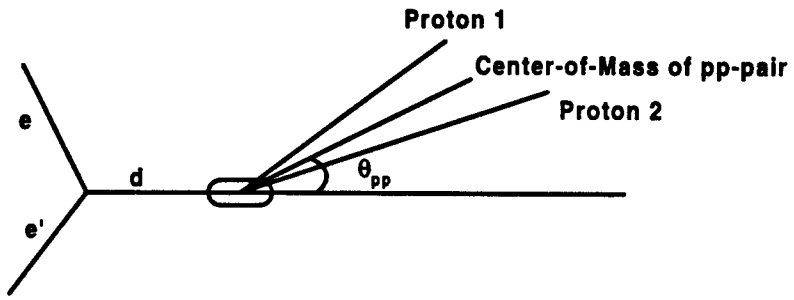

Figure 3.26: A figure showing the relevant quantities of the double scattering. On the left the incident electron e and the scattered electron e′ are shown. The recoil deuteron is traveling from the primary reaction vertex to the right in the figure. In the secondary target a CE reaction takes place and the proton-proton pair of the final states is shown (the recoil neutron is left out from the figure). The momentum vector of the center-of-mass (CM) of the pp-pair is shown. The polar angle θ_{pp} is defined as the angle between the direction of the CM of the pp-pair and the direction of the incident recoil deuteron. The azimuthal angle ϕ_{CM} is defined as the angle between the normals of the $\vec{P}_{e'}\vec{P}_{\mathrm{d}}$ scattering plane and the $\vec{P}_{\mathrm{d}}\vec{P}_{\mathrm{CM}}$ scattering plane.

Hodoscope Position	Angular Coverage (°)	Bin Size (°)
2	0-21.7	1.67
3	0-26.0	2.00

Table 3.6: A table over the θ_{CM} coverage for hodoscope positions 2 and 3.

cuts of the Start detectors (cuts on the energy loss of the incident particles in POLDER), and the cut on the coincidence time measurement between the two arms (the TOF cuts). The effectiveness of the δ_{corr} cut was illustrated in Figure 3.11. The combination of these redundant selection criteria reduced the contribution from the remaining background (mainly coming from random coincidences between electrons and protons) to less than 0.2% [133].

3.4 Analysis of Events

The event selection process described above was used both for the calibration data and the JLab data. The analysis of the calibration data has been described in ref. [71]. Identical cuts were applied to both the calibration and the JLab data, i.e. the same deuteron- and CE-cuts were used. Whenever a cut was modified both the calibration and the JLab data were reanalyzed with the new modified cut. The angular distribution of the CM of the CE pp-pairs was split into 12 bins in ϕ_{CM} (30°/bin) and 13 bins in θ_{CM}. The angular coverage per θ-bin was varied with the incident deuteron energies as shown in Table 3.6. The values of the unpolarized efficiency and the tensor moments of the calibration data are shown

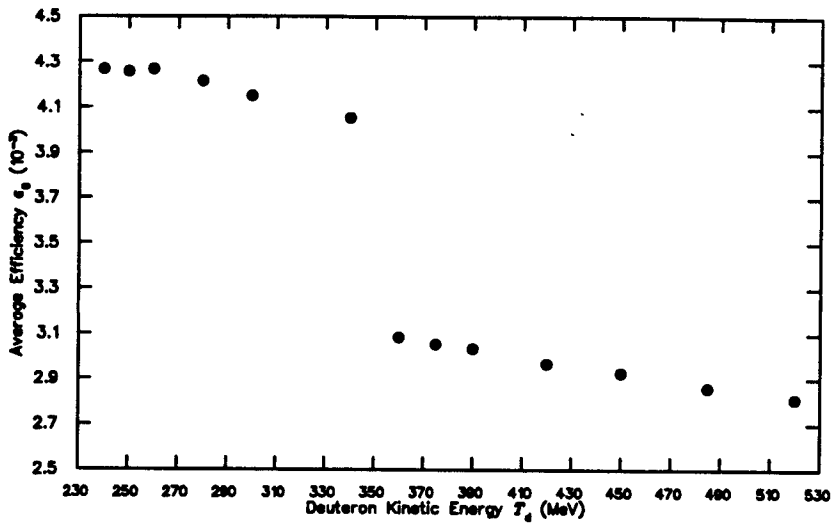

Figure 3.27: The average unpolarized efficiency ϵ_0, i.e. $\frac{\#\text{ of CE}-\text{events}}{\#\text{ of e}-\text{d events}}$, for hodoscope positions 2 (T_d=240-340 MeV) and 3 (T_d=360-520 MeV) of the calibration experiment at Saturne.

in Figure 3.27, Figure 3.28, Figure 3.29, and Figure 3.30. It should be pointed out that what is shown is the average efficiencies and the average analyzing powers, i.e. these quantities summed over θ_{CM}. The average analyzing power is evaluated as:

$$T_{ij} \equiv \frac{\sum_n \epsilon_0(\theta_n) T_{ij}(\theta_n)}{\sum_n \epsilon_0(\theta_n)}. \tag{3.6}$$

For the JLab data one proceeds in the analysis using the selected e-d and e-CE-events. By using the angular distribution of the center-of-mass (CM) of CE pp-pairs, $N_{CE}(\theta, \phi)$, one can directly compute the polarized efficiency:

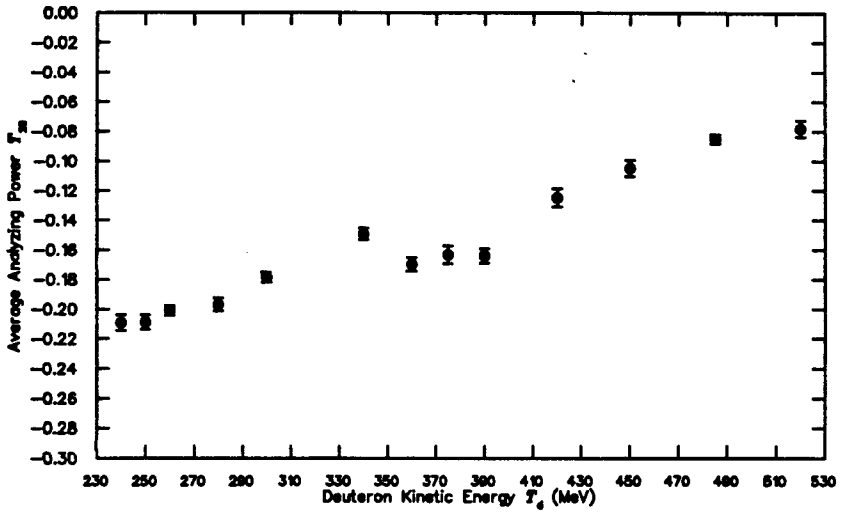

Figure 3.28: The average analyzing power T_{20} for hodoscope positions 2 ($T_{\rm d}$=240-340 MeV) and 3 ($T_{\rm d}$=360-520 MeV) of the calibration experiment at Saturne.

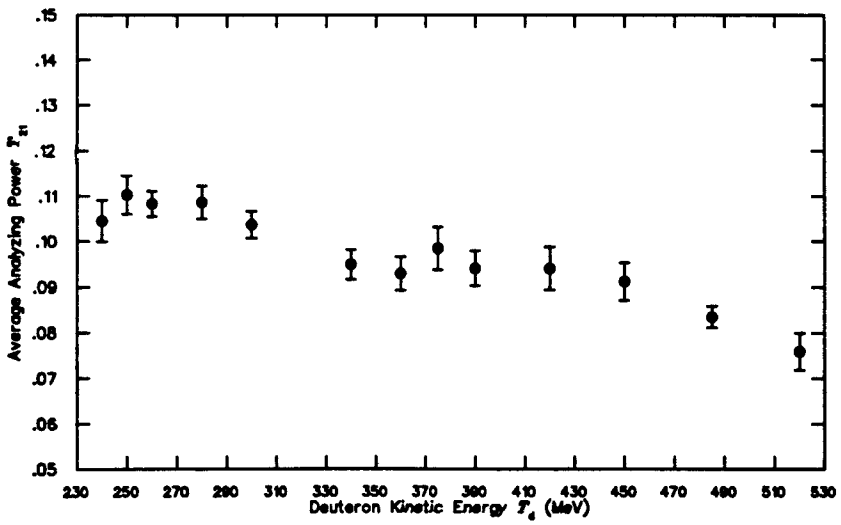

Figure 3.29: The average analyzing power T_{21} for hodoscope positions 2 ($T_{\rm d}$=240-340 MeV) and 3 ($T_{\rm d}$=360-520 MeV) of the calibration experiment at Saturne.

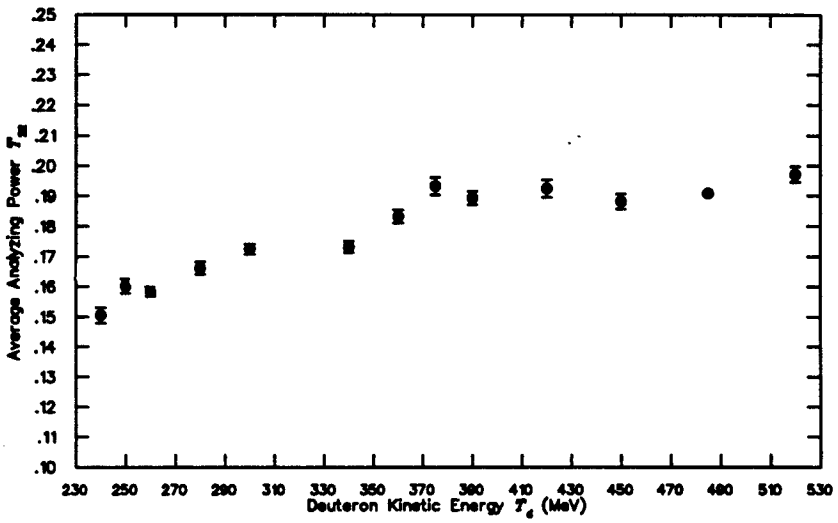

Figure 3.30: The average analyzing power T_{22} for hodoscope positions 2 ($T_{\rm d}$=240-340 MeV) and 3 ($T_{\rm d}$=360-520 MeV) of the calibration experiment at Saturne.

$$\epsilon(\theta,\phi) = \frac{\mathrm{N_{CE}}(\theta,\phi)}{\mathrm{N_{ed}}}. \tag{3.7}$$

A representative distribution of the efficiencies of individual runs for kinematical point 6 is shown in Figure 3.31. For each run the efficiency ϵ has been summed over both $\phi_{\rm CM}$ and $\theta_{\rm CM}$. The properly weighted mean values for these summed efficiencies for kinematical points 4, 5, and 6 are shown in Table 4.1 in Chapter 4.

Before utilizing Equation 2.1, one needs to know the unpolarized cross sections and analyzing powers at the kinetic energies of the deuterons used in the JLab experiment. This leads us to two topics: determination of the kinetic energy of the recoil deuterons and interpolation of the results of the calibration experiment.

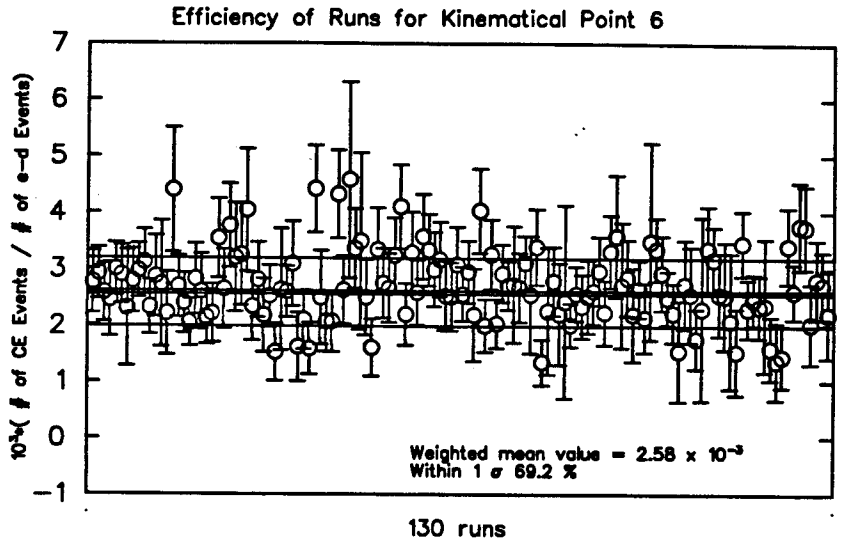

Figure 3.31: The efficiency $\epsilon = \frac{N_{CE}}{N_{ed}}$ of individual runs of kinematical point 6. The efficiencies have been summed over both θ_{CM} and ϕ_{CM}. The efficiencies of all 130 runs of data point 6 are shown. The horizontal double line indicates the weighted mean while the two solid lines above and below it correspond to the mean value $\pm 1\sigma$.

These topics are discussed in the next section.

3.4.1 Determination of Deuteron Kinetic Energy, Interpolation and Target Length Correction

The kinetic energy of the recoil deuterons can be determined in three alternative ways (the three different quantities are labeled td1, td2, and td3) and the functional dependencies are: td1 = $T_d(E_e, \delta)$, td2 = $T_d(E_e, \theta_{HMS})$, and td3 = $T_d(\delta, \theta_{HMS})$, where E_e is the energy of the incident electron beam, δ was defined in Equation 3.2, and θ_{HMS} is the measured scattering angle of the scattered electron. In order to minimize the uncertainty, the td2 quantity was selected. i.e.

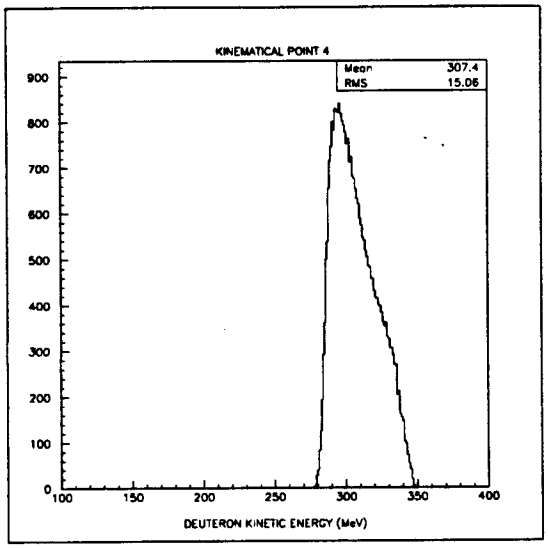

Figure 3.32: The deuteron kinetic energy T_{d} distribution for kinematical point 4.

$T_{\mathrm{d}} = T_{\mathrm{d}}(E_{\mathrm{e}}, \theta_{\mathrm{HMS}})$ and with the full expression:

$$T_{\mathrm{d}} = E_{\mathrm{beam}} - \frac{E_{\mathrm{beam}}}{1 + \frac{2E_{\mathrm{beam}} \sin^2\left(\frac{\theta_{\mathrm{e}}}{2}\right)}{M_{\mathrm{d}}}}. \tag{3.8}$$

The deuteron kinetic energy distributions for the three kinematical points presented in this work are shown in Figure 3.32, Figure 3.33, and Figure 3.34. The deuteron kinetic energy distributions had large widths and they were not symmetric as the figures show.

The unpolarized efficiency and the tensor moments were measured for 19 different deuteron kinetic energies at Saturne. In order to know these quantities exactly at the kinetic energies used at JLab an interpolation was performed on an event by event basis. The kinetic energy dependence used in the interpolation was:

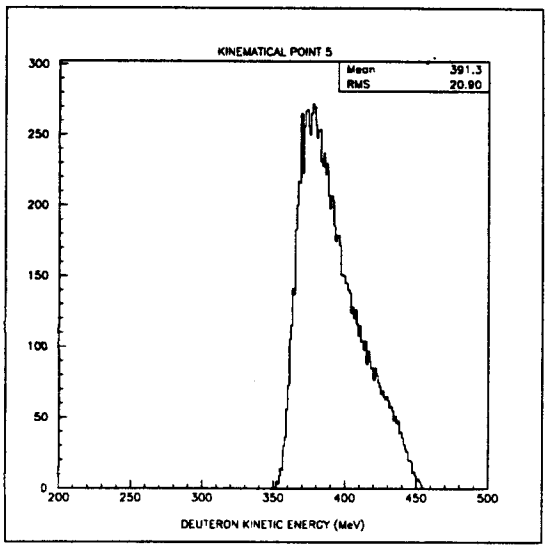

Figure 3.33: The deuteron kinetic energy T_{d} distribution for kinematical point 5.

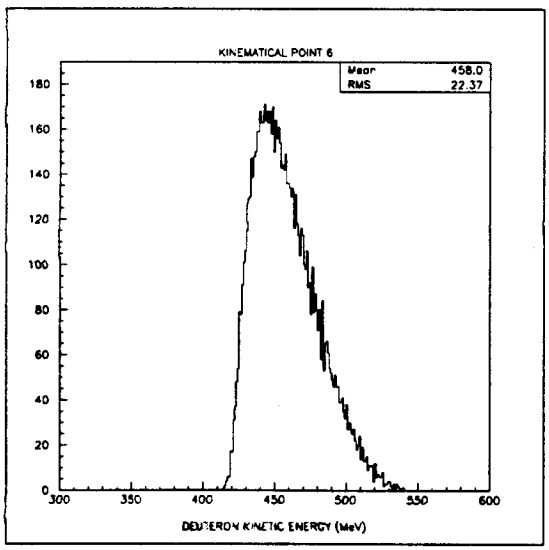

Figure 3.34: The deuteron kinetic energy T_{d} distribution for kinematical point 6.

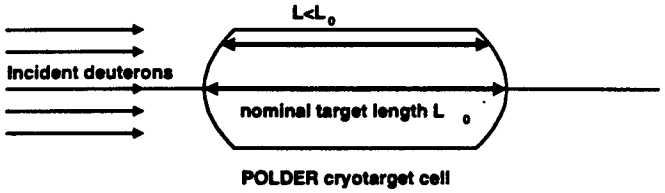

Figure 3.35: A schematic view of the POLDER target cell. The target cell will appear to have different effective lengths depending on where the incident deuteron hits the target. The further away from the center of the target the incident deuteron hits the cell the shorter ($L < L_0$) will the target appear to be.

$$y = a + \frac{b}{T_d} + \frac{c}{T_d^2}. \tag{3.9}$$

There is no overlap in the kinetic energies of the deuterons for the different hodoscope positions. This is illustrated in Figure 3.27, where one can see a sudden jump in the unpolarized efficiency ϵ_0 when going from $T_d = 340$ MeV of hodoscope position 2 to $T_d = 360$ MeV of hodoscope position 3.

The unpolarized efficiencies obtained through the interpolation procedure were additionally corrected for the variable length of the POLDER target. The end cap windows of the POLDER target cell were convex shaped and hence the effective target length is a function of radial distance as illustrated in Figure 3.35. Therefore this target length correction was needed [119, 71]. Typical target correction values were 0.96, 0.97, and 0.98 for kinematical points 4, 5, and 6, respectively.

Knowing the unpolarized efficiency, the tensor moments, and the corrected

polarized efficiency at the same deuteron kinetic energy one can proceed to extract the tensor moments. This is the topic of the next paragraph.

3.4.2 Extraction of the Tensor Moments

The tensor moments were obtained using a fitting procedure which adjusted the t_{ij} in Equation 3.10 such that the angular distribution of the interpolated calibration data best reproduced the relative angular distribution of the JLab data. The angular distribution of counts obtained at JLab, $N^{JLab}(\theta_i, \phi_j)$, combined with the theoretical expression based on the unpolarized cross section and the measured analyzing powers

$$N^{th}(\theta_i, \phi_j) = k\ N_0(\theta_i)[1 + t_{20}T_{20}(\theta_i) + 2t_{21}T_{21}(\theta_i)\cos(\phi_j) + 2t_{22}T_{22}(\theta_i)\cos(2\phi_j)], \tag{3.10}$$

were used to extract the tensor moments. In Equation 3.10, k is a free parameter which should equal unity if the efficiency of POLDER is the same between the calibration at Saturne and the JLab t_{20} measurement. A maximum likelihood method was utilized, and because of the low number of counts per bin the measured data was assumed to follow a Poisson distribution. The χ^2 expression in the Poisson case is [134]:

$$\chi^2 = 2\sum_{i=2}^{9}\sum_{j=1}^{12}\{[N^{th}(\theta_i,\phi_j) - N^{JLab}(\theta_i,\phi_j)] + N^{JLab}(\theta_i,\phi_j)\ln[\frac{N^{JLab}(\theta_i,\phi_j)}{N^{th}(\theta_i,\phi_j)}]\}. \tag{3.11}$$

The χ^2 minimization was carried out using MINUIT [129]. In order to take into account the statistical errors of the unpolarized cross section and of the analyzing powers this minimization was carried out 1,000 times. The $N_0(\theta_i)$ and $T_{ij}(\theta)$ values used in the minimization were picked from appropriate Gaussian distributions which had widths (i.e. standard deviations) corresponding to the uncertainties in the calibration experiment.

It is possible to exclusively extract the t_{20} tensor moment by summing the counts of the ϕ_{CM}-bins (which corresponds to integrating over ϕ in the theoretical expression). This extraction procedure was labeled a "t_{20}-fit" while the extraction of all three tensor moments t_{ij} simultaneously was labeled a "t_{ij}-fit".

The distributions of the polar angle of the center of mass of the CE pp-pairs, θ_{CM}, were divided into 13 bins and the azimuthal angle distributions were divided into 12 bins. Representative histograms of the θ_{CM} angle for kinematical points 4, 5, and 6 are shown in Figure 3.36. As can be seen only bins up to the 9^{th} bin get populated and clearly one does not need to include the higher bins in the fit. The first bin was also excluded from the fit as it is most sensitive to potential problems with the alignment of the detector elements. However, its exclusion was not of great significance. Representative histograms of the ϕ_{CM} angle for

kinematical points 4, 5, and 6 are shown in Figure 3.36.

First, k is kept free, and its deviation from 1 after the fit is a measure of the quality of the extraction. The results for the three kinematical points 4, 5, and 6 of the t_{20} fit in which k was kept free are shown in Figure 3.37, Figure 3.38, and Figure 3.39. As can be seen the fits for data point 4 and 6 are excellent while kinematical point 5 is problematic. The issue of point 5 is discussed in detail in Section 3.5 below. Once the k-parameter was determined to be acceptable the tensor moments t_{ij} were extracted from a t_{ij}-fit where the k-parameter was fixed to unity. These results are presented in Chapter 4. The ϕ_{CM} distributions of kinematical point 4 as used in a t_{ij}-fit are illustrated in Figure 3.40.

3.4.3 Experimental Asymmetries

For the t_{20} measurement the θ_{CM} distributions of the calibration and JLab experiments are compared and, in addition, the ϕ_{CM} behavior is important for determining the t_{21} and t_{22} tensor moments. Any asymmetries in θ_{CM} or ϕ_{CM} due to other sources than the CE reactions must be identified and corrected for. These kind of asymmetries are labeled "experimental asymmetries". They can be investigated by introducing two factors, A(θ,ϕ) and B(θ,ϕ)*, in the Equation 2.1 for the polarized efficiency:

*The reader should not confuse these factors with the deuteron structure functions $A(Q^2)$ and $B(Q^2)$

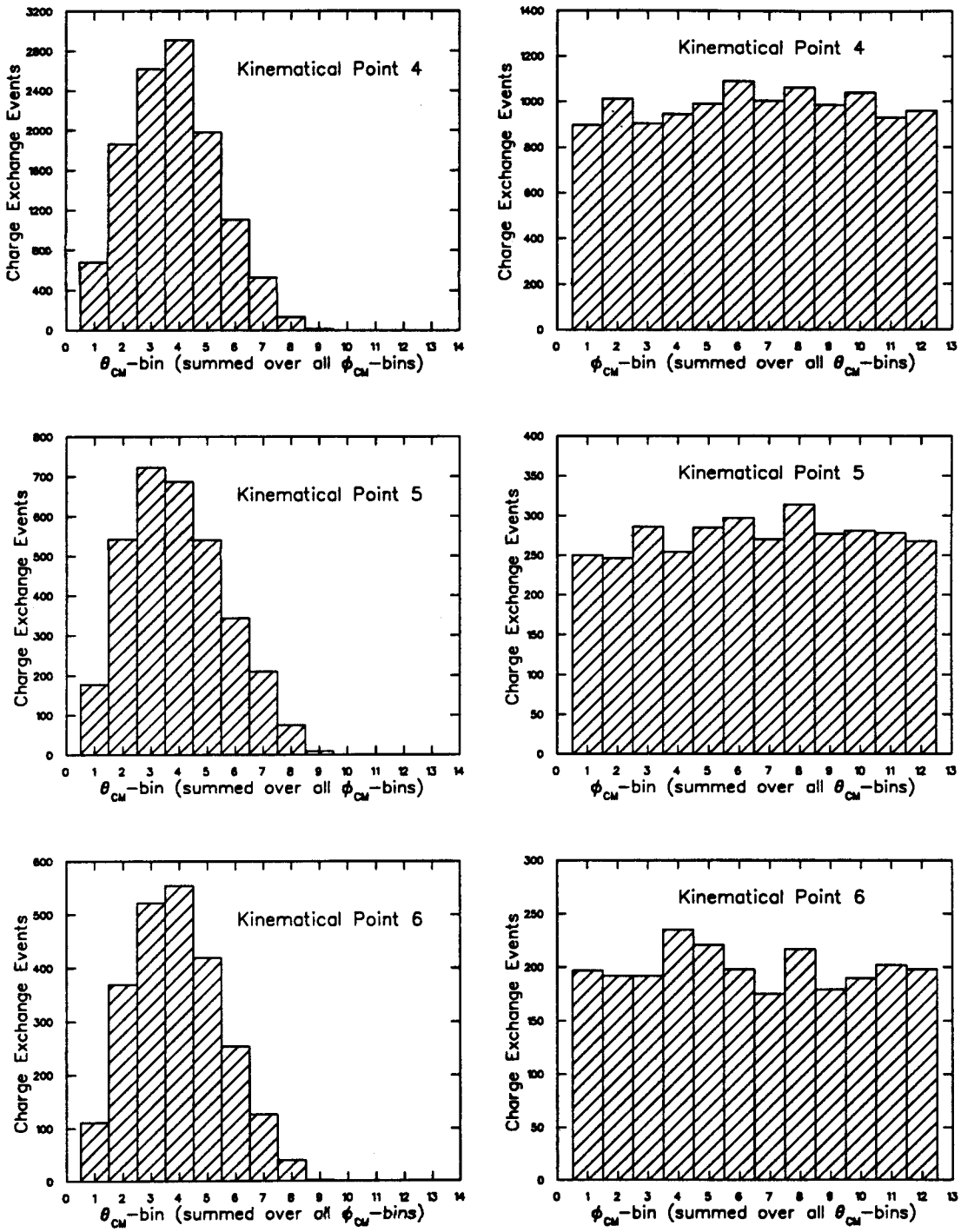

Figure 3.36: The θ_{CM} and ϕ_{CM} distributions of the CE events for kinematical point 4, 5, and 6. The θ_{CM} distribution is summed over all ϕ_{CM} bins and the ϕ_{CM} distribution is summed over all θ_{CM} bins.

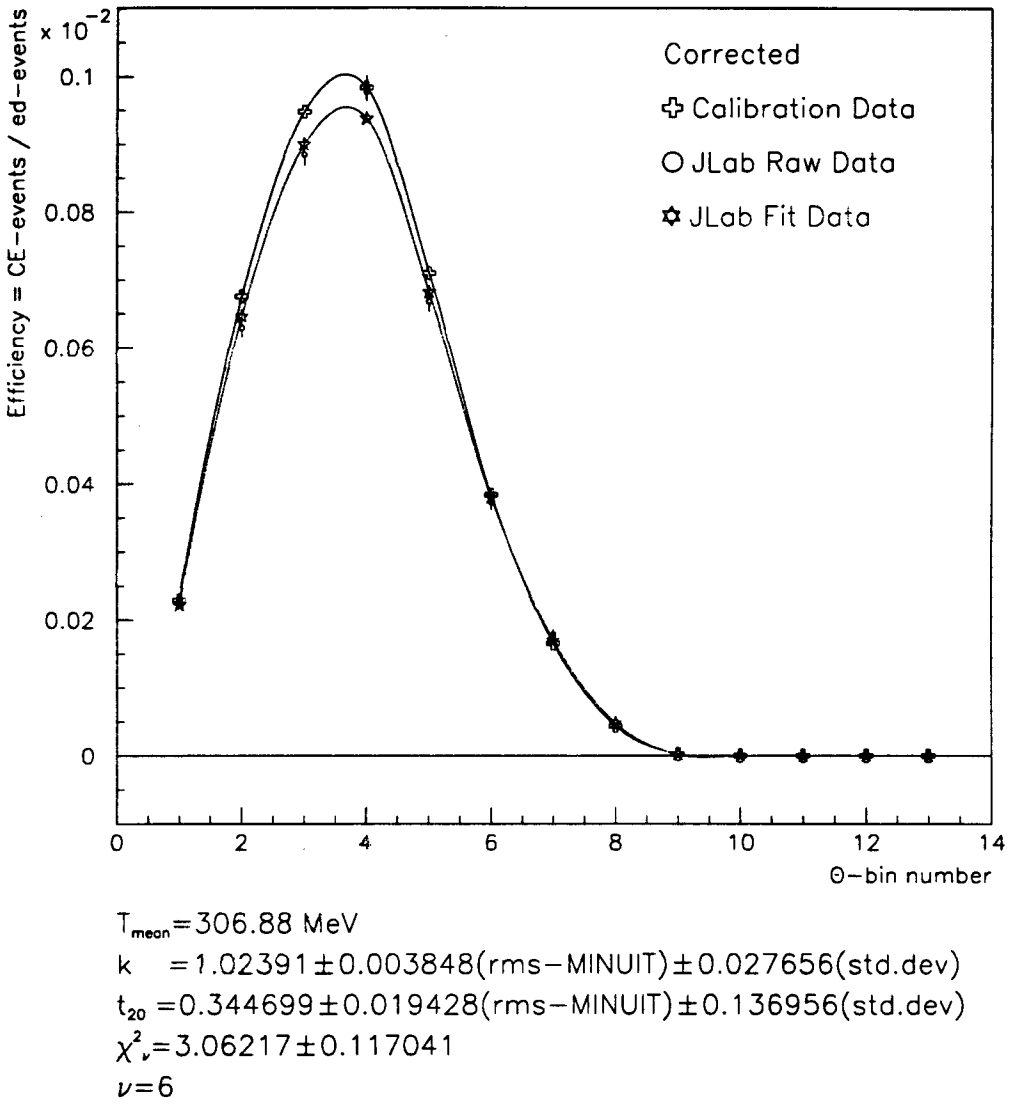

Figure 3.37: Kinematical point 4. The efficiency of both the calibration experiment and of the JLab experiment as a function of the θ_{CM} angle of the pp-pair. Legend: the crosses correspond to the calibration data, the open circles to the JLab data, and the stars represent the fit. A spline curve is drawn through the calibration data points, and also through the data points of the fit.

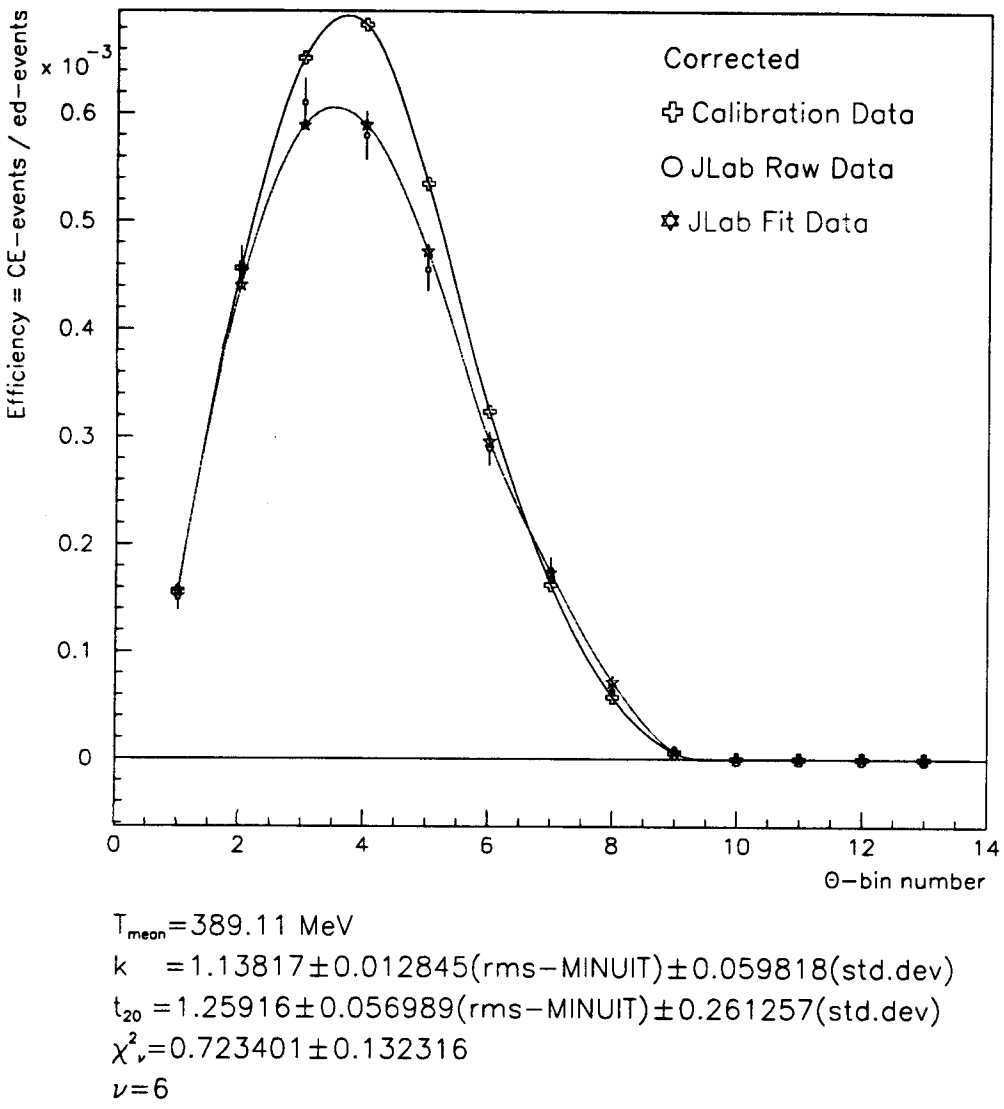

Figure 3.38: Kinematical point 5. The efficiency of both the calibration experiment and of the JLab experiment as a function of the θ_{CM} angle of the pp-pair. Legend: the crosses correspond to the calibration data, the open circles to the JLab data, and the stars represent the fit. A spline curve is drawn through the calibration data points, and also through the data points of the fit.

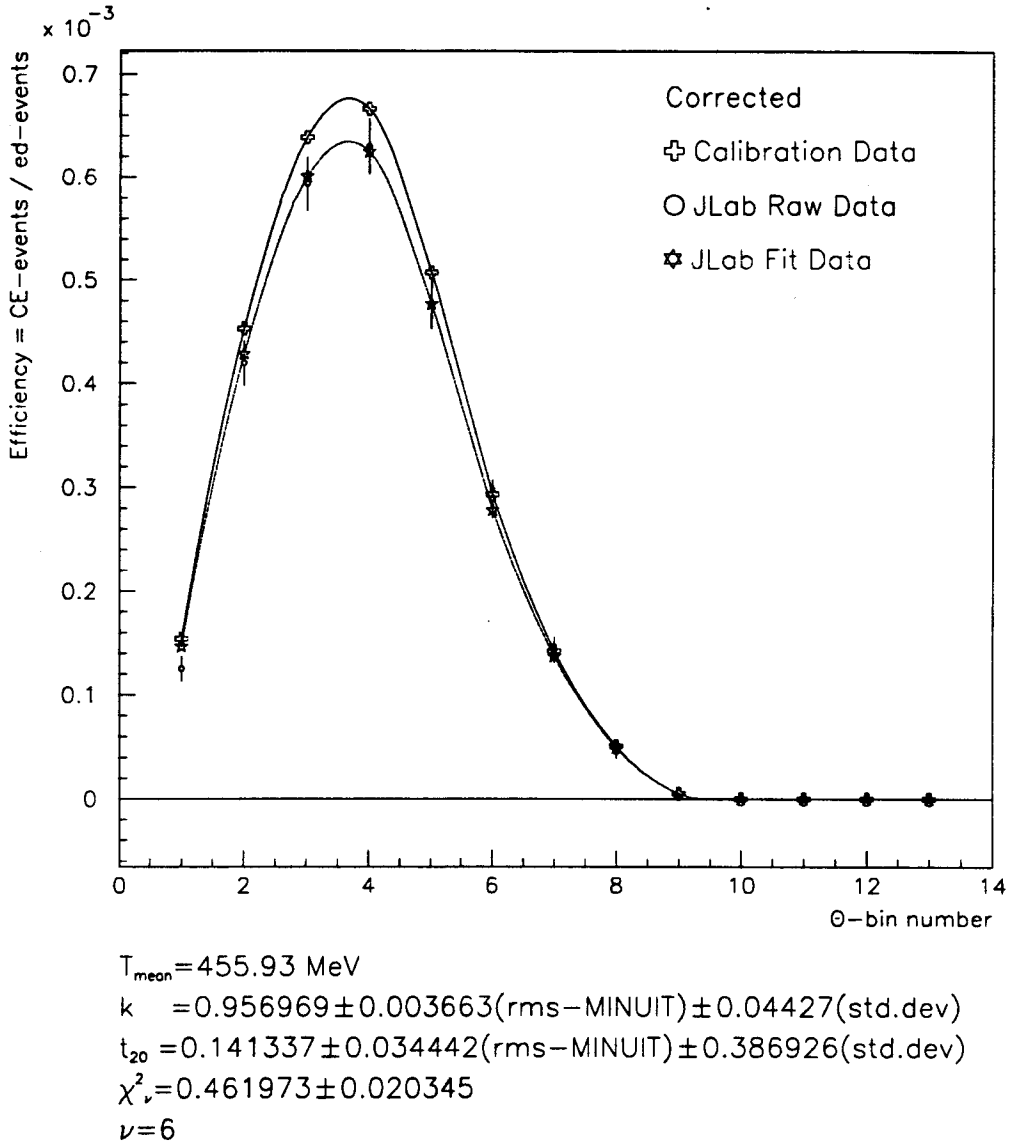

Figure 3.39: Kinematical point 6. The efficiency of both the calibration experiment and of the JLab experiment as a function of the θ_{CM} angle of the pp-pair. Legend: the crosses correspond to the calibration data, the open circles to the JLab data, and the stars represent the fit. A spline curve is drawn through the calibration data points, and also through the data points of the fit.

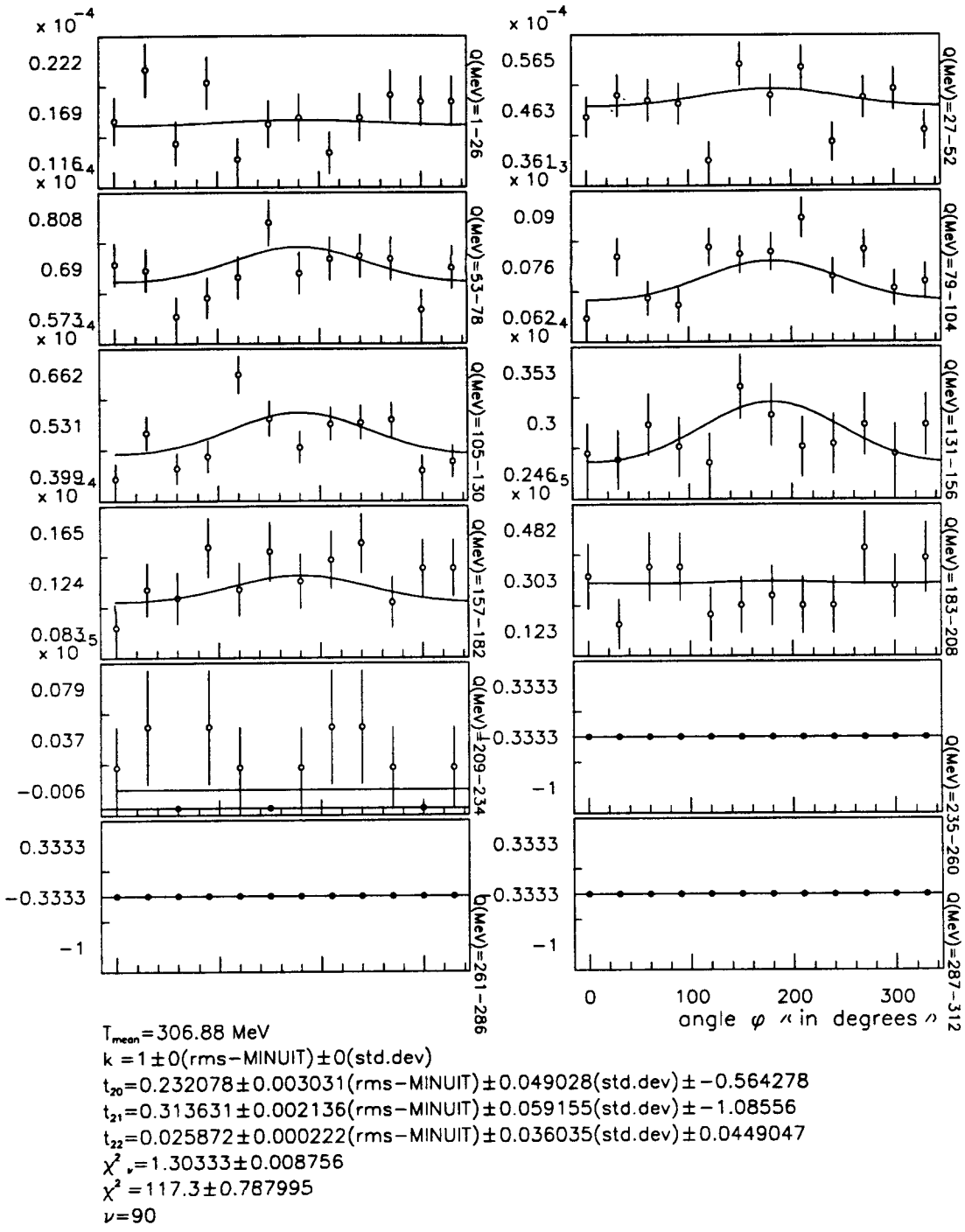

Figure 3.40: The measured JLab efficiency $\epsilon(\theta_{\rm CM}, \phi_{\rm CM})$ vs. the azimuthal angle $\phi_{\rm CM}$ $(0-360°)$ for kinematical point 4. In the figure twelve subfigures are shown that correspond to the $\theta_{\rm CM}$ binning. In the figure the momentum, labeled Q, of the CE recoil neutron is used in the binning but that corresponds effectively to a $\theta_{\rm CM}$ binning.

$$\epsilon(\theta,\phi) = \epsilon_0(\theta,\phi)[1 + t_{20}\ T_{20}(\theta) + 2t_{21}T_{21}(\theta)\cos(\phi)$$
$$+2t_{22}T_{22}(\theta)\cos(2\phi)]\ \times \mathrm{A}(\theta,\phi) + \mathrm{B}(\theta,\phi). \tag{3.12}$$

The factor A(θ,ϕ) is different from unity if there are asymmetries intrinsic to the detectors or the data analysis. For example a bad alignment of the detector elements, that is wrong offset parameters used in the alignment (described in Section 3.2), would cause a non-zero value for A(θ,ϕ). The B(θ,ϕ) factor would be non-zero if there were contributions from background particles, but there was no evidence for a B(θ,ϕ) contribution in E94018 [131].

A(θ,ϕ) can be expanded in a Fourier series:

$$\mathrm{A}(\theta,\phi) = \sum_{n=0}^{\infty}[\ \mathrm{a_n}(\theta)\cos(\phi) +\ \mathrm{b_n}(\theta)\sin(\phi)], \tag{3.13}$$

and hence the a_n and b_n coefficients associated with the different trigonometric components will give a measure of the asymmetries. The zeroth term a_0 is defined as:

$$\int_0^{2\pi} \mathrm{A}(\theta,\phi)\mathrm{d}\phi = \mathrm{a_0} = 1. \tag{3.14}$$

A slightly different formulation may also be used in studying the experimental asymmetries (both formulations were used). Using the four different polarization

states of the Saturne deuteron beam one can form combinations corresponding to unpolarized, vector polarized, and tensor polarized states. The expression for an unpolarized beam is [114]:

$$R_0(\theta) = N_5(\theta,\phi) + N_6(\theta,\phi) + N_7(\theta,\phi) + N_8(\theta,\phi). \tag{3.15}$$

For completeness, the expression for vector polarization is:

$$R_V(\theta,\phi) = \frac{N_5(\theta,\phi) + N_7(\theta,\phi) - N_6(\theta,\phi) - N_8(\theta,\phi)}{N_5(\theta,\phi) + N_6(\theta,\phi) + N_7(\theta,\phi) + N_8(\theta,\phi)}, \tag{3.16}$$

and for tensor polarization:

$$R_T(\theta,\phi) = \frac{N_5(\theta,\phi) + N_6(\theta,\phi) - N_7(\theta,\phi) - N_8(\theta,\phi)}{N_5(\theta,\phi) + N_6(\theta,\phi) + N_7(\theta,\phi) + N_8(\theta,\phi)}. \tag{3.17}$$

The unpolarized beam should have no ϕ dependence so equating Equation 3.15 with:

$$\begin{aligned} &u_1 + u_2 \sin\left(\phi - \frac{\pi}{2}\right) + u_3 \sin\left[2\left(\phi - \frac{\pi}{2}\right)\right] \\ &+u_4 \cos\left(\phi - \frac{\pi}{2}\right) + u_5 \cos\left[2\left(\phi - \frac{\pi}{2}\right)\right], \end{aligned} \tag{3.18}$$

gives a measure (the u_n coefficients) of the experimental asymmetries. The following relationship exists between the a_n, b_n and u_n coefficients: ($a_1 \propto u_2/u_1$),

($a_2 \propto u_5/u_1$), ($b_1 \propto u_4/u_1$), and ($b_2 \propto u_3/u_1$). In Figure 3.41 the observed asymmetries are shown. Only u_4 shows a slightly larger asymmetry for hodoscope position 2 (T_d=240-340 MeV). This was only observed in the Maryland analysis, however, its effect was negligible although it was still taken into account in the tensor moment extraction. In general, the influences of all non-zero asymmetry coefficients on the extracted values of the tensor moments were estimated. The effect of the experimental asymmetries is tabulated along with the other systematic errors in Table 3.7, Table 3.8, and Table 3.9.

3.5 Determination of Systematic Errors

The systematic errors can be cast into six different categories:

I & IV:

Systematic errors inherent in the POLDER analysis and the systematic error associated with the HMS δ_{corr} cut were estimated by varying the various cuts and reanalyzing the data. The δ_{corr} cut was varied by $\pm 0.5\%$ around its nominal value, the α cut was varied by $\pm 1°$, and the external cone cut radius was varied by ± 1 cm. This was done for all three kinematical points (4, 5, and 6). Whenever it was deemed necessary to double check the obtained results even more variations of the cut limits were carried out. The results of this variation method for the t_{20} values are shown in Figure 3.42, Figure 3.43, and Figure 3.44. The systematic errors on the tensor moments t_{21} and t_{22} were determined in the same fashion.

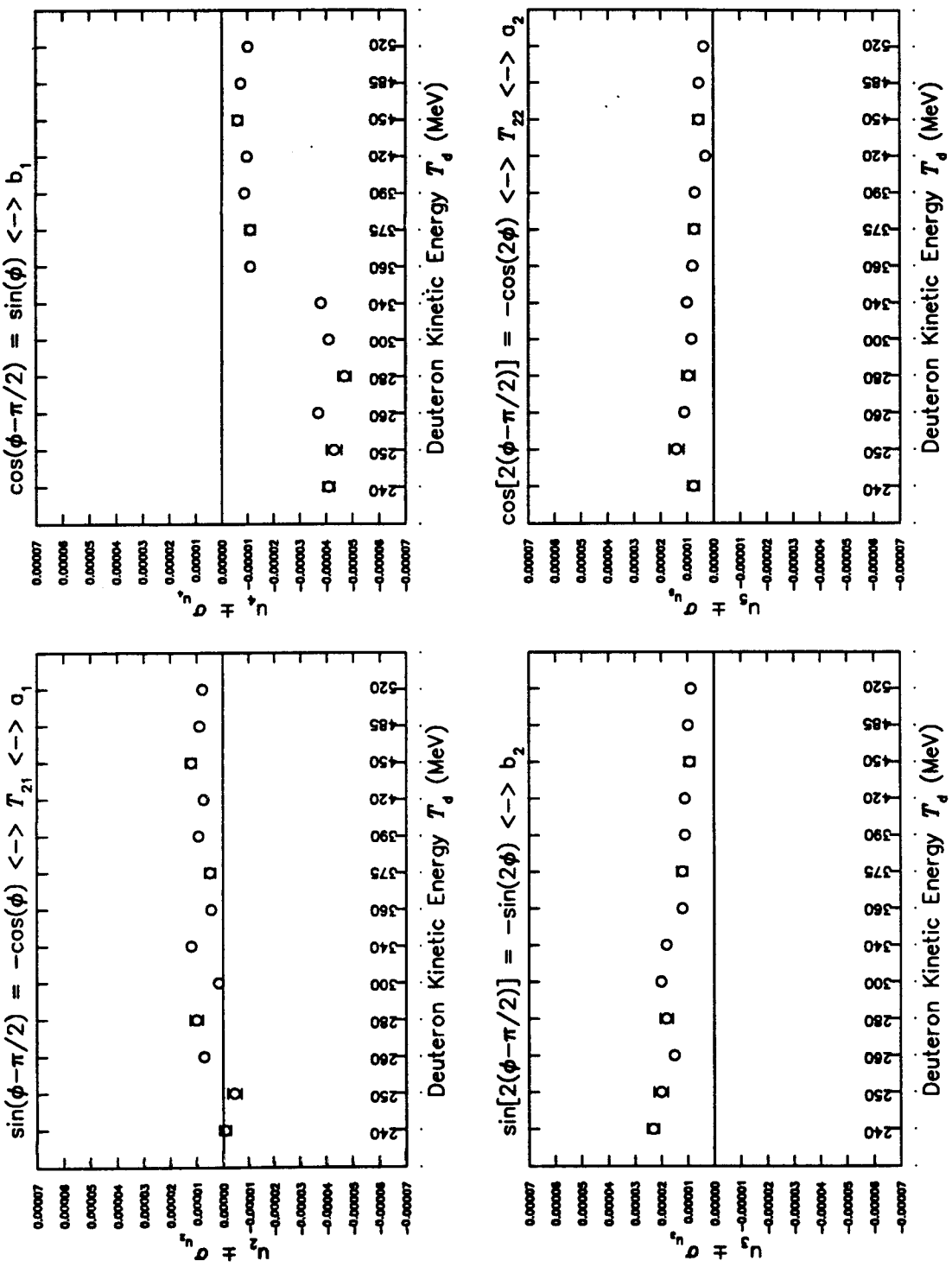

Figure 3.41: The values of the experimental asymmetry coefficients u_2, u_3, u_4, and u_5 at the various calibration energies for hodoscope positions 2 and 3.

II:

Systematic errors which stem from the kinetic energy of the recoil deuterons. There are four sources for this uncertainty: the electron scattering angle θ_e, the incident electron beam energy E_e, the offset of the electron beam, and finally an error associated with the shape of the kinetic energy distribution. This category of systematic error was quantified by the Saclay analysis group and is documented in ref. [11].

III:

A third category of systematic errors stems from the calibration. Errors on the analyzing powers T_{ij} and systematic errors due to the interpolation procedure belong to this category. Normally all calibration energies are used in the interpolation. For example the values of the unpolarized efficiency ϵ_0 of all calibration energies are utilized in computing the ϵ_0 value at a kinetic energy of the deuterons corresponding to a JLab data point. The systematic error in this interpolation procedure was estimated by excluding one calibration energy at a time and gauging its effect on the results of the interpolation. Moreover, a systematic error in the polarization of the deuteron beam used in the POLDER calibration was taken into account [135, 131, 71] as mentioned above in Section 2.1.1. Finally an error associated with the stability of the k-parameter was also considered.

V:

The fifth category simply consists of the uncertainty due to the experimental

asymmetries which were already discussed above. This systematic error was negligible for kinematical point 5 while a Δt_{20}=0.003 and a Δt_{20}=0.001 were applied for kinematical point 4 and 6, respectively.

VI:

The last category is associated only with kinematical point 5. The θ_{CM} distribution of point 5 did not match exactly the expected behavior from Equation 2.1. A symptom of this was a very flat χ^2 distribution and hence an abnormally large uncertainty associated with the k parameter. Therefore a contribution to the systematic error of t_{20} of Δt_{20}=0.1 was added quadratically to the overall systematic error of point 5.

The systematic errors from the various categories were all combined quadratically and they are shown in Table 3.7, Table 3.8, and Table 3.9.

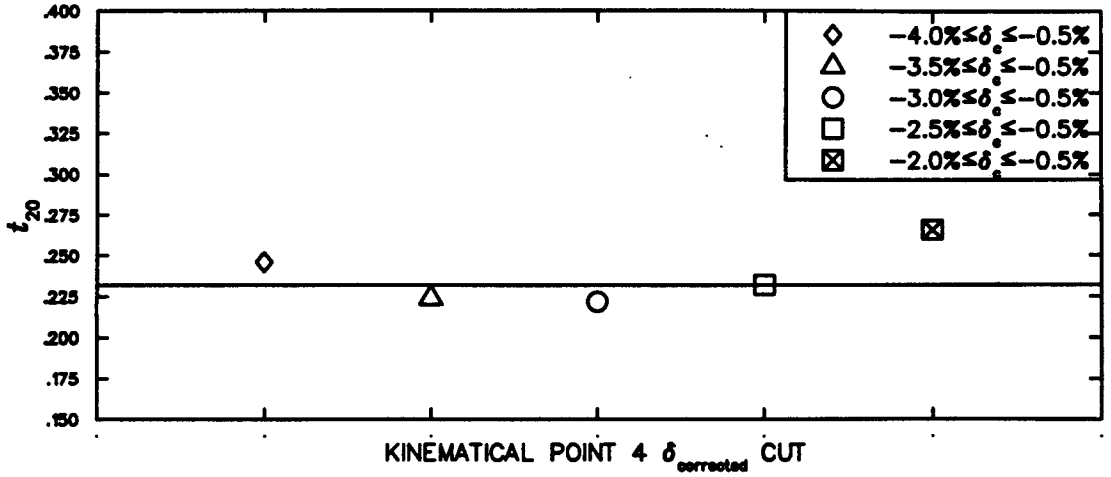

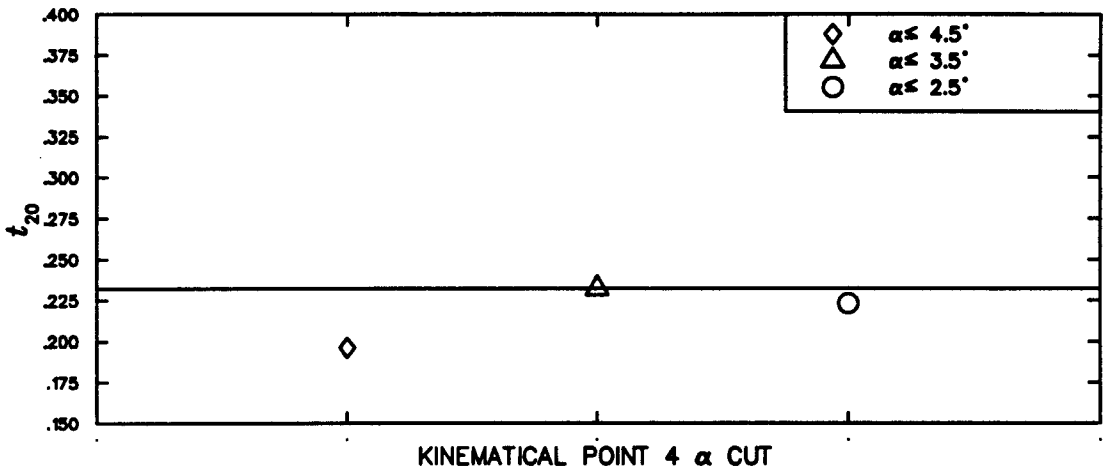

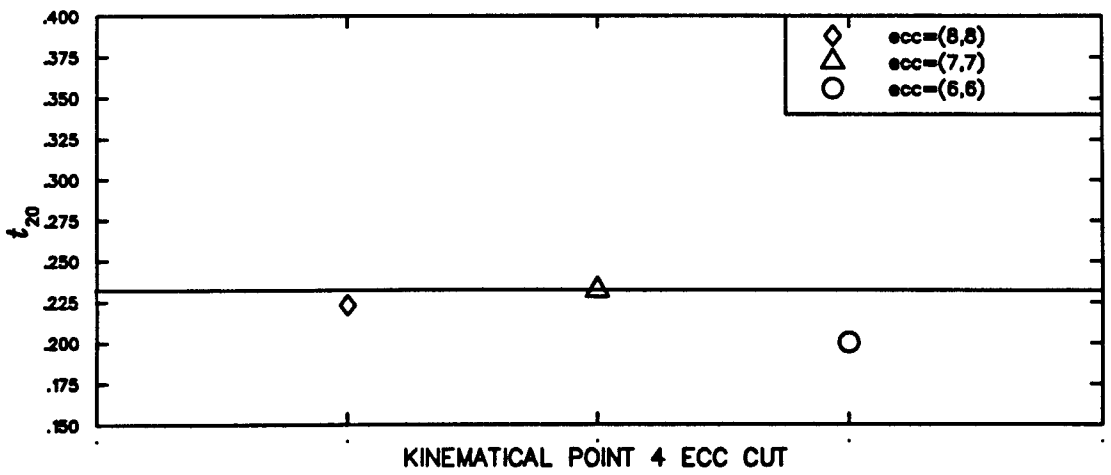

Figure 3.42: Systematical errors of the tensor moment t_{20} for kinematical point 4. The observed variation in the t_{20} values due to the cut dependence should be compared to the statistical uncertainty of 0.049.

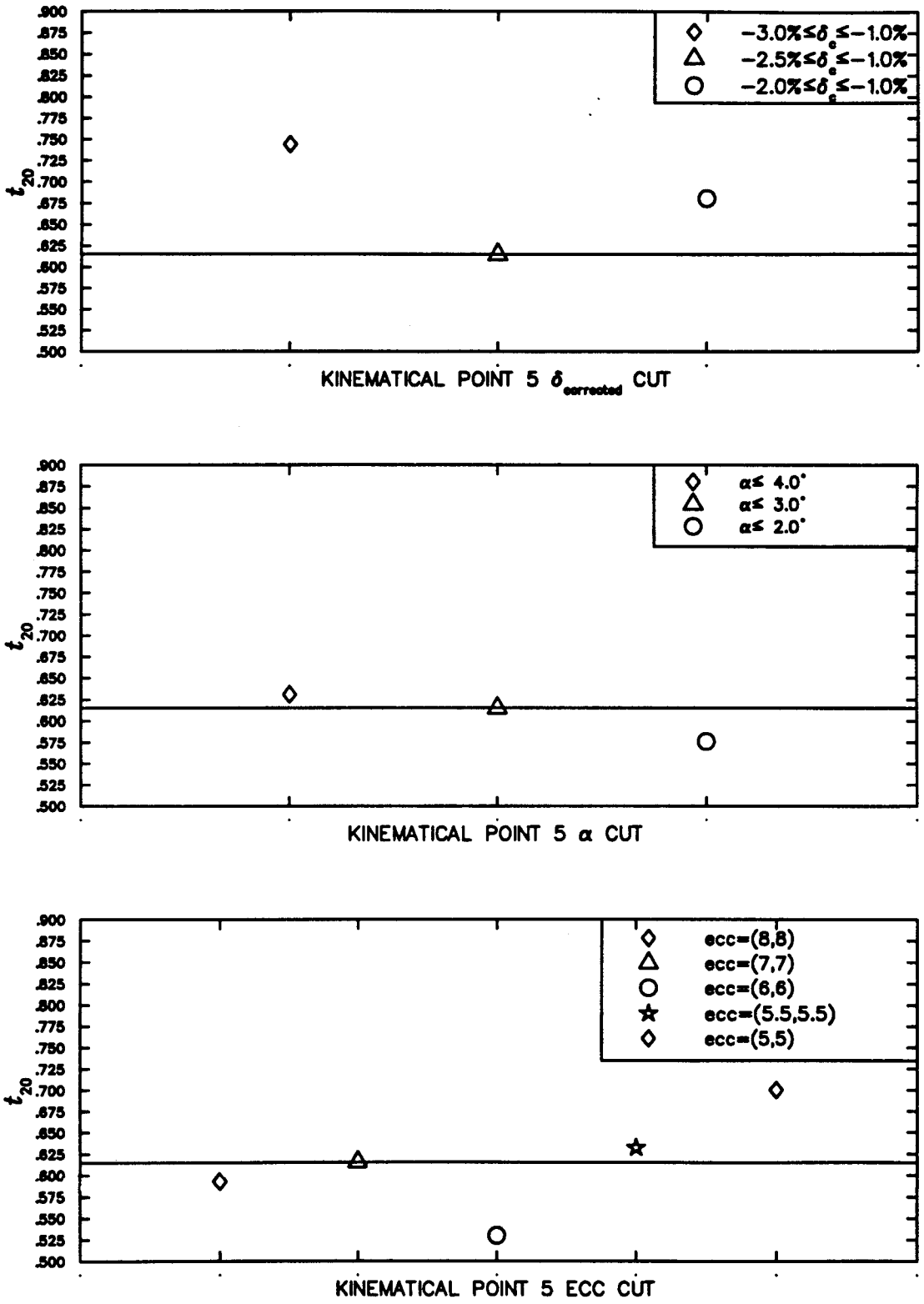

Figure 3.43: Systematical errors of the tensor moment t_{20} for kinematical point 5. The observed variation in the t_{20} values due to the cut dependence should be compared to the statistical uncertainty of 0.101.

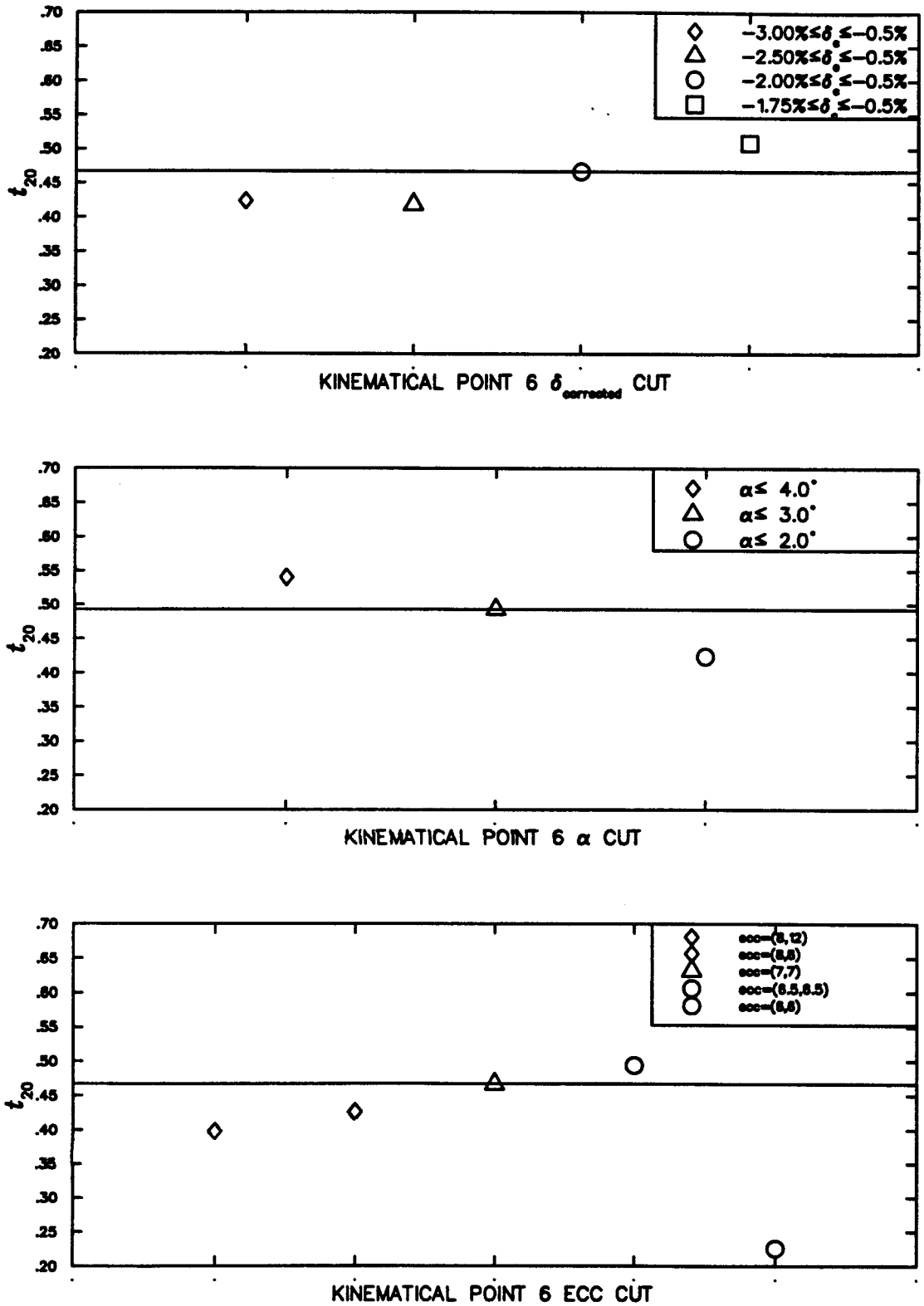

Figure 3.44: Systematical errors of the tensor moment t_{20} for kinematical point 6. The observed variation in the t_{20} values due to the cut dependence should be compared to the statistical uncertainty of 0.170.

Category	Systematic Error	t_{20} Kinematical Point	4	5	6
I	δ_{corr}		.022	.064	.044
II	T_d	θ_e, E_e, electron beam offset (MeV)	2.4	3.6	4.9
		T_d distribution shape (MeV)	1.8	2.4	2.5
		Subtotal (MeV)	3.00	4.33	5.50
		Subtotal (based on $\frac{\partial t_{20}}{\partial T_d}$)	.004	negl.	.006
III	Calibration	analyzing power T_{20}	.003	.009	.014
		interpolation	.008	.010	.011
		beam polarization	.008	.017	.014
		k-parameter stability	.029	.064	.044
		Subtotal	.031	.068	.050
IV	POLDER analysis	α-cut	.018	.028	.056
		ECC cut	.016	.085	.048
		Subtotal	.024	.090	.074
V	Experimental asymmetry		.003	negl.	.001
VI	Special case		N/A	.100	N/A
		TOTAL	.045	.164	.100
		Statistical Error	.049	.101	.170

Table 3.7: Table of the systematic errors on t_{20}.

Category	Systematic Error	t_{21} Kinematical Point	4	5	6
I	δ_{corr}		.018	.013	.012
II	T_d	θ_e, E_e, electron beam offset (MeV)	2.4	3.6	4.9
		T_d distribution shape (MeV)	1.8	2.4	2.5
		Subtotal (MeV)	3.0	4.3	5.5
		Subtotal (based on $\frac{\partial t_{21}}{\partial T_d}$)	.002	.001	.001
III	Calibration	analyzing power T_{21}	.002	.002	.001
		interpolation	.001	.002	.007
		beam polarization	.007	.006	.001
		k-parameter stability	.002	.003	negl.
		Subtotal	.008	.007	.007
IV	POLDER analysis	α-cut	.012	.018	.020
		ECC cut	.032	.006	.026
		Subtotal	.034	.019	.033
V	Experimental asymmetry		.063	.018	.015
VI	Special case		N/A	.003	N/A
		TOTAL	.074	.030	.039
		Statistical Error	.059	.114	.146

Table 3.8: Table of the systematic errors on t_{21}.

Category	Systematic Error	t_{22} Kinematical Point	4	5	6
I	δ_{corr}		.014	.046	.018
II	T_d	θ_e, E_e, electron beam offset (MeV)	2.4	3.6	4.9
		T_d distribution shape (MeV)	1.8	2.4	2.5
		Subtotal (MeV)	3.0	4.3	5.5
		Subtotal (based on $\frac{\partial t_{22}}{\partial T_d}$)	.001	.001	.001
III	Calibration	analyzing power T_{22}	negl.	negl.	.001
		interpolation	negl.	negl.	.001
		beam polarization	negl.	negl.	.004
		k-parameter stability	negl.	negl.	negl.
		Subtotal	negl.	negl.	negl.
IV	POLDER analysis	α-cut	.016	.014	.012
		ECC cut	.002	.026	.030
		Subtotal	.016	.030	.032
V	Experimental asymmetry		.012	.010	.008
VI	Special case		N/A	.000	N/A
		TOTAL	.024	.058	.038
		Statistical Error	.036	.058	.071

Table 3.9: Table of the systematic errors on t_{22}.

Chapter 4

Results

In this Chapter the results from the Maryland (UMCP) data analysis will be presented together with the combined results of the E94018 collaboration [136]. It should be noted that the UMCP results are included in the "combined results" of E94018. These combined results of E94018 have been reported in references [133, 137].

Before the measured tensor moments t_{ij} can be compared to the predictions of various theoretical models, some corrections (transformations) must be carried out. First, what has been measured are values of the tensor moments at the polarimeter POLDER at specific electron scattering angles θ_e (these are labeled $t_{ij}^{P}(\theta_e)$). As the recoil deuterons are transported through the deuteron magnetic channel the spin of the deuterons precess in the magnetic field and a correction to the tensor moments must be applied. This correction transforms the $t_{ij}^{P}(\theta_e)$ values to true tensor moment values at the primary target (labeled $t_{ij}(\theta_e)$). Next the

Kinematical Point	4	5	6
θ_e (°)	27.6	23.4	20.3
Q (fm^{-1})	5.44	6.13	6.63
T_d(MeV)	306.88	389.11	455.93
# of CE-events	11,825	3,306	2,396
# of ed-events	2,958,978	1,185,261	879,466
Efficiency ϵ_{pol} (10^{-3})	4.00 ± 0.37	2.79 ± 0.49	2.72 ± 0.56
k_free (tij-fit)	1.026±0.028	1.150±0.061	0.966±0.045
χ^2_ν (k_fixed tij-fit)	1.3033±0.0088	1.0410±0.0066	1.1941±0.0036
$t^P_{20}(\theta_e)$ UMCP	.232±.049±.045	.615±.101±.164	.467±.170±.010
$t^P_{20}(\theta_e)$ comb.	.252±.047±.053	.581±.093±.142	.470±.177±.062
$t^P_{21}(\theta_e)$ UMCP	.314±.059±.074	.260±.114±.030	.083±.146±.039
$t^P_{21}(\theta_e)$ comb.	.247±.057±.095	.233±.097±.054	.065±.153±.058
$t^P_{22}(\theta_e)$ UMCP	.026±.036±.024	-.024±.058±.058	-.121±.071±.038
$t^P_{22}(\theta_e)$ comb.	.042±.035±.036	-.005±.054±.048	-.130±.073±.047

Table 4.1: A table of the extracted tensor moments $t^P_{ij}(\theta_e)$ for the three kinematical data points 4, 5, and 6. Both the results from the Maryland analysis (UMCP) and the combined results of E94018 are shown. Note: the Maryland results are included in the "combined results". The quantities shown in the top part of the table, for example the deuteron kinetic energy, is from the Maryland analysis. The uncertainties given are the statistical followed by the systematic. In cases where only one error is given it corresponds in this table to only a statistical uncertainty.

values of the tensor moments $t_{ij}(\theta_e)$ are transformed to tensor moments at specific electron scattering angles, either 0° or 70°. The quantity $t_{20}(0°)$, labeled $\tilde{t}_{20}$, corresponds to a tensor moment t_{20} without any contribution from the $G_M(Q^2)$ form factor. In the literature it is common to give the tensor moment values at either 70°, i.e. $t_{ij}(70°)$, or at 0°, i.e. $\tilde{t}_{20}$. These corrections (transformations) are described in more detail in the next few paragraphs.

The values of $t_{ij}^P(\theta_e)$ that were obtained for kinematical points 4, 5, and 6 in the UMCP analysis are shown together with the values based on the combined results of E94018 in Table 4.1. More detailed information of the UMCP analysis is also given in the same table. The value of $t_{ij}^P(\theta_e)$ of the different institutes involved in the analysis are shown in Table 4.2.

4.1 Deuteron Spin Precession Correction

The precession of the deuteron spin in a magnetic field (the field of the dipole magnet of the deuteron channel in the case of the JLab t_{20} measurement) has been described in ref. [53] and the relevant formalism for making the necessary correction was also derived in the same document. The three deuteron tensor moments get *mixed* due to the precession. The tensor moments after the spin precession, i.e. at POLDER, can be expressed as functions of the tensor moments at the primary target:

	Q (fm^{-1})	θ_e (°)	$t_{20}^P(\theta_e)$	$t_{21}^P(\theta_e)$	$t_{22}^P(\theta_e)$
1					
CEA	4.10	35.7	-.596±.036±.136	.379±.049±.096	.130±.040±.029
ISN	4.09	35.8	-.614±.122	.373±.075	-.027±.061
MIT	4.07	35.8	-.665±.038±.161	.413±.053±.096	.115±.044±.036
2					
CEA	4.45	33.3	-.387±.024±.049	.306±.034±.052	.014±.024±.017
ISN	4.45	33.6	-.416±.037	.227±.048	.014±.036
MIT	4.47	33.6	-.316±.034±.065	.313±.045±.041	-.028±.034±.022
3					
CEA	5.09	29.7	.141±.033±.034	.244±.042±.053	.007±.029±.023
MIT	5.09	29.9	.154±.033±.048	.194±.043±.060	-.008±.029±.021
4					
CEA	5.48	27.4	.267±.044±.036	.221±.055±.043	.072±.033±.013
UMCP	5.44	27.6	.232±.050±.045	.314±.059±.074	.026±.036±.024
MIT	5.50	27.6	.255±.049±.057	.210±.058±.055	.028±.036±.017
5					
CEA	6.16	23.0	.552±.087±.111	.211±.097±.062	.012±.050±.030
UMCP	6.13	23.4	.615±.101±.164	.260±.114±.030	-.024±.058±.058
6					
CEA	6.65	19.8	.474±.184±.058	.045±.161±.094	-.140±.076±.043
UMCP	6.63	20.3	.467±.170±.100	.083±.146±.039	-.121±.071±.038

Table 4.2: Table of the values of deuteron tensor moments as measured at POLDER $t_{ij}^P(\theta_e)$ of the different institutes involved in the analysis. Whenever only one error bar is given it corresponds to the total of quadratically combined statistical and systematic errors.

$$\begin{pmatrix} t_{20}^{\mathrm{P}} \\ t_{21}^{\mathrm{P}} \\ t_{22}^{\mathrm{P}} \end{pmatrix} = \begin{pmatrix} 1-(\frac{3}{2})\sin^2(\lambda) & \sqrt{\frac{3}{2}}\sin(2\lambda) & \sqrt{\frac{3}{2}}\sin^2(\lambda) \\ -\sqrt{\frac{3}{8}}\sin(2\lambda) & \cos(2\lambda) & (\frac{1}{2})\sin(2\lambda) \\ \sqrt{\frac{3}{8}}\sin^2(\lambda) & -(\frac{1}{2})\sin(2\lambda) & (\frac{1}{2})[1+\cos^2(\lambda)] \end{pmatrix} \begin{pmatrix} t_{20} \\ t_{21} \\ t_{22} \end{pmatrix}$$

where $\lambda = \gamma(\mu_{\mathrm{d}} - 1)\theta_{\mathrm{B}}$; and γ is the relativistic Lorentz factor, μ_{d} is the deuteron magnetic dipole moment, and θ_{B} is the bend angle (30°). By performing a matrix inversion one gets:

$$\begin{pmatrix} t_{20} \\ t_{21} \\ t_{22} \end{pmatrix} = \begin{pmatrix} c_{00} & c_{01} & c_{02} \\ c_{10} & c_{11} & c_{12} \\ c_{20} & c_{21} & c_{22} \end{pmatrix} \begin{pmatrix} t_{20}^{\mathrm{P}} \\ t_{21}^{\mathrm{P}} \\ t_{22}^{\mathrm{P}} \end{pmatrix}$$

The elements c_{nm} of the matrix C were computed for the JLab experiment [135] and the relevant ones for kinematical points 4, 5, and 6 are shown in Table 4.3. The fact that one was also able to measure t_{21} and t_{22} at JLab simultaneously with the t_{20} measurement means that one can in a consistent manner use one's own measured t_{21} and t_{22} values in applying this correction. In contrast, for the Bates 1991 experiment the tensor moments t_{21} and t_{22} had to be estimated using the world data for $A(Q^2)$, $B(Q^2)$, and the extracted G_{Q} [12]. The spin precession corrected tensor moment values are shown in Table 4.4 together with the corresponding values based on the E94018 combined results.

Kinematical Point	c_{00}	c_{01}	c_{02}	c_{10}	c_{11}	c_{12}	c_{20}	c_{21}	c_{22}
4	.989	.212	.009	-.106	.985	.087	.005	-.087	.996
5	.988	.220	.010	-.110	.984	.090	.005	-.090	.996
6	.987	.227	.011	-.113	.983	.093	.005	-.093	.996

Table 4.3: A table of the matrix elements c_{mn} which were used in the deuteron spin precession correction.

Kinematical Point	4	5	6
Q (fm^{-1})	5.44	6.13	6.63
$t_{20}(\theta_e)$ UMCP	.296±.050±.047	.665±.103±.162	.478±.171±.013
$t_{20}(\theta_e)$ comb.	.301±.048±.056	.625±.094±.141	.477±.178±.063
$t_{21}(\theta_e)$ UMCP	.287±.069±.073	.186±.136±.035	.018±.177±.038
$t_{21}(\theta_e)$ comb.	.220±.056±.094	.166±.096±.056	-.001±.152±.058
$t_{22}(\theta_e)$ UMCP	.000±.036±.025	-.044±.059±.058	-.126±.072±.038
$t_{22}(\theta_e)$ comb.	.022±.035±.037	-.023±.054±.048	-.133±.074±.047

Table 4.4: A table of the extracted tensor moments $t_{ij}(\theta_e)$ for the three kinematical data points 4, 5, and 6. Both the results from the Maryland (UMCP) analysis and the combined results of E94018 are shown. Note: the Maryland results are included in the "combined results".

4.2 Tensor Moments at $\theta_e = 0°$ and $\theta_e = 70°$

As it is customary in the literature to quote the deuteron tensor moments t_{ij} at an electron scattering angle of $\theta_e = 70°$ the expressions necessary for these transformations will next be written out. The transformation of $t_{20}(\theta_e)$ to $t_{20}(70°)$ is carried out with:

$$t_{20}(70°) = t_{20}(\theta_e) + \frac{B(Q^2)\left[\tan^2(\frac{70°}{2}) - \tan^2(\frac{\theta_e}{2})\right]}{A(Q^2) + B(Q^2)\tan^2(\frac{70°}{2})}\left[-t_{20}(\theta_e) - \frac{1}{2\sqrt{2}}\right]. \tag{4.1}$$

The $t_{21}(\theta_e)$ to $t_{21}(70°)$ transformation can be written as $t_{21}(70°) = R \times t_{21}(\theta_e)$ with R defined as:

$$R = \frac{\cos(\frac{\theta_e}{2})}{\cos(\frac{70°}{2})} \times \frac{\left[1 + \eta\sin^2(\frac{70°}{2})\right]^{\frac{1}{2}}}{\left[1 + \eta\sin^2(\frac{\theta_e}{2})\right]^{\frac{1}{2}}} \times \frac{\left[A(Q^2) + B(Q^2)\tan^2(\frac{\theta_e}{2})\right]}{\left[A(Q^2) + B(Q^2)\tan^2(\frac{70°}{2})\right]}. \tag{4.2}$$

Finally the expression utilized in the $t_{22}(\theta_e)$ to $t_{22}(70°)$ transformation is written as:

$$t_{22}(70°) = t_{22}(\theta_e) \times \left[\frac{A(Q^2) + B(Q^2)\tan^2(\frac{\theta_e}{2})}{A(Q^2) + B(Q^2)\tan^2(\frac{70°}{2})}\right]. \tag{4.3}$$

The resulting values of the tensor moments $t_{ij}(70°)$ for the three kinematical points 4, 5, and 6 are shown in Table 4.5. The combined results of E94018 for the tensor moments $t_{ij}(70°)$ for all six kinematical points are shown in Table 4.6.

Kinematical Point	4	5	6
Q (fm^{-1})	5.44	6.13	6.63
$t_{20}(70°)$ $\left(\begin{smallmatrix}\pm\Delta stat.\\ \pm\Delta syst.\end{smallmatrix}\right)$	$.287\pm.067\left(\begin{smallmatrix}\pm.049\\ \pm.046\end{smallmatrix}\right)$	$.660\pm.191\left(\begin{smallmatrix}\pm.102\\ \pm.161\end{smallmatrix}\right)$	$.476\pm.172\left(\begin{smallmatrix}\pm.171\\ \pm.013\end{smallmatrix}\right)$
$t_{21}(70°)$ $\left(\begin{smallmatrix}\pm\Delta stat.\\ \pm\Delta syst.\end{smallmatrix}\right)$	$.340\pm.119\left(\begin{smallmatrix}\pm.082\\ \pm.086\end{smallmatrix}\right)$	$.224\pm.169\left(\begin{smallmatrix}\pm.164\\ \pm.042\end{smallmatrix}\right)$	$.022\pm.220\left(\begin{smallmatrix}\pm.215\\ \pm.046\end{smallmatrix}\right)$
$t_{22}(70°)$ $\left(\begin{smallmatrix}\pm\Delta stat.\\ \pm\Delta syst.\end{smallmatrix}\right)$	$.000\pm.044\left(\begin{smallmatrix}\pm.036\\ \pm.025\end{smallmatrix}\right)$	$-.044\pm.083\left(\begin{smallmatrix}\pm.059\\ \pm.058\end{smallmatrix}\right)$	$-.126\pm.081\left(\begin{smallmatrix}\pm.072\\ \pm.038\end{smallmatrix}\right)$

Table 4.5: A table of the values of the measured tensor moments t_{ij} at an electron scattering angle of $\theta_e = 70°$ for the three kinematical data points 4, 5, and 6. The statistical (top) and systematic (bottom) errors of the tensor moments are shown in parentheses. These errors were combined in quadrature and the resulting total errors are also shown.

Kinematical Point	Q (fm^{-1})	$t_{20}(\theta_e = 70°)$	$t_{21}(\theta_e = 70°)$	$t_{22}(\theta_e = 70°)$
1	4.09	$-.535 \pm .174$	$.510 \pm .136$	$.082 \pm .053$
2	4.46	$-.323 \pm .089$	$.355 \pm .105$	$-.026 \pm .046$
3	5.09	$.180 \pm .053$	$.234 \pm .102$	$-.017 \pm .040$
4	5.47	$.293 \pm .073$	$.261 \pm .130$	$.022 \pm .050$
5	6.15	$.619 \pm .168$	$.200 \pm .134$	$-.023 \pm .072$
6	6.64	$.474 \pm .188$	$-.001 \pm .198$	$-.133 \pm .087$

Table 4.6: A table showing the tensor moments $t_{ij}(\theta_e = 70°)$ for all six kinematical data points based on the combined results of E94018. The statistical and systematical errors were combined in quadrature and the resulting total errors are given.

Kinematical Point	4	5	6
Q (fm^{-1})	5.44	6.13	6.63
$t_{20}(0°)$ $\left(\begin{smallmatrix}\pm\Delta stat.\\ \pm\Delta syst.\end{smallmatrix}\right)$	$.297\pm.069\left(\begin{smallmatrix}\pm.050\\ \pm.047\end{smallmatrix}\right)$	$.666\pm.192\left(\begin{smallmatrix}\pm.103\\ \pm.162\end{smallmatrix}\right)$	$.478\pm.172\left(\begin{smallmatrix}\pm.171\\ \pm.013\end{smallmatrix}\right)$

Table 4.7: A table of the values of the measured tensor moment t_{20} at an electron scattering angle of 0° for the three kinematical data points 4, 5, and 6. The statistical (top) and systematic (bottom) errors of the tensor moment are shown in parentheses. These errors were combined in quadrature and the resulting total errors are also shown.

The $\tilde{t}_{20}$ quantity is defined such that the $G_M(Q^2)$ form factor contribution is neglected. Equation 1.24 shows that this corresponds to quoting t_{20} for an electron scattering angle of 0°. The expression used in transforming $t_{20}(\theta_e)$ to $\tilde{t}_{20}$ is:

$$\tilde{t}_{20} = \left[\frac{A(Q^2) + B(Q^2)\tan^2(\frac{70°}{2})}{A(Q^2)}\right] t_{20}(\theta_e) + \left(\frac{B(Q^2)}{2\sqrt{2}A(Q^2)}\right)\tan^2\left(\frac{\theta_e}{2}\right), \tag{4.4}$$

and the values of $\tilde{t}_{20}$ for the three kinematical data points 4, 5, and 6 are shown in Table 4.7.

4.3 Comparison of Results to Model Predictions

4.3.1 Tensor Moments

A brief overview of previous experiments that measured t_{20} was given in Chapter 1. Next a comparison of first the previously measured data and the new JLab data will be made and second a comparison of the JLab data to the predictions of theoretical models will follow. In comparing to previous data attention will be paid in particular to the Bates data from 1991 which partially overlap the same four momentum transfer regime as the new JLab data. It should also be noted that the most recent data from NIKHEF is of importance as it represents a modern measurement of the internal gas target type for which it was for the first time ever possible to determine absolutely the polarization of the deuterium gas target *in situ*.

t_{20}

Before comparing the new JLab data with theoretical predictions one needs to compare the new data to the existing data for a consistency check of the experimental measurements themselves. The momentum transfer regime of the new JLab data overlaps only partially with the momentum transfers covered in the Bates 1991 data as shown in Figure 4.1. The two lowest four momentum transfer points ($Q = 4.09$ fm^{-1} and $Q = 4.46$ fm^{-1}) of JLab overlap with the two highest

four momentum transfer points ($Q = 4.22$ fm^{-1} and $Q = 4.62$ fm^{-1}) of Bates. A rough comparison shows that on the one hand the JLab data agrees with the $Q = 4.22$ fm^{-1} data point of Bates within slightly more than one error bar. On the other hand the JLab data and the $Q = 4.62$ fm^{-1} data point of Bates agree quite well. Generally speaking the results of the two measurements are rather consistent with each other although there is a clear trend of the Bates data being lower than the new JLab data.

Next we compare predictions from the main categories of theoretical models*. In Figure 4.1 predictions based on a non-relativistic model, a relativistic model, a hybrid quark-hadron model, and pQCD model are shown together with the old experimental data and the new JLab data. In light of the new JLab data some conclusions about the main model categories can be drawn. Predictions of pQCD clearly fail in the momentum transfer regime of 4 fm^{-1} to 7 fm^{-1}. Measurements at much higher four momentum transfers are clearly necessary before any hope of a pQCD description becoming valid can be realized. This is in accordance with the estimate by Kobushkin and Syamtomov. Their analysis shows that quark degrees of freedom would start to strongly affect the behavior of the deuteron electromagnetic form factors at four momentum transfers of the order of $Q \simeq 16$ fm^{-1} [51]. Another obvious pitfall is the lack of structure in

*We are limited to models for which we obtained numerical results from the authors. However, a brief review of most models which are found in the literature was given in Section 1.3.

the pQCD predictions. As can be seen in Figure 4.1 the tensor moment t_{20} changes rather rapidly in this momentum transfer regime while a monotonous linear behavior is predicted by pQCD. On the other hand the non-relativistic model which includes both meson exchange currents and relativistic corrections describes the new JLab data well. If the prediction had slightly lower values at the four momentum transfers of the four highest data points of JLab then an even more excellent agreement would be achieved. The model of Phillips, Wallace, and Devine, which represents the category of relativistic theories, is based on the 3 dimensional reduction of the Bethe Salpeter equation. The shape of this prediction is similar to the non-relativistic one except that it rises from the minimum of t_{20} at slightly higher Q but it provides overall an excellent agreement. The hybrid quark-hadron models are represented by a model by Lomon et al. In contrast to the above mentioned non-relativistic and relativistic models it does not agree quite as well with the JLab data, slightly overestimating t_{20}.

Having made this comparison of experimental data to the different main categories of theoretical models we will next focus on a few of the models. The non-relativistic model which uses the Argonne v_{18} NN-potential is very successful in predicting t_{20}. This is evident in Figure 4.2 where both a prediction based on an impulse approximation (IA) and a prediction based on the IA with meson exchange current (MEC) corrections and relativistic corrections (RC) are shown. One expects the new JLab t_{20} data to favor the full Argonne v_{18} calculation,

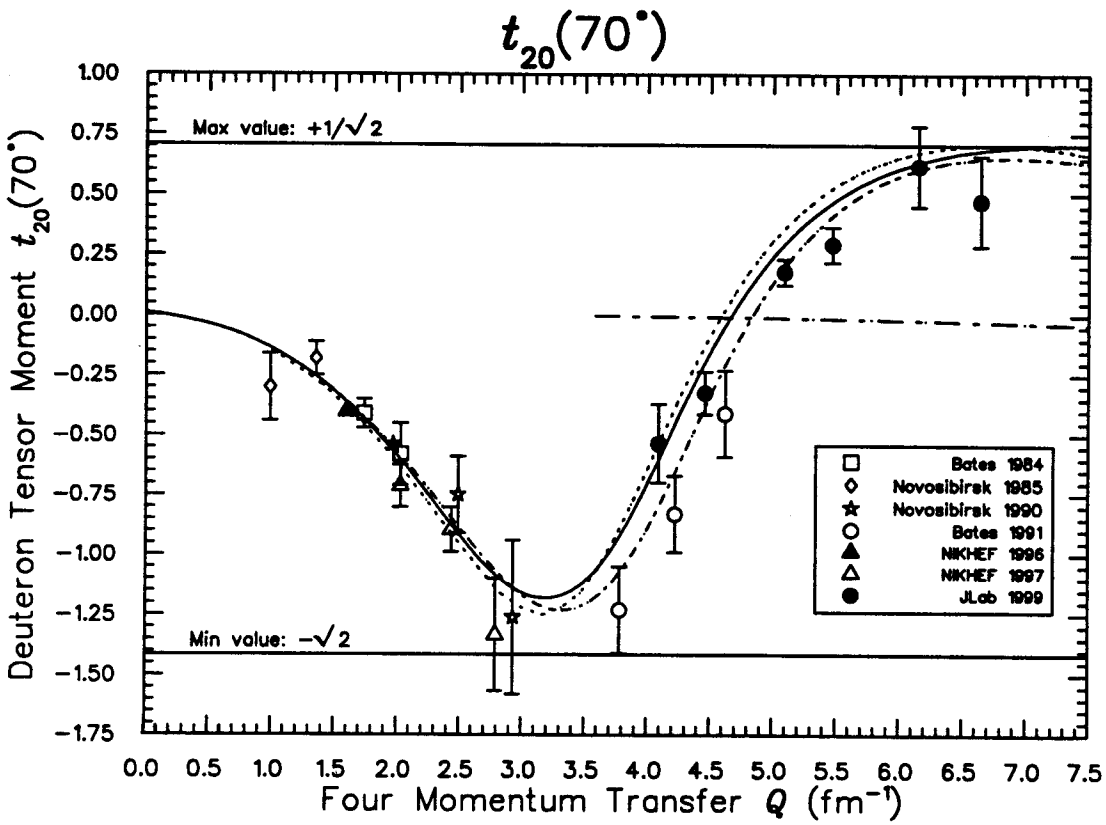

Figure 4.1: The deuteron tensor moment $t_{20}(70°)$ vs. the four momentum transfer Q. Previous experimental data and the new JLab data are shown together with representative predictions of models from different categories: non-relativistic model with full line (NRIA+MEC+RC) [17]; a relativistic model with dashed-dotted line [28]; hybrid quark-hadron model with dotted line [42]; and a pQCD prediction with long dash-dotted line [48].

i.e. the IA+MEC+RC prediction. It is namely known that it is necessary to include meson exchange current contributions in order to improve the predictions of the non-relativistic models in the other deuteron observables and also for three-nucleon systems. The main questions have been which MECs to include and also, for example, the strength of the coupling constants used in evaluating these MEC contributions. Even the signs of the MEC contributions are sometimes debatable.

Two relativistic calculations are also shown in Figure 4.2. The dashed-dotted line represents the calculation by Phillips, Wallace, and Devine. The dashed line represents the light front dynamics (LFD) calculation of Carbonell and Karmanov. The calculation by Phillips et al. gives slightly larger values for t_{20} than the LFD calculation by Carbonell et al. However, generally both agree well with the new JLab data. The double line represents the hybrid quark-hadron model by Lomon, which slightly overestimates t_{20}. It is in particular in disagreement with the Bates 1991 data. Finally two pQCD predictions are also shown in Figure 4.2. The dash-dotted line represents the prediction of Brodsky et al. and the dashed line the model by Kobushkin and Syamtomov. As mentioned above, these models do not appear to be applicable at these four momentum transfers.

This work focused on kinematical points 4, 5, and 6 of the JLab data, i.e. the three highest four momentum transfers, with Q= 5.47 fm^{-1}, 6.15 fm^{-1}, and 6.64 fm^{-1}, so it is of particular interest to consider the necessity and validity of the relativistic models. The absolute value of the tensor moment t_{20} is plotted

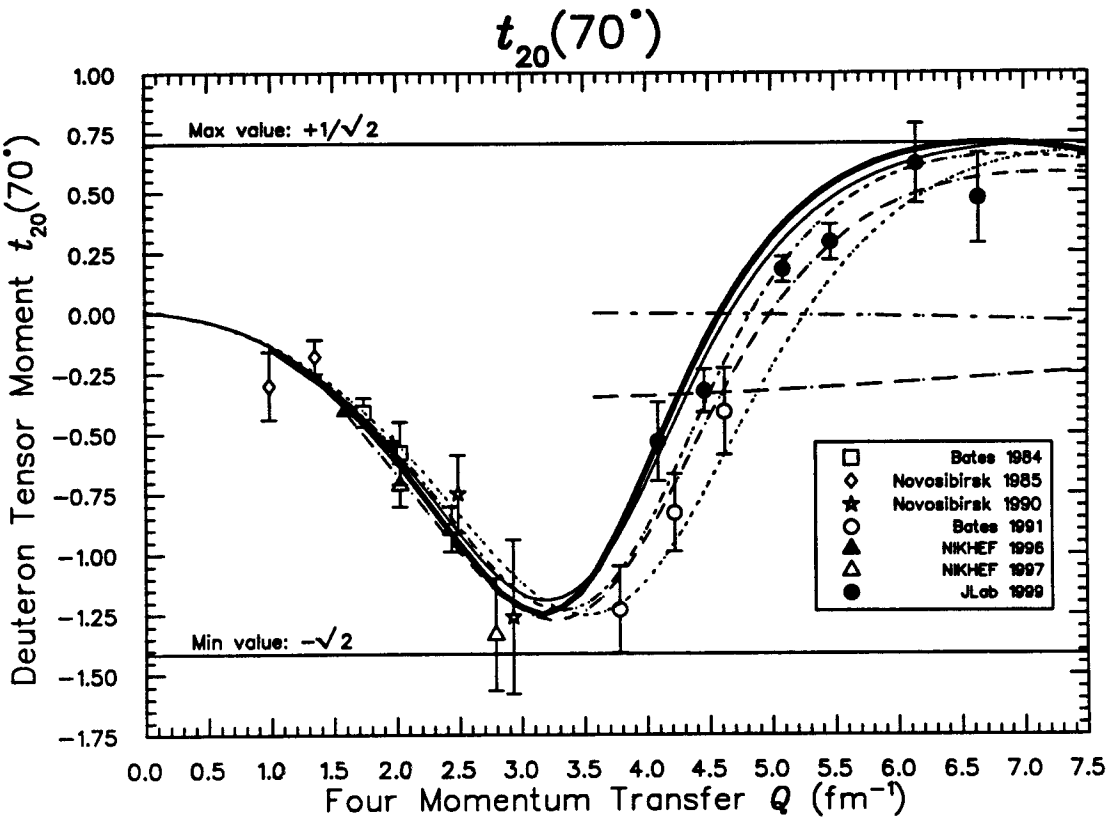

Figure 4.2: The deuteron tensor moment $t_{20}(70°)$ vs. the four momentum transfer Q. Previous experimental data and the new JLab data are shown together with predictions of various theoretical models: non-relativistic models by Wiringa et al. with dotted line (NRIA) and full line (NRIA+MEC+RC) [17]; the relativistic model by Phillips et al. with a dashed-dotted line [28]; the relativistic model by Carbonell et al. with a dashed line [32]; the hybrid quark-hadron model by Lomon et al. with a double line [42]; the pQCD prediction by Brodsky et al. with long dash-dotted line [48]; and the pQCD prediction by Kobushkin et al. with a long dashed line [50].

in Figure 4.3 using a logarithmic vertical axis. This emphasizes the differences between the presented relativistic models. The 3D equal-time model of Phillips et al. is represented with a solid line, while the equally off-shell formalism model of Hummel and Tjon is represented with dash-dotted line. Van Orden et al. used a "one nucleon on mass shell" formalism and their model is shown with a dashed line. The light front dynamics formalism by Carbonell et al. already mentioned above is shown with a dotted line. The conclusion one must draw is that the t_{20} predictions of these relativistic models are so similar that combined with the limiting precision of even the new JLab t_{20} measurement one cannot effectively discriminate among these models. However, further comparison to t_{21}, t_{22}, G_C, G_Q, $A(Q^2)$, and $B(Q^2)$ follow below and that will allow some discrimination among the relativistic models.

t_{21}

Although the main goal of the E94018 experiment was to measure t_{20} it was also possible and desirable to measure t_{21} and t_{22}. As will be seen, t_{21}, in particular, provides some welcome discrimination among the theoretical models. The predictions of the non-relativistic model based on the Argonne v_{18} potential is shown in Figure 4.4. Both the impulse approximation (IA) and the "full" calculation (IA+MEC+RC) are shown. Both of them agree very well with the new JLab data and also the old Bates 1991 data. The relativistic model by Phillips

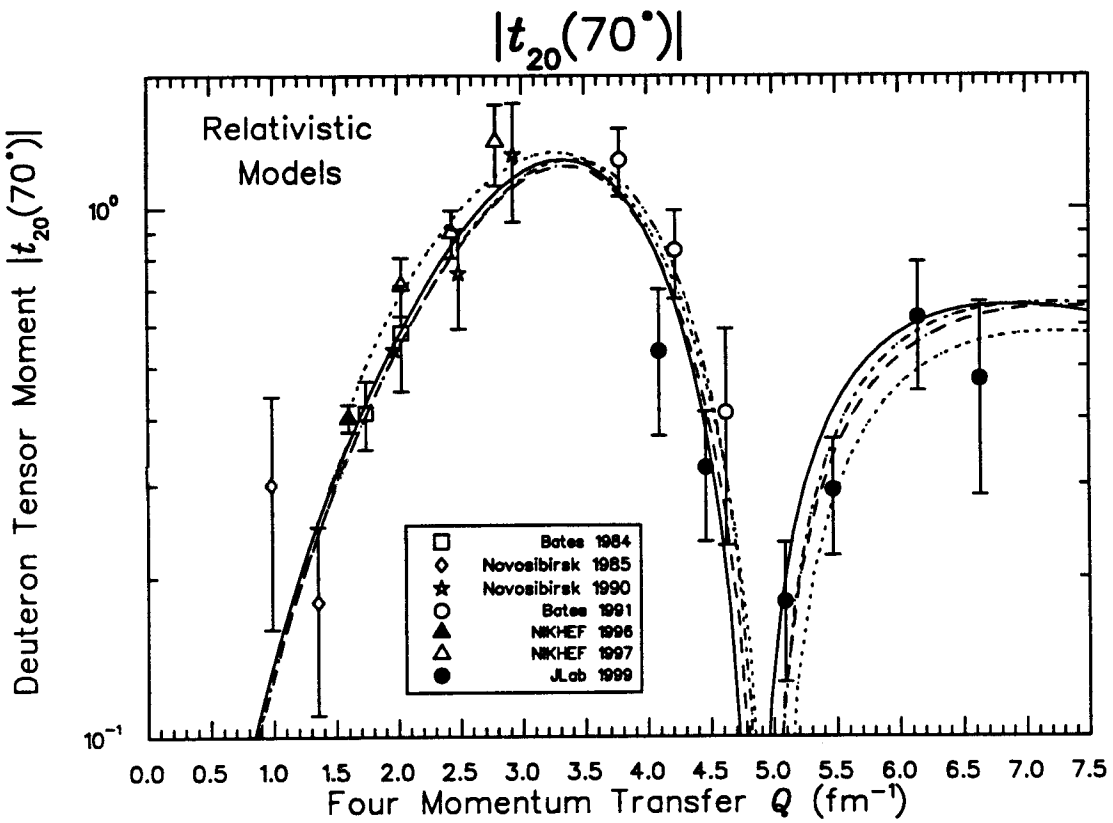

Figure 4.3: The absolute value of the deuteron tensor moment $t_{20}(70°)$ plotted on a logarithmic vertical axis vs. the four momentum transfer Q. Previous experimental data and the new JLab data are shown together with predictions of only relativistic models: solid line by Phillips et al. [28]; dash-dotted line by Hummel et al. [24]; dashed line by van Orden et al. [19]; and dotted line by Carbonell et al. [32].

et al. underestimates t_{21} although their prediction falls within a distance of 1.5 σ from the experimental data points. Carbonell and Karmanov's light front dynamics calculation underestimates even more t_{21} and does clearly more poorly than Phillips et al.'s model. The double line represents the hybrid quark-hadron model by Lomon. It agrees well with the JLab t_{21} data although it predicts lower values of t_{21} compared to the full non-relativistic calculation by Wiringa et al. Not surprisingly the pQCD predictions of both Brodsky et al. and Kobushkin et al. do not predict t_{21} any better than t_{20}.

t_{22}

Using Equation 1.26 and Equation 1.21 one can rewrite t_{22} as

$$t_{22} = \frac{-3B(Q^2)}{8\sqrt{3}(1+\eta)\left[A(Q^2) + B(Q^2)\tan^2(\frac{\theta_e}{2})\right]} \propto \frac{B}{A + B\tan^2(\frac{\theta_e}{2})}\ , \tag{4.5}$$

and as $A(Q^2)$ is typically an order of magnitude larger than $B(Q^2)$ at the covered four momentum transfers in question, the value of t_{22} should be consistent with zero. Four out of the six measured t_{22} values are consistent with zero and the lowest and highest Q data points are consistent with zero within 1.5 σ. The t_{22} measurement is a good consistency check for the JLab E94018 experiment but as can be seen from Figure 4.5 it does not provide any discrimination power between the different models.

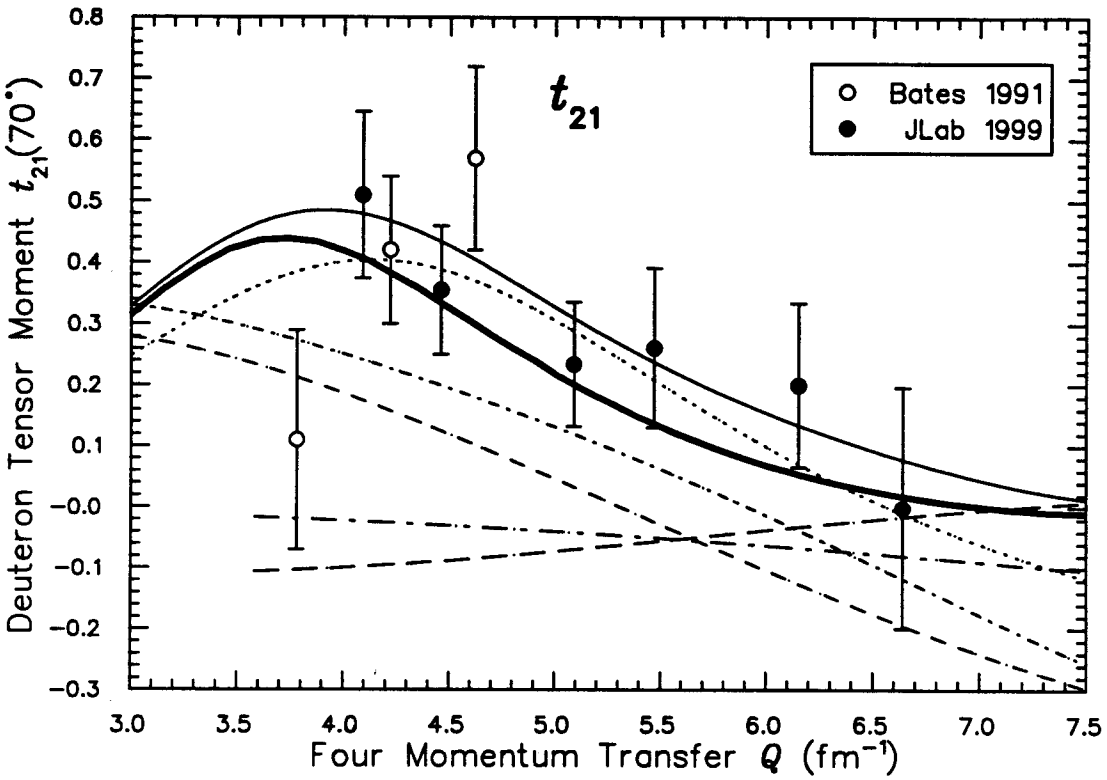

Figure 4.4: The deuteron tensor moment $t_{21}(70°)$ vs. the four momentum transfer Q. Previous experimental data and the new JLab data are shown together with predictions of various theoretical models: dotted line (NRIA) and full line (NRIA+MEC+RC) by Wiringa et al. [17]; dashed-dotted line by Phillips et al. [28]; dashed line by Carbonell et al. [32]; double line by Lomon et al. [42]; long dash-dotted line by Brodsky et al. [48] and long dashed line by Kobushkin et al. [50].

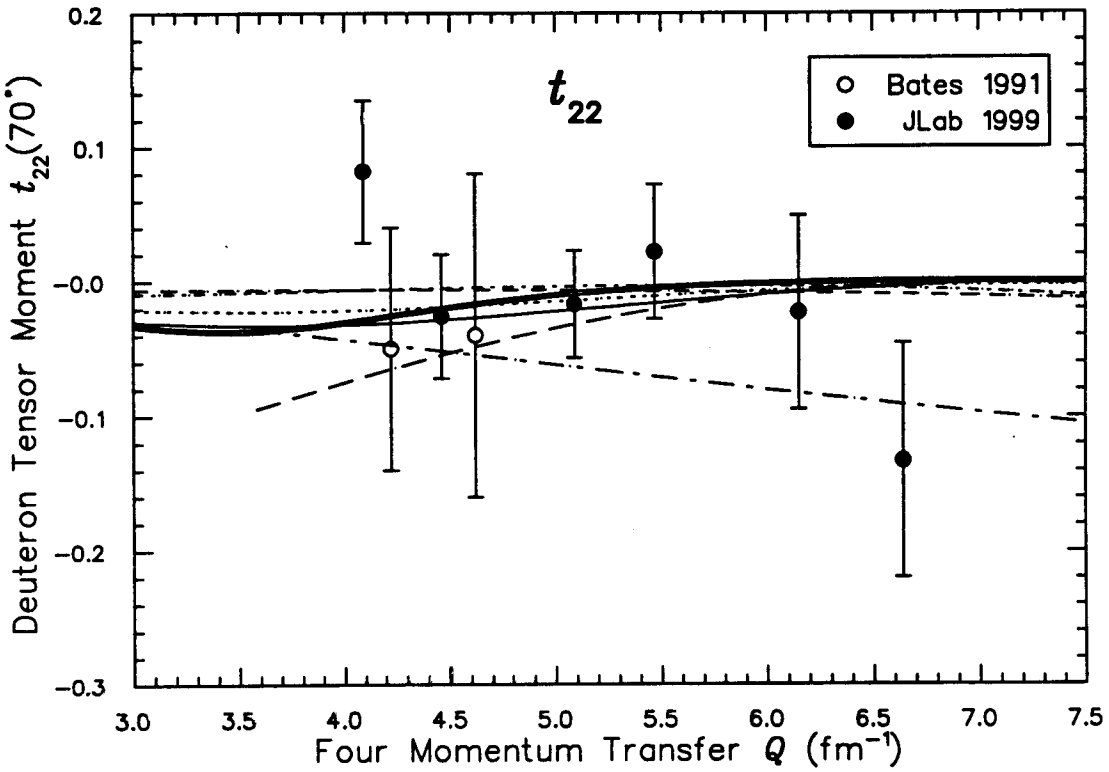

Figure 4.5: The deuteron tensor moment $t_{22}(70°)$ vs. the four momentum transfer Q. Previous experimental data and the new JLab data are shown together with predictions of various theoretical models: dotted line (NRIA) and full line (NRIA+MEC+RC) by Wiringa et al. [17]; dashed-dotted line by Phillips et al. [28]; dashed line by Carbonell et al. [32]; double line by Lomon et al. [42]; long dash-dotted line by Brodsky et al. [48] and long dashed line by Kobushkin et al. [50].

Kinematical Point	Q (fm^{-1})	$G_C \times 10^2$	G_Q
4	5.44	$-.362 \pm .020$	$.0848^{+.0014}_{-.0015}$
5	6.13	$-.353^{+.103}_{-.045}$	$.033^{+.013}_{-.004}$
6	6.63	$-.203^{+.034}_{-.045}$	$.0248^{+.0019}_{-.0034}$

Table 4.8: A table of the values of the separated electromagnetic form factors G_C and G_Q for kinematical data points 4, 5, and 6.

4.3.2 Deuteron Form Factors

The separation of the deuteron electromagnetic form factors G_C and G_Q is described in Appendix C and only the results will be discussed in this Section. The combined results of E94018 for the G_C form factor is shown in Figure 4.6 together with the Bates 1991 results and four theoretical predictions. A comparison of the Bates data with the new JLab data for G_C shows that they do not agree within an error bar. The zero crossing of G_C is of great interest and the Bates data suggest a zero crossing at roughly 4.5 fm^{-1} while the JLab data suggest a crossing at the lower value of roughly 4.0 fm^{-1}. The presently existing world data suggest a zero crossing at 4.21 ± 0.08 fm^{-1} [137].

As can be seen the non-relativistic model needs the MEC and RC corrections in order to reproduce the JLab data. This full Argonne v_{18} model does again an excellent job of predicting the data. The two relativistic models by Phillips et al. and Carbonell et al. do well, too. However, they both slightly underestimate the

Kinematical Point	Q (fm^{-1})	$G_C \times 10^2$	G_Q
1	4.09	-.120±.162	$.399^{+.007}_{-.008}$
2	4.46	-.255±.064	.261±.006
3	5.09	-.396±.028	.122±.004
4	5.47	-.345±.031	.079±.003
5	6.15	-.312±.060	$.033^{+.005}_{-.007}$
6	6.64	$-.189^{+.036}_{-.051}$	$.023^{+.002}_{-.004}$

Table 4.9: A table showing the deuteron charge and quadrupole form factors G_C and G_Q, respectively, for all six kinematical data points based on the combined results of E94018.

magnitude of G_C and of these two models the LFD model is marginally better. The hybrid quark-hadron model by Lomon, represented by a double line in Figure 4.6, overestimates the magnitude of G_C and agrees poorly with the data. This model predicts a zero crossing of G_C at the lowest Q location (~ 4.0 fm^{-1}).

The values for the quadrupole form factor G_Q based on the combined results of E94018 is shown in Figure 4.7 together with predictions of four theoretical models. The Bates 1991 data and the new JLab data on G_Q are consistent with each other. The full Argonne v_{18} non-relativistic model (IA+MEC+RC) does a good job in predicting G_Q. However, for the highest Q data point there exists a discrepancy between the Argonne model and the JLab result. Meanwhile the IA of the Argonne v_{18} model and the relativistic model of Phillips et al. clearly

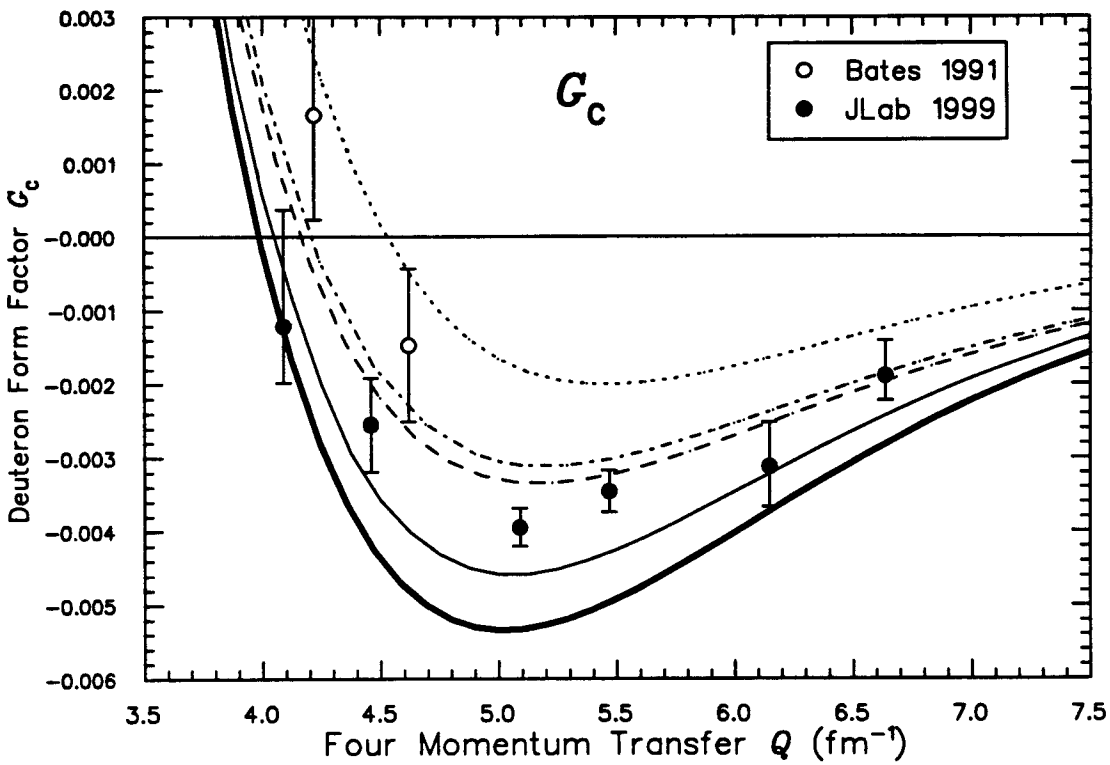

Figure 4.6: The deuteron electric monopole form factor G_C vs. the four momentum transfer Q. Previous experimental data and the new JLab data are shown together with predictions of various theoretical models: dotted line (NRIA) and full line (NRIA+MEC+RC) by Wiringa et al. [17]; dashed-dotted line by Phillips et al. [28]; dashed line by Carbonell et al. [32]; and double line by Lomon et al. [42].

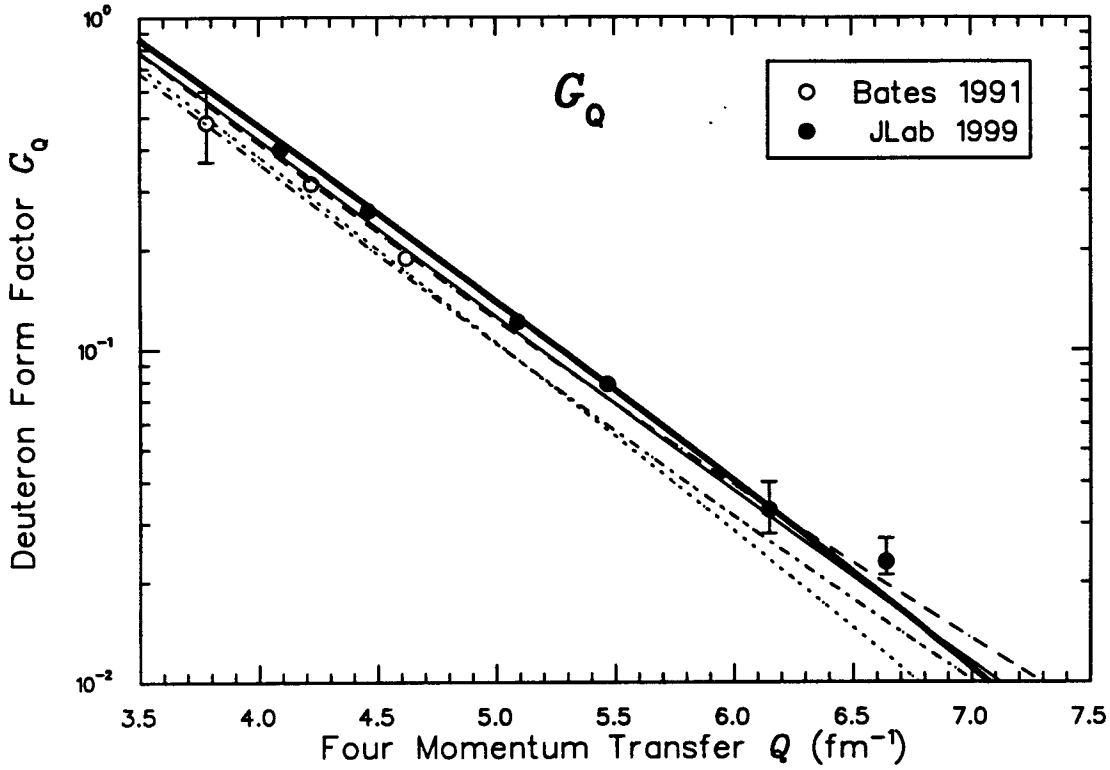

Figure 4.7: The deuteron electric monopole form factor G_Q vs. the four momentum transfer Q. Previous experimental data and the new JLab data are shown together with predictions of various theoretical models: dotted line (NRIA) and full line (NRIA+MEC+RC) by Wiringa et al. [17]; dashed-dotted line by Phillips et al. [28]; dashed line by Carbonell et al. [32]; and double line by Lomon et al. [42].

underestimates G_Q. The LFD model of Carbonell does the very best job of all models in predicting G_Q. Even the slightly higher value of G_Q at the highest Q point of the JLab data is correctly predicted by the LFD model. The hybrid quark-hadron model by Lomon is in agreement with the measured data up to 6.3 fm^{-1}, at higher four momentum transfers it starts underestimating G_Q.

4.3.3 Deuteron Structure Functions

The longitudinal structure function $A(Q^2)$ and the transverse structure function $B(Q^2)$ of the deuteron cannot be ignored in evaluating the success of a particular theoretical model in describing the deuteron.

In Figure 4.8 the world data and in particular the new data from JLab Hall A and from Hall C on $A(Q^2)$ are shown together with predictions of various theoretical models*. We consider only the four momentum transfer range of E94018; that is, we do not consider the higher Q^2 data of the new $A(Q^2)$ data of Hall A, which extends out to $\sim$ 12 fm^{-1}. As can be seen the non-relativistic model based on the Argonne v_{18} model does a good job as long as the MEC contributions and relativistic corrections are included. The dashed-dotted line represents the relativistic calculation by Phillips, Wallace, and Devine. Their prediction underestimates $A(Q^2)$. The relativistic calculation by Carbonell and Karmanov (dashed line) predicts $A(Q^2)$ quite well. There is a slight discrepancy between the Hall A and Hall C $A(Q^2)$ data in that the Hall C measurements give values for $A(Q^2)$ that are systematically higher by about 10% (the systematic errors of the two experiments were 5-6%). The Hall A data supports the non-relativistic Argonne v_{18} model while the Hall C data supports the light front dynamics calculation by Carbonell and Karmanov. The hybrid quark-hadron model by Lomon is in fair agreement with the $A(Q^2)$ data although it slightly

*The JLab Hall C $A(Q^2)$ data were taken concurrently with the t_{20} results presented here.

overestimates $A(Q^2)$ from roughly 4 fm^{-1} to 6 fm^{-1}.

In Figure 4.9 the world data on $B(Q^2)$ are shown together with predictions of various theoretical models. Again we limit ourselves mainly to the four momentum transfer range of E94018. The two relativistic predictions, the equal time calculation by Phillips, Wallace, and Devine (dashed-dotted line) and the light front dynamics calculation by Carbonell and Karmanov (dashed line), both underestimate $B(Q^2)$, and the predictions for the diffractive minimum of $B(Q^2)$ are at much too low four momentum transfer Q. The prediction for the diffractive minimum of $B(Q^2)$ is best made (however, still not good) by the impulse approximation of the non-relativistic Argonne v_{18} model. The IA prediction underestimates $B(Q^2)$ but including MEC contributions and relativistic corrections brings the model in agreement with the experimental data. However, the diffractive minimum is at the same time shifted to too high four momentum transfers. The hybrid quark-hadron model by Lomon agrees with the SLAC data but underestimates $B(Q^2)$ at Q higher than 5.5 fm^{-1}. The prediction of the diffractive minimum of this model is closest to what the SLAC data suggest. However, none of the models is able to reproduce well all the facets of the $B(Q^2)$ data. The reader should note the similarities between the behaviors of t_{21} and the $B(Q^2)$. For example the zero crossings of both quantities are dictated by G_M.

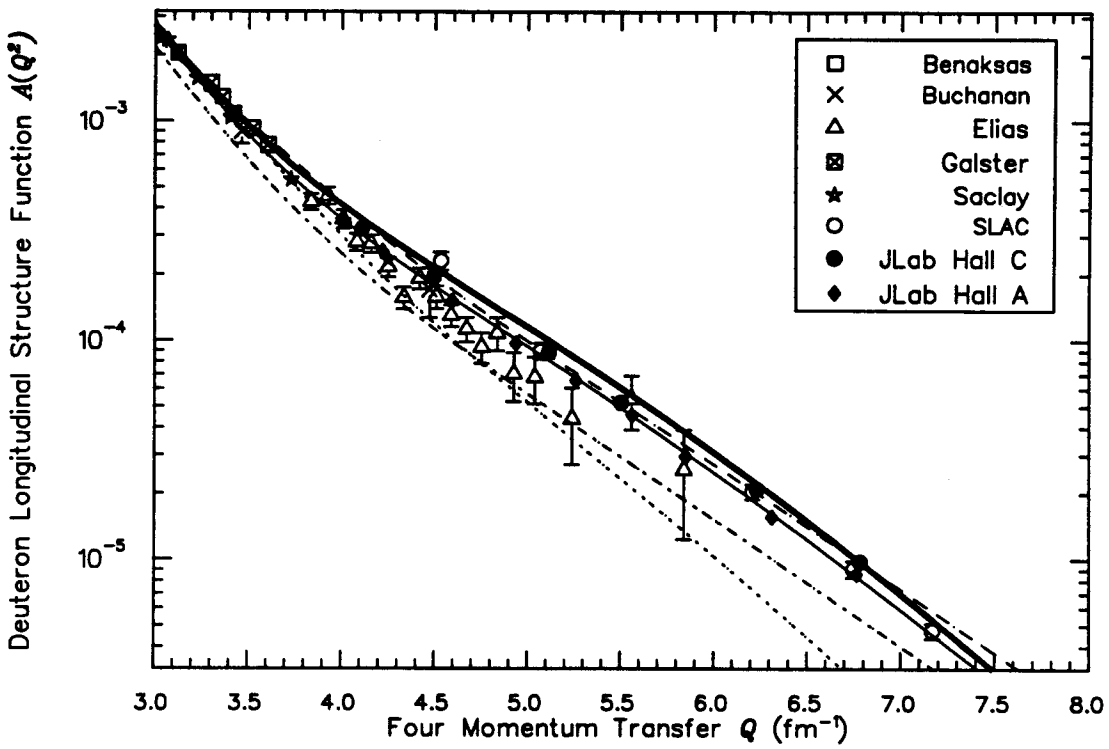

Figure 4.8: The deuteron longitudinal structure function $A(Q^2)$ vs. the four momentum transfer Q. Previous experimental data and the JLab Hall A and Hall C data are shown together with predictions of various theoretical models: dotted line (NRIA) and full line (NRIA+MEC+RC) by Wiringa et al. [17]; dashed-dotted line by Phillips et al. [28]; dashed line by Carbonell et al. [32]; and double line by Lomon et al. [42].

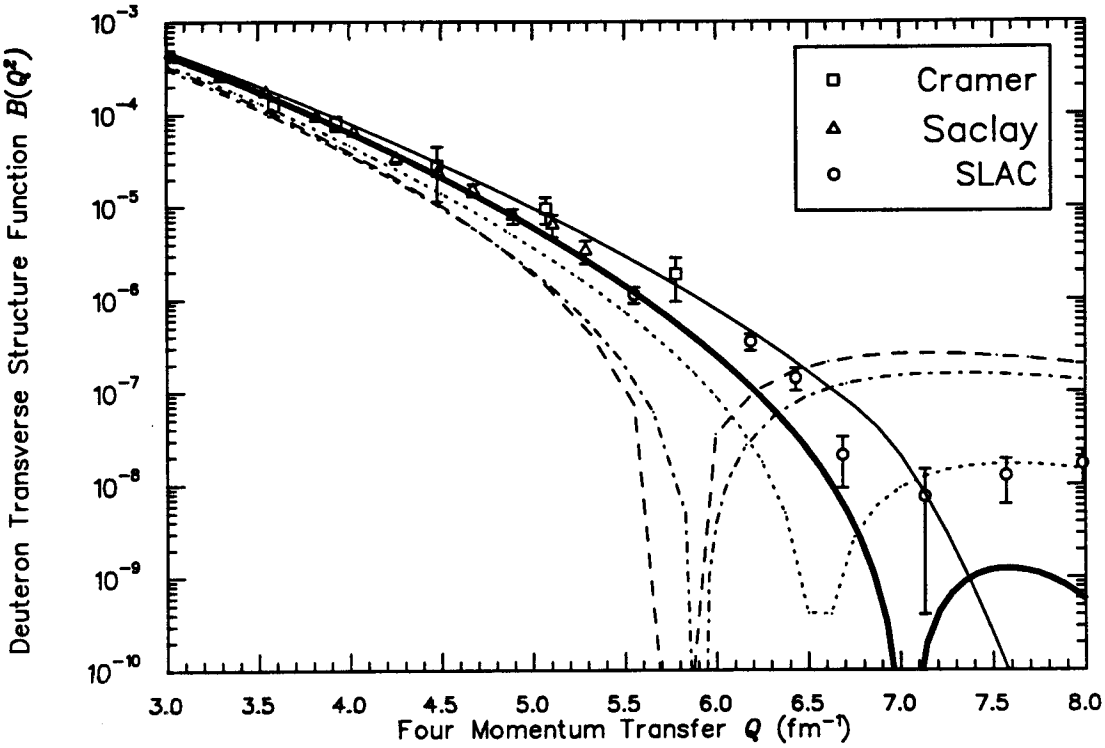

Figure 4.9: The deuteron transverse structure function $B(Q^2)$ vs. the four momentum transfer Q. Previous experimental data and the JLab Hall A and Hall C data are shown together with predictions of various theoretical models: dotted line (NRIA) and full line (NRIA+MEC+RC) by Wiringa et al. [17]; dashed-dotted line by Phillips et al. [28]; dashed line by Carbonell et al. [32]; and double line by Lomon et al. [42].

4.4 Summary & Conclusions

The deuteron tensor moments t_{20}, t_{21}, and t_{22} have been measured in the four momentum transfer Q range of 4.1 fm^{-1} to 6.6 fm^{-1} by the E94018 collaboration at JLab. Four measurements were done above $Q = 4.6$ fm^{-1} and gave valuable new results for a previously unexplored energy regime. These new results confirmed theoretical predictions and also brought new structure to the t_{20} behavior at the highest Q. There is also a trend of the new JLab data being consistently higher than the Bates 1991 data. A new high precision measurement in the Q range of 3.5 fm^{-1} to 5 fm^{-1} would solve this experimental discrepancy and is therefore desirable. In addition, the deuteron longitudinal structure function $A(Q^2)$ was measured concurrently during this experiment. Combining the results for the deuteron tensor polarization t_{20} with the results of the E94018 $A(Q^2)$ measurement and the world data on the deuteron transverse structure function $B(Q^2)$ enabled a separation of the deuteron electromagnetic form factors G_C and G_Q. The new JLab G_C values have brought a lot of new information. Previous G_C data have been scarce. The new JLab data suggest a lower Q location of the zero crossing of G_C compared to the 1991 Bates data. Consequently, the JLab data implies a *stronger* nucleon-nucleon interaction at short distances. The JLab G_C data determine the magnitude of $|G_C|$ at four new momentum transfers from roughly 4.5 fm^{-1} to 6.7 fm^{-1}. The predictions for the magnitude of $|G_C|$ by the various theoretical models have been scattered but are now significantly constrained by

the new data. The new JLab G_Q results confirm the theoretical predictions for four momentum transfers from 4.5 fm^{-1} to 6.7 fm^{-1}. However, refinements of the theoretical calculations are called for by the new data at particularly the highest $Q \simeq 6.7$ fm^{-1} where all models underestimate the quadrupole form factor G_Q.

The new JLab data confirms that predictions based on pQCD are not applicable at these four momentum transfers which is in agreement with recent estimates [51] that call for four momentum transfers of $Q \simeq 16$ fm^{-1}.

The non-relativistic meson-nucleon model based on the Argonne v_{18} nucleon-nucleon potential predicts very well the polarization observables t_{20} and t_{21}, and also the charge monopole form factor G_C, as well as the deuteron longitudinal structure function $A(Q^2)$. Its prediction for the G_Q form factor is good while its $B(Q^2)$ prediction is poor.

The modern relativistic calculations by Phillips et al. (the equal time 3D Bethe-Salpeter equation method) and by Carbonell et al. (the light front dynamics approach) predict the deuteron observables quite well, too. They do equally well for t_{20}. On the one hand the t_{21} prediction by Phillips et al. is in slightly better agreement with data than the prediction by Carbonell et al. On the other hand these roles are reversed in the case of G_C. However, the predictions of Carbonell et al. for G_Q and $A(Q^2)$ are in better agreement with data than the prediction by Phillips et al. The observables t_{22} and $B(Q^2)$ do not have any discriminating power between these two relativistic models. Hence one

can conclude that the light front dynamics model is slightly more successful in depicting the deuteron than the equal time 3D reduced Bethe-Salpeter equation model is.

The hybrid quark-hadron model by Lomon does a good job in predicting t_{20}, t_{21}, G_Q, $A(Q^2)$ and (compared to the other models) does the best job in predicting $B(Q^2)$.

Thus one can conclude that the deuteron polarization observables t_{20} and t_{21} are, in general, well understood. However, there is still room for improvement in both the experimental measurements and the theoretical calculations. On the experimental side there is a need for extremely high precision experiments to discriminate between the various models, particularly through the zero crossing of G_C. Moreover, it is desirable to go to even higher four momentum transfers which poses the challenge of exploring new potentially suitable analyzing reactions. The new results from JLab clearly aid in refining the theoretical models and should also hopefully help in developing them.

With regard to the deuteron transverse structure function $B(Q^2)$ there is a clear need for new measurements and also for development of the theoretical calculations. In fact, the $B(Q^2)$ structure function has recently been measured in Hall A at JLab [138].

All in all, the two-nucleon system is rather well understood although there is as above mentioned room for further improvements and refinements. As has

been mentioned above the non-relativistic meson-nucleon model (Argonne v_{18} full impulse approximation) is very successful in explaining the deuteron, that is a two-nucleon system. It has been pointed out by Henning et al. [139] that there exists considerable freedom in constructing these types of models and that agreement with experimental data can easily be reached when only one nucleus is considered (a two-nucleon or a three-nucleon nucleus). But these "standard" non-relativistic meson-nucleon models have been unable to account simultaneously for the electromagnetic properties of the two-nucleon and three-nucleon systems. Creating a theoretical model that would encompass both two-nucleon and three-nucleon nuclei remains a challenging goal for the future.

4.4.1 Future Prospects

In 1999 a new run was carried out in Novosibirsk at VEPP-3 in which the analyzing power T_{20} was measured at four different four momentum transfers Q: 2.9 fm^{-1}, 3.3 fm^{-1}, 3.6 fm^{-1}, and 4 fm^{-1} [140]. These momentum transfers are in the dip region of t_{20} while individual experiments have so far mainly been mapping out the fall region (1-3 fm^{-1}) and rise region (3.8-5.5 fm^{-1}) of t_{20}. These measurements are also close to the zero crossing of G_C so it will be of quite great interest to see the results of the analysis of this new data.

The feasibility of a new JLab measurement of the deuteron polarization observables utilizing polarimetry has also been considered [141]. The cross section

for elastic electron deuteron scattering scales as: $\frac{d\sigma}{d\Omega} \propto \frac{E^2}{Q^4}$. With a beam energy upgrade at JLab to 12 GeV this would imply higher or equal count rates to the ones used for E94018 for four momentum transfers Q lower than or equal to 11.5 fm^{-1}. The highest Q for E94018 was 6.8 fm^{-1} so extending a t_{20} measurement to 11.5 fm^{-1} would constitute a substantial improvement. However, a four momentum transfer of Q=11.5 fm^{-1} corresponds to the recoil deuterons having kinetic energies of 1080 MeV. That is the new measurement would cover deuteron kinetic energies from about 500 MeV to 1000 MeV. This leads to the question of what polarimeter to use. Also, with the shutdown of the Saturne laboratory the problem of the existence of a source of polarized deuterons that is necessary for polarimeter calibration arises. In summary, the prospects for utilizing the forthcoming higher energies at JLab (12 GeV) to measure t_{20} at even higher Q look rather dim at this moment in time.

However, in the few-nucleon physics community there exists an interest for measuring t_{20} at four momentum transfers less than 1 GeV^2 ($\simeq$ 5 fm^{-1}) [142]. This is both the region where predictions of various models differ most and where G_C crosses zero. A collaboration is constructing a new large acceptance spectrometer (BLAST = Bates Large Acceptance Spectrometer Toroid) at the MIT-Bates Linear Accelerator Laboratory. Combining BLAST with the internal tensor polarized deuterium target from NIKHEF provides an opportunity of a precision measurement of T_{20} and T_{22} in the three reaction channels $^2\vec{H}$ (e, e'd), $^2\vec{H}$ (e, e'p)n,

and $^{2}\overleftrightarrow{\mathrm{H}}\,(\gamma, \mathrm{pn})\mathrm{e}'$ in the four momentum transfer Q range of 1.8 fm^{-1} to 4.7 fm^{-1} [143].

Appendix A

The Jefferson Lab E94018 Collaboration

D. Abbott [5], A. Ahmidouch [10], H. Anklin [8], J. Arvieux [11,12], J. Ball [1,11], S. Beedoe [10], E. Beise [3], L. Bimbot [12], W. Boeglin [8], H. Breuer [3], R. Carlini [5], N. Chant [3], S. Danagoulian [10], K. Dow [7], J. E. Ducret [1], J. Dunne [5], L. Ewell [3], L. Eyraud [4], C. Furget [4], M. Garçon [1], R. Gilman [6], C. Glashausser [6], P. Gueye [5], K. Gustafsson [3], K. Hafidi [1], A. Honegger [2], J. Jourdan [2], S. Kox [4], G. Kumbartski [6], L-C. Lu [4], A. Lung [5], D. Mack [5], P. Markowitz [8], J. McIntyre [6], D. Meekins [5], F. Merchez [4], J. Mitchell [5], R. Mohring [3], H. Mrktchyan [9], S. Mtingwa [10], D. Pitz [3], L. Qin [5], J-S. Réal [4], R. Ransome [6], P. Roos [3], P. Rutt [6], R. Sawafta [10], W. Schmitt [13], S. Stepanyan [9], E. Stephenson [13], R. Tieulent [4], E. Tomasi-Gustafsson [1,11], W. Turchinetz [7], K. Vansyoc [5], J. Volmer [5], E. Voutier [4], W. Vulcan [5], C. Williamson [7], S. Wood [5], C. Yan [5], J. Zhao [2], W. Zhao [7],

[1]DAPNIA/SPhN, Commisariat a l'Energie Atomique/Saclay, 91191 Gif-sur-Yvette, France
[2]Basel Institut für Physik, Basel, Switzerland
[3]University of Maryland, College Park, MD 20742
[4]Institut des Sciences Nucléaires de Grenoble, IN2P3-UJF, 38026 Grenoble, France
[5]Thomas Jefferson National Accelerator Facility, Newport News, Virginia 23606
[6]Rutgers University, Piscataway, New Jersey 08855
[7]MIT-Bates Linear Accelerator, Middleton, Massachusetts 01949
[8]Flordia International University, Miami, Flordia 33199
[9]Yerevan Physics Institute, 375036 Yerevan, Armenia
[10] North Carolina A. & T. State University, Greensboro, North Carolina 27411
[11] LNS-Saclay, 91191 Gif-sur-Yvette, France
[12] IPNO, IN2P3, BP1, 91406 Orsay, France
[13] IUCF, 2401 Milo B. Sampson Lane, Bloomington, IN 47405, USA

Appendix B

Luminosity Scans

The JLab E94018 experiment measured the deuteron longitudinal structure function $A(Q^2)$ in addition to the deuteron tensor moment t_{20}. The $A(Q^2)$ measurement is a precision measurement of an absolute cross section. The uncertainty in the determination of the density of the cryogenic target directly affects the precision with which the absolute cross section can be measured. The purpose of this Appendix is to describe how the reduction in the cryotarget density was determined. Moreover, the objective is to continue the documentation of the analysis results of the luminosity scan data carried out by the author for the Hall C of JLab. The analysis of the luminosity scan data was documented in 1996 [144] and this is an update which adds basic information about two additional scans from 1996 (November and December) and the two final scans in 1997 (April and September). Results from the Dec'96 and Sept'97 scans, which were performed under similar conditions, are presented and compared.

B.1 Introduction

One can categorize target materials which are used in fixed target experiments based on their phases: solid, liquid, and gaseous. As a fixed target is exposed to a beam of particles it absorbs the energy which is given off by the traversing incident particles. For solid targets there is an upper limit on how much energy can be deposited before the target starts melting. In a gaseous target the thermal motion of the target particles will redistribute the deposited energy and the density of the target gas decreases due to the heating. By monitoring the temperature and the pressure of the target one knows the density of the target gas at all times. A liquid target exposed to a beam of particles poses a more complicated situation. A certain amount of energy can be absorbed by the target liquid without significantly changing the density of the liquid. However, if the target liquid starts boiling then a drastic change in the target density will take place. The boiling may be limited to local hot spots or may take place along the entire path of the particle beam within the cryogen. Target boiling and its associated target density changes have been considered in references [145, 146, 147].

B.2 Hall C

The Hall C cryotargets were operated in (2 K) subcooled states. The operating parameters for liquid hydrogen were (T,P)=(19 K, 1.2 atm) and for liquid

deuterium they were (T,P)=(22 K, 1.2 atm). The 2 K subcooling buffer lessens the sensitivity of the cryotarget to fluctuations in beam heating conditions from, for example, sudden changes in the beam current. The utilization of the fast raster system was an additional and crucial safety guard against target density reductions. The operating frequencies of the fast raster system were: 16.8 kHz (horizontal) and 22.9 kHz (vertical), which translates into approximate sweeping speeds of 6,700 $\frac{cm}{s}$ (horizontal) and 9,200 $\frac{cm}{s}$ (vertical) for a $\pm$ 1 mm rastering amplitude. These sweeping speeds are to be compared to the cryogen flow velocity given below.

A critical component in the heat dissipation scheme is the fan of the cryotarget loop. The geometrical dimensions of the fan which has a screw-like blade and was operated at 4020 rpm (67 Hz), are shown in Table B.1. Assuming a fan efficiency of about 40% [148] gives a displacement of roughly 3510 $\frac{cm^3}{s}$ for the cryotarget fan. Flow diverters were installed inside the cryotarget cells in order to increase the flow velocity of the cryogen at the location where the electron beam traverses the cryogen. By considering the aperture of the flow diverters one can estimate the net flow velocity of the cryogen. The relevant geometrical dimensions of the flow diverters of the 1996 cryotarget cells are given in Table B.2. Based on the volume displacement of the fan and the aperture area of the flow diverters it can be inferred that the net flow velocity is in excess of 100 $\frac{cm}{s}$ for all target cells. Although the net flow velocity does not necessarily describe

the flow on a microscopic level, some general characteristics of the fluid can be inferred from the Reynolds number. An estimate of the Reynolds number of the cryogen flow in the target system based on [149, 150]:

$$\mathrm{Re} = \frac{\rho\, U\, L}{\mu}, \tag{B.1}$$

where ρ is the mass density of the cryogen, U is the velocity scale, L is the length scale, and μ is the viscosity of the fluid (cryogen) can be done. To get a lower bound on the Reynolds numbers in the cryotarget cells one studies the case with liquid hydrogen in the long target cell. The applicable values of $(\rho, U, L, \mu) = (0.0696\ \frac{\mathrm{g}}{\mathrm{cm}^3}, 100\ \frac{\mathrm{cm}}{\mathrm{s}}, 4.26\ \mathrm{cm}, 0.011\ \frac{\mathrm{g}}{\mathrm{cm\ s}})$ give a Reynolds number of $\mathrm{Re} \sim 2,700$. This is only a rough estimate based on the geometry at the flow diverters. If one considers the flow in the pipes between the target cell block and the heat exchanger the Reynolds number estimate changes to $\mathrm{Re} \sim 7,200$. Both of these estimates fall in the transition regime between laminar flow and turbulent flow. In the case of turbulent flow one would expect more efficient mixing of the cryogen and hence a faster redistribution of the heat deposited by the electron beam. But no firm conclusion about the characteristics of the flow can be drawn. The flow diverters were modified for the 1997 run in order to decrease the aperture and thus even further increase the net flow velocity. The lengths of the target cells used in 1996 and 1997 are shown in Table B.3.

Blade outer diameter (cm)	7.15
Blade inner diameter (cm)	4.28
Blade pitch (cm)	5.06
Fan speed (rpm)	4020

Table B.1: A table of characteristics of the Hall C cryotarget fan.

Target Cell	4 cm	12 cm
Width (cm)	4.52	2.54
Length (cm)	2.38	13.18
Area (cm^2)	10.76	33.48

Table B.2: A table of the geometrical dimensions of the flow diverters of the cryotarget cells of 1996.

Year	Cryogen	Short target cell (cm)
1996	LH2	4.36 ± 0.01
1997	LH2	4.53 ± 0.01
1996	LD2	4.17 ± 0.01
1997	LD2	4.45 ± 0.01

Table B.3: Table of the lengths of the short target cells used in the luminosity scans in 1996 and 1997 [104, 103].

B.3 Scans

Several dedicated luminosity scans (also labeled "high beam current scans") where the yield was measured as a function of the electron beam current have been performed. The first scans were performed during the commissioning of the Hall C cryotarget in April 1996 and since then altogether nine scans have been performed of which five were documented in ref. [144]. The various beam conditions and the kinematics used for the two standard Hall C spectrometers (HMS/SOS) during the last four scans are shown in Table B.4.

An optimized scheme for performing these scans was developed during 1996 and 1997. The goal was to detect a high rate of inelastically scattered electrons in the HMS and/or SOS spectrometers and simultaneously measure the integrated charge in order to compute a yield. An absolute cross section measurement was not performed but a relative normalization to the yield at the lowest beam current was carried out. Still, high rate was needed in order to accumulate high statistics in a reasonable amount of time as the goal was to look for systematic changes in the yield of $< 1\%$. In its simplest form the yield was defined as:

$$\text{yield} = \frac{\#\text{ of detected scattered electrons}}{\text{integrated charge}}. \tag{B.2}$$

Hardware scalers were used in the beginning to determine the number of scattered electrons but due to significant contamination from random trigger at

high rates it was necessary to use tracked data [144]. The momentum settings of the spectrometers were chosen such that inelastically scattered electrons gave a broad spectrum across the entire focal plane of each spectrometer. Loose cuts on β ($0.8 \leq \beta \leq 1.1$), δ ($-8\% \leq \delta \leq +8\%$), and the reconstructed ytar quantity (-3.5 cm $<$ ytar $< +3.5$ cm, see Section 3.3.1) of the tracked data were applied. The yield was evaluated as:

$$Y = PS \times \epsilon_{\text{tracking}} \times c_{\text{computer}} \times \frac{\#\text{tracks}}{Q_{\text{integrated}}}, \tag{B.3}$$

where PS is the prescaling factor used, $\epsilon_{\text{tracking}}$ is the tracking efficiency, c_{computer} is a correction factor for the computer dead time, "#tracks" is the number of tracks of inelastically scattered electrons that are left after the cuts have been applied, and $Q_{\text{integrated}}$ is the measured integrated charge.

The integrated charge was measured with BCM2 for the Dec'96 scan and with BCM1 for the Sept'97 scan. BCM calibrations were performed immediately prior to the luminosity scans to optimize the accuracy of the charge measurements.

Because there had been some indications that the electron beam spot size varied over time it was deemed necessary to measure the spot size in conjunction with the luminosity scans. The beam spot size was determined with pulsed beam at low currents (5-10 μA) with a superharp scan. The beam spot size was measured before the Dec'96 scan, with a resulting (FWHM) of (190×46) μm^2. A superharp scan was performed both before and immediately after the Sept'97

luminosity scan and the measured beam spot sizes were (FWHM): before (140 × 95) μm^2, and after (100 × 50) μm^2. The beam spot sizes were during both scans normal, in other words small compared to the scale of the raster amplitudes.

A calibration of the rastering amplitudes was also performed prior to the Dec'96 scan and the rastering amplitudes used during the Sept'97 scan were reliable.

In summary, the Sept'97 scan was carried out under the best prepared, defined and controlled circumstances and thus gives the most reliable results. Results from this scan will next be presented together with results from the Dec'96 scan.

B.4 Results

The 4 cm LH2 target cell was used in the Dec'96 scan. The results shown in Figure B.1, Figure B.2, and Figure B.3 are based on a yield evaluated with the HMS spectrometer quantities plus integrated charges from BCM2. Two different rastering amplitudes, ± 0.7 mm and ± 1.57 mm, were used during this scan. As illustrated in these three figures the observed reduction in yield shows a linear dependence on the electron beam current divided by the rastering amplitude. One may have expected the yield to be linearly dependent on the the rastering amplitude squared, that is the area over which the fast raster sweeps. However, due to the flow diverters of the target cells (see Figure 2.16) the net flow is mainly one-dimensional which could possibly explain the observed dependence. As shown

Date	11/16/1996	12/22/1996	4/13/1997	9/11/1997
Logbook	#13, p.18	#14, p.51	#15, p.113	#21, p.110
Run #s	12216-12247	13145-13169	14064-14111	16197-16229
Electron beam energy E_e (GeV)	4.045	2.445	1.645	2.445
Electron beam current I_e range (μA)	17-76	5-84	20-105	5-110
Cryotarget cell (cm)	4	4	4 & 12	4 & 12
Cryogen	LH2	LH2	LH2 & LD2	LH2 & LD2
Kinematics:				
θ_{HMS} (°)	40.0	40.0	35.8	40
θ_{SOS} (°)	40.0	40.0	N/A	N/A
P_{HMS} ($\frac{GeV}{c}$)	-1.5	-1.0	-0.8	-1.0
P_{SOS} ($\frac{GeV}{c}$)	-1.5	-1.0	N/A	N/A
Prescale factor:				
HMS	1-3	2-11	10-200	2-60
SOS	3-8	2-74	N/A	N/A
COIN	∞	∞	N/A	N/A
HMS $\frac{3}{4}$ scintillator rate (kHz)	1.8	14.9	95	120

Table B.4: Conditions during the luminosity scans from the November 16, 1996 scan through the September 11, 1997 scan.

in Figure B.2 a fit to a straight line was carried out, with a resulting slope of $(-.0383 \pm .0054)\ \frac{\%mm}{\mu A}$, which translates into a yield reduction of $(3.83 \pm 0.54)\%$ at an electron beam current of 100 μA using a ± 1 mm rastering amplitude. The fan speed used in 1996 in the LH2 target loop was 60 Hz.

Three target cells were used in the Sept'97 luminosity scan. The results for the 4 cm LD2 target are shown in Figure B.4. The electron beam current was varied from 5 μA to 110 μA. However, despite the excellent linearity of BCM1, the 5 μA data point was not included in the fit because of the large relative error on the integrated charge measurement at this low current. The resulting slope is $(-.0241 \pm .0053)\ \frac{\%mm}{\mu A}$ which translates into a yield reduction of $(2.41 \pm 0.53)\%$ at an electron beam current of 100 μA using a ± 1 mm rastering amplitude. The fan speed in the LD2 target loop was 67 Hz. The results for the same target loop but for the long, 12 cm, target cell are shown in Figure B.5. There are only two data points; they give a slope of $(-.0234 \pm .0115)\ \frac{\%mm}{\mu A}$ which translates into a yield reduction of $(2.34 \pm 1.15)\%$ at an electron beam current of 100 μA using a ± 1 mm rastering amplitude. This result is in quite good agreement with the results of the shorter (4 cm) target cell although the latter result has quite a substantial uncertainty.

Finally, the results for the 4 cm LH2 target are shown in Figure B.6. Again the 5 μA data point was not included in the fit. The resulting slope is $(-.0115 \pm .0045)\ \frac{\%mm}{\mu A}$ which translates into a yield reduction of $(1.15 \pm 0.45)\%$ at an electron

beam current of 100 μA using a $\pm$1 mm rastering amplitude. A data point at 5 μA (marked with a cross) is also shown in the figure. This data was taken with the fast raster turned off. Despite the substantial uncertainty at this low electron beam current a clear drop in the yield can be observed. In addition, a fan speed test was performed at beam currents in excess of 100 μA. The fan of the LH2 loop was normally run at 60 Hz. A decrease of the speed to 40 Hz clearly caused a drop in the yield (data point marked with a star in the figure). An increase to 89 Hz hardly changed the yield at all (data point marked with an open square in the figure) and a further increase to 100 Hz gave a yield indistinguishable from the 89 Hz yield (thus not shown in the figure).

The statistical uncertainties of the Sept'97 scan were less than 0.3% and the systematic uncertainty associated with the integrated charge measurement was 0.2 μA at any current, that is between 0.2% and 2%. In the Dec'96 scan the statistical uncertainties were less than 0.5% and the systematic uncertainties similar to those of the Sept'97 scan.

There is a clear difference between the result of the 4 cm LH2 of the Dec'96 scan and the Sept'97 scan. However, the cryotarget was modified before the 1997 run. The flow diverters were modified to decrease the aperture and increase the net flow velocity. This a possible explanation for the observed smaller yield reduction in the 1997 luminosity scan data compared to the 1996 luminosity scan data. The effect of a difference in the length of target cell itself is unclear,

however, the 1997 "4 cm" target cell was 3.9% longer than the 1996 "4 cm" target cell.

Comparing the Sept'97 LD2 and LH2 results show a larger yield reduction for the LD2 target cells. Simply based on the values of the stopping powers and the densities of the two cryogens one does not expect any significant difference. However, there have been indications of a lower fan efficiency in liquid deuterium compared to liquid hydrogen which would lead to a lower net flow velocity and hence possibly could explain the observed difference.

The $A(Q^2)$ measurement of E94018 was performed at 80 μA using a $\pm$ 1 mm raster amplitude. Based on the results reported in this Appendix a yield reduction of (1.93 $\pm$ 0.53) % is expected and a corresponding correction should be made to the cross section results of the E94018 $A(Q^2)$ data. However, the correction actually used for ref. [125] was (1.3 $\pm$ 1.3) %.

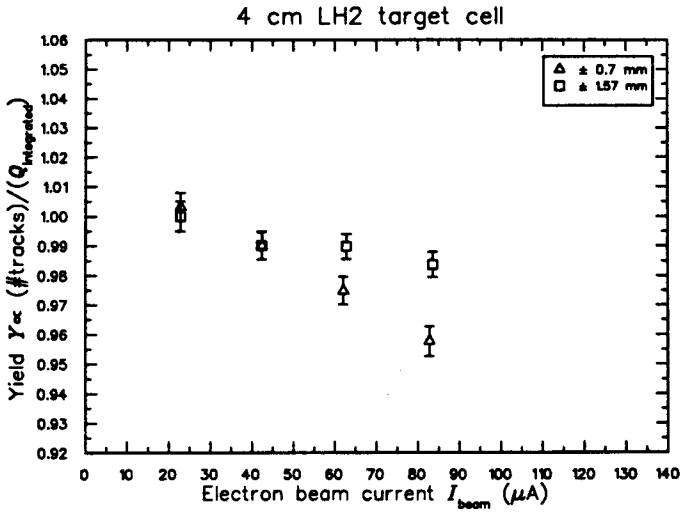

Figure B.1: The data from the December 1996 luminosity scan plotted as the yield vs. the electron beam current. Two different rastering amplitudes, ± 0.7 mm and ± 1.57 mm, were used, as the legend implies. The scan was carried out using the 4 cm LH2 target cell and the HMS spectrometer was used to detect the scattered electrons.

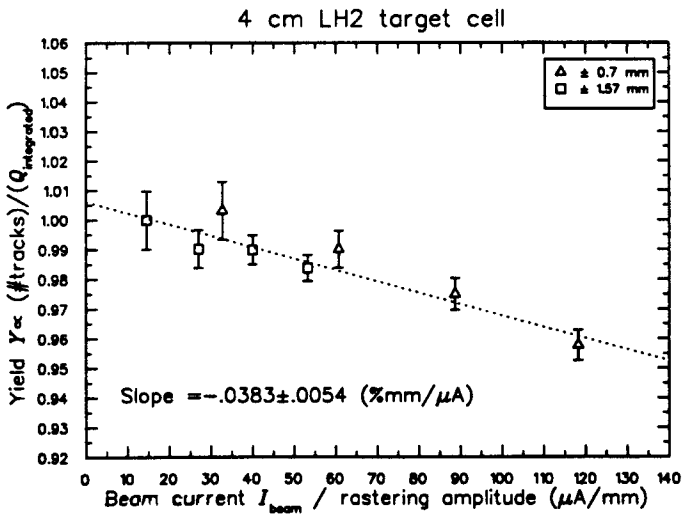

Figure B.2: The data from the December 1996 luminosity scan plotted as the yield vs. the electron beam current divided by the rastering amplitude. A linear relationship is apparent and the slope for the fitted straight line gives a 3.83 ± 0.54% yield reduction at 100 μA using a ± 1 mm rastering amplitude.

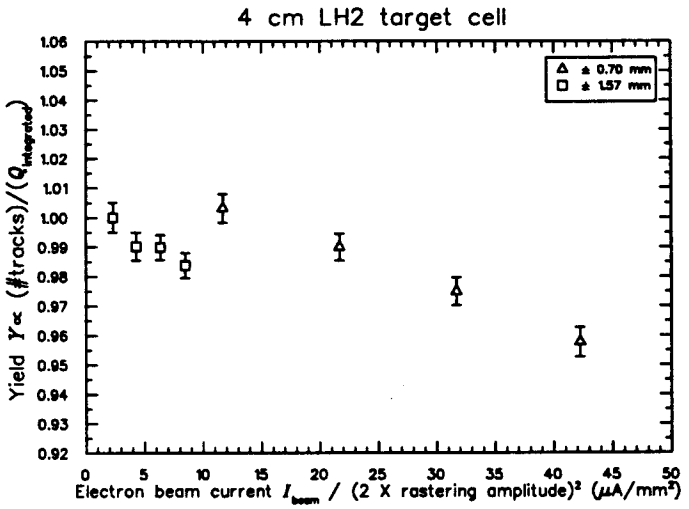

Figure B.3: The data from the December 1996 luminosity scan plotted as the yield vs. the electron beam current divided by the rastering amplitude squared. As this corresponds to the intensity of the rastering pattern of the electron beam on the target one would expect a linear relationship, but that only seems to be the case for each rastering amplitude separately.

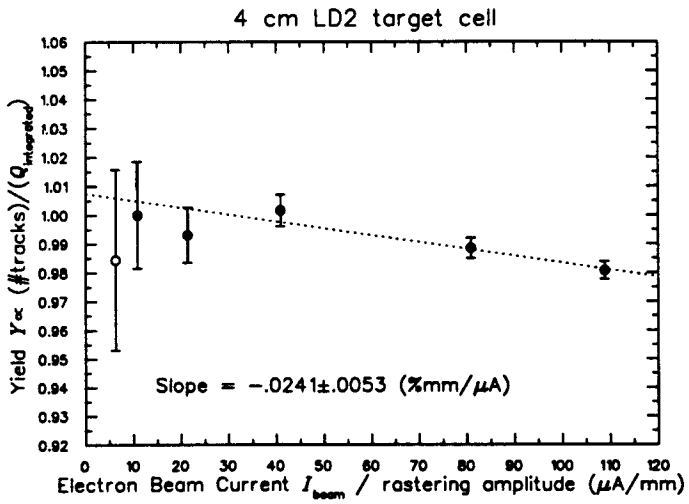

Figure B.4: The results from the September 1997 luminosity scan for the 4 cm LD2 target cell. The data point at 5 μA (marked with an open circle) was not included in the fit. The fan speed was 67 Hz and the integrated charge was measured with BCM1. The resulting slope corresponds to a 2.41 $\pm$ 0.53% yield reduction at 100 μA with a $\pm$ 1 mm rastering amplitude.

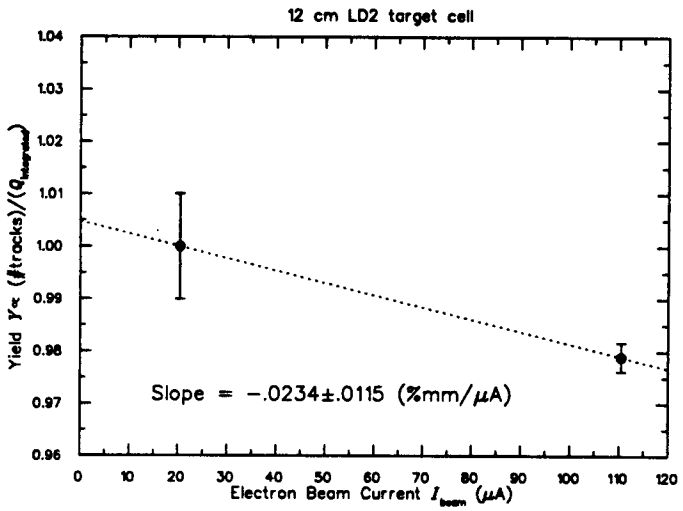

Figure B.5: The results from the September 1997 luminosity scan for the 12 cm LD2 target cell. The fan speed was 67 Hz and the integrated charge was measured with BCM1. The resulting slope corresponds to a $2.34 \pm 1.15\%$ yield reduction at 100 μA with a $\pm$ 1 mm rastering amplitude.

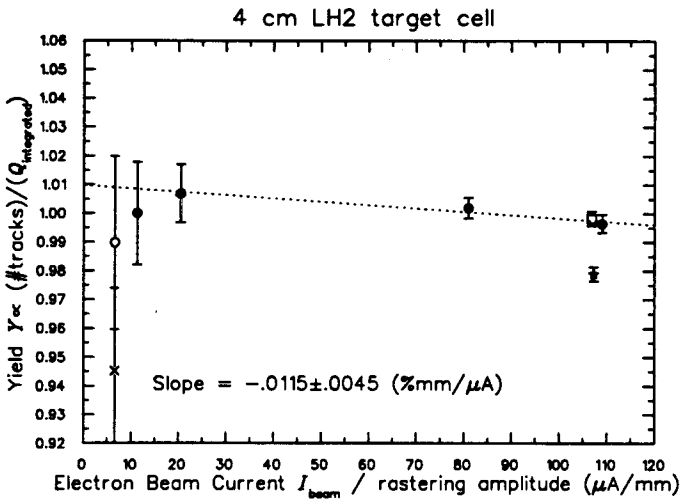

Figure B.6: The results from the September 1997 luminosity scan for the 4 cm LH2 target cell. At 5 μA a test consisting of turning off the fast raster was performed (marked with a cross). The second 5 μA data point (open circle) was neither included in the fit while the data points marked with filled circles were included. The resulting slope corresponds to a $1.15 \pm 0.45\%$ yield reduction at 100 μA with a $\pm$ 1 mm rastering amplitude. At 110 μA a fan speed test was carried out. The standard speed was f=60 Hz. The legend is: f=40 Hz (star), and f=89 Hz (open square).

Appendix C

Separation of the Deuteron Form Factors

An important goal of E94018 was to perform a separation of the deuteron charge monopole form factor G_C and the charge quadrupole form factor G_Q. Methods for separating the form factors have been discussed in references [151, 152]. The one followed here is from ref. [151]. The formalism associated with the separation will next be presented.

The deuteron form factors $G_C(Q^2)$, $G_Q(Q^2)$, and $G_M(Q^2)$ are the three unknowns while the three constraints are Equation 1.20, Equation 1.21, and Equation 1.24. These expressions can be simplified by introducing: $\alpha = \frac{1}{2} + (1 + \eta)\tan^2(\frac{\theta}{2})$, $\tilde{A} = A - 2\eta G_M^2/3$, the reduced form factor $g_C = G_C/\sqrt{\tilde{A}}$, and also the reduced form factor $g_Q = 2\eta G_Q/3\sqrt{\tilde{A}}$. Next one can write:

$$\tilde{t}_{20} = \frac{(A + B\tan^2(\frac{\theta}{2}))t_{20} + \sqrt{2}\alpha B/4(1+\eta)}{\tilde{A}}, \tag{C.1}$$

$$g_{\mathrm{Q}}^2 + 2g_{\mathrm{C}}g_{\mathrm{Q}} = p, \tag{C.2}$$

and

$$g_{\mathrm{C}}^2 + 2g_{\mathrm{Q}}^2 = 1. \tag{C.3}$$

Solving for g_Q one gets:

$$g_{\mathrm{Q}}^2 = \frac{(2+p) \pm \sqrt{\Delta}}{9}, \tag{C.4}$$

where

$$\Delta = 8(1-\mathrm{p})(\frac{1}{2}+\mathrm{p}), \tag{C.5}$$

and g_C can be expressed as:

$$g_{\mathrm{C}} = \frac{p - g_{\mathrm{Q}}^2}{2g_{\mathrm{Q}}}. \tag{C.6}$$

There will be several solutions and care must be taken in choosing the right solution. Details have been given in ref. [151].

Instead of directly using measured $B(Q^2)$ values in the separation calculation the indirect way of using measured G_{M} values was chosen as the relative errors

Kinematical point	Q (fm^{-1})	Scattering angle θ_e (°)	$A(Q^2) \times 10^4$	t_{20}	G_M
4	5.44	27.6	.567±.045	.296±.050	.000±.036
5	6.13	23.4	.232±.021	.665±.103	-.044±.059
6	6.63	20.3	.122±.012	.478±.171	-.126±.072

Table C.1: The values of the input parameters used in the deuteron form factor separation process.

Kinematical Point	Q (fm^{-1})	$G_C \times 10^2$	G_Q
4	5.44	$-.362 \pm .020$	$.0848^{+.0014}_{-.0015}$
5	6.13	$-.353^{+.103}_{-.045}$	$.033^{+.013}_{-.004}$
6	6.63	$-.203^{+.034}_{-.045}$	$.0248^{+.0019}_{-.0034}$

Table C.2: A table of the values of the separated electromagnetic form factors G_C and G_Q for kinematical data points 4, 5, and 6.

on G_M are smaller than on $B(Q^2)$. The values of $A(Q^2)$ and of G_M at the E94018 four momentum transfers were obtained from parametrizations to the existing world data [131]. The input values used in the separation process are shown in Table C.1. The dominant uncertainties in the separated form factors G_C and G_Q stem from the uncertainty in the t_{20} values. Hence an estimate of the form factors errors was made by changing in the separation calculation the input values of t_{20} within its error bar and observe the effect on the form factor values. The obtained values are shown in Table C.2. These results are discussed in Section 4.3.2.

BIBLIOGRAPHY

[1] S. Kox and E. J. Beise, Measurement of the Deuteron Tensor Polarization at Large Momentum Transfers in d(e, e' $\overleftrightarrow{d}$) Scattering, Proposal for PAC 6 of CEBAF PR-94018, JLab, 1993.

[2] S. Kox and E. J. Beise, Measurement of the Deuteron Tensor Polarization at Large Momentum Transfers in d(e, e' $\overleftrightarrow{d}$) Scattering, Proposal for PAC 8 of CEBAF PR-94018, JLab, 1994.

[3] K. S. Krane, *Introductory Nuclear Physics*, John Wiley & Sons, New York, 1988.

[4] P. E. Hodgson, E. Gadioili, and E. G. Erba, *Introductory Nuclear Physics*, Oxford University Press, New York, 1997.

[5] S. S. M. Wong, *Introductory Nuclear Physics*, Prentice-Hall, Englewood Cliffs, 1990.

[6] T. W. Donnelly et al., Ann. Phys. **169**, 247 (1986).

[7] F. Halzen and A. D. Martin, *Quarks & Leptons: An Introductory Course in Modern Particle Physics*, John Wiley & Sons, New York, 1984.

[8] D. V. Bugg and C. Wilkin, Phys. Lett. **152**, 37 (1985).

[9] D. V. Bugg and C. Wilkin, Nucl. Phys. **A467**, 575 (1987).

[10] J. Carbonell, M. B. Barbaro, and C. Wilkin, Nucl. Phys. **A529**, 653 (1991).

[11] K. Hafidi, PhD thesis, University of Paris XI/Orsay, 1999, (unpublished) DAPNIA/SPHN-99-05T.

[12] I. The, PhD thesis, Massachusetts Institute of Technology, 1992, (unpublished).

[13] M. Lacombe et al., Phys. Rev. **C21**, 861 (1980).

[14] M. M. Nagels, T. A. Rijken, and J. J. de Swart, Phys. Rev. **D17**, 768 (1978).

[15] R. V. Reid, Ann. Phys. **50**, 411 (1968).

[16] R. Machleidt, K. Holinde, and C. Elster, Phys. Rep. **149**, 1 (1987).

[17] R. B. Wiringa, V. G. J. Stoks, and R. Schiavilla, Phys. Rev. **C51**, 38 (1995).

[18] E. E. Salpeter and H. A. Bethe, Phys. Rev. **84**, 1232 (1951).

[19] J. W. van Orden, N. Devine, and F. Gross, Phys. Rev. Lett. **75**, 4369 (1995).

[20] F. Gross, J. W. van Orden, and K. Holinde, Phys. Rev. **C45**, 2094 (1992).

[21] J. W. van Orden, Technical Report CEBAF-TH-94-20, JLab, 1994, (unpublished).

[22] F. Gross and D. O. Riska, Phys. Rev. **C36**, 1928 (1987).

[23] E. Hummel and J. A. Tjon, Phys. Rev. **C42**, 423 (1990).

[24] E. Hummel and J. A. Tjon, Phys. Rev. **C49**, 21 (1994).

[25] N. K. Devine and S. J. Wallace, Phys. Rev. **C48**, R973 (1993).

[26] D. R. Phillips and S. J. Wallace, Phys. Rev. **C54**, 507 (1996).

[27] D. R. Phillips, Electron-Deuteron Scattering in Relativistic Theory of Hadrons, Technical report, 1998, arXiv:nucl-th/9811007.

[28] D. R. Phillips, S. J. Wallace, and N. K. Devine, Electron Deuteron Scattering in a Current-Conserving Description of Relativistic Bound States: Including Meson-Exchange Current Contributions, Technical report, 1999, arXiv:nucl-th/9906086.

[29] D. R. Phillips, S. J. Wallace, and N. K. Devine, Phys. Rev. **C58**, 2261 (1998).

[30] J. Carbonell and V. A. Karmanov, Nucl. Phys. **A581**, 625 (1994).

[31] J. Carbonell, B. Desplanques, V. A. Karmanov, and J.-F. Mathiot, Phys. Rep. **300**, 215 (1998).

[32] J. Carbonell and V. A. Karmanov, Eur. Phys. J. **A6**, 9 (1999).

[33] F. Coester and A. Ostebee, Phys. Rev. **C11**, 1836 (1975).

[34] P. L. Chung, F. Coester, B. D. Keister, and W. N. Polyzou, Phys. Rev. **C37**, 2000 (1988).

[35] L. L. Frankfurt, T. Frederico, and M. Strikman, Phys. Rev. **C48**, 2182 (1993).

[36] A. Buchmann, Y. Yamauchi, and A. Faessler, Nucl. Phys. **A496**, 621 (1989).

[37] H. Ito and A. Faessler, Nucl. Phys. **A470**, 626 (1987).

[38] H. Ito and L. S. Kisslinger, Phys. Rev. **C40**, 887 (1989).

[39] E. Lomon et al., Ann. Phys. **125**, 309 (1980).

[40] P. LaFrance and E. L. Lomon, Phys. Rev. **D34**, 1341 (1986).

[41] P. Gonzalez, P. LaFrance, and E. L. Lomon, Phys. Rev. **D35**, 2142 (1987).

[42] P. G. Blunden, W. R. Greenberg, and E. L. Lomon, Phys. Rev. **C40**, 1541 (1989).

[43] E. L. Lomon, Quark Substructure and Isobar Effects on Deuteron Form Factors, Technical report, 2000, arXiv:nucl-th/0002026.

[44] E. Braaten, S. Townsend, and L. Carson, Phys. Lett. **B235**, 147 (1990).

[45] E. Witten, Nucl. Phys. **B223**, 422 (1983).

[46] E. Nyman and D. O. Riska, Nucl. Phys. **A468**, 473 (1987).

[47] C. E. Carlson and F. Gross, Phys. Rev. Lett. **53**, 127 (1984).

[48] S. Brodsky and J. R. Hiller, Phys. Rev. **D46**, 2141 (1992).

[49] C. E. Carlson, Nucl. Phys. **A508**, 481c (1990).

[50] A. Kobushkin and A. Syamtomov, Phys. Rev. **D49**, 1637 (1994).

[51] A. Kobushkin and A. Syamtomov, Phys. At. Nucl. **58**, 1477 (1995).

[52] M. E. Schulze et al., Phys. Rev. Lett. **52**, 597 (1984).

[53] M. E. Schulze, PhD thesis, Massachusetts Institute of Technology, 1983, (unpublished).

[54] M. Garçon et al., Nucl. Phys. **A508**, 445c (1990).

[55] I. The et al., Phys. Rev. Lett. **67**, 173 (1991).

[56] M. Garçon et al., Phys. Rev. **C49**, 2516 (1994).

[57] V. F. Dmitriev et al., Phys. Lett. **157B**, 143 (1985).

[58] B. B. Voitsekhovskii et al., JETP Lett. **43**, 733 (1986).

[59] A. V. Evstigneev et al., Nucl. Instru. Methd. **A238**, 12 (1985).

[60] R. Gilman et al., Phys. Rev. Lett. **65**, 1733 (1990).

[61] Z.-L. Zhou et al., Phys. Rev. Lett. **82**, 687 (1999).

[62] P. de Witt Huberts et al., Nucl. Phys. **A553**, 845c (1993).

[63] M. Ferro-Luzzi et al., Phys. Rev. Lett. **77**, 2630 (1996).

[64] M. Bouwhuis et al., Phys. Rev. Lett. **82**, 3755 (1999).

[65] M. Bouwhuis, PhD thesis, Utrecht University, 1998, (unpublished) ISBN 90-393-1754-2.

[66] A. Boudard, CERN Courier **39** (1999).

[67] J. Arvieux et al., Nucl. Instru. Methd. **A273**, 48 (1988).

[68] A. Boudard, PhD thesis, 1984, (unpublished) CEA-n-2386.

[69] E. J. Stephenson, Notes on the Sign of t_{21}, 1996, Internal Report of the t_{20} Collaboration.

[70] J. Arvieux, F. Benmokhtar, A. Frahi, and J.-S. Réal, Correction of the Beam Depolarization in Calibration, 1998, Internal Report of the t_{20} Collaboration.

[71] L. Eyraud, PhD thesis, Joseph Fourier University, 1998, (unpublished) Internal Report ISN-98-101 of the ISN-institute, Grenoble.

[72] L. Cardman, Nucl. Phys. News **6** (1996).

[73] C. S. Armstrong, PhD thesis, College of William & Mary, 1998, (unpublished).

[74] J. R. Delayen, Development of an Upgrade of the CEBAF Acceleration System, Technical Report JLAB-ACC-98-08, JLab, 1998, (unpublished).

[75] J. R. Arrington, PhD thesis, California Institute of Technology, 1998, (unpublished).

[76] B. M. Dunham, Jefferson Lab, A Status Report, Technical Report JLAB-ACC-96-01, JLab, 1996, (unpublished).

[77] G. A. Krafft, Status of the Continuous Electron Beam Accelerator Facility, in *Proc. of the 1994 International Linac Conference*, pages 9–13, Tsukuba, Japan, 1994.

[78] R. Legg, Operating Experience at CEBAF, in *Proc. of the 1995 Eur. Part. Accel. Conf.*, 1995.

[79] G. Niculescu, PhD thesis, Hampton University, 1998, (unpublished).

[80] C. Armstrong, Beam Current Measurement in Hall C, Technical report, JLab Hall C, 1996, (unpublished).

[81] G. Niculescu, Resonant Cavities used as Beam Current Monitors, Technical report, JLab Hall C, 1995, (unpublished).

[82] D. Mack, Current Monitoring in Hall C, Technical report, JLab Hall C, 1997, (unpublished).

[83] K. B. Unser, The Parametric Current Transformer, a Beam Current Monitor Developed for LEP, Technical Report CERN-SL/91-42-BI, CERN, 1991, (unpublished).

[84] J. Bergoz, *Parametric Current Transformer Instruction Manual*, 01170 Crozet, France, 1991.

[85] C. Bochna, PhD thesis, University of Illinois at Urbana-Champaign, 1999, (unpublished).

[86] C. Yan et al., Nucl. Instru. Methd. **A365**, 261 (1995).

[87] P. Gueye et al., Summary of BPM/Superharp Comparsion, Technical report, JLab Hall C, 1996, (unpublished).

[88] G. Krafft et al., How the Linac Beam Position Monitors "Work", Technical Report CEBAF-TN-93-004, JLab, 1993, (unpublished).

[89] D. Meekins, PhD thesis, College of William & Mary, 1998, (unpublished).

[90] B. Terbrug, PhD thesis, University of Illinois at Urbana-Champaign, 1999, (unpublished).

[91] C. Yan et al., Nucl. Instru. Methd. **A365**, 46 (1995).

[92] J. Reinhold, Phase Corrections for the Hall C Fast Raster, Technical report, JLab Hall C, 1996, (unpublished).

[93] J. Reinhold, Use of Fast Raster Information in the Engine, Technical report, JLab Hall C, 1996, (unpublished).

[94] D. van Westrum, PhD thesis, University of Colorado, 1998, (unpublished).

[95] P. Gueye et al., Hall c Beam Energy Measurement, Technical report, JLab Hall C, 1996, (unpublished).

[96] P. Gueye et al., Hall C Beam Energy Correction: Hysteresis with Different Current Limits and Beam Energy Monitoring by the Hall C Arc Spectrometer, Technical report, JLab Hall C, 1998, (unpublished).

[97] D. Mack, 1998, JLab Hall C Electronic Logbook, Entry number 4209.

[98] J. Mitchell, Hall C Cryogenic Target and Scattering Chamber, Technical report, JLab Hall C, 1995, (unpublished).

[99] J. Mitchell, Design Proposal for the CEBAF Hall C Cryogenic Target Heat Exchangers, Technical report, JLab Hall C, 1995, (unpublished).

[100] A. Aron, 1996, private communication.

[101] J. Mitchell, Hall C Cryogenic Target and Scattering Chamber System Controls, Technical report, JLab Hall C, 1995, (unpublished).

[102] K. Gustafsson, Hall C Target Control Data Logging and Retrieval, Technical report, JLab Hall C, 1996, (unpublished).

[103] F. Duncan, Hall C cryogenic Target User Manual, Technical report, JLab Hall C, 1997, (unpublished).

[104] B. Terburg, Cebaf hall C Cryogenic Target Documentation for the Expert Volume i & ii, Technical report, JLab Hall C, 1996, (unpublished).

[105] M. Wiseman et al., High Power Electron Beam Dumps at CEBAF, Technical Report JLAB-ACT-97-02, JLab, 1997, (unpublished).

[106] R. M. Mohring, PhD thesis, University of Maryland, College Park, 1999, (unpublished).

[107] A. Honegger, PhD thesis, University of Basel, 1999, (unpublished).

[108] O. K. Baker et al., Nucl. Instru. Methd. **A367**, 92 (1995).

[109] F. Merchez et al., Nucl. Instru. Methd. **A275**, 133 (1989).

[110] T. Motobayashi et al., Phys. Lett. **B233**, 69 (1989).

[111] S. Kox et al., Phys. Lett. **B266**, 264 (1991).

[112] S. Kox et al., Nucl. Phys. **A556**, 621 (1993).

[113] S. Kox et al., Nucl. Instru. Methd. **A346**, 527 (1994).

[114] J.-S. Réal, PhD thesis, Joseph Fourier University, 1994, (unpublished) Internal Report ISN-94-05 of the ISN-institute, Grenoble.

[115] C. Furget et al., Phys. Rev. **C51**, 1562 (1995).

[116] J. Goy, PhD thesis, Joseph Fourier University, 1997, (unpublished).

[117] D. Pitz, PhD thesis, University of Paris XI/Orsay, 1999, (unpublished).

[118] M. K. Jones et al., Status of the Focal Plane Polarimeter for Hall A at TJNAF, in *AIP Conference Proceedings 412, 6th Conference,Intersections between Particle and Nuclear Physics*, edited by T. W. Donnelly, page 342, Big Sky, Montana, 1997.

[119] J. Ball, Polder lh_2 target geometry, 1998, Internal Report of the t_{20} Collaboration.

[120] W. Zhao, PhD thesis, Massachusetts Institute of Technology, 1999, (unpublished).

[121] D. Abbott et al., The coda system and its performance in the first online experiments at CEBAF, in *Proceedings of the 1995 IEEE Conference on Real-Time Computing Applications in Nuclear, Particle and Plasma Physics*, pages 147–151, 1995.

[122] Experimental and Physics Industrial Control System (EPICS), 1984, Los Alamos National Laboratories.

[123] J. N. Butler et al., Physics Today , 50 (1996).

[124] L. Lu, Summary of t_{20} Data Analysis for Point#1 and Point#2, 1998, Internal Report of the t_{20} Collaboration.

[125] D. Abbott et al., Phys. Rev. Lett. **82**, 1379 (1999).

[126] Physica, URL http://www.triumf.ca/physica/html/homepage.html.

[127] Physics Analysis Workstation, URL http://wwwinfo.cern.ch/asd/paw/index.html.

[128] Perl, URL http://www.perl.com/pace/pub.

[129] F. James and M. Roos, Comput. Phys. Commun. **10**, 343 (1975), CERN D506 (Long Writeup).

[130] J.-S. Réal, 1999, private communication.

[131] Proceedings of the t_{20} Collaboration Meeting in Boston, 1998.

[132] M. Garçon, Note on Statistical Errors for t_{20}, 1997, Internal Report of the t_{20} Collaboration.

[133] D. Abbott et al., Measurement of Tensor Polarisation in Elastic Electron-Deuteron Scattering at Large Momentum Transfer, Technical report, 2000, arXiv:nucl-ex/0001006.

[134] Particle Data Group, Eur. Phys. J. **C3**, 69 (1998).

[135] Proceedings of the t_{20} Collaboration Meeting in Grenoble, 1998.

[136] J.-S. Réal, 2000, private communication.

[137] D. Abbott et al., Eur. Phys. J. **A 7**, 421 (2000).

[138] J. Gomez and G. Petratos, Measurement of the Electric and Magnetic Structure Functions of the Deuteron at Large Momentum Transfers, Proposal E91026, JLab, 1991.

[139] H. Henning et al., Phys. Rev. **C52**, R471 (1995).

[140] M. Garçon, 1999, private communication.

[141] R. Gilman, Prospects for t_{20} with 12 GeV Beam, in *JLab Physics and Instrumentation with 6-12 GeV Beams Workshop*, 1998.

[142] W. Turchinetz, Deuteron Elastic Form Factors: Opportunity for BLAST?, in *Proceedings of the Second Workshop on Electronuclear Physics with Internal Targets and the Bates Large Acceptance Spectrometer Toroid (BLAST)*, MIT, Cambridge, Massachusetts, 1998, http://mitbates.mit.edu/blast/workshop/proceedings/.

[143] W. Bertozzi et al., A Study of the Deuteron Structure using Tensor Polarized Deuterium and the BLAST detector, Proposal to the pac of mit-bates, MIT-Bates, 2000.

[144] K. Gustafsson, Cryotarget Density Dependence on Beam Current, Technical report, JLab Hall C, 1996, (unpublished).

[145] J. Mitchell, Global and Local Beam Heating in the Hall C Cryo Targets, Technical report, JLab Hall C, 1995, (unpublished).

[146] J. Dunne, Sources of Error in Determining the Target Density, Technical report, JLab Hall C, 1996, (unpublished).

[147] J. Mitchell, High Power Test of Hall C Cryogenic Target, Technical report, JLab Hall C, 1996, (unpublished).

[148] F. Duncan, 1996, private communication.

[149] D. J. Tritton, *Physical Fluid Dynamics*, Oxford University Press, New York, 1988, ISBN 0-19-854493-6.

[150] G. K. White, *Experimental Techniques in Low-Temperature Physics*, Oxford University Press, New York, 1987, ISBN 0-19-851381X.

[151] M. Garçon, Considerations on the Form Factors Extraction, 1999, Internal Report of the t_{20} Collaboration.

[152] W. Zhao et al., Note on Separation of G_C and G_Q, 1998, Internal Report of the t_{20} Collaboration.

Curriculum Vitae

Kenneth Kurt Severus Gustafsson

The author was born on November 24, 1968 in Pargas, Finland. He graduated from Pargas svenska gymnasium in May 1987. From 1987 to 1992 (apart from a military service period from June 1988 to May 1989) he attended the University of Helsinki where he received his M.S. (thesis) in November 1992. He received his M.S. (non-thesis) from University of Maryland, College Park in August 1996.

Publications:

Measurement of Tensor Polarisation in Elastic Electron-Deuteron Scattering at Large Momentum Transfer, D. Abbott, et al. (JLab E94-018 Collaboration), Phys. Rev. Lett., **84**, 5053-5057 (2000).

Phenomenology of the Deuteron Electromagnetic Form Factors, D. Abbott, et al., (JLab E94-018 Collaboration), Eur. Phys. J. A **7**, 421-427 (2000).

Coherent π^0 Photoproduction on the Deuteron up to 4 GeV, D. Meekins, et al. (JLab E89-012 Collaboration), Phys. Rev. C, **60**, R052201 (1999).

Precise Measurement of the Deuteron Elastic Structure Function $A(Q^2)$, D. Abbott, et al. (JLab E94-018 Collaboration), Phys. Rev. Lett., **82**, 1379-1382 (1999).

Measurements of Deuteron Photodisintegration up to 4.0 GeV, C. Bochna, et al. (JLab E89-012 Collaboration), Phys. Rev. Lett., **81**, 4576-4579 (1998).

Longitudinal and Transverse Cross Sections in the $^1H(e,e'K^+)\Lambda$ *Reaction*, G. Niculescu, et al. (JLab E93-018 Collaboration), Phys. Rev. Lett., **81**, 1805-1808 (1998).

Bag Structure of the Infinite Order Skyrmion, K. Gustafsson and D. O. Riska, Nucl. Phys. **A571**, 645-666 (1994).

Talks Presented:

Measurement of the Tensor Moments t_{20}, t_{21}, and t_{22} in the Momentum Transfer, Q^2, Range of 0.65 GeV^2 to 1.75 GeV^2 in Elastic ed-scattering, American Physical Society, Atlanta, Georgia, March 1999.

Measurement of t_{20} in the Momentum Transfer, Q, range of 4.1 fm^{-1} to 6.8 fm^{-1} in Elastic ed-scattering, American Physical Society, Columbus, Ohio, April 1998.

Results of Density Studies of the TJNAF Hall C Cryotarget, American Physical Society, Washington D.C., April 1997.

Hall C Cryotarget: Error in Target Density $\times$ Target Length, Pion Form Factor Workshop, Jefferson Lab, January 1996.